Non-Invasive Determination of the Location and Distribution of Free-Phase Dense Nonaqueous Phase Liquids (DNAPL) by Seismic Reflection Techniques

Final Report

Tasks 1, 2, 3, 4, 5,
6, 7, 8, 9, 10, and 11

Reporting Period Stating Date: September, 1998

Reporting Period Ending Date: December, 2002

by

Michael G. Waddell
William J. Domoracki
&
Jerome Eyer

January, 2003

DOE AWARD NUMBER DE-AR26-98FT40369

This page is intentionality blank

Non-Invasive Determination of the Location and Distribution of Free-Phase Dense Nonaqueous Phase Liquids (DNAPL) by Seismic Reflection Techniques

Final Report

Tasks 1, 2, and 3

Reporting Period Starting Date: September, 1998

Reporting Period Ending Date: December, 2002

by

Michael G. Waddell
William J. Domoracki

&
Jerome Eyer

Earth Sciences and Resources Institute
University of South Carolina
Columbia, South Carolina

January, 2003

DOE Award Number DE-AR26-98FT40369

Disclaimer

This report was prepared as an account of work sponsored by an agency of the United States Government. Neither the United States Government nor any agency thereof, nor any of their employees, makes any warranty, express or implied, or assumes any legal liability or responsibility, for the accuracy, completeness, or usefulness of any information, apparatus, product, or process disclosed, or represents that its use would not infringe privately owned rights. Reference herein to any specific commercial product, process, or service by trade name, trademark, manufacturer, or otherwise does not necessarily constitute or imply its endorsement, recommendation, or favoring by the United States Government or any agency thereof. The views and opinions of authors expressed herein do not necessarily state or reflect those of the United States Government or any agency thereof.

Abstract

The Earth Sciences and Resources Institute, University of South Carolina is conducting a proof of concept study to determine the location and distribution of subsurface DNAPL carbon tetrachloride (CCl_4) contamination at the 216-Z-9 crib, 200 West area, DOE Hanford Site, Washington by use of two-dimensional high-resolution seismic reflection surveys and borehole geophysical data. The study makes use of recent advances in seismic reflection amplitude versus offset (AVO) technology to directly detect the presence of subsurface DNAPL. The techniques proposed are noninvasive means of site characterization and direct free-phase DNAPL detection.

This final report covers the results of Tasks 1, 2, and 3. Task (1) contains site evaluation and seismic modeling studies. The site evaluation consists of identifying and collecting preexisting geological and geophysical information regarding subsurface structure and the presence and quantity of DNAPL. The seismic modeling studies were undertaken to determine the likelihood that an AVO response exists and its probable manifestation. Task (2) is the design and acquisition of 2-D seismic reflection data to image areas of probable high concentration of DNAPL. Task (3) is the processing and interpretation of the 2-D data.

During the commission of these tasks four seismic reflection profiles were collected. Subsurface velocity information was obtained by vertical seismic profile surveys in three wells. The interpretation of these data is in two parts. Part one is the construction and interpretation of structural contour maps of the contact between the Hanford Fine unit and the underlying Plio/Pleistocene unit and of the contact between the Plio/Pleistocene unit and the underlying caliche layer. These two contacts were determined to be the most likely surfaces to contain the highest concentration CCl_4. Part two of the interpretation uses the results of the AVO modeling to locate any seismic amplitude anomalies that might be associated with the presence of high concentrations of CCl_4. Based on the modeling results three different methods of AVO analysis were preformed on the seismic data: enhanced amplitude stacks, offset range limited stacks, and gradient stacks. Seismic models indicate that the reflection from the contact between the Hanford Fine and the Plio/Pleistocene should exhibit amplitude variations where there are high concentrations of CCl_4. A series of different scenarios were modeled. The first scenario is the Hanford Fine pores are 100% saturated with CCl_4 and the underlying Plio/Pleistocene pores are saturated with air. In this scenario the reflection coefficients are slightly negative at the small angles of incidence and become increasing more negative at the larger angles of incidence (dim-out). The second scenario is the Hanford Fine pores are saturated with air and Plio/Pleistocene pores are saturated with CCl_4. In this scenario the reflection coefficients are slightly positive at the small angles of incidence and become negative at the large angles of incidence (polarity reversal). Finally the third scenario is both the Hanford Fine and the Plio/Pleistocene pores are saturated CCl_4. In this scenario the reflection coefficients at the small angles of incidence are slightly positive, but much less than background response, and with increasing angle of incidence the reflection coefficients become slightly more positive. On the field data areas where extraction wells have high concentrations of CCl_4 a corresponding dim-out and/or a polarity reversal is noted.

At the contact between the Plio/Pleistocene and the caliche the models indicate that the presence of CCl_4 should cause a noticeable positive increase in the seismic amplitude (bright spot) if the Plio/Pleistocene pores are saturated with air and the caliche pores are saturated with CCl_4. If the Plio/Pleistocene pores are saturated with CCl_4 and the caliche pores are saturated with air the reflection coefficients on the near offsets are negative and the reflection coefficients on the far offsets

are positive (polarity reversal). The last scenario considers the situation where both the Plio/Pleistocene and caliche pores are saturated with CCl_4. In this case the reflection coefficients are slightly positive and become more positive as the angles of incidence increase. On the seismic data the amplitudes along the Plio/Pleistocene-caliche contact increase in areas where well control indicates high concentrations of CCl_4.

Based upon the results of Tasks 1-3 it appears likely that AVO seismic techniques can be used to detect high concentrations of CCl_4. This conclusion, however, is predicated upon the assumption that the seismic models are correct. As a cautionary note, some of the model parameters were, by necessity, based upon mathematically derived results. To verify the results some of the AVO anomalies should be tested via drilling or direct push methods.

Table of Contents

List of Figures

List of Tables

List of Enclosures

1.0 Introduction

This final report is for Tasks 1-3 of project DE-AR26-98FT40369. Subsequent to the success of using high-resolution seismic reflection surveying and amplitude versus offset (AVO) analysis to image DNAPL in the subsurface at the DOE Savannah River Site M area, South Carolina (Waddell and Domoracki, 1997), it was proposed that another site with drastically different geologic setting be tested using these techniques. The area adjacent to the 216-Z-9 crib at the 200 West area, DOE Hanford Site, Washington was selected (Figure 1). When this project was conceived assumptions were made as to the availability of certain types of data, e.g. limited amounts of borehole geophysical logs and existing core data. These assumptions were not ill conceived, but were based upon the authors' experience doing similar type of work at other DOE sites. As a contingency, it was proposed that if data were not available, one test hole would be drilled to obtain the data necessary for modeling and seismic acquisition design. However, because of budget constraints and the cost of drilling a well in the 200 West area, a new well could not be drilled.

2.0 Executive Summary

This final report is for Tasks 1-3 of project DE-AR26-98FT40369. After the success of using high-resolution seismic reflection surveying and applying amplitude versus offset (AVO) analysis to image dense non-aqueous phase liquids (DNAPL) in the subsurface at the DOE Savannah River Site M area, South Carolina (Waddell and Domoracki, 1997) it was proposed that another site with different geologic conditions be tested using this technique. The new study area is adjacent to the 216-Z-9 crib at the 200 West area, DOE Hanford Site, Washington. At 200 West area there is a large subsurface plume of highly concentrated carbon tetrachloride (CCl_4). When this project was conceived assumptions were made as to the availability of certain types of data, e.g. limited amounts of borehole geophysical logs and existing core data. Unfortunately, these assumptions were overly optimistic. As a contingency it was proposed that if certain data were not available, one test hole would be drilled to gather data necessary for modeling and seismic acquisition design. However, due to budget constraints and the cost of drilling a well at the 200 West area, a well could not be drilled.

The initial proposed research was a 14 month proof of concept study to determine the location and distribution of subsurface DNAPL (carbon tetrachloride) contamination at the 200 West area, DOE Hanford Site by the use of two-dimensional high-resolution seismic reflection data and borehole geophysical surveys. The specific project objectives were:

- Subsurface imaging of geologic sinks where DNAPL can pool.
- Direct detection of DNAPL by use of the seismic reflection amplitude versus offset (AVO) method.

Task 1 consisted of a site visit to familiarize Earth Sciences and Resources Institute personnel with the site geology at the 200 West area and to collect any pertinent geologic and geophysical data. After the site visit, it was necessary to return to the 200 West area and collect

compressional (P) and shear (S) wave velocity data and density information from wells in the vicinity of the Z-9 crib.

The velocity and density data were used in Task 2 for design and collection of the 2-D high-resolution seismic reflection data. In Task 2, four seismic lines were acquired using a 120 channel 24 bit seismograph and a high frequency vibrator source. The source and receiver intervals were only one meter (3.28 ft.) apart to yield dense subsurface coverage.

Task 3 dealt with the processing of the four seismic lines and interpretation of the 2-D data. The quality of the seismic data was good and two principal horizons were mapped on the seismic lines. The first horizon is the contact between the Hanford Fine and the Plio/Pleistocene (Figures 23, 25-27). The second horizon is contact between the Plio/Pleistocene and the caliche layer (Figures 23, 25-27). Existing well data indicates that these two layers are located where the highest concentrations of CCl_4 are found.

Amplitude versus offset (AVO) analysis involves the comparison of modeled responses with field data to find a deviation from an expected background response. The expected background response is usually assumed to be water saturated rock. In this study the background response is an air saturated aquifer. If DNAPL is present in free-phase and in large enough quantities, then AVO analysis, similar to that used in the petroleum industry, can be done to determine a response. An important aspect of this project is the modeling to determine the type of seismic AVO response, if any that the presence of CCl_4 would cause. In this final report the full Zoeppritz equations (1919) (modified by Graul, 2001) instead of the commonly used Shuey's (1985) approximation of the Zoeppritz equations is used to express the angle dependent reflectivity in terms of P wave velocity, bulk density, and Poisson's ratio.

Seismic models indicate that the contact between the Hanford Fine and the Plio/Pleistocene should exhibit seismic reflection amplitude variations where high concentrations of CCl_4 are present. A series of different scenarios were modeled for this interface. The first scenario assumes that the Hanford Fine pores are 100% saturated with CCl_4 and the underlying Plio/Pleistocene pores are saturated with air. In this scenario the reflection coefficients are slightly negative at the small angles of incidence and become increasing more negative at the larger angles of incidence (dim-out). The second scenario assumes that the Hanford Fine pores are saturated with air and Plio/Pleistocene pores are saturated with CCl_4. In this scenario the reflection coefficients are slightly positive at the small angles of incidence and become negative at the large offsets of incidence (polarity reversal). Finally the third scenario assumes that both the Hanford Fine and the Plio/Pleistocene pores are saturated CCl_4. In this scenario the reflection coefficients at the small angles of incidence are positive, but much less than background response, and with increasing angle of incidence the reflection coefficients become slightly more positive. Based on the modeling results three different methods of AVO analysis were preformed on the seismic data, the first was enhanced amplitude stacks, the second was offset range limited stacks, and the third was gradient stacks. In areas where extraction wells have high concentrations of CCl_4 a corresponding dim-out and/or a polarity reversal is noted on the seismic data.

At the contact between the Plio/Pleistocene and the caliche the models indicate that if the Plio/Pleistocene pores are air-filled and the caliche pores are saturated with CCl_4 the presence of CCl_4 should cause a noticeable positive increase in the seismic amplitude (bright spot). If the Plio/Pleistocene pores are saturated with CCl_4 and the caliche pores are saturated with air, the reflection coefficients on the near offsets are negative and the reflection coefficients on the far offsets are positive (polarity reversal). The last scenario is that both the Plio/Pleistocene and caliche pores are saturated with CCl_4. In this case the reflection coefficients are slightly positive and become more positive as the angle of incidence increases. On the seismic data the amplitude along the Plio/Pleistocene-caliche contact increases in areas where well control indicates high concentrations of CCl_4. This suggests that the seismic reflection amplitudes are affected by the presence of CCl_4 in agreement with the models.

It appears that the surface seismic data imaged areas where seismic amplitude anomalies are associated with high concentrations of carbon tetrachloride. This assertion has to be taken with some caution. The P wave, S wave, and density values for the fluid-filled rock were mathematically derived. It is recommended that either a new well be drilled or an existing well deepened so that core samples from the Hanford Fine unit, Plio/Pleistocene unit, and caliche layer can be taken in order to acquire better density and pore content information.

3.0 Project Objectives

The research as initially proposed was a 14 month proof of concept study to determine the location and distribution of subsurface DNAPL (carbon tetrachloride) contamination at the 200 West area, DOE Hanford Site by the use of two and three-dimensional high-resolution seismic reflection data and borehole geophysical surveys. The specific objectives of the research were:

- Subsurface imaging of geologic sinks where DNAPL can pool.
- Direct detection of DNAPL by use of the seismic reflection amplitude versus offset (AVO) method.

All the project objectives would be accomplished in three tasks as outlined in the modified management plan.

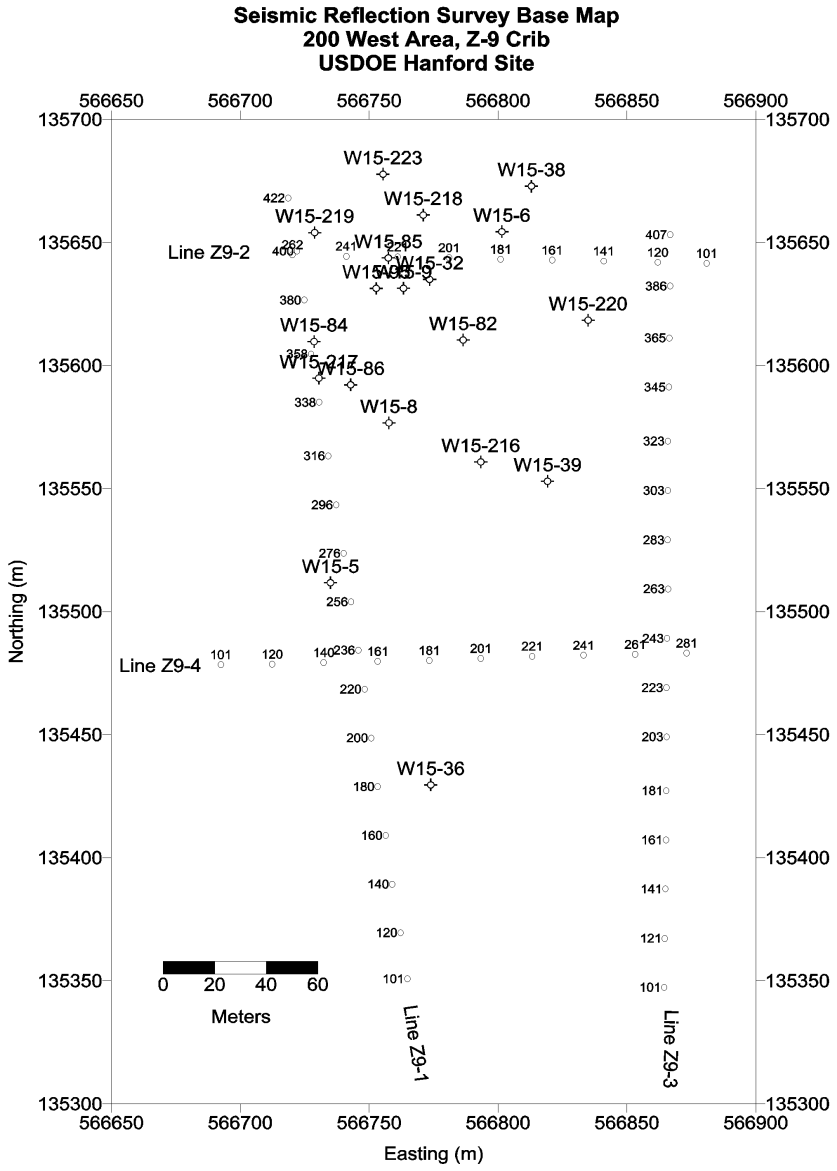

Figure 1. Location map of the seismic reflection lines and key wells at the 216-Z-9 crib, 200 West area, DOE Hanford Site.

4.0 General Geology of Hanford Area

The Department of Energy Hanford Site is located within the Pasco Basin in southeastern Washington state. The Pasco Basin is a structural basin on the Columbia Plateau formed in the pre-Miocene or early Miocene. Major structural elements of the basin include east-west trending synclines and anticlines. Those that are present in the area of this project, the 200 West area, include the Cold Creek syncline and the apparent unnamed anticline that encompasses the Gable Mountain area. The 200 West site is located on the north flank of the Cold Creek syncline (Figure 2).

The Pasco Basin contains Miocene continental flood basalts, Pliocene to early Pleistocene fluvial detritus, Pleistocene glaciofluvial outwash, and a thin layer of Holocene sands, silts and clay (Figure 3). In the area of the 200 West facility more than 150 meters (500 ft.) of these sediments overlie the Miocene basalt units. Because of the depositional history of these sediments they are extremely heterogenous and facies changes occur over very short distances.

The sediments were derived from provenances both local and distant. Local sources were the Miocene basaltic outcrops in the immediate area within the Pasco Basin. Distant sources include the Idaho Batholith, Idaho portion of the Rocky Mountains, the Cascade Mountains to the west, the Okanogen Highlands, and the Wallowa Terrane units. These distant sources contributed detritus primarily during the Pleistocene cataclysmic floods which occurred during the middle Wisconsin interglacial period. These deposits are between 11,250 to 18,000 years b.p. (Waitt, 1980; Baker and Bunder, 1985).

4.1 Previous Work and New Data Generated

Some, but not all, of the major references are noted under the *References* section. Those that are noted are those that were used in this report for background information. These were mostly working documents and publications dealing specifically with the Hanford site and the 200 West area.

This report integrates information generated from previous work with data generated with the current DOE sponsored project. New data generated in the 200 West area consists primarily of seismic profile data and vertical seismic profile data. These are discussed in detail in other portions of this report. We have drawn extensively from past projects in order to build on the knowledge of a contaminant movement in the near subsurface environment for this site.

4.2 Correlation of Stratigraphic Units

In the fluvial environment that exists in the Pasco Basin it is exceptionally difficult to correlate sedimentary units. Facies changes are rapid and in the coarse clastic facies that exist there fossils are not present. In some of the fine grained sediments and in the lacustrine units some paleontology and palynology data has been generated in order to assign relative ages. Absolute dating has also been previously done in examining timing of the flood events in the Pleistocene units. In the current project, no additional dating has been attempted.

In the 216-Z-9 crib area well 299-W15-32 was used to anchor the interpretations. A vertical seismic profile was collected in the well and an attempt was made to correlate the sample log, done in 1995 when the well was drilled, with the VSP. The interpretation of the units and ages is a combination of those data. Velocities do not necessarily correlate with these picks because of rapid lithology changes. Velocities are indicative of these lithology changes, particularly where the size of sediment particles change rapidly and the contrast causes large velocity differences. Ages of the units are not based on fossil or absolute dating methods but are tied to previously dated units by other work at the 200 West area at Hanford.

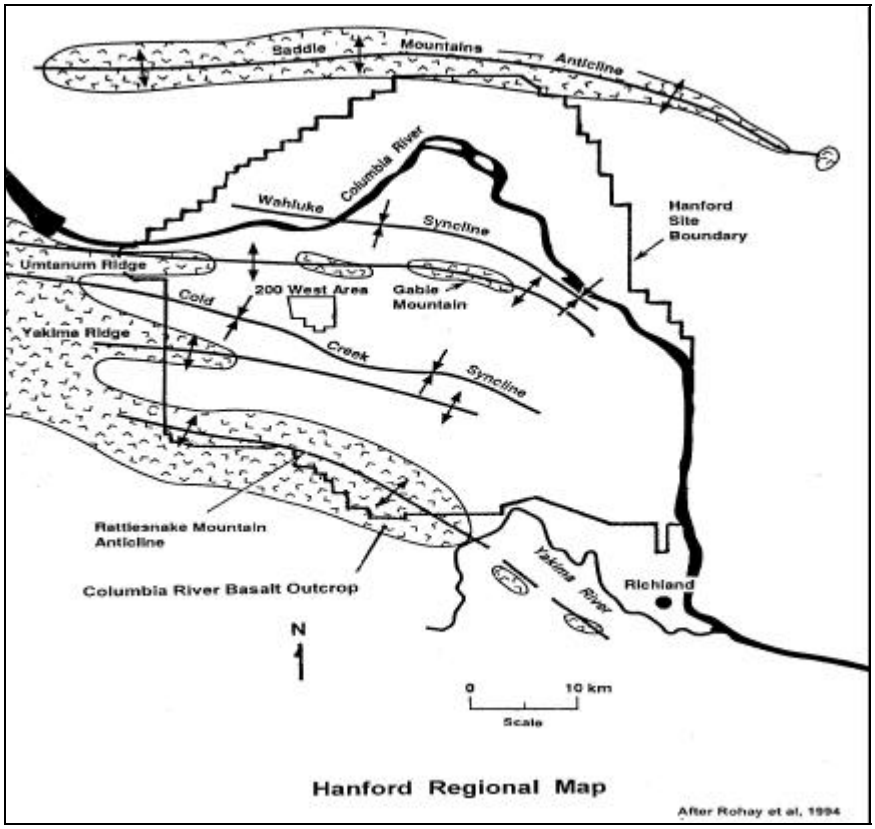

Figure 2. Generalized regional geologic map of the Hanford Site. After (Rohay et al., 1994).

Generalized Stratigraphy of the 200W Site, Hanford			
Age	Strat. Unit	Subdivisions	Descriptions
Holocene			Eolian sands which form a veneer on the surface
Pleistocene	**Hanford**	***Upper Fine***	Fining upward sands; gravely sand; Discontinuous unit
		Upper Coarse	Gravels with interbedded sands
		Fine	Sand with some gravel
		Lower Coarse	Gravels
		Lower Fine	Interbedded silt and fine sand
Plio - Pleistocene		***Locally Derived***	Reworked sediments from Ringold and Basalt; gravels, sands, silts with carbonate cemented sandy gravels
		Caliche Zone	Carbonated cemented/fossil soil zone
Pliocene	**Ringold**	***Upper Ringold Unit***	Fluvial and lacustrine fine grained sediments; pinches out in the 200 West area
Miocene ? ? ?		***Unit E***	Fluvial gravels and sands
		Lower mud	Clays and silts; overbank deposits
		Unit A	Fluvial gravels and sands
Miocene	**Columbia River**	***Basalts***	Tholeiitic basalts

Figure 3. Generalized stratigraphic column for the 200 West area at Hanford. Note that at the 216-Z-9 crib area the Hanford Fine directly overlies the Plio/Pleistocene.

5.0 Amplitude Versus Offset Modeling: Results and Discussion

5.1 Theory

In the 1960's petroleum companies recognized that in young sediments (Tertiary age) large seismic amplitudes were associated with gas saturated sands. However, it was soon realized that not all large seismic amplitudes represented hydrocarbon accumulations. The classification of these early normal incidence (NI) reflectivity (bright spot) anomalies involved involved three different scenarios based upon a water saturated state and a hydrocarbon saturated state (for this discussion a sand/shale or sand/clay interface). The scenarios are classified by changes in NI reflectivity from a water saturated sand to a gas or hydrocarbon bearing sand.

The three scenarios are:

- Dim-out: a large positive amplitude that is reduced to a smaller positive amplitude,
- Phase reversal: a small positive amplitude that changes to small negative amplitude and
- Bright spot: a negative amplitude increasing to a large negative amplitude.

The dim-out is generally associated with a large acoustic impedance contrast and is a technique for inferring lithology. Bright spot anomalies are generally used for interpreting lithology and estimating sand thickness. Phase reversal reflections are not generally reliable because geologic features (e.g. faults) can cause the reflections to appear to reverse phase. Thus, a reflection phase reversal does not necessarily indicate a change in lithology (Verm and Hilterman, 1995). The bright spot technique was the first direct hydrocarbon indicator.

In 1984 Ostrander published a article entitled "Plane-wave reflection coefficients for gas sands at non-normal angles of incidence." Ostrander investigated the phenomenon of compressional wave reflection amplitude variation with angle of incidence and changes in Poisson's ratio (equation 1) at interfaces between geologic media with differing pore fluid content. His work was the beginning of quantitative research into using offset dependent reflectivity to explore for hydrocarbon resources. Poisson's ratio is defined as the ratio of transverse strain to longitudinal strain and can be expressed in terms of P wave and S wave velocity (Sheriff, 1991):

$$s = \frac{1/2\left(V_p{}^2 - 2V_s{}^2\right)}{\left(V_P{}^2 - V_s{}^2\right)} \qquad (1)$$

s = Poisson's ratio
V_p = compressional wave velocity
V_s = shear wave velocity

Much of Ostrander's work was based upon Koefoed's 1955 work on determining the reflection coefficients of plane longitudinal waves reflected at a boundary between two elastic media. Koefoed

noted that if there were two elastic media with the top medium having a smaller Poisson's ratio than the underlying medium there would be an increase in the reflection coefficient with increasing angle of incidence. He also observed that if Poisson's ratio of the lower medium was lower than the overlying medium, the opposite would occur with a decrease in the reflection coefficient with an increase in the angle of incidence. Another observation showed that the relative change in reflection coefficient increases as the velocity contrast between two media decreases. Koefoed also noted that if the Poisson's ratio for two media were increased but kept equal, the reflection coefficient at the larger angles of incidence would also increase. Ostrander (1984) found that changes in Poisson's ratio caused by the presence of hydrocarbons in the pore space had dramatic effect on the P wave reflection coefficients and that these effects gave rise to seismic amplitude anomalies that were detectable on field data.

In order to understand amplitude versus offset (AVO) analysis, one has to understand offset dependent reflectivity. Offset dependent reflectivity is defined as the variation of the reflection and transmission coefficients with changing incident angle (Castagna and Backus, 1993). The offset refers to source to receiver separation. Increasing source to receiver separation results in increasing the angle of incidence for raypaths as measured from the normal to a horizontal interface. Coincident source and receiver locations results in what is termed normal incidence, i.e. vertical transmission and reflection from a horizontal interface. This is the what the stacked seismic profile nominally represents. The amplitude of the reflected and transmitted waves are described by the reflection and transmission coefficients. The following discussion describes the equations and theory used to determine amplitude for both the reflected and transmitted waves at an acoustic boundary for normal incident energy and non-normal incident energy, i.e. offset dependent reflectivity. Note that this discussion is for a simplistic single interface model. The majority of reflections observed on a seismic profile are the superposition of events from multiple layers and have a more complex AVO response.

As implemented in the petroleum industry, AVO analysis involves comparing modeled AVO responses to field data to find a deviation from an expected background response. The expected background response is usually taken to be a water saturated reservoir; hence, the deviation from the expected response is an indication of hydrocarbon presence but does not indicate quantity. DNAPLs have acoustic characteristics that are very different than most pore fluids encountered at environmental contamination sites. Therefore, if DNAPL is present in free-phase and in large enough quantities, similar types of analyses as those performed for the petroleum industry can be applied to directly detect the presence of DNAPL.

An understanding of reflection AVO techniques can be obtained by a review of elastic wave propagation. A P wave incident on a boundary between two linear elastic homogeneous isotropic (LEHI) media generates four types of waves: 1) transmitted P wave, 2) reflected P wave, 3) reflected S wave, 4) a transmitted S wave (Figure 4).

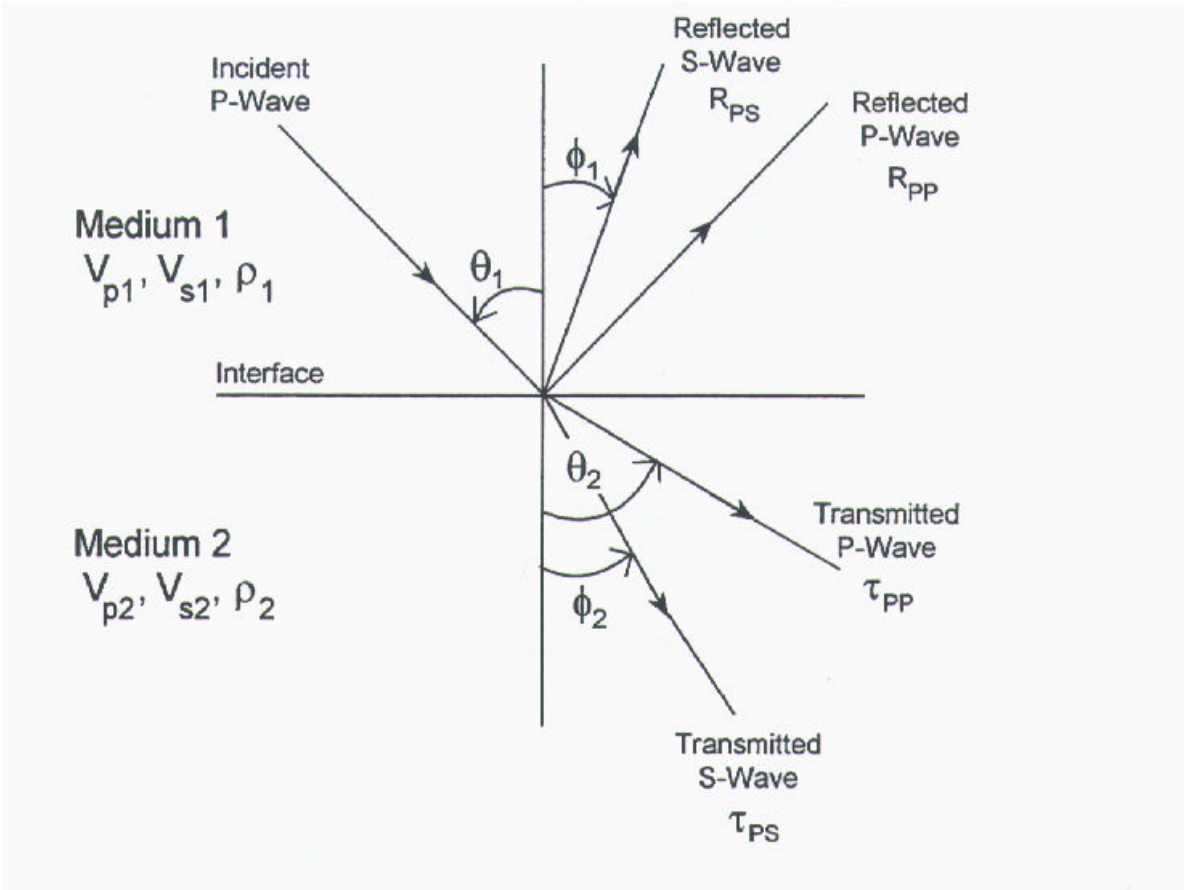

Figure 4. Elastic waves generated at a boundary. A P wave incident at an angle ? on a boundary between two linear elastic homogenous isotropic (LEHI) materials generates four wave types: reflected P, reflected S, transmitted P, transmitted S. The angles of reflection and refraction are governed by Snell's law from optics. The material properties of the media are described by the P wave velocity, density, and Poisson's ratio. The S wave velocity can be found from the P wave velocity and Poisson's ratio.

depend upon the P wave and S wave velocities, the density of the two media, and the angles of incidence and refraction as determined from Snell's Law (equation 2).

Snell's Law,

$$p = \frac{\sin\Theta_1}{V_{P_1}} = \frac{\sin\Theta_2}{V_{P_2}} = \frac{\sin\varphi_1}{V_{S_1}} = \frac{\sin\varphi_2}{V_{S_2}} \qquad (2)$$

V_{p1} = P wave velocity in medium 1,
V_{p2} = P wave velocity in medium 2,
V_{s1} = S wave velocity in medium 1,
V_{s2} = S wave velocity in medium 2,
Θ_1 = incident P wave angle,
Θ_2 = transmitted P wave angle,
ϕ_1 = reflected S wave angle,
ϕ_2 = transmitted S wave angle, and
p = ray parameter.

The reflection coefficient of the P wave as a function of the incident angle, $R_p(\Theta)$, is defined as the ratio of the amplitude of the reflected P wave to that of the incident P wave (Castagna and Backus, 1993) (equation 3). The P wave transmission coefficient, $T_p(\Theta)$, is the ratio of the amplitude of the transmitted P wave to that of the incident P wave (Castagna and Backus, 1993). The P wave reflection coefficient, R_p ,at normal incidence is given by the following equation:

$$R_p = \frac{I_{p_2} - I_{p_1}}{I_{p_2} + I_{p_1}} = \frac{1}{2} * \frac{\Delta I_p}{I_{pa}} \approx \frac{1}{2} * \ln * \frac{I_{p_2}}{I_{p_1}} \qquad (3)$$

I_{p2} = acoustic impedance of medium 2 = $\rho_2 V_{p2}$
ρ_2 = density of medium 2
I_{p1} = acoustic impedance of medium 1 = $\rho_1 V_{p1}$
ρ_1 = density of medium 1
I_{pa} = average acoustic impedance across the interface = $(I_{p2}+I_{p1})/2$, and
ΔI_p = $I_{p2}-I_{p1}$.
The P-wave transmission coefficient at normal incidence T_p is given by:

$$T_p = 1-R_{p.} \qquad (4)$$

The variation of the reflection and transmission coefficients with incident angle and source to receiver offset is referred to as offset dependent reflectivity (Castagna and Backus, 1993). The values of the reflection and transmission coefficients for non-normal angles of incidence are given by the Zoeppritz (1919) equations. The Zoeppritz equations are given below (modified Graul, 2001)(equation 5):

(5)

$$\begin{bmatrix} R(q_1) \\ S(q_1) \\ Tp(q_1) \\ Ts(q_1) \end{bmatrix} = \begin{bmatrix} \sin(q_1) & \cos(f_1) & -\sin(q_2) & \cos(f_2) \\ -\cos(q_1) & \sin(f_1) & -\cos(q_2) & -\sin(f_2) \\ \sin(2q_1) & \frac{a_1}{b_1}.\cos(2f_1) & r_2 {b_2}^2.\frac{a_1}{r_1 b_1}.\frac{\sin(2q_2)}{a_2} & -\frac{r_2}{r_1}.\frac{b_2}{b_1}.a_1.\cos(2f_2) \\ \cos(2f_1) & -\frac{b_1}{a_1}.\sin(2f_1) & -\frac{r_2}{r_1}.\frac{a_2}{a_1}.\cos(2q_2) & -\frac{r_2}{r_1}.\frac{b_2}{a_1}.\sin(2q_2) \end{bmatrix}^{-1} \begin{bmatrix} -\sin(q_1) \\ -\cos(q_1) \\ -\sin(2q_1) \\ -\cos(2f_1) \end{bmatrix}$$

where a and ß are P wave and S wave velocity respectively.

NI (normal incidence reflection coefficient) and PR (Poisson reflectivity) are defined as:

(6)

$$\mathrm{NI} = \frac{r_2 V_{p2} - r_1 V_{p1}}{r_2 V_{p2} + r_1 V_{p1}} = \frac{I_{p2} - I_{p2}}{I_{p2} + I_{p1}}$$

I_{p1} is the acoustic impedance

I_{p2} is the acoustic impedance

(7)

$$\mathrm{PR} = \frac{s_2 - s_1}{\left(1 - s_{\mathrm{avg}}\right)^2}$$

s is Poisson's ratio.

(Verm and Hilterman, 1995). Reflection AVO can be thought of as a combination of normal incidence reflectivity and a far offset reflectivity, or "Poisson reflectivity," that arises primarily as a result of changes in the Poisson's ratio between media.

AVO analysis can be implemented in many ways. Often the common depth point (CDP) gather is transformed from a function of offset to incident angle. This transformation requires knowledge of the root mean square (RMS) velocity, which is ideally obtained from borehole sonic logs. In the absence of sonic logs a rough estimate of the RMS velocity can be obtained from the normal moveout (NMO) stacking velocities. After transformation to a function of incident angle, stacks can be generated for various angle ranges. These offset range limited stacks can be used to reveal the reflection response as a function of incident angle. In other analyses the transformed CDP gathers are compared to model responses. Still other analyses involve extracting the NI and PR coefficients from a common depth point (CDP) gather by fitting either Equation (6) or (7) to the amplitudes. The NI and PR coefficients are cross-plotted to reveal deviations from a background trend that may represent pore fluid changes.

5.2 Modeling

The most important aspect of this study is the AVO modeling. The modeling determines the type of AVO response, e.g. dim-out, bright spot, or phase reversal that might be expected to occur because of the presence of DNAPL. The modeling also establishes the background response, i.e. the expected AVO behavior if no contaminant is present. Agreement between field data and models is then used to infer the presence or absence of DNAPL.

At the 200 West area it is believed that the CCl_4 is accumulating along two geological contacts that are not laterally continuous. The upper contact is between the Hanford Fine and the Plio/Pleistocene and the lower contact is between the Plio/Pleistocene and the caliche. In the 216-Z-9 trench area the highest concentration of CCl_4 was found in well 299-W15-217 at the Hanford Fine-Plio/Pleistocene contact (Figure 1) (Rohay et al., 1994; Rohay personal communication, 1999). In wells 299-W15-219, 218, and 223 high concentrations of CCl_4 were encountered in the Pliocene/Pleistocene at or near the contact with the caliche layer (Figure 1). The units have differing composition and properties, i.e. grain size, compaction, and cementation that results in contrasting acoustic impedances at the contacts. A series of models were generated for the two primary geologic contacts, Hanford Fine-Plio/Pleistocene (Model series 1) and Plio/Pleistocene-caliche layer (Model series 2) to investigate the AVO response in the presence and absence of CCl_4 in the pore space.

In the interim report, models were generated using Shuey's approximation to the Zoeppritz equations. In this final report the full Zoeppritz equations were used (equation 5) rather than an approximation because it was found that the results varied significantly according to the approximation used. At the time of publishing the interim report all the initial velocities were taken from the VSP collected in well 299-W15-32 and the density values were from published values in Rohay and others (1994). Since the completion of the interim report a core sample from each of the Hanford Fine, Plio/Pleistocene, and caliche layers from well 299-W14-7 were supplied to the research team. All of the cores were sent to Core Lab Petroleum Services so that P wave velocity, S wave velocity, density, porosity, and mineralogy could be determined for each sample. Analyses were performed on the samples from the Hanford Fine and Plio/Pleistocene. The caliche sample was too friable for analysis. Consequently, the P wave and S wave velocities for the caliche are from the VSPs conducted in wells 299-W15-32 and 299-W15-217. The density value for the caliche was calculated from the P wave velocity using Gardner's equation (Gardner et al., 1974).

In the models that follow results are shown first using model parameters derived from the VSP data, as was presented in the interim report, and then using model parameters derived from the core analyses. In Tables 1 and 2 the P wave and S wave velocities of the units without CCl_4 were determined from either VSPs in wells 299-W15-32 and 299-W15-217 or core samples (Figure 1). In Table 2 the Hanford Fine and Plio/Pleistocene velocities were derived from core samples from well 299-W14-7. Velocities used for the caliche layer were derived from the VSP data in well 299-W15-32. The density values for the Hanford Fine and Plio/Pleistocene were also derived from core samples. The density value used for the caliche was derived from Gardner's equation. In Table 1 the low density of the caliche as compared to calcium carbonate suggests that it might have vuggy porosity or that clays and sand may be present in the caliche. If this is so, then CCl_4 might accumulate within the pores of this unit.

Table 1. AVO modeling parameters using velocities from VSPs in wells 299-W15-32 and 299-W15-217 and densities from Rohay and others (1994).

Lithology	V_p m/s	V_p m/s	Density g/cc
Hanford Fine w/air	620	394	1.56
Hanford Fine w/ CCl_4	1270	327	2.26
Plio/Pleistocene w/air	1351	679	1.79
Plio/Pleistocene w/ CCl_4	1671	596	2.32
Caliche w/air	2103	679	1.49
Caliche w/ CCl_4	1966	447	2.58

Table 2. AVO modeling parameters using core derived velocities and density values.

Lithology	V_p m/s	V_s m/s	Density g/cc
Hanford Fine w/air	847	523	1.38
Hanford Fine w/ CCl_4	1547	432	1.58
Plio/Pleistocene w/air	947	470	1.64
Plio/Pleistocene w/ CCl_4	1475	522	2.19
Caliche* w/air	2478	1219	2.18
Caliche w/ CCl_4	2788	1213	2.40

* The velocity values are derived from VSP measurements and the density value is calculated using Gardner's equation.

To determine the AVO response that might arise from CCl_4 saturated sediments it is necessary to have the corresponding velocity and density values for the CCl_4 saturated sediments. The velocities and densities of the units saturated with CCl_4 were mathematically derived. The Gassmann theory of fluid saturated rocks (e.g. White, 1983) was used to find the velocity of the CCl_4 saturated sediments. The bulk density of the saturated sediments is a simple weighted average governed by the porosity. The porosity of the units was assumed to be 14.2-37.5 percent, which is common for loosely consolidated to semiconsolidated sediments.

Gassmann theory assumes that motion of pore fluid is negligible compared to the motion of the fluid filled rock itself, i.e. the fluid and rock move together. In addition, it is assumed that the seismic frequencies are low, less than a megahertz. Because the shear modulus, μ, is not affected by fluid saturation, the formulation by Gassmann is for the bulk modulus, k, of the fluid-filled rock. Once this value is obtained, the P wave velocity is found by following formula:

$$V_p = \left(\frac{K + \frac{4}{3}\mu}{\rho} \right)^{\frac{1}{2}} \tag{8}$$

The S wave velocity is moderately depressed by the introduction of fluids. Because S waves cannot propagate in fluids the velocity is influenced only by density change. The formula for S wave velocity is:

$$V_s = \left(\frac{\mu}{\rho} \right)^{\frac{1}{2}} \tag{9}$$

where ρ, is the bulk density, which combines both the rock density and fluid density.

Gassmann's equation for the bulk modulus of a fluid filled rock is as follows:

$$K_w = K_{dry} + \frac{(1 - \frac{K_{dry}}{K_{ma}})^2}{\frac{\varphi}{K_{fl}} + (1 - \frac{\varphi}{K_{ma}}) - \frac{K_{dry}}{K_{ma}}} \tag{10}$$

K_w = Bulk modulus of the fluid-filled rock
K_{dry} = Bulk modulus of the rock skeleton (aggregate of grains)
K_{ma} = Bulk modulus of matrix (individual grains)
K_{fl} = Bulk modulus of the pore fluid
μ_w = Shear modulus of the fluid-filled rock
μ_d = Shear modulus of the rock skeleton
μ_w = μ_d

In calculating the bulk modulus of the geologic units saturated with CCl_4 (Table 1), the following assumptions were made:

- K_{dry} is equal to the bulk modulus calculated from the measured P wave and S wave velocity from the VSP and the density reported by Rohay and others (1994). It is also assumed that the pore space is filled with air.
- K_{ma} is the weighted average of bulk moduli of the framework grains (percent quartz, rock fragments, feldspar, and clay (kaolinite)) calculated from modal analyses published by Wright, Conca, and Chen (1994).
- K_{fl} is the bulk modulus of the fluid mixture using Wood's equation (11):

$$K_f = \frac{K_{CCl_4} * K_{air}}{K_{air} * S_{CCl_4} + K_{CCl_4} * S_{air}} \tag{11}$$

K_{CCl4} = bulk modulus of CCl_4
K_{air} = bulk modulus of air
S_{CCl4} = fractional CCl_4 saturation
S_{air} = fractional air saturation

The density values for each of the units filled with CCl_4 and air were calculated using the following equation:

$$\rho_b = (1-\varphi)\rho_{ma} + S_{CCl_4} * \varphi * \rho_{CCl_4} + S_{air} * \varphi * \rho_{air} \tag{12}$$

ρ_{ma} = density of matrix grains
ρ_{Ccl4} = density of CCl_4
ρ_{air} = density of air
S_{CCl4}= fractional CCl_4 saturation
S_{air} = fractional air saturation
φ = fractional percent porosity

The models of the Hanford Fine-Plio/Pleistocene contact include: both units with empty pore spaces (100% air saturation), the Hanford Fine saturated with 100% percent CCl_4 and the Plio/Pleistocene air-filled, and both the Hanford Fine and the Plio/Pleistocene saturated with CCl_4 (Model series 1). The models of the Plio/Pleistocene-caliche layer contact include both units 100%

air-filled, Plio/Pleistocene saturated with 100% CCl_4 and the caliche pores air-filled, both units saturated with 100% CCl_4, and the Plio/Pleistocene air-filled with the caliche pores 100% saturated with CCl_4 (Model series 2).

Model 1 represents the change in reflection coefficient as a function of angle of incidence at the contact of the Hanford Fine with the Plio/Pleistocene using velocities from VSP and densities from Rohay and others (1994). The modeled background response, i.e. assuming that the Hanford Fine and Plio/Pleistocene pore spaces are 100% saturated with air, indicates a strong positive reflection coefficient, which on the seismic sections would be a displayed as a positive amplitude (Figure 5 red line). Also note that at approximately 22^0 angle of incidence the reflection coefficient sharply ramps up. This point is the critical angle where the refracted ray grazes the interface between the media. If CCl_4 is introduced into the Hanford Fine and the Plio/Pleistocene pore spaces remain saturated with air, the reflection coefficient becomes slightly negative (Model 1)(Figure 5 green line). Therefore, high concentrations of CCl_4 along the contact of the Hanford Fine with the Plio/Pleistocene should be manifested as a low amplitude negative reflection or as a dim-out. A seismic profile that crosses a high concentration of CCl_4 in the Hanford Fine should exhibit a strong positive amplitude becoming weaker in amplitude and then reversing to a slight negative amplitude over the contaminant. If the pore spaces in both the Hanford Fine and Plio/Pleistocene are saturated with CCl_4, the results are similar, but not as dramatic as the previous scenario (Figure 5 blue line). Also note in this scenario that the critical angle is approximately 45^0.

Model 1A represents the change in reflection coefficient as a function of angle of incidence at the contact of the Hanford Fine with the Plio/Pleistocene using velocities using velocities and densities values derived from core analysis of samples from well 299-W14-7 (Figure 6). The modeled background response, the pore space in both units filled with air, is a positive reflection coefficient that becomes more positive with increasing angles of incidence. On the seismic sections this would be a displayed as a positive amplitude (Figure 5 red line). Also note that at approximately 55^0 the reflection coefficient sharply ramps up. This point is the critical angle. The greatest difference between Model 1 and Model 1A is that when the core derived values are used, the background response reaches critical angle at a much higher incident angle than when the values from the VSP are used. If CCl_4 is introduced into the Hanford Fine at the contact and the Plio/Pleistocene pore spaces remains saturated with air, the reflection coefficient is more negative than on the previous model and with increasing incident angle becomes much more negative (Model 1A)(Figure 6 green line). Therefore, high concentrations of CCl_4 along the contact of the Hanford Fine with the Plio/Pleistocene would be displayed as a low amplitude negative reflection or as a dim-out. A seismic profile that crosses a high concentration of CCl_4 in the Hanford Fine should exhibit a strong positive amplitude, that becomes weaker in amplitude and then reverses to a slight negative amplitude over the contaminant. If the pore spaces in both the Hanford Fine and Plio/Pleistocene are saturated with CCl_4 the results are similar to the background response. The difference is, with CCl_4 saturated pores, the

amplitudes are significantly less positive. With increasing incidence angle the graph remains flat and the background response reflection coefficient increases substantially. If the model is correct, under this particular scenario it appears that only on the far offsets (high incidence angles) would there be a enough separation between the background response and the model CCl_4 response to be detectable on the seismic data. Also note in this scenario the critical angle is approximately 60^0.

Model 2 is the reflection coefficient versus angle of incidence curves for the contact between the Plio/Pleistocene and the caliche (Figure 7) using P wave and S wave velocities from VSP data in well 299-W15-32 and density values from Rohay and others (1994). The first scenario considers both units to be air-filled (background response red line). The reflection coefficient is positive and increases with increasing offset (incident angle) out to the critical angle of approximately 32^0 (Figure 7). The second scenario considers the Plio/Pleistocene with pores spaces 100% saturated with CCl_4 and the caliche to be filled with air. Under this scenario the reflection coefficient starts slightly negative, becomes positive at approximately 35^0 degrees, and reaches the critical angle at approximately 45^0. This is 15^0 farther out than the background response (Figure 7 green line). The third scenario assumes that the pores spaces in both the Plio/Pleistocene and caliche are 100% saturated with CCl_4 (Figure 7 blue line). Under this scenario the reflection coefficient starts at the same point as the background response; however, as the angle of incidence increases the reflection coefficients increase but at a much lower rate until the curve reaches the critical angle at approximately 50^0 (Figure 7). The final scenario (Figure 8) assumes that the caliche layer pore spaces are saturated with 100% CCl_4 and the overlying Plio/Pleistocene pores spaces are 90% to 100% saturated with air, or less than 10% CCl_4 (Figure 7 purple line). The introduction of CCl_4 only in the caliche causes the reflection coefficient to almost double in magnitude. On a seismic section this phenomenon is known as a bright spot. In this case, on a seismic profile that crosses a high concentration of CCl_4 in the Plio/Pleistocene, the amplitude at the contact becomes more positive than the amplitudes outside of the contamination zone.

Model 2A shows a series of reflection coefficient versus incident angle models for the contact between the Plio/Pleistocene and the caliche (Figure 8). The P wave velocities, S wave velocities, and density values for the Plio/Pleistocene were derived from core analysis from well 299-W14-7. The P wave and S wave values used in the modeling for the caliche are from a VSP in well 299-W15-32 and the density value used is derived from the P wave velocity using Gardner's equation. The first scenario considers both units to be air-filled (background response red line). When this background response is compared with the background response for the same model in the interim report and in Model 2 they are all very similar. The reflection coefficient is positive and increases with increasing offset (incident angle) out to the critical angle of approximately 32^0 (Figure 8). The second scenario is the Plio/Pleistocene pores spaces 100% saturated with CCl_4 overlying the caliche with the caliche pore spaces filled with air. Under this scenario the reflection coefficients start with a higher positive reflection coefficient than the background response between 5^0 and 15^0. It slightly decreases with increase in incident angle until the model merges with the background model at 25^0 degrees, which is

where this model reaches critical angle (Figure 8 green line). The third scenario assumes that the pores spaces in both the Plio/Pleistocene and caliche are 100% saturated with CCl_4 (Figure 8 blue line). This scenario, the reflection coefficient starts at a slightly higher reflection coefficient than the previous scenario where only the Plio/Pleistocene is saturated with CCl_4. The reflection coefficient remains flat until the critical angle is reached at approximately 25^0 (Figure8). Under this scenario the difference between this model and the background is possibly large enough to be detected on seismic data as a bright spot. The final scenario (Figure 8) is assuming the caliche layer pore spaces are saturated with 100% CCl_4 and the overlying Plio/Pleistocene pore spaces are 90% to 100% saturated with air, or less than 10% CCl_4 (Figure 8 purple line). The introduction of CCl_4 in the caliche almost triples the reflection coefficient above background response, but also causes the critical angle to be reached at only 12^0 angle of incidence (Figure 8).

The model study suggests that at the 200 West area the introduction of CCl_4 into pore spaces causes significant changes in the P wave reflection coefficient as a function of offset for the interfaces studied. Furthermore, these changes should be visible on zero-offset stacked seismic sections. It must be noted that these models represent only single interfaces. The seismic section represents the superposition of many responses from several interfaces in the subsurface positioned in time according to the subsurface velocity field. If the overlying and underlying units at an interface are thin as compared to the wavelength of the seismic impulse, the observed response is a composite caused by interference of the superposed waveforms. For this reason a primary goal of seismic recording is to record the highest frequency signals possible to resolve closely spaced interfaces.

Model 1

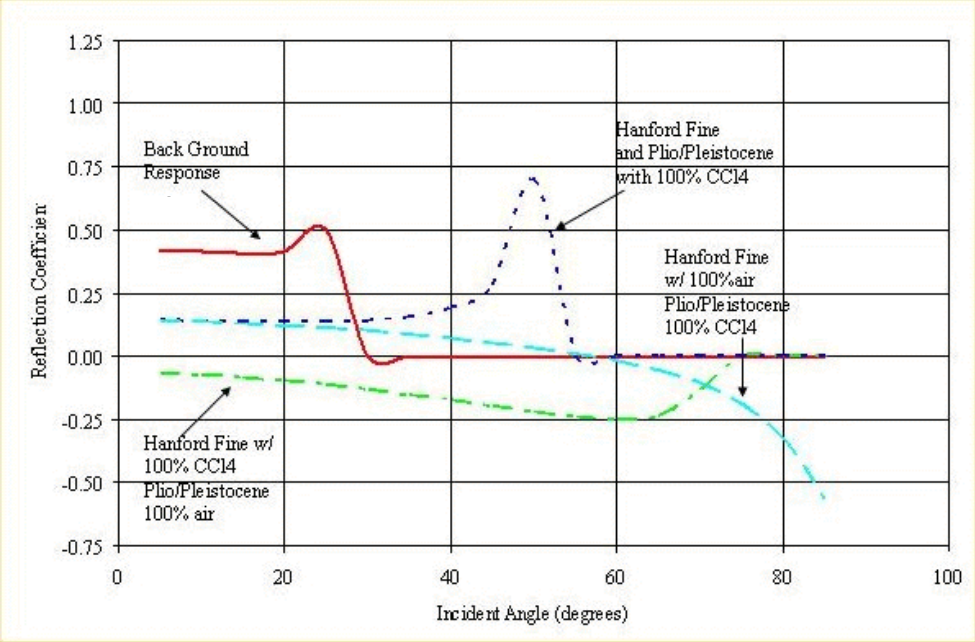

Figure 5. Graph of reflection coefficient versus angle of incidence for the Hanford Fine-Plio/Pleistocene contact using parameters derived from VSP. Air saturated Hanford Fine overlying air saturated Plio/Pleistocene (red line), 100% CCl_4 saturated Hanford Fine overlying 100% air saturated Plio/Pleistocene (green line) and 100% CCl_4 saturated Hanford Fine overlying 100% CCl_4 saturated Plio/Pleistocene(short dash blue line). P wave and S wave values obtained from a VSP in Well 299-W15-32 and density values obtained from published values by Rohay and others (1994).

Model 1A

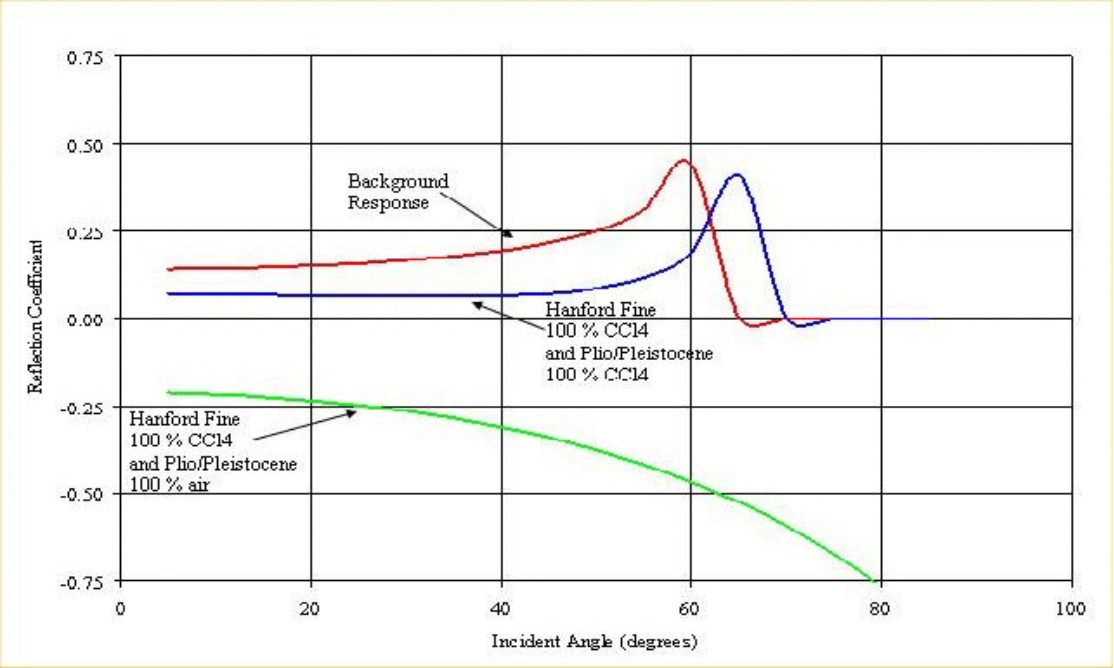

Figure 6. Graph of reflection coefficient versus angle of incidence for the Hanford Fine-Plio/Pleistocene contact using parameters derived from core samples. Air saturated Hanford Fine overlying air saturated Plio/Pleistocene (red line), 100% CCl_4 saturated Hanford Fine overlying 100% air saturated Plio/Pleistocene (green line) and 100% CCl_4 saturated Hanford Fine overlying 100% CCl_4 saturated Plio/Pleistocene(blue line). P wave, S wave velocities and density values are derived from core samples from well 299-W14-7.

Model 2

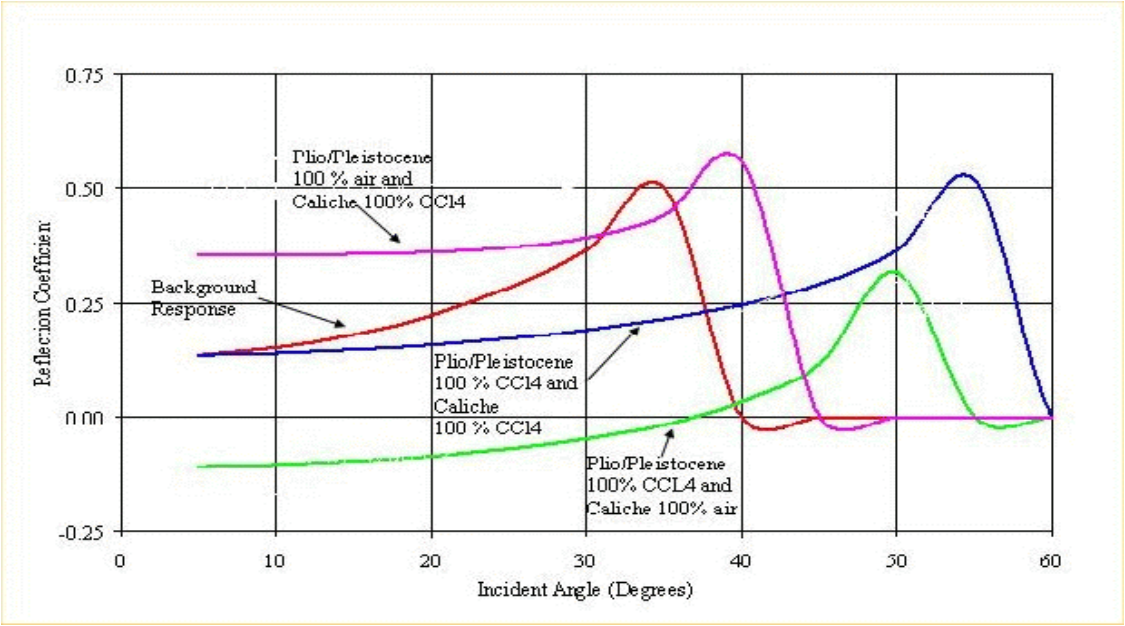

Figure 7. Graph of reflection coefficient versus angle of incidence for the Plio/Pleistocene-caliche layer contact using parameters derived from VSP. The red line is the background response if both the Plio/Pleistocene and caliche pores are filled with air. The green line is the response if the Plio/Pleistocene pores are 100 % saturated with CCl_4 and the caliche pores are 100 % saturated with air. The blue line is the expected response if the both the Plio/Pleistocene and caliche pores are saturated with 100 % CCl_4. The purple line is the expected response if the Plio/Pleistocene pores are 100 % saturated with air and the caliche pores are 100 % saturated with CCl_4. The velocity values were derived from the VSP in well 299-W15-32 and the density values are from published results Rohay and others (1994).

Model 2A

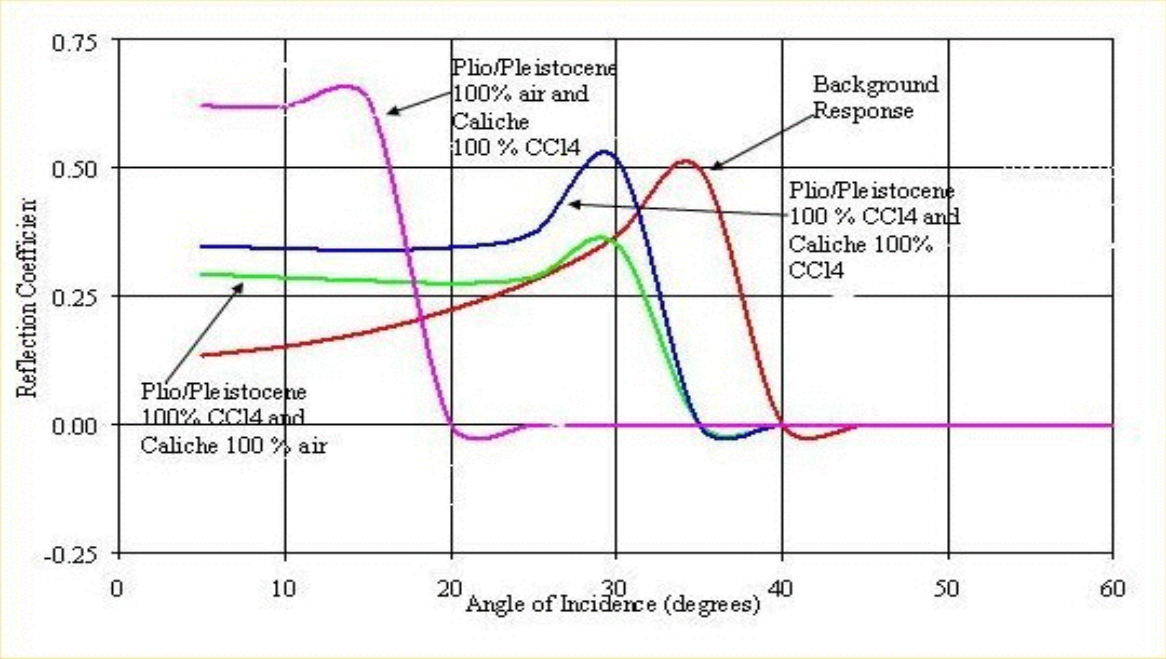

Figure 8. Graph of reflection coefficient versus angle of incidence for the Plio/Pleistocene-caliche layer contact using parameters derived from core samples. The red line is the background response if both the Plio/Pleistocene and caliche pores are filled with air. The green line is the response if the Plio/Pleistocene pores are 100 % saturated with CCl_4 and the caliche pores are 100 % saturated with air. The blue line is the expected if the both the Plio/Pleistocene and caliche pores are saturated with 100 % CCl_4. The purple line is the expected response if the Plio/Pleistocene pores are 100 % saturated with air and the caliche pores are 100 % saturated with CCl_4 . The velocity and density values for the Plio/Pleistocene are from core analysis. The caliche velocities were derived from the VSP in well 299-W15-32 and the density value for the caliche was derived by Gardner's equation.

6.0 Seismic Reflection Data Acquisition: Results and Discussion

In January 1999 ESRI-USC collected vertical seismic profiles in three wells in the vicinity of the 216-Z-9 Crib in the 200 West area. This was followed by recording four 2-D seismic profiles around the crib in March 1999 (Figure 1).

6.1 Vertical Seismic Profiles

6.1.1 Vertical Seismic Profile Acquisition

Compressional wave (P) and shear wave (S) vertical seismic profiles (VSPs) were collected in wells 299-W15-32, 299-W15-82, and 299-W15-217. The VSPs were collected to obtain data on the P and S wave velocity field of the geologic strata at, above, and below the known DNAPL contamination. The velocity data were used to construct seismic models to determine the probable amplitude versus offset (AVO) response that would be recorded by the surface seismic survey. In addition, subsurface velocity information was needed to perform high-fidelity ties between the surface seismic profiles and the well lithology picks. Using the velocity versus depth curves obtained from the VSPs the horizon times on the seismic data were converted to depth.

Seismic recordings were made at one meter (3.28 ft.) increments from the bottom of the well to approximately one meter (3.28 ft.) below land surface using a three geophone (1 vertical, 2 horizontal) Geostuff sonde and a 7.3 kg (16 lb.) sledge hammer source. A Geometrics Strataview seismograph recorded the output from the geophones and stored 1024 milliseconds (ms) of data digitized at 0.125 ms intervals. For P wave acquisition a vertical steel cylinder was placed on the ground and struck six times. Each hit was vertically summed to the preceding hits in the seismograph and written to disk as a single record for each level. For S wave acquisition strike plates were mounted on the ends of a 2.4 m (8 ft.) horizontal plank and a truck was driven on the plank to couple the plank to the ground. Each end of the plank was struck six times, first from one side of the vehicle and then the other. The summed records for each source orientation were written to disk separately for each level.

The VSP data were noisy and little reflected signal was apparent in the raw records (Figure 9). Well construction reports indicate that the annular space between the casing and the borehole is filled with bentonite. The resulting poor coupling of the casing to the formation probably accounts for the poor VSP record quality. Considerable experimentation was necessary to optimally record the data. Tests were done by varying the offset of the source from the well and by varying the number of source hits. Because of the uncertain data quality, well 299-W15-32 was logged twice for P waves to ensure that usable data were recorded. The recording parameters for each VSP are summarized in Table 3.

VSP Field Records

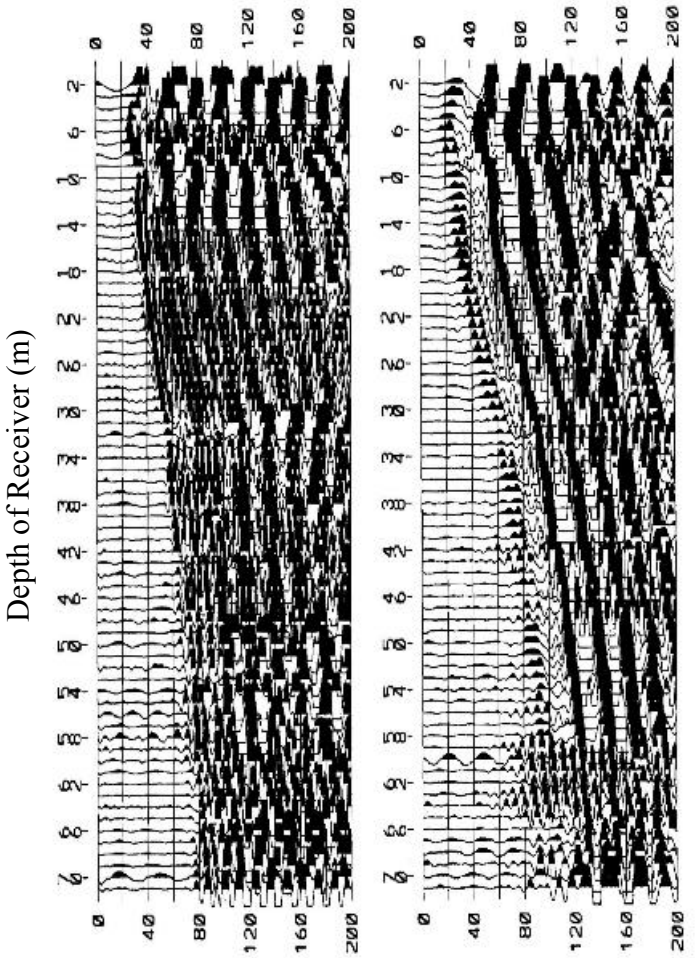

Time (ms)

P wave VSP **S wave VSP**

Figure 9. Raw VSP data from well 299-W15-32. P wave VSP (left) and S wave VSP (right). Bandpass filter: 30-150 Hz.

Table 3. Summary of VSP recording parameters.

	299-W15-32	**299-W15-82**	**299-W15-217**
Recorded depth P wave (m from TOC)	1-71, 2-71	1-22	2-36
Recorded depth S wave (m from TOC)	2-71	1-22	2-36
Source offset P wave (m)	6, 10.03	5.55	6.0
Source offset S wave (m)	10	6.0	6.06
No. of hits P-wave, S-wave	6, 6, (6,6)	6, (6,6)	6, (6,6)
Depth increment (m)	1	1	1
Sample rate (ms)	0.125	0.125	0.125
Record length (ms)	1024	1024	1024

6.1.2 VSP Data Processing

The generalized data processing flow for the VSP data appears in Figure 10. In the field some rudimentary data processing was performed for QA/QC purposes using the Seismic Image Software, Ltd. VISTA seismic processing software. The infield QA/QC proved to be invaluable given the low signal-to-noise ratio of the data.

First arrival times were picked on the P wave records and the better of the two channels on the S wave records. These times were corrected for source offset from the borehole to true vertical travel time (TVT), or zero-offset time, using a straight raypath assumption. The velocity profile, average velocity and interval velocity, for each borehole was computed (Figs. 11-19, Tables 4-9). The average velocity (total depth divided by total time) from the surface to the recording depth is used to convert recording time to depth. The interval velocity, or velocity of the material between recording levels, is an approximate indicator of lithologic changes in the borehole. The VSP records were heavily edited and the computed interval velocities smoothed. Generally, the S wave VSP records were better quality than that the P wave records. Despite the poor quality of the field records, useful velocity information was obtained from the boreholes. This is confirmed by the consistency of the interval velocity curves among the wells.

For correlation to the surface seismic data, displays of the up-going wavefield data were shifted to two-way reflection time (twice TVT) and narrow (3-10 trace) front corridor stacks were produced (Figure 20 and Figure 24). Because the time-depth relationship for the front corridor stack is known, the depth to the reflectors in the subsurface can be determined.

Generalized Vertical Seismic Profile Data Processing Flow

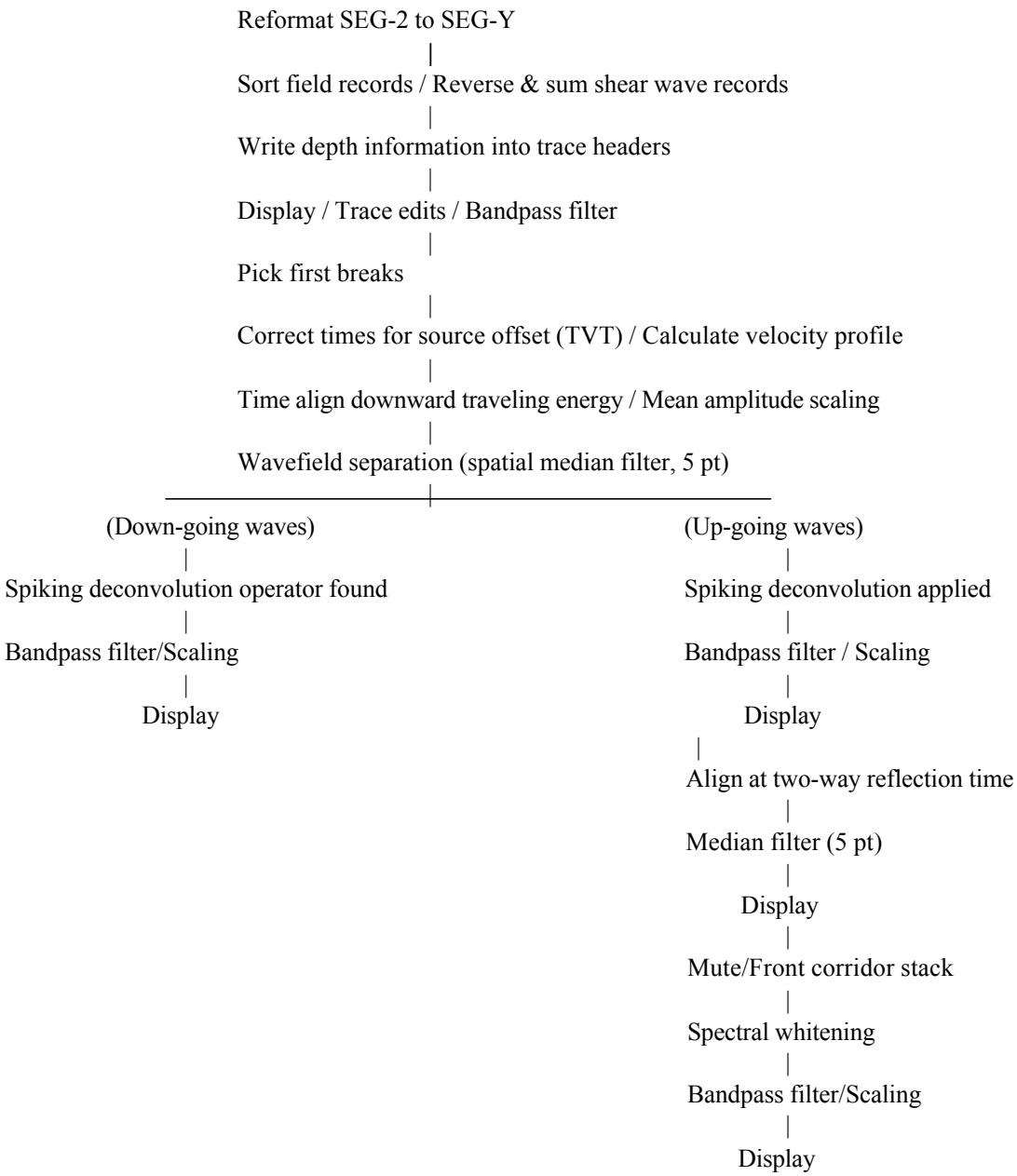

Figure 10. Vertical seismic profile (VSP) data processing flow.

Table 4. P wave velocity table from well 299-W15-32.

Well 299-W15-32

P Wave Vertical Seismic Profile

GL = 202.627 m TOC = 203.487 m

(Offset = 10.03 m)

Seq.	Depth (TOC)	Pick Time	Depth (GL)	True Vertical Time	Average Velocity	Interval Velocity	Two-way Time
No.	(m)	(ms)	(m)	(ms)	(m/s)	(m/s)	(ms)
70	2	30.50	1.14	3.44	331	331	6.89
69	3	29.40	2.14	6.13	349	372	12.27
68	4	27.50	3.14	8.22	382	480	16.43
67	5	25.63	4.14	9.78	423	640	19.56
66	6	25.00	5.14	11.40	451	616	22.80
65	7	25.38	6.14	13.25	463	541	26.50
64	8	28.25	7.14	16.38	436	319	32.77
63	9	31.00	8.14	19.53	417	317	39.07
62	10	32.25	9.14	21.72	421	457	43.44
61	11	33.63	10.14	23.91	424	457	47.82
60	12	32.25	11.14	23.97	.	.	.
59	13	32.25	12.14	24.86	488	2099	49.72
58	14	32.25	13.14	25.64	513	1294	51.27
57	15	32.88	14.14	26.82	527	845	53.64
56	16	33.75	15.14	28.14	538	759	56.27
55	17	35.00	16.14	29.73	543	628	59.45
54	18	36.25	17.14	31.29	548	641	62.57
53	19	37.75	18.14	33.04	549	572	66.07
52	20	38.25	19.14	33.88	565	1185	67.76
51	21	40.00	20.14	35.81	562	519	71.61
50	22	41.13	21.14	37.16	569	738	74.32
49	23	42.13	22.14	38.38	577	822	76.75
48	24	43.63	23.14	40.03	578	604	80.06

47	25	44.75	24.14	41.32	584	773	82.65
46	26	46.13	25.14	42.85	587	657	85.69
45	27	47.38	26.14	44.24	591	720	88.47
44	28	48.38	27.14	45.38	598	874	90.76
43	29	49.63	28.14	46.75	602	730	93.50
42	30	51.13	29.14	48.35	603	626	96.69
41	31	53.38	30.14	50.66	595	434	101.30
40	32	54.63	31.14	51.00	599	741	104.00
39	33	56.00	32.14	53.46	601	686	106.91
38	34	56.25	33.14	53.84	616	2626	107.68
37	35	56.88	34.14	54.57	.	.	.
36	36	56.50	35.14	54.33	.	.	.
35	37	57.13	36.14	55.05	657	2477	110.10
34	38	57.88	37.14	55.88	665	1206	111.76
33	39	58.38	38.14	56.46	676	1718	112.92
32	40	59.88	39.14	58.01	675	647	116.01
31	41	60.88	40.14	59.06	680	945	118.13
30	42	61.88	41.14	60.12	684	948	120.24
29	43	63.38	42.14	61.66	683	650	123.32
28	44	69.00	43.14	67.21	.	.	.
27	45	67.30	44.14	65.63	.	.	.
26	46	69.00	45.14	67.36	670	526	134.71
25	47	70.00	46.14	68.40	675	957	136.80
24	48	70.50	47.14	68.96	684	1805	137.91
23	49	73.00	48.14	71.47	.	.	.
22	50	72.00	49.14	70.55	697	1259	141.09
21	51	72.00	50.14	70.60	.	.	.
20	52	74.50	51.14	73.11	.	.	.
19	53	74.50	52.14	73.16	713	1148	146.32
18	54	75.13	53.14	73.83	720	1497	147.65
17	55	75.38	54.14	74.12	.	.	.
16	56	75.88	55.14	74.66	739	2414	149.31
15	57	76.50	56.14	75.31	745	1532	150.62
14	58	77.38	57.14	76.21	750	1102	152.43
13	59	77.38	58.14	76.25	.	.	.
12	60	76.50	59.14	75.42	.	.	.
11	61	79.63	60.14	78.55	766	1287	157.09
10	62	77.50	61.14	76.48	.	.	.
9	63	80.38	62.14	79.35	783	2476	158.71
8	64	80.88	63.14	79.88	790	1903	159.76

7	65	81.50	64.14	80.52	797	1555	161.04
6	66	82.88	65.14	81.91	.	.	.
5	67	81.38	66.14	80.46	.	.	.
4	68	83.13	67.14	82.22	817	1769	164.44
3	69	83.88	68.14	82.99	.	.	.
2	70	84.00	69.14	83.13	832	2192	166.26
1	71	84.25	70.14	83.40	841	3680	166.80

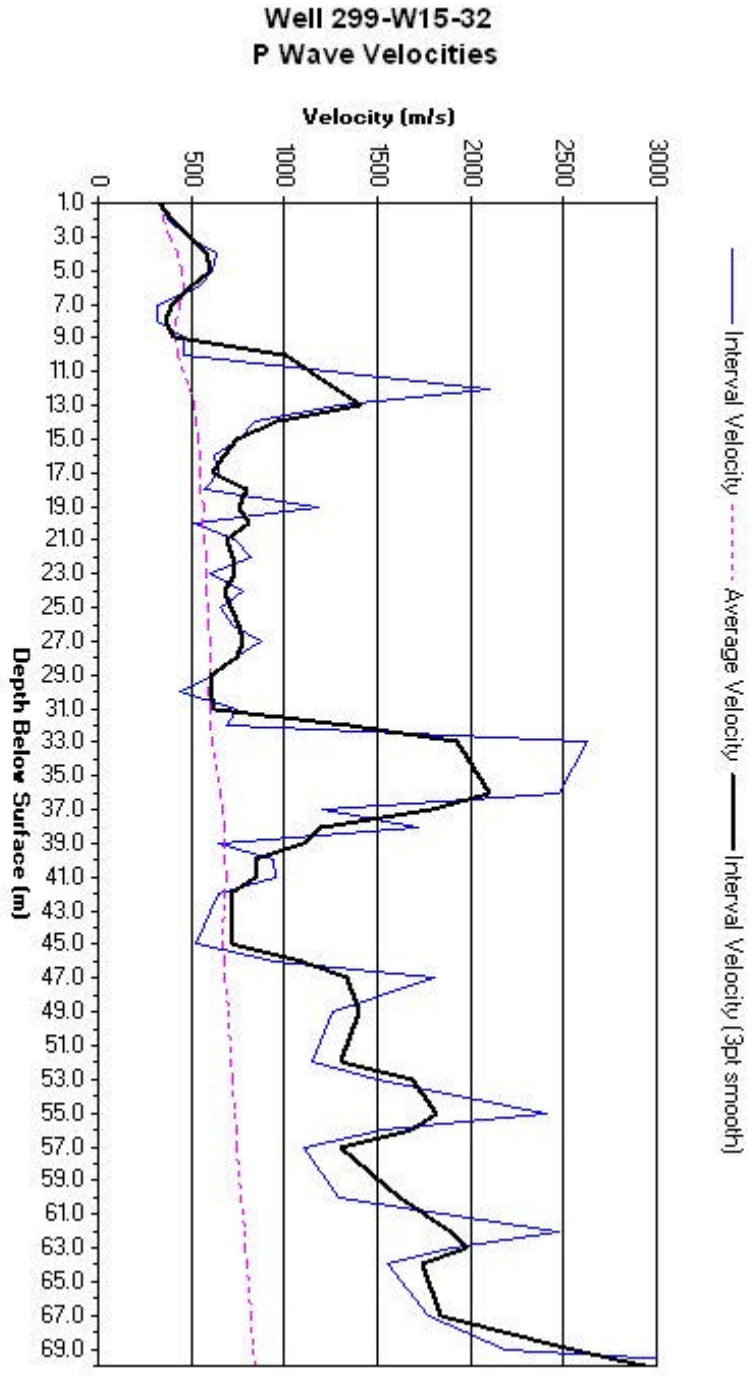

Figure 11. Graph of P wave interval velocity, smoothed interval velocity, and average velocity versus depth in well 299-W15-32.

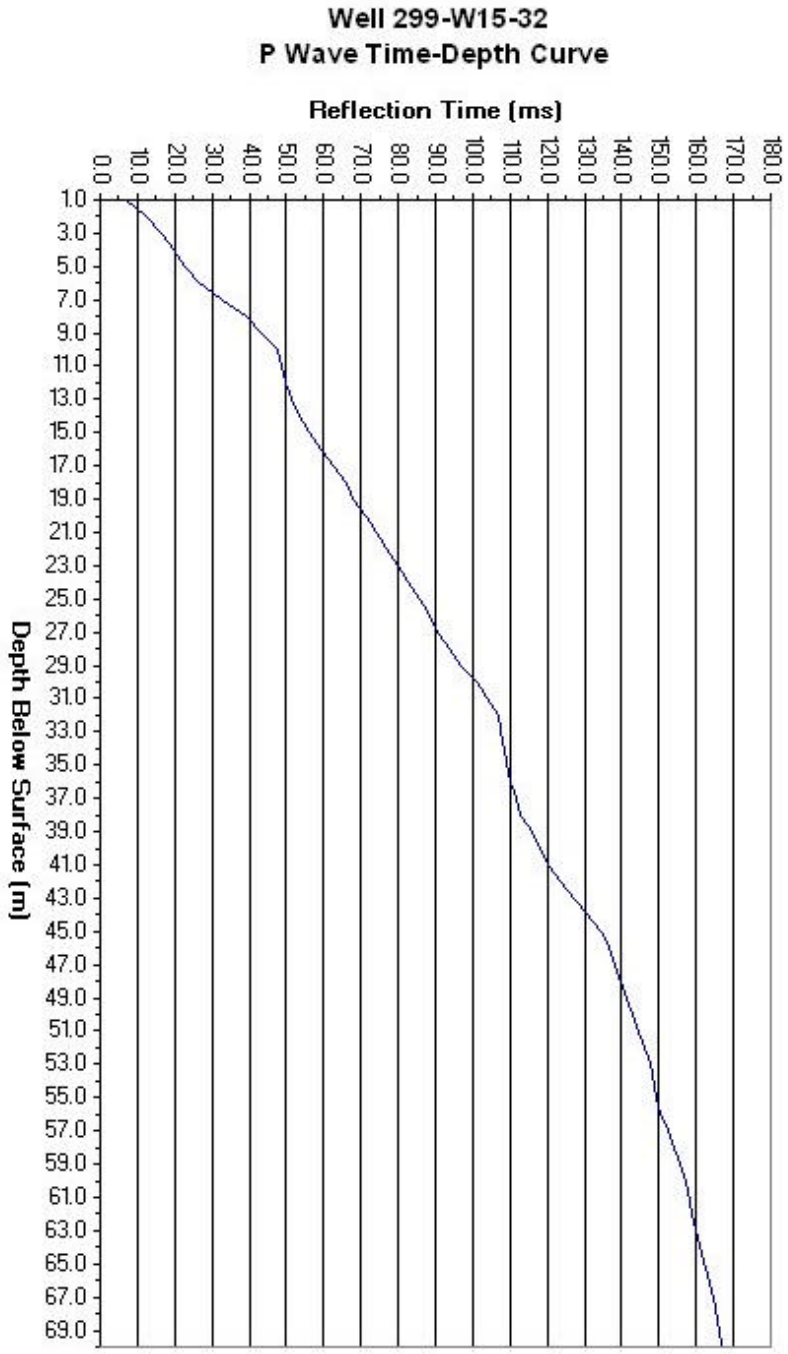

Figure 12. P wave time-depth curve for well 299-W15-32.

Table 5. S wave velocity table from well 299-W15-32.

Well 299-W15-32

S Wave Vertical Seismic Profile

GL = 202.627 m TOC = 203.487 m

(Offset = 10.0 m)

Seq.	Depth (TOC)	Pick Time	Depth (GL)	True Vertical Time	Average Velocity	Interval Velocity	Two-way Time
No.	(m)	(ms)	(m)	(ms)	(m/s)	(m/s)	(ms)
70	2.0	51.25	1.14	5.80	196	196	11.61
69	3.0	50.88	2.14	10.65	201	207	21.29
68	4.0	47.13	3.14	14.12	222	288	28.24
67	5.0	44.25	4.14	16.93	245	356	33.85
66	6.0	41.25	5.14	18.86	273	518	37.71
65	7.0	42.00	6.14	21.98	279	321	43.95
64	8.0	43.63	7.14	25.35	282	296	50.71
63	9.0	48.25	8.14	30.46	267	196	60.92
62	10.0	51.13	9.14	34.50	265	248	68.99
61	11.0	53.50	10.14	38.09	266	278	76.18
60	12.0	53.50	11.14	39.81	.	.	.
59	13.0	54.88	12.14	42.36	287	469	84.72
58	14.0	54.25	13.14	43.17	304	1233	86.34
57	15.0	54.50	14.14	44.50	318	754	88.99
56	16.0	55.88	15.14	46.63	325	469	93.25
55	17.0	57.13	16.14	48.56	332	516	97.13
54	18.0	58.88	17.14	50.86	337	436	101.71
53	19.0	61.00	18.14	53.42	340	390	106.84
52	20.0	62.75	19.14	55.62	344	455	111.23
51	21.0	64.88	20.14	58.11	347	401	116.22
50	22.0	66.38	21.14	60.01	352	528	120.01
49	23.0	68.38	22.14	62.32	355	432	124.64
48	24.0	70.13	23.14	64.38	359	486	128.75

47	25.0	72.50	24.14	66.98	360	384	133.96
46	26.0	74.13	25.14	68.88	365	526	137.76
45	27.0	78.13	26.14	72.97	.	.	.
44	28.0	78.13	27.14	73.31	370	451	146.62
43	29.0	80.75	28.14	76.09	370	360	152.18
42	30.0	82.88	29.14	78.39	372	434	156.78
41	31.0	85.50	30.14	81.15	371	363	162.30
40	32.0	87.63	31.14	83.43	373	438	166.87
39	33.0	90.13	32.14	86.06	373	381	172.12
38	34.0	90.75	33.14	86.88	381	1219	173.76
37	35.0	92.13	34.14	88.42	386	652	176.83
36	36.0	93.63	35.14	90.05	390	610	180.11
35	37.0	95.50	36.14	92.04	393	503	184.08
34	38.0	97.25	37.14	93.91	396	536	187.81
33	39.0	96.63	38.14	93.47	.	.	.
32	40.0	98.75	39.14	95.68	409	1129	191.35
31	41.0	99.50	40.14	96.55	416	1146	193.10
30	42.0	99.75	41.14	96.93	.	.	.
29	43.0	104.75	42.14	101.92	.	.	.
28	44.0	104.75	43.14	102.04	423	546	204.09
27	45.0	106.63	44.14	103.99	424	513	207.99
26	46.0	109.25	45.14	106.66	.	.	.
25	47.0	109.00	46.14	106.53	433	790	213.05
24	48.0	110.50	47.14	108.09	.	.	.
23	49.0	110.25	48.14	107.95	446	1410	215.89
22	50.0	111.38	49.14	109.14	450	835	218.29
21	51.0	111.75	50.14	109.59	458	2229	219.18
20	52.0	113.50	51.14	111.39	459	556	222.78
19	53.0	113.88	52.14	111.84	466	2216	223.68
18	54.0	116.88	53.14	114.86	.	.	.
17	55.0	116.63	54.14	114.69	472	702	229.38
16	56.0	118.50	55.14	116.60	473	524	233.20
15	57.0	118.00	56.14	116.17	.	.	.
14	58.0	119.38	57.14	117.59	486	2011	235.19
13	59.0	121.88	58.14	120.12	484	396	240.23
12	60.0	123.25	59.14	121.53	487	710	243.05
11	61.0	123.88	60.14	122.20	492	1477	244.40
10	62.0	124.50	61.14	122.87	498	1503	245.73
9	63.0	124.38	62.14	122.80	.	.	.
8	64.0	125.50	63.14	123.96	509	1839	247.91

7	65.0	126.88	64.14	125.37	512	709	250.73
6	66.0	126.38	65.14	124.92	.	.	.
5	67.0	126.75	66.14	125.33	.	.	.
4	68.0	126.75	67.14	125.37	.	.	.
3	69.0	129.88	68.14	128.50	530	1275	257.01
2	70.0	132.00	69.14	130.64	529	468	261.28
1	71.0	132.63	70.14	131.30	534	1511	262.60

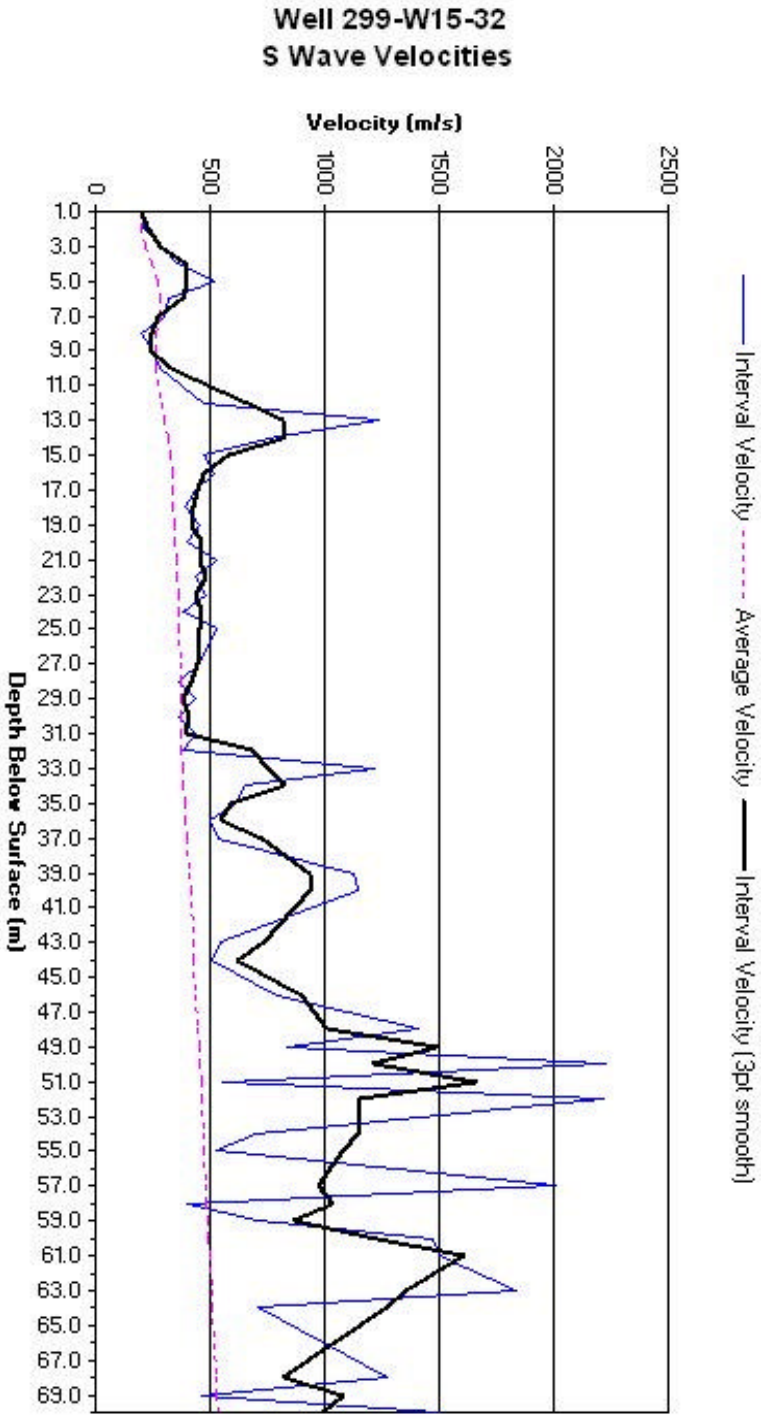

Figure 13. Graph of S wave interval velocity, smooth interval velocity, and average velocity versus depth in well 299-W15-32.

Table 6. P wave velocity table from well 299-W15-82.

Well 299-W15-82

P Wave Vertical Seismic Profile

GL = 201.195 m TOC = 201.918 m

(Offset = 5.55 m)

Seq.	Depth (TOC)	Pick Time	Depth (GL)	True Vertical Time	Average Velocity	Interval Velocity	Two-way Time
No,	(m)	(ms)	(m)	(ms)	(m/s)	(m/s)	(ms)
22	1	23.38	0.3	1.18	236	236	2.36
21	2	22.00	1.3	4.98	257	263	9.96
20	3	22.38	2.3	8.56	266	279	17.13
19	4	22.88	3.3	11.71	280	317	23.43
18	5	23.38	4.3	14.35	298	379	28.71
17	6	21.75	5.3	15.06	350	1418	30.12
16	7	21.75	6.3	16.36	384	769	32.72
15	8	24.00	7.3	19.15	380	359	38.29
14	9	26.63	8.3	22.18	373	330	44.36
13	10	27.63	9.3	23.77	390	630	47.53
12	11	27.50	10.3	24.25	424	2088	48.49
11	12	28.25	11.3	25.39	444	873	50.78
10	13	28.13	12.3	25.67	478	3565	51.34
9	14	29.00	13.3	26.79	496	892	53.58
8	15	29.88	14.3	27.88	512	917	55.77
7	16	31.25	15.3	29.40	520	658	58.81
6	17	32.38	16.3	30.68	531	785	61.35
5	18	34.38	17.3	32.76	.	.	.
4	19	34.25	18.3	32.78	557	943	65.59
3	20	34.75	19.3	33.42	.	.	.
2	21	34.75	20.3	33.54	605	2699	67.08

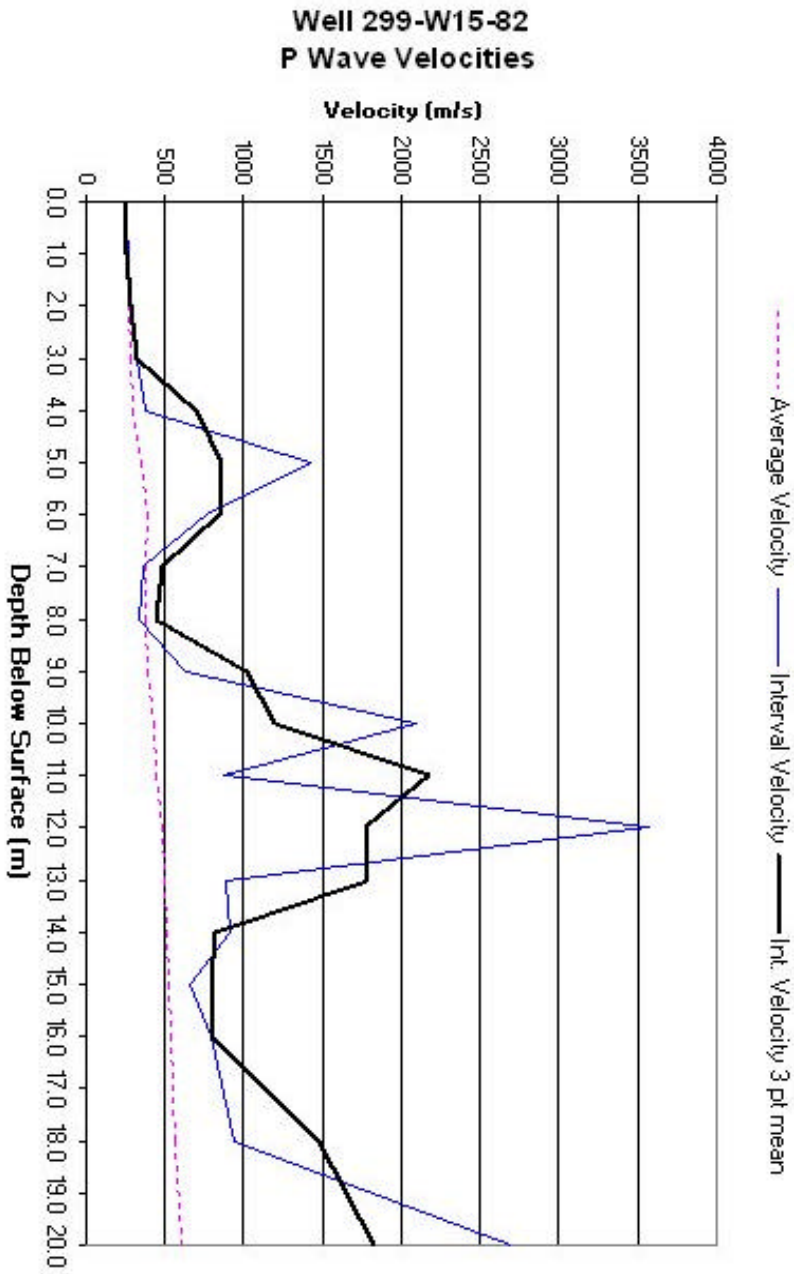

Figure 14. Graph of P wave interval velocity, smoothed interval velocity, and average velocity versus depth in well 299-W15-82.

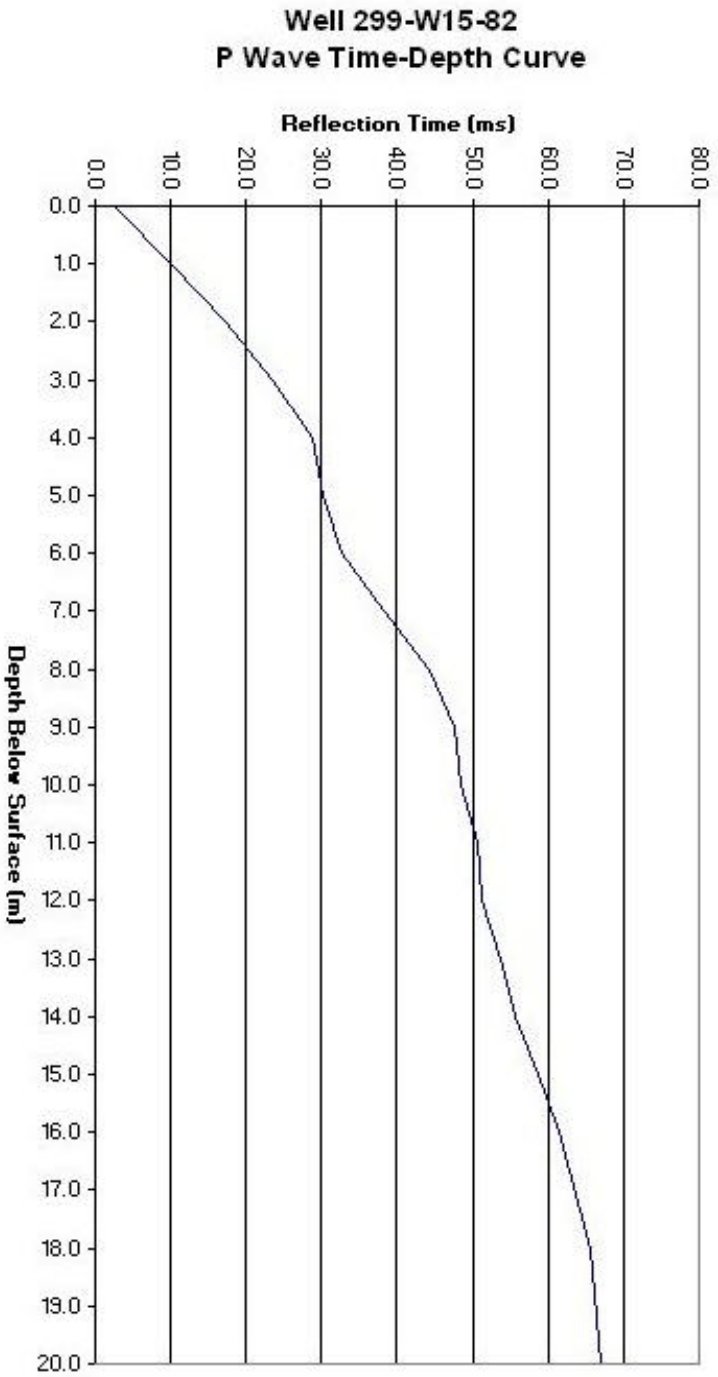

Figure 15. P wave time-depth curve for well 299-W15-82.

Table 7. S wave velocity table from well 299-W15-82.

Well 299-W15-82

S Wave Vertical Seismic Profile

GL = 201.195 m TOC = 201.918 m

(Offset = 6.0 m)

Seq.	Depth (TOC)	Pick Time	Depth (GL)	True Vertical Time	Average Velocity	Interval Velocity	Two-way Time
No,	(m)	(ms)	(m)	(ms)	(m/s)	(m/s)	(ms)
22	1	33.50	0.3	1.55	179	179	3.10
21	2	34.75	1.3	7.24	177	176	14.47
20	3	33.63	2.3	11.94	191	213	23.87
19	4	36.40	3.3	17.45	188	181	34.90
18	5	37.00	4.3	21.48	199	248	42.96
17	6	35.13	5.3	23.20	227	580	46.40
16	7	35.63	6.3	25.76	244	391	51.51
15	8	35.25	7.3	27.20	268	694	54.40
14	9	35.75	8.3	28.95	286	572	57.89
13	10	34.13	9.3	28.66	.	.	.
12	11	43.88	10.3	37.90	.	.	.
11	12	48.63	11.3	42.93	.	.	.
10	13	43.88	12.3	39.42	311	382	78.85
9	14	45.88	13.3	41.81	318	419	83.62
8	15	47.75	14.3	44.02	324	452	88.04
7	16	49.00	15.3	45.61	335	630	91.22
6	17	52.63	16.3	49.38	330	265	98.76
5	18	53.50	17.3	50.54	342	864	101.08
4	19	58.13	18.3	55.23	331	213	110.46
3	20	60.25	19.3	57.53	335	435	115.06
2	21	58.88	20.3	56.46	.	.	.
1	22	67.88	21.3	65.33	326	256	130.66

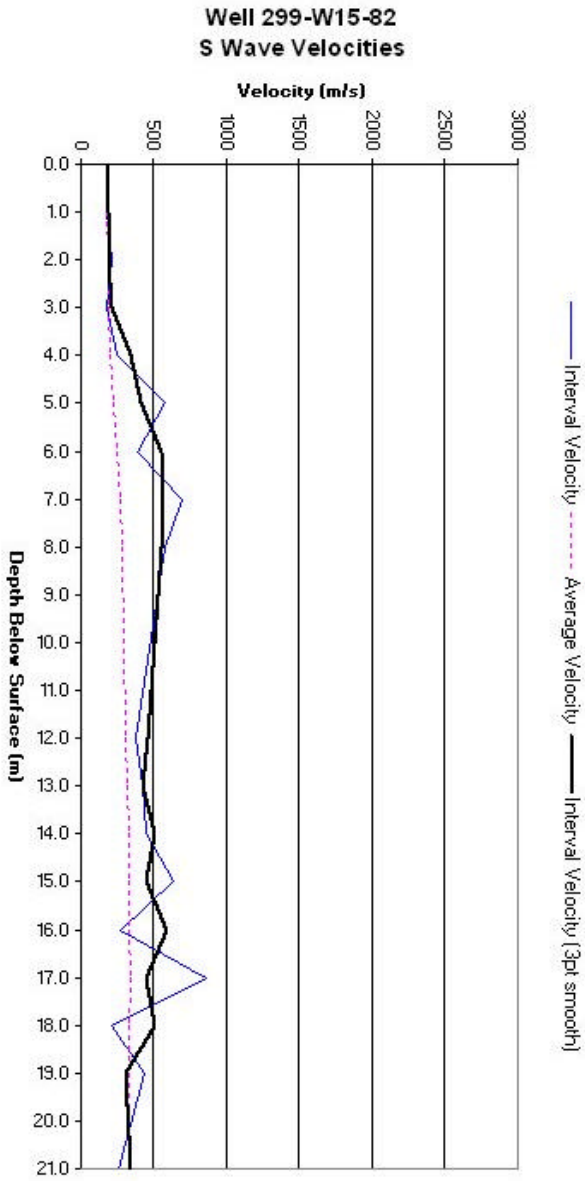

Figure 16. Graph of S wave interval velocity, smoothed interval velocity, and average velocity versus depth in well 299-W15-82. The picks for this well were heavily edited.

Table 8. P wave velocity table from well 299-W15-217.

Well 299-W15-217

P-Wave Vertical Seismic Profile

GL = 203.82 m TOC = 204.82 m

(Offset = 6.0 m)

Seq.	Depth (TOC)	Pick Time	Depth (GL)	True Vertical Time	Average Velocity	Interval Velocity	Two-way Time
No.	(m)	(ms)	(m)	(ms)	(m/s)	(m/s)	(ms)
35	2	23.70	1.0	3.87	259	259	7.74
34	3	24.38	2.0	7.65	262	264	15.30
33	4	23.00	3.0	10.21	294	390	20.42
32	5	23.00	4.0	12.68	316	406	25.35
31	6	23.38	5.0	14.88	336	453	29.77
30	7	23.88	6.0	16.81	357	521	33.61
29	8	25.00	7.0	18.90	370	476	37.81
28	9	26.50	8.0	21.13	379	450	42.25
27	10	26.50	9.0	21.98	410	1167	43.97
26	11	27.25	10.0	23.31	429	756	46.61
25	12	29.00	11.0	25.40	433	477	50.80
24	13	29.38	12.0	26.23	458	1212	52.45
23	14	29.63	13.0	26.86	484	1588	53.71
22	15	30.38	14.0	27.88	502	976	55.76
21	16	30.50	15.0	28.28	531	2506	56.56
20	17	30.88	16.0	28.88	554	1671	57.76
19	18	31.63	17.0	29.79	571	1092	59.59
18	19	33.50	18.0	31.75	567	511	63.50
17	20	34.75	19.0	33.11	574	736	66.21
16	21	36.00	20.0	34.45	581	743	68.91
15	22	37.00	21.0	35.55	591	912	71.10
14	23	38.60	22.0	37.21	591	601	74.43
13	24	40.50	23.0	.	.	.	.

12	25	40.63	24.0	39.39	609	918	78.79
11	26	42.38	25.0	41.19	607	558	82.38
10	27	44.25	26.0	43.10	603	524	86.19
9	28	44.75	27.0	43.66	618	1758	87.33
8	29	46.25	28.0	45.20	619	649	90.41
7	30	47.63	29.0	46.62	622	704	93.25
6	31	49.25	30.0	48.28	622	605	96.55
5	32	50.38	31.0	49.44	627	855	98.89
4	33	51.50	32.0	50.60	632	865	101.20
3	34	54.30	33.0	53.41	618	356	106.81
2	35	55.38	34.0	54.52	624	898	109.04

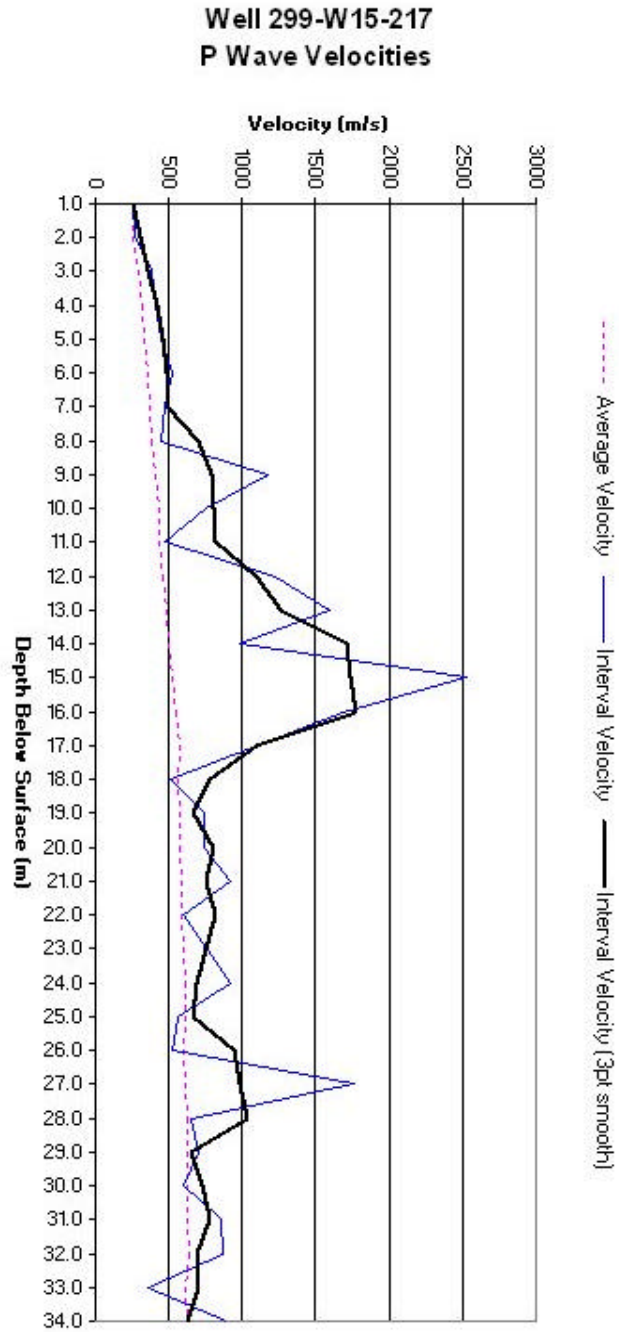

Figure 17. Graph of P wave interval velocity, smoothed interval velocity, and average velocity versus depth in well 299-W15-217.

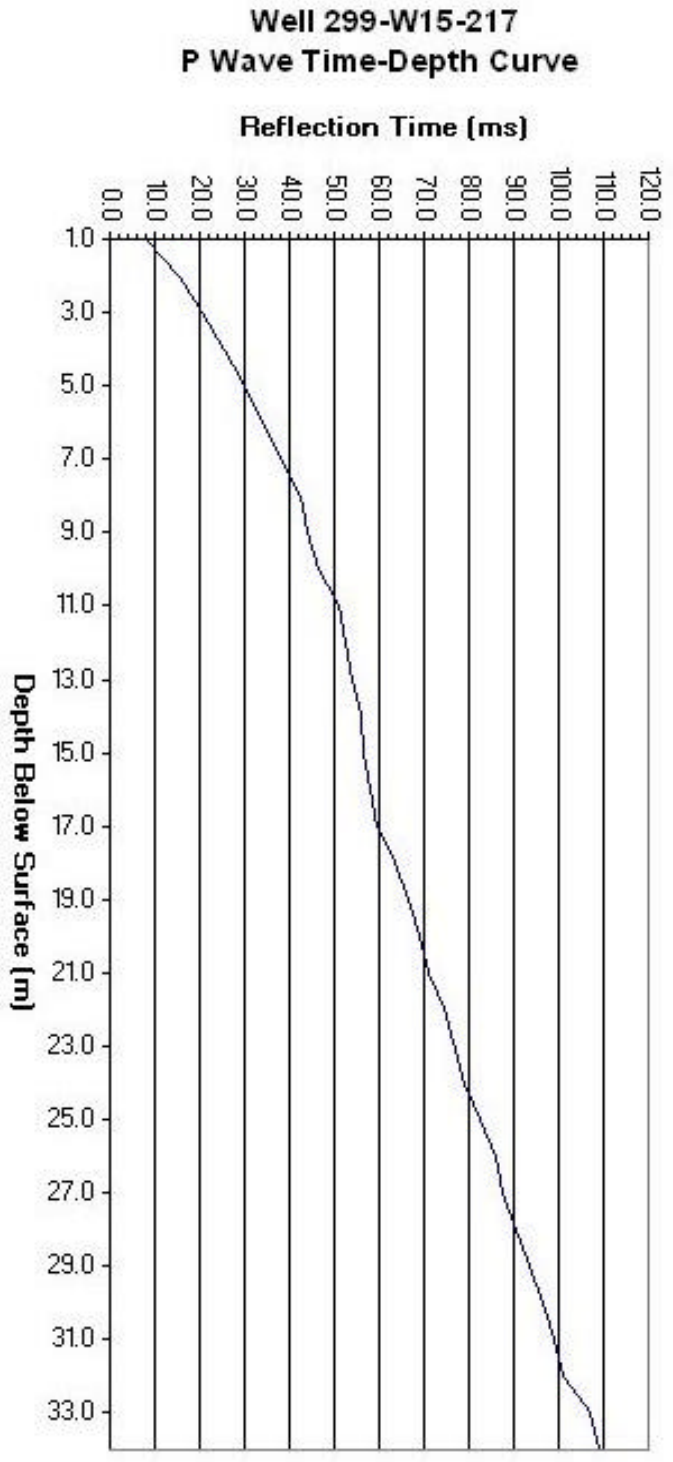

Figure 18. P wave time-depth curve for well 299-W15-217.

Table 9. S wave velocity table from well 299-W15-217.

Well 299-W15-217

S-Wave Vertical Seismic Profile

GL = 203.82 m TOC = 204.82 m

(Offset = 6.06 m)

Seq.	Depth (TOC)	Pick Time	Depth (GL)	True Vertical Time	Average Velocity	Interval Velocity	Two-way Time
No.	(m)	(ms)	(m)	(ms)	(m/s)	(m/s)	(ms)
35	2	28.63	1.0	4.67	215	215	9.35
34	3	29.63	2.0	9.30	215	216	18.60
33	4	30.88	3.0	13.71	219	227	27.42
32	5	33.63	4.0	18.54	216	207	37.07
31	6	36.38	5.0	23.16	216	216	46.32
30	7	36.13	6.0	25.43	236	441	50.85
29	8	36.75	7.0	27.79	252	423	55.58
28	9	38.50	8.0	30.69	261	344	61.39
27	10	42.13	9.0	34.95	258	235	69.90
26	11	43.13	10.0	36.89	271	516	73.78
25	12	48.00	11.0	42.04	.	.	.
24	13	46.40	12.0	41.42	290	441	82.84
23	14	48.10	13.0	43.60	298	459	87.20
22	15	49.13	14.0	45.09	311	671	90.18
21	16	49.38	15.0	45.79	328	1434	91.57
20	17	51.40	16.0	48.07	333	438	96.14
19	18	52.13	17.0	49.10	346	966	98.21
18	19	53.63	18.0	50.83	354	580	101.66
17	20	55.75	19.0	53.11	358	437	106.23
16	21	59.88	20.0	57.31	.	.	.
15	22	58.80	21.0	56.50	372	592	112.99
14	23	64.38	22.0	62.07	.	.	.
13	24	64.00	23.0	61.89	372	371	123.78
12	25	67.50	24.0	65.45	.	.	.

11	26	67.63	25.0	65.73	380	521	131.45
10	27	69.38	26.0	67.57	385	543	135.14
9	28	71.75	27.0	70.01	386	410	140.02
8	29	73.63	28.0	71.96	389	511	143.93
7	30	75.88	29.0	74.28	390	433	148.55
6	31	77.63	30.0	76.09	394	550	152.19
5	32	81.75	31.0	80.23	386	242	160.46
4	33	83.25	32.0	81.80	391	639	163.59
3	34	85.40	33.0	84.00	393	455	167.99
2	35	88.13	34.0	86.76	392	361	173.53
1	36	88.88	35.0	87.58	400	1228	175.15

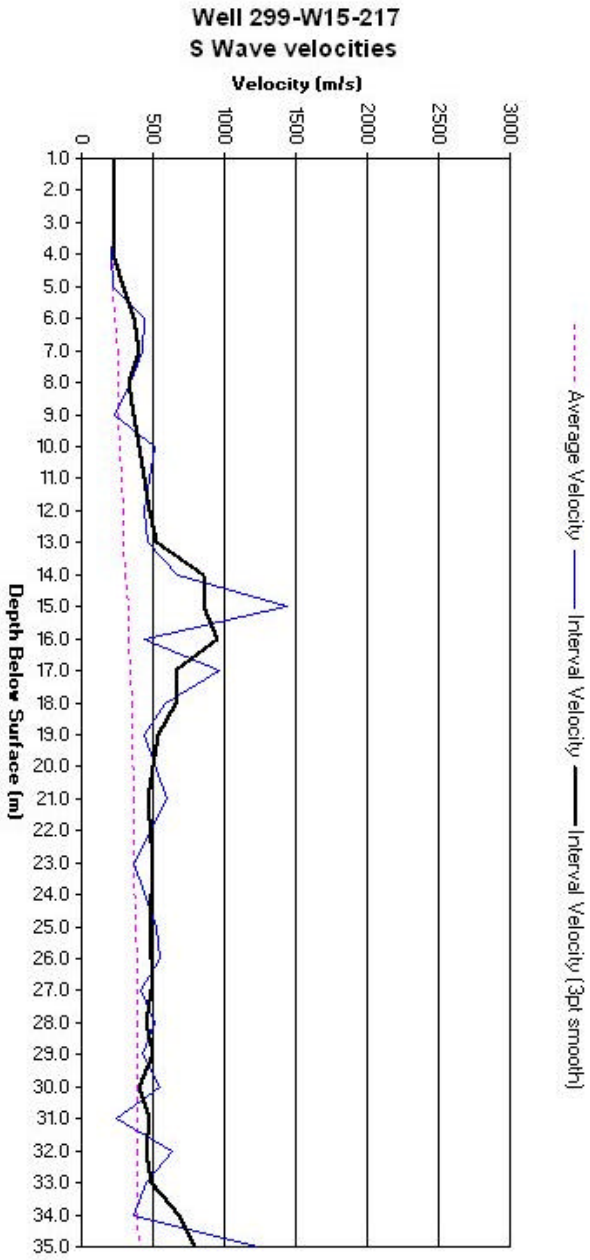

Figure 19. Graph of S wave interval velocity, smoothed interval velocity, and average velocity versus depth in well 299-W15-217.

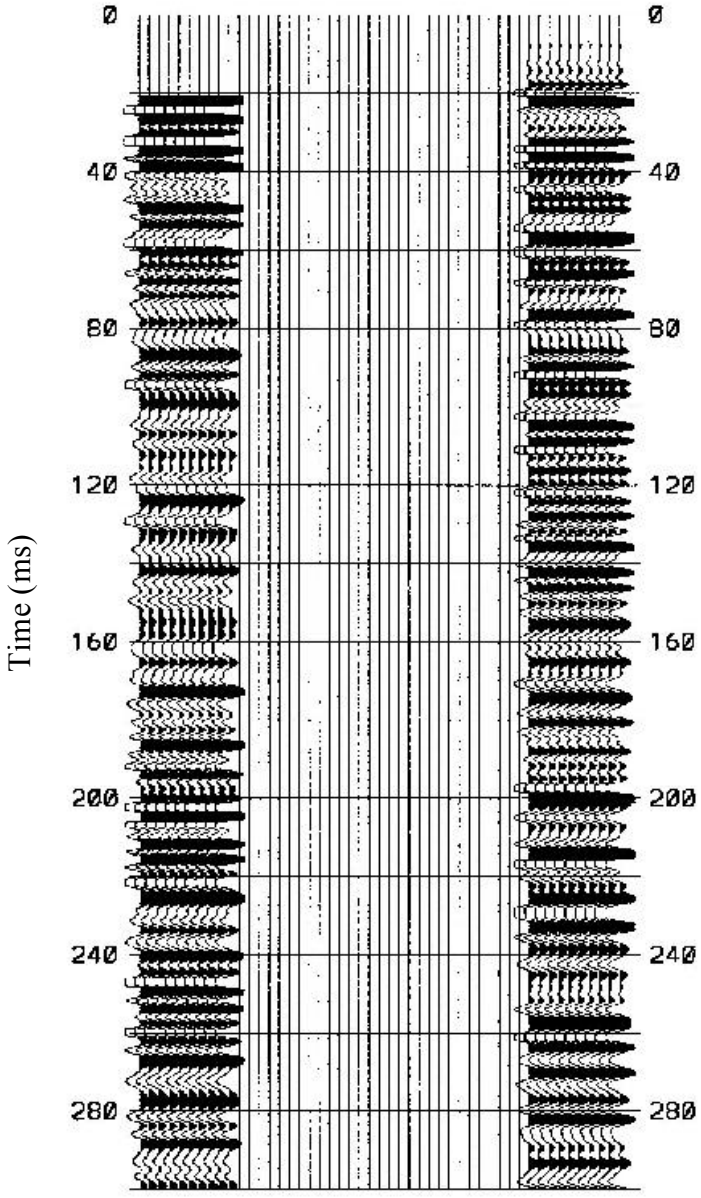

Figure 20. Front corridor stacks from wells 299-W15-32 and 299-W15-217. To find the depth of a reflector on stacked seismic section, the front corridor stack is matched against the seismic section at the well tie point. Because the depth of any refection (to TD) on the front corridor stack is known from the time-depth tables, interpretations made on the surface seismic data can be reliably converted to depth. Passband 60-300 Hz.

6.2 Seismic Reflection Profiles

6.2.1 Seismic Reflection Acquisition

Four seismic reflection profiles were collected to encompass the 216-Z-9 Crib (Figure 1). These profiles are designated lines Z-9-1, Z-9-2, Z-9-3, and Z-9-4 (Figures 23, 25, 26, and 27. A single vibrator seismic source and a 120 channel Geometrics Strataview seismograph were used to record the data. Because the caliche layer at the top of the Ringold Formation is a strong acoustic boundary and is near the DNAPL contaminated layers, the seismic acquisition parameters were chosen to optimally image this interval. Other considerations included having adequate temporal and spatial sampling necessary for high-resolution recording and to attenuate acoustic noise. The parameters used to record the 2-D seismic profiles are listed in Table 10.

Test records indicated that ground roll was a severe problem in this area and was present throughout the recording band. The requirement to do high-resolution recording, however, prohibited the use of source and receiver arrays used normally to attenuate ground roll. Consequently, data processing techniques and a lowering of the vibrator drive level helped to attenuate ground roll.

The receiver group spacing and shot interval were set at one meter (3.28 ft) and three geophones were bunched at each recording station. This arrangement resulted in 60 CMP fold data nominally. Shorter group and shot intervals were impractical because the footprint of the vibrator pad was approximately one meter (3.28 ft). To reduce the effect of wind noise each geophone group was buried approximately 15 cm (6 inches) deep. The spread was designed to have equal numbers of positive and negative offsets after NMO muting on the caliche layer; however, because of the low velocity of the overburden the fold of the target reflector is only about 30. An asymmetric split spread recording geometry was used because a symmetric split-spread would yield little velocity information on the deeper layers.

After extensive field testing the vibrator sweep was set at 30-300 Hz for six seconds and six sweeps were summed per VP. The test program indicated that higher frequencies were not returned from the target horizon. The low frequencies were needed to image deeper layers and to stabilize residual statics computations and deconvolution operators. The 300 Hz high-end of the sweep, if returned from the subsurface, results in approximately one meter vertical resolution at the level of the Plio/Pleistocene-Hanford Fine contact. The Vibroseis data were recorded uncorrelated. This allowed the flexibility to correlate the data with a synthetic sweep and allow more data processing options.

Table 10. Summary of seismic reflection profile recording parameters.

Type of survey	P wave seismic reflection
Station interval	1 meter
Source	Industrial Vehicles International (IVI) MiniVib high-frequency vibrator 12000 lb. peak force.
Source interval	1 meter on half stations
Type of sweep	Linear
Sweep frequencies	30 to 300 Hz
Sweep length	6 seconds
Source Offset (Pad)	1.5 m nominal
Record Length	7 seconds
Listen time	1 second (7 s RL – 6 s sweep)
Recording instrument	Geometrics RX 24 bit A/D resolution
Number of channels	120
Instrument Gain	48 dB fixed
Field Correlator	None
Sample interval	0.5 millisecond
Data format	SEG-2
Data redundancy	60 Fold
Geophones	Geospace 40 Hz vertical 3 per station
Near offset	0.5 m (inline), 1.58 m (straight line)
Far offset	40.5 m, 78.5 m
Cable Geometry	40.5 m--0.5 m --VP--0.5 m--78.5 m

6.2.2 Seismic Reflection Data Processing

During acquisition the seismic data were processed to brute stack sections daily for QA/QC purposes. The term "brute stack" is used to mean a stack section with no field or residual statics and with only a few velocity analyses performed. These sections were essential to ensure that survey objectives were being met and that the data quality was consistent throughout the survey. The platform used to process the data in the field was a 333 MHz, 128 MB RAM Dell laptop computer with 15 GB of internal and external disk space operating under Microsoft Windows NT. The computer was equipped with the Seismic Image Software, Ltd. VISTA seismic processing package and the Seismic Micro-Technology Kingdom seismic interpretation software.

After completion of the field survey extensive detailed seismic data processing was performed at ESRI's Environmental Geophysics Laboratory on the campus of the University of South Carolina. To process the data the Landmark Graphics Corp. petroleum industry ProMAX software operational on a Sun Microsystems Ultra-60 workstation was used. The generalized flow used to process the data is shown in Figure 21.

The data processing effort was directed towards imaging the subsurface from the middle of the Hanford Fine Formation, where DNAPL contamination is known to exist, to the caliche layer at the top of the Ringold Formation. The processing parameters determined in the field were used as a starting point for the laboratory processing. Data processing began with the raw uncorrelated field data because of the greater stability of the ProMAX algorithms compared to the PC software. Differences between the infield data processing and the laboratory data processing effort include: greater numbers of velocity analysis locations, surface consistent amplitude scaling, surface consistent deconvolution, refraction statics, surface consistent automatic residual statics, spectral whitening, and FX deconvolution.

The field data processing revealed that a major problem existed with surface wave energy in this area to the extent that no reflections are visible in the raw correlated field records (Figure 22). Only after deconvolution, spectral whitening, and low-cut bandpass filtering are reflections visible (Figure 22). Experiments with F-K and Tau-p two-dimensional filtering techniques to attenuate surface energy were only partly successful and resulted in significantly lower frequency content. The only two-dimensional filtering technique to yield acceptable results was a simple center-weighted 3 trace by 3 sample mix. This intrashot mix was applied to all the shots.

Refraction statics were computed and applied to three of the lines. Refractions could be picked for only about half the shots on line Z-9-4. On this line the loss of refraction energy is probably caused by a near surface velocity inversion. The application of automatic residual statics proved to be critical to the quality of the stack sections. Because of the low signal-to-noise ratio of the data, the maximum stack power technique was used and the maximum allowable static shift was set at 3 ms. The optimum

residual statics computation gate was found to be 160 ms centered on the caliche layer and the pilot trace was an 11 trace sum.

To enhance the continuity of the stacked data a 3 pt trace mix and FX deconvolution were applied. The data were migrated using a finite difference technique and filtered to a 60-280 Hz passband in the area of the interest. For interpretation purposes the sections are displayed at a datum of 205 m (672.6 ft.) using a datum correction velocity of 1000 m/s (3281 ft/s).

Seismic Data Processing Flow

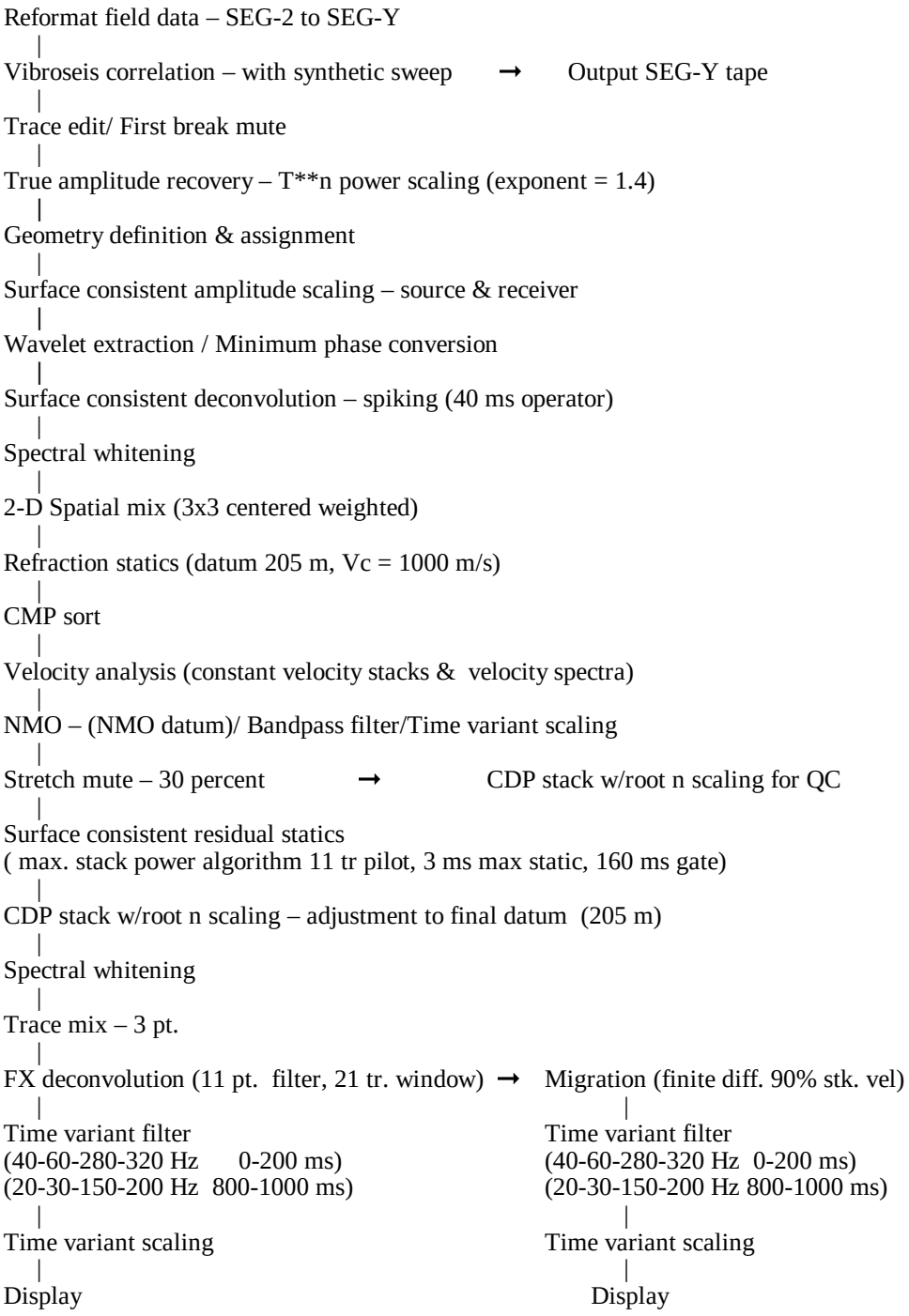

Figure 21. Data processing flow for surface seismic lines. Flow to produce seismic sections for structural/stratigraphic interpretation.

Raw and Processed Field Record

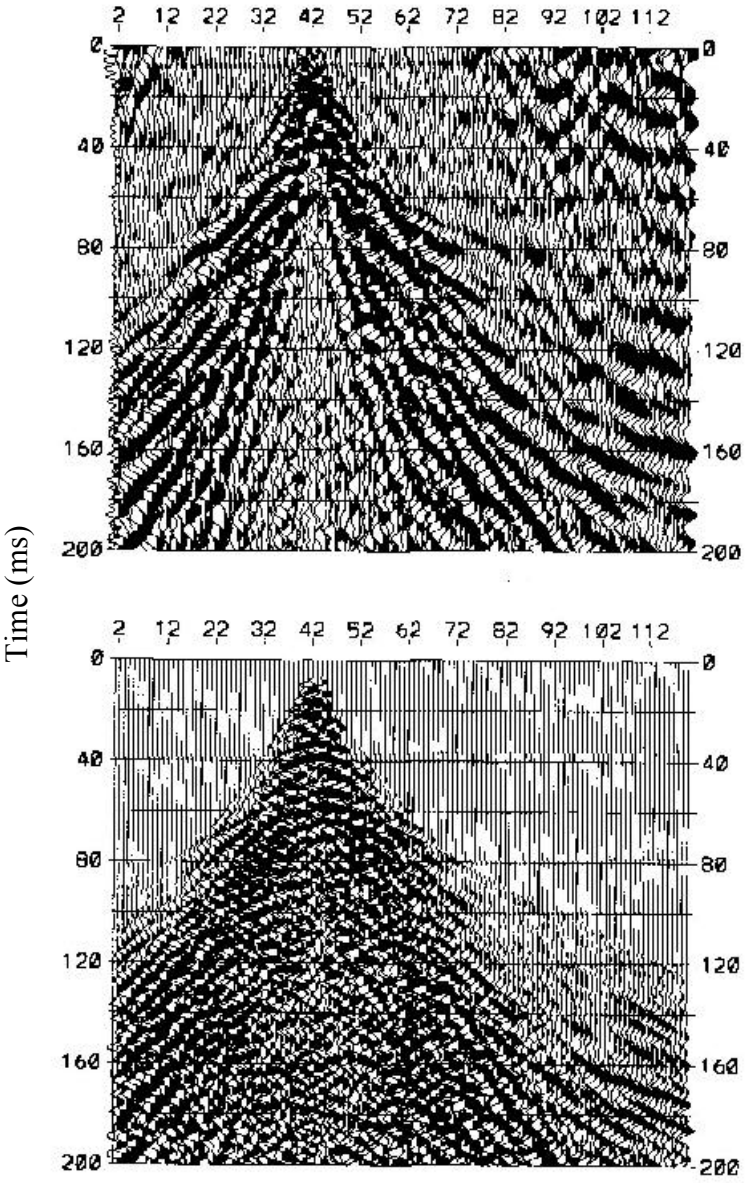

Figure 22. Raw and processed field record from line Z-9-1. Top figure is a raw field file. Note the strong ground roll and hint of a reflection at 50 ms. Bottom figure is the same as the top after preprocessing was applied. After preprocessing ground roll is attenuated and reflection events are clearer. AGC 200 ms.

7.0 Seismic Interpretation

The first phase of the interpretation was to determine which reflections correspond to the Plio/Pleistocene boundary and the caliche zone. The significance of these reflectors is that the DNAPL tends to accumulate in the vicinity of these two levels in the subsurface. A VSP was acquired in well 299-W15-32 (Figure 24) to establish a tie between the geologic units and the seismic events present in the survey data. The seismic lines were planned to tie wells in the vicinity of the crib that have high concentrations of CCl_4 (Figure 1).

7.1 Stratigraphic and Structural Interpretation

7.1.1 Seismic Line Z-9-1

Seismic Line Z-9-1 was shot from south-southeast to north-northwest along the west side of the crib (Figure 23). Three events were interpreted on the line. The uppermost event (red line) is a mappable boundary within the Hanford Formation. It separates an upper unit that has distinctive amplitude characteristics from the unit below the contact. The green event at approximately 0.120 s corresponds to the top of the Plio/ Pleistocene boundary (base of the Hanford Fine). This event is somewhat discontinuous, but mappable. Average depth to this unit is approximately 33 meters (108 ft.). The data indicates incisement of this layer by the overlying Pleistocene Hanford Fine unit. Within the unit overlying the Hanford Fine there are two features outlined in orange between SP 205-255 and SP 260-320 (Figure 23) that have been interpreted as possible channels. Also in the Hanford Fine interval on line Z-9-1 there appears to be a channel between SP 330-383.

The blue event is the top of caliche marker (Figure 23). It also corresponds roughly to the top of the Pliocene Ringold Formation and, based on interpretation of the geologic data, it is the surface upon which the DNAPL is most likely accumulating. It is a high amplitude event that is mappable over the entire survey. Amplitude intensity drops in the vicinity of SP 166-196. Downcutting by the overlying Plio/Pleistocene appears to have occurred from SP 163 to the end of the line making the south end of the line structurally higher. However, the overall dip direction is from north to south.

The Plio/Pleistocene interval displays a rather uniform parallel reflection pattern indicative of deposition in a lower energy environment (Figure 23). This unit was probably a fill unit consisting of silt and clay deposited during a low energy fluvial cycle. The upper boundary displays erosional truncation by the overlying Pleistocene Hanford Fine. Downlap occurs on to the top of the Plio/Pleistocene.

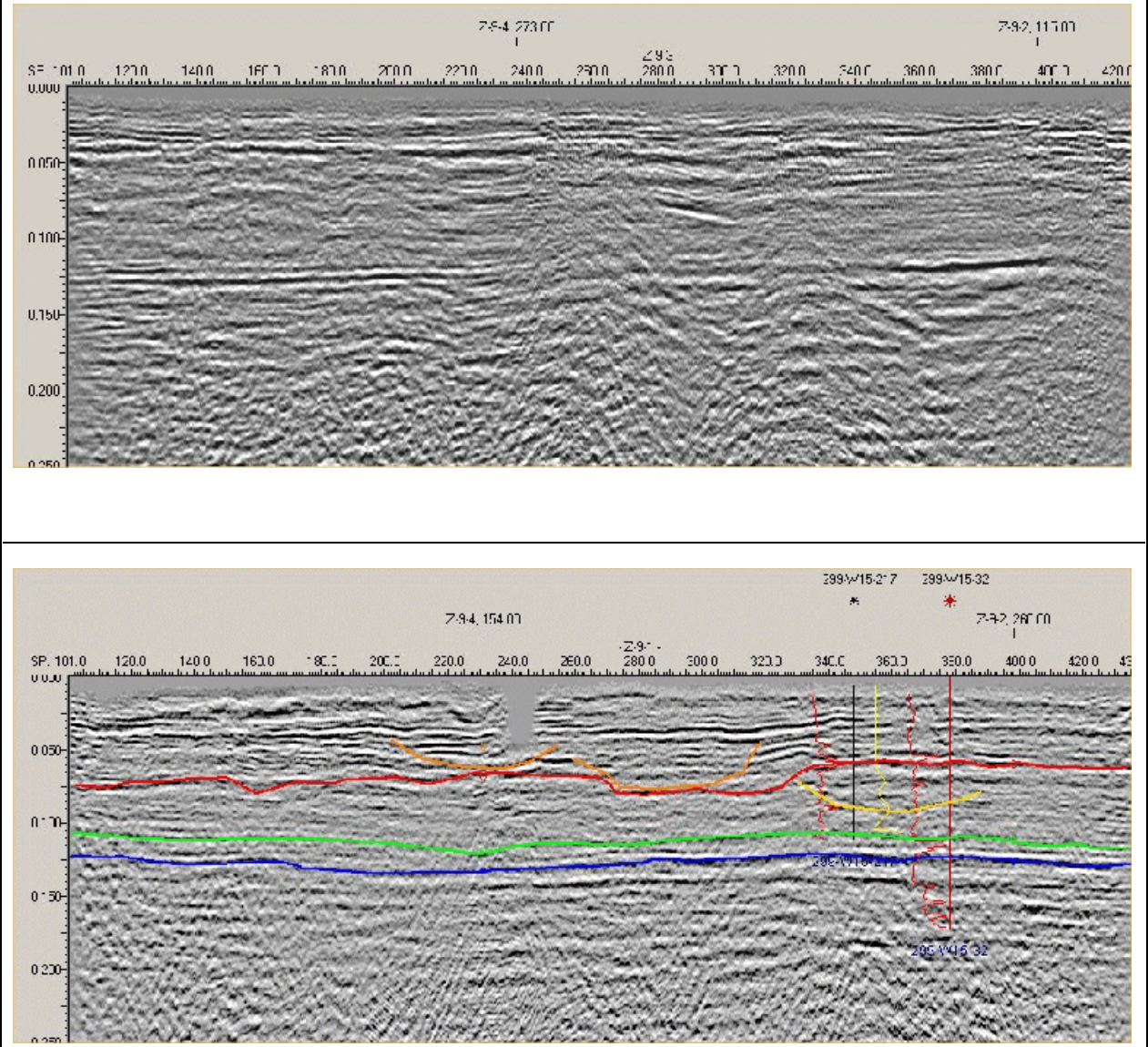

Figure 23. Seismic line Z-9-1. Green horizon is top of Plio/Pleistocene. Blue horizon is top of caliche. Red horizon is a mappable boundary within the Hanford Formation. The orange and yellow lines are interpreted as channels within the Hanford Formation. The red log left of the well is interval velocity and the yellow log right of the well is CCl_4 concentration. Notice the highest concentration (deflection right) is directly above the Hanford Fine-Plio/Pleistocene contact.

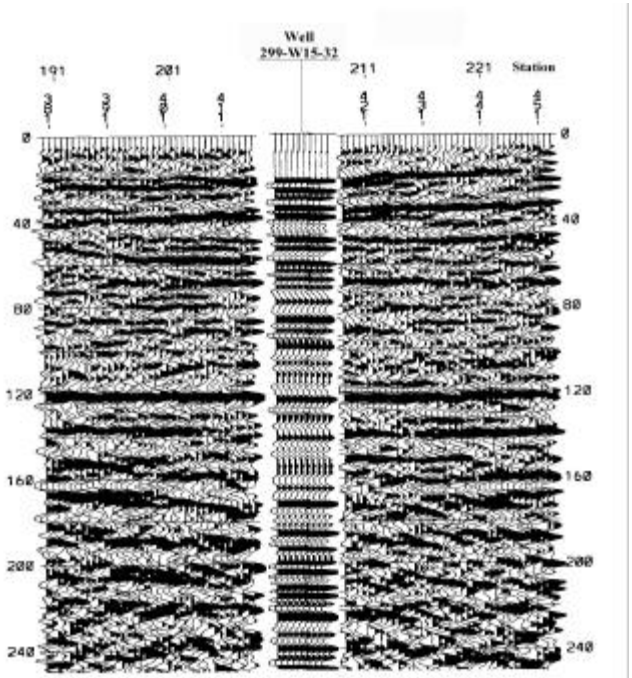

Figure 24. VSP correlation well 299-W15-32 to seismic line Z-9-2.

7.1.2 Seismic Line Z-9-2

Seismic line Z-9-2 was shot from east to west along the northern boundary of the crib area and intersects lines Z-9-1 and Z-9-3 (Figures 1 and 25). The uppermost horizon (red line) is a mappable contact within the Hanford Formation and may be the contact between the Hanford coarse unit and the underlying Hanford Fine unit. The green marker (Figure 25) is the top of the Plio/Pleistocene boundary. The event on this line is generally flat across the line and is more continuous than on line Z-9-1. A channel (yellow line Figure 25) is incised into the Plio/Pleistocene boundary from SP 109-165. The internal characteristics of the Plio/Pleistocene are similar to line Z-9-1 displaying flat lying concordant internal events. The top of caliche (blue event, Figure 25) is a high amplitude event and continuous across the section. Average depth to this unit is 36 meters (119 ft.). Below the caliche is interpreted a large channel in the Pliocene Ringold Formation between SP 105-160.

Well 299-W15-217 is projected on to the line and well 299-W15-32 is located adjacent to the line (Figure 1). The red log is the P wave interval velocity and the yellow log is CCl_4 concentration (Figure 25). The highest concentrations of CCl_4 are found directly above the Plio/Pleistocene contact.

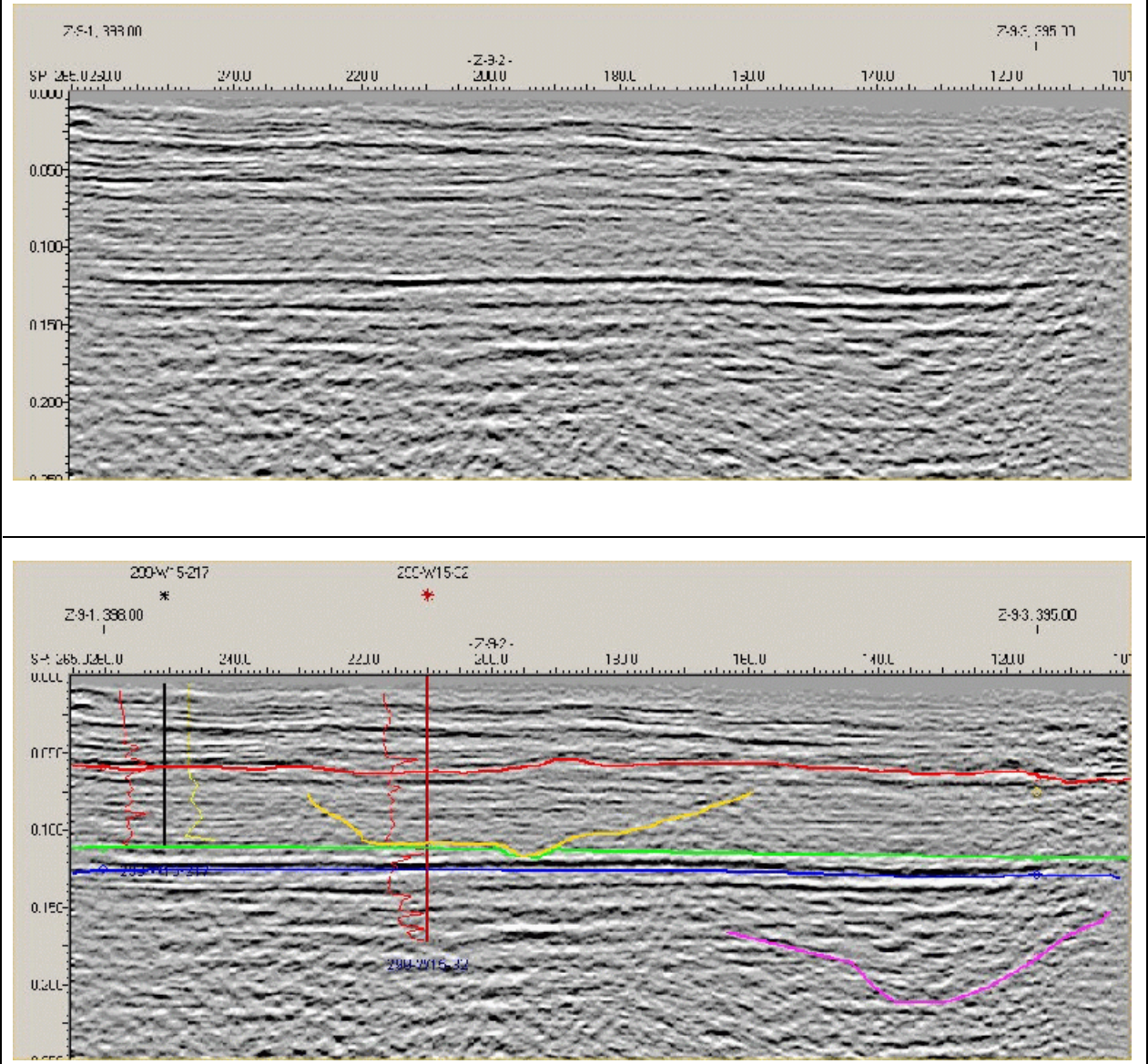

Figure 25. Seismic line Z-9-2. Green horizon is top of Plio/Pleistocene. Blue horizon is top of caliche. Red horizon is a mappable contact within the Hanford Formation. A channel (yellow line) is interpreted within the Hanford Formation. Another large channel (purple line) is interpreted within the Ringold Formation. The red logs are P wave interval velocity and the yellow log is CCl_4 concentration. Notice that the highest concentrations (deflection right) are directly above the Hanford Fine-Plio/Pleistocene contact.

7.1.3 Seismic Line Z-9-3

Seismic Line Z-9-3 is a north-south trending profile east of the crib that intersects lines Z-9-2 and Z-9-4. The top of Plio/Pleistocene reflection is discontinuous, but mappable along the line (green event, Figure 26). Average depth to the Plio/Pleistocene is approximately 34-35 meters (112-115 ft.). The layer has an overall dip from south to north of approximately 3 meters (10 ft.). The top of caliche reflection is continuous and has high amplitudes across the section (blue event). It dips approximately 3-4 meters (10-13 ft.) north to south along the line.

7.1.4 Seismic Line Z-9-4

Seismic Line Z-9-4 is an east-west trending line south of the crib that intersects lines Z-9-1 and Z-9-3. The green event (Figure 27) is the top of the Plio/Pleistocene and dips from east to west approximately 10 meters (33 ft.). The event is very discontinuous, but still mappable along the line. The blue event (Figure 27) is the top of the caliche. This horizon dips very gently from east to west. The amplitude of the event is high and is mappable the over the length of the line.

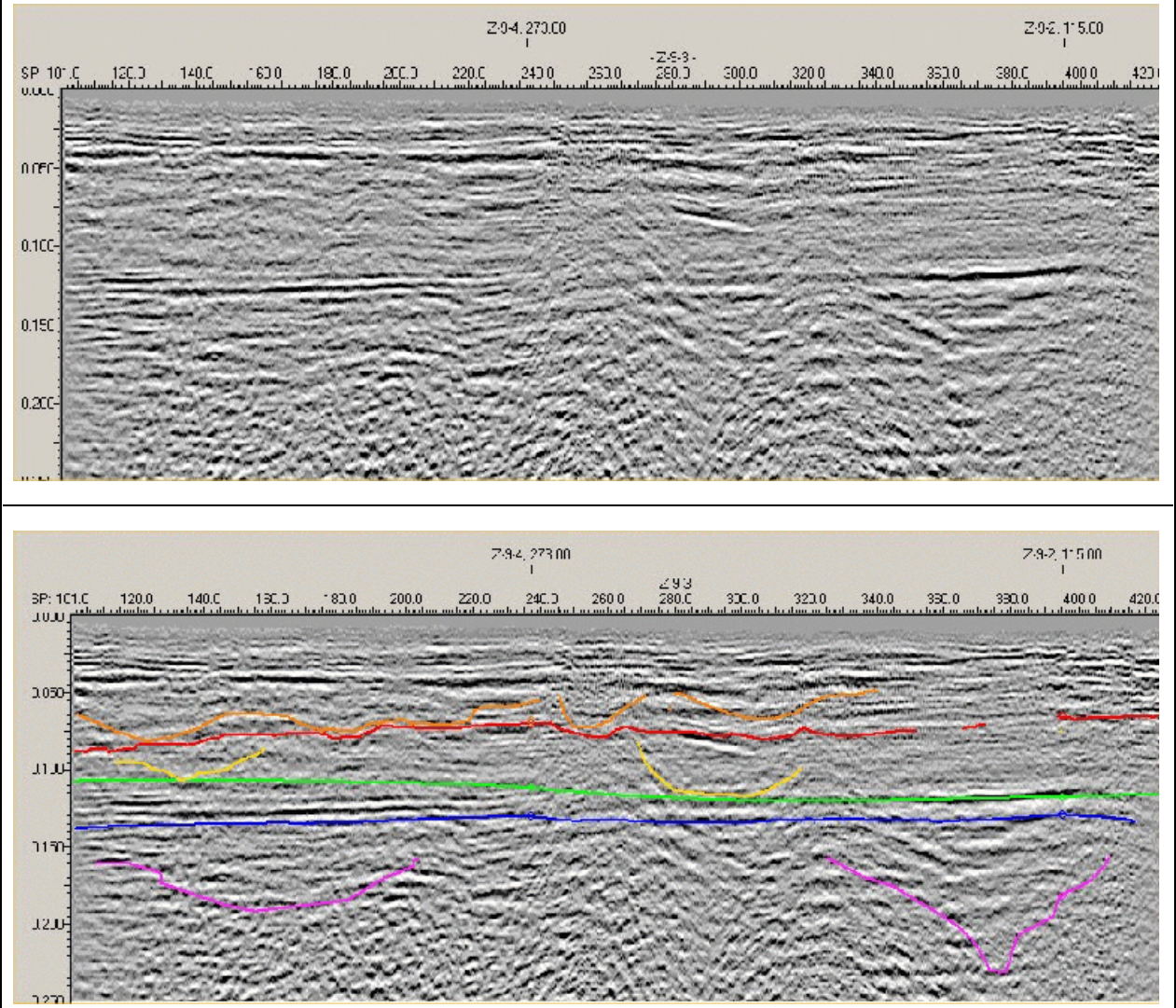

Figure 26. Seismic line Z-9-3. Green horizon is top of Plio/Pleistocene. Blue horizon is top of caliche. Red horizon is a mappable boundary within the Hanford Formation. The yellow and orange lines are interpreted as channels within the Hanford Formation. The purple lines are interpreted as a channels within the Ringold Formation.

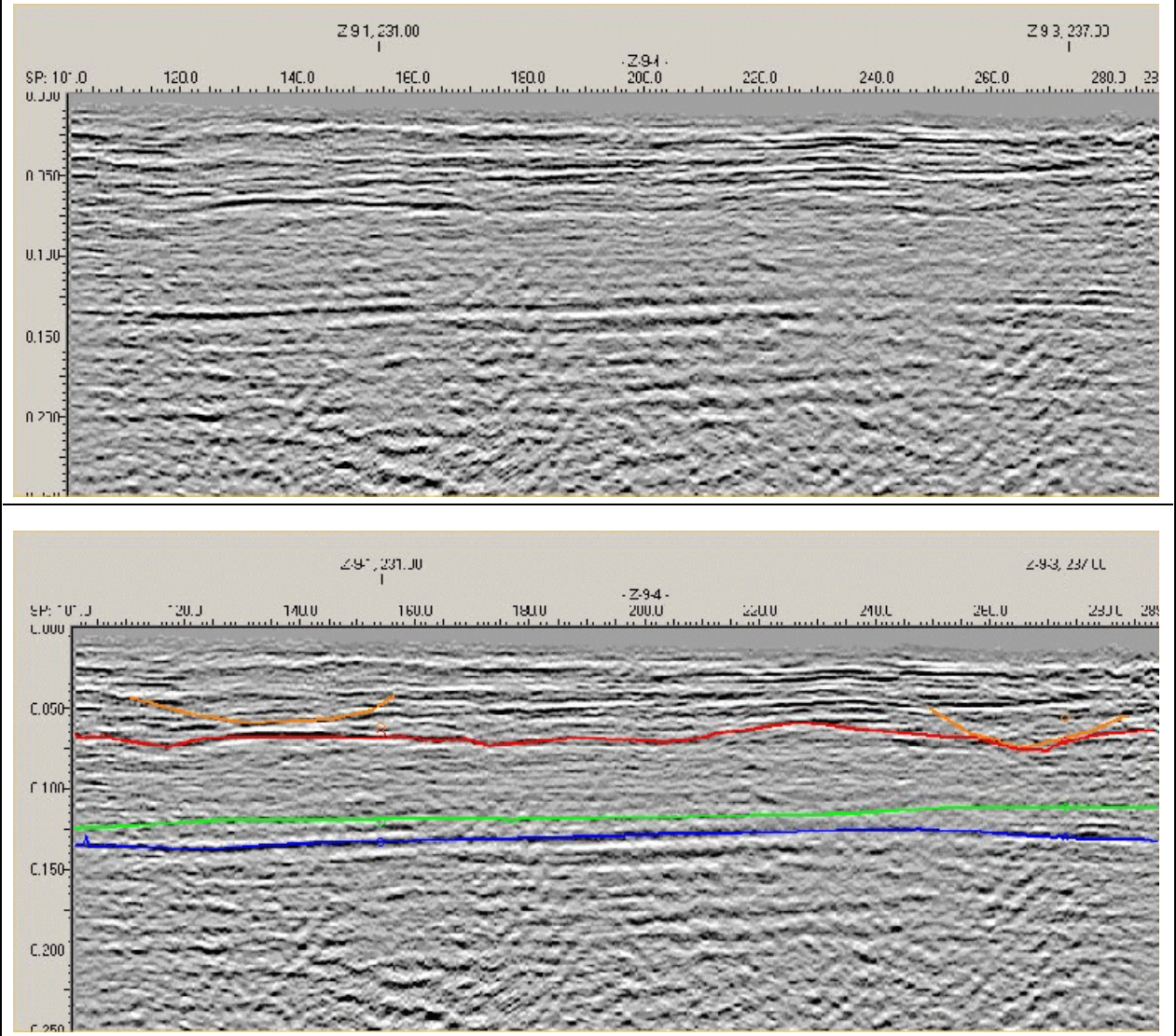

Figure 27. Seismic line Z-9-4. Green horizon is top of Plio/Pleistocene. Blue horizon is top of caliche. Red horizon is a mappable boundary within the Hanford Formation. The orange lines are interpreted as channels within the Hanford Formation.

7.2 Structural Interpretation - Structural Contour Maps

Structure contour maps were generated on two horizons: the Plio/ Pleistocene (green event) and the top of caliche (blue event). A structural high on the Plio/Pleistocene surface is located on line Z-9-1 at SP 340 near well 299-W15-217. The surface dips to the north/northeast and possibly east from this high (Figure 28). Another structural high is on the southern end of line Z-9-3. The movement of DNAPL in the subsurface is more dependent on structure than groundwater flow. Given the location of the source of entry for the solvents into the ground, the most likely flow direction for DNAPL would be to the north/northeast and possibly east of the Plio/Pleistocene high present on line Z-9-1 (Figure 28). A cautionary note: the greater the distance from the seismic lines, the more unreliable are the contours.

A similar structural picture is observed on the top of caliche map (Figure 29). A structural high exists on line Z-9-1 near the tie with line Z-9-2 and well 299-W15-217. The geologic characteristics of this surface would indicate that this would be the most likely place for the DNAPL to collect. Any DNAPL flowing along this surface, assuming that crib is the source, would be by gravity flow to the north/northeast, east, and southeast.

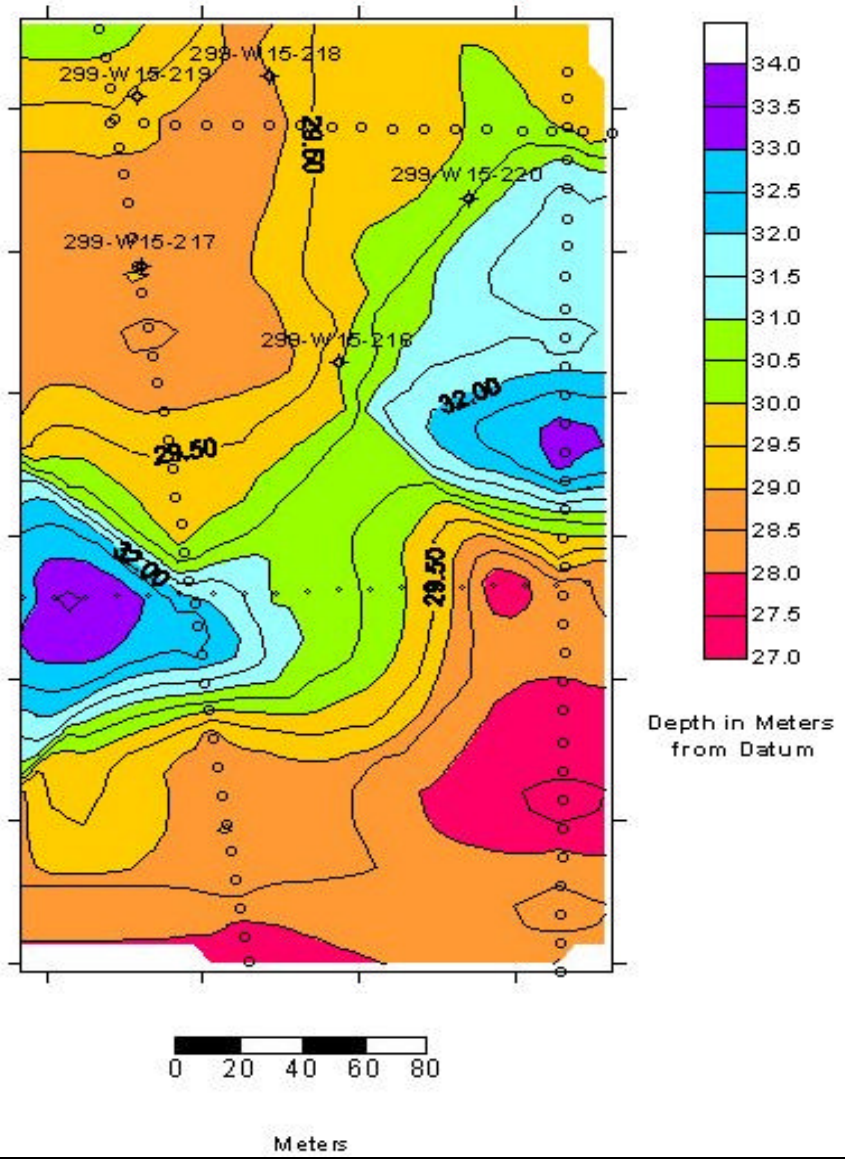

Figure 28. Structural contour map top of Plio/Pleistocene.

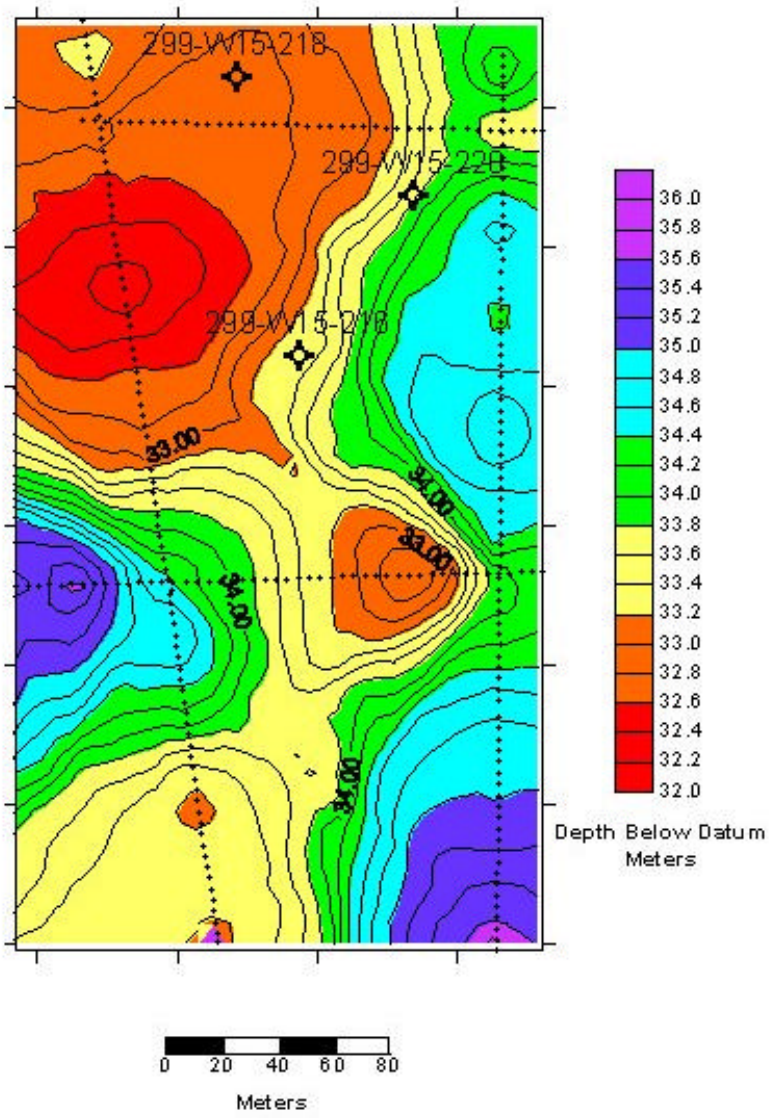

Figure 29. Structural contour map top of caliche.

7.3 Direct Detection of DNAPL

At the 200 West area the DNAPL is carbon tetrachloride (CCl_4). The solvent is present both in the vadose zone and the saturated zone. Carbon tetrachloride is found throughout the 65 meter (213 ft.) thick vadose zone where the highest concentrations of CCl_4 are associated with the Hanford Fine and the Plio-Pleistocene units located approximately 35-40 meters (115-131 ft.) below ground surface (Rohay et al. 1994).

Based upon the modeling presented in this report amplitude anomalies should occur along the Hanford Fine-Plio/Pleistocene and Plio/Pleistocene-caliche contacts where DNAPL has accumulated. Variations in the amplitude values along these horizons are observed in the field data. Presented in this report are two sets of models, one set using velocities from VSPs and density values that were either from published data or empirically derived from the P wave velocity and another set using laboratory core measurements. The observed amplitude changes that are attributed to the presence of CCl_4 correlate with the models made using the parameters derived from the VSPs. A possible explanation is that the core derived parameters are from a single point which was measured from a small core plug. The velocities derived from the VSP are from a much larger volume of material adjacent to the borehole. The amplitudes observed on the seismic data are the result of the compressional wave passing though a volume of material and therefore the VSP data represents more closely the actual seismic velocities.

Three methods of AVO analysis were preformed on the data set. The first type of AVO analysis is enhanced amplitude analysis. Each line was processed through a standard processing flow to generate the sections used for structural interpretation. To enhance the amplitude variation an additional processing step was taken. The amplitude value for each trace sample was replaced by 10 raised to the power of the original scaled amplitude. This step had the effect of boosting the high amplitude data exponentially while suppressing the low amplitude values. This technique was used primarily to enhance the possible increase in positive amplitudes if CCl_4 is present along the Plio/Pleistocene-caliche contact.

The second AVO analysis technique is offset range limited stacks. Based on the modeling (Figures 5 and 7) scenarios, both at the Hanford Fine-Plio/Pleistocene and the Plio/Pleistocene-caliche contacts can exhibit significant amplitude variation with angle of incidence under certain conditions. Offset limited range stacks are used when the reflection coefficient at large angles of incidence (long offsets) is sufficiently different than that at small angles of incidence (short offsets) so stacking ranges of offsets will reveal the change in reflection coefficient. The range of angles used in the offset range stack is determined from the AVO modeling.

The third method AVO analysis, which was applied primarily at the Plio/Pleistocene-caliche contact, is gradient analysis. Castagna and others (1998) stated that AVO interpretation could be

enhanced by crossplotting the AVO intercept (A) and gradient (B) provided that reasonable petrophysical parameters are used so that a well defined background trend in the A-B plane is present. The B term (gradient) is the second term from the Shuey (1985) approximation of the Zoeppritz equations, which describes the theoretical amplitude response from 15-30 degrees of incidence (immediate angles of offset). In the shallow subsurface the background trend is generally positive. Any deviation from the background trend is a very good indicator of the presence of DNAPL or a change in the lithology. Simply put, the AVO gradient is the change in slope of the reflection coefficient with increase in offset (Graul, 2001). In Figure 7 the slope of the curve on each of the graphs (reflection coefficient versus offset) is the gradient.

7.4 Top of Plio/Pleistocene AVO Analysis

The amplitudes along the top of Plio/Pleistocene event should decrease due to the presence of CCl_4. The magnitude of the amplitude decrease is controlled by CCl_4 saturation in either or both the Hanford Fine and the Plio/Pleistocene (Figure 5). In contrast, the top of caliche event displays a significant increase in amplitude if CCl_4 is present (Figure 7). The interpretation of the Hanford Fine-Plio/Pleistocene event was made on the standard processed sections. No enhancement was necessary to identify any decrease in amplitude (dim-out) along this event.

7.4.1 Line Z-9-1 Color Variable Density Display

A dim-out along the Plio/Pleistocene event occurs from SP 335-398 on Z-9-1 (Figure 30). This dim out is also located where $CCl4_4$ is being extracted directly above the Hanford Fine-Plio/Pleistocene contact. On Figure 30 the blue log to the right of well 299-W15-217 shows the concentration of CCl_4. A secondary anomaly occurs between SP 200-220 northeast of well 299-W15-217.

7.4.2 Line Z-9-2 Color Variable Density Display

Line Z-9-2 (Figure 31) displays low amplitude values between SP 155-190 and SP 240-265. These low amplitudes are believed to be associated with the presence of CCl_4 because of the high concentrations of CCl_4 in nearby well 299-W15-217 at the Hanford Fine-Plio/Pleistocene contact.

7.4.3 Line Z-9-3 Color Variable Density Display

Line Z-9-3 (Figure 32) displays amplitude decreases between SP 250-320 and SP 325- 360. Even though there appear to be a dim outs, which would suggest the present of CCl_4, the data quality is poor. Because the data quality is poor, it cannot be determined whether the amplitude decreases are caused by the presence of CCl_4 or some other factor such as a lithology change.

7.4.4 Line Z-9-4 Color Variable Density Display

No dim-outs occur over the length of line Z-9-4 (Figure 33).

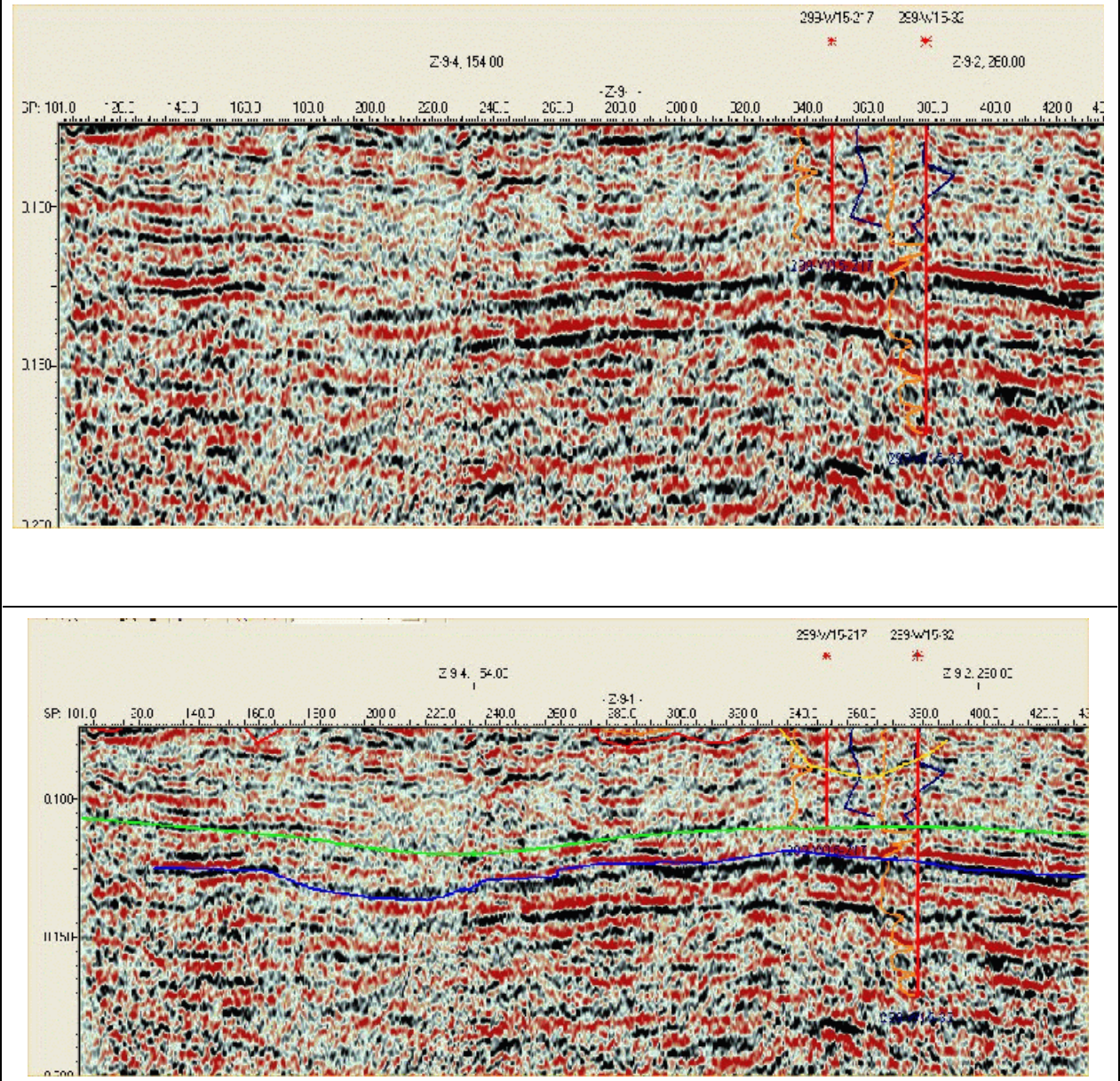

Figure 30**.** Color variable density display of seismic profile Z-9-1. The upper figure is without interpretation and the lower figure is with interpretation. The green line is the contact between the Hanford Fine and the Plio/Pleistocene. The blue line is the contact between the Plio/Pleistocene and the caliche layer. The orange log to the left of the well is P wave interval velocity and the blue log is CCl_4 concentration. Black indicates the highest amplitude and red indicates the lowest amplitude. The light bluish-grey colors indicate negative or low amplitudes.

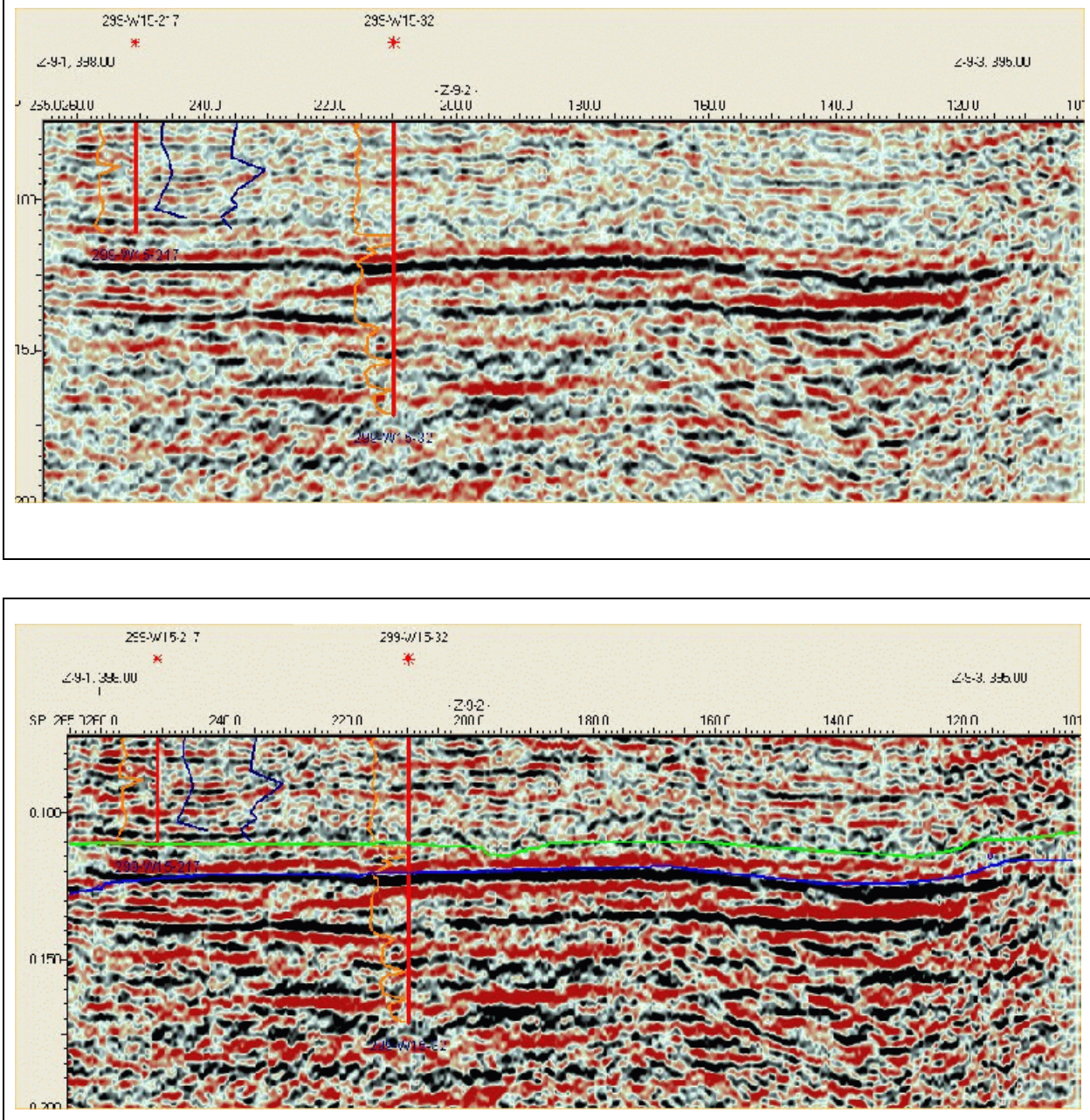

Figure 31. Color variable density display of seismic profile Z-9-2. The upper figure is without interpretation and the lower figure is with interpretation. The green line is the contact between the Hanford Fine and the Plio/Pleistocene. The blue line is the contact between the Plio/Pleistocene and the caliche layer. The orange log to the left of the well is P wave interval velocity and the blue log is CCl_4 concentration. Black indicates the highest amplitude and red indicates the lowest amplitude. The light bluish-grey colors indicate negative or low amplitudes.

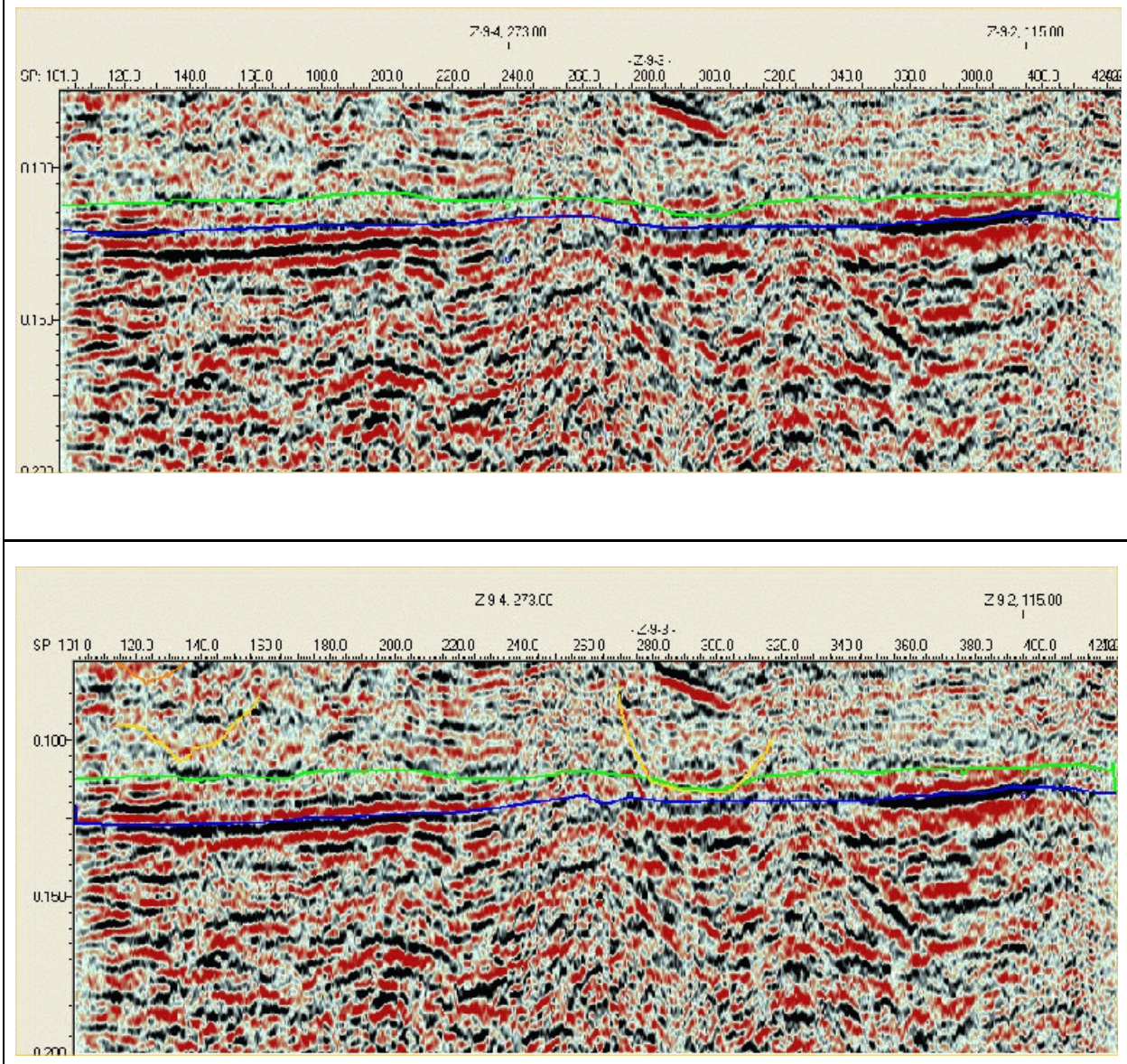

Figure 32. Color variable density display of seismic profile Z-9-3. The upper figure is without interpretation and the lower figure is with interpretation. The green line is the contact between the Hanford Fine and the Plio/Pleistocene. The blue line is the contact between the Plio/Pleistocene and the caliche layer. Black indicates the highest amplitude and red indicates the lowest amplitude. The light bluish-grey colors indicate negative or low amplitudes.

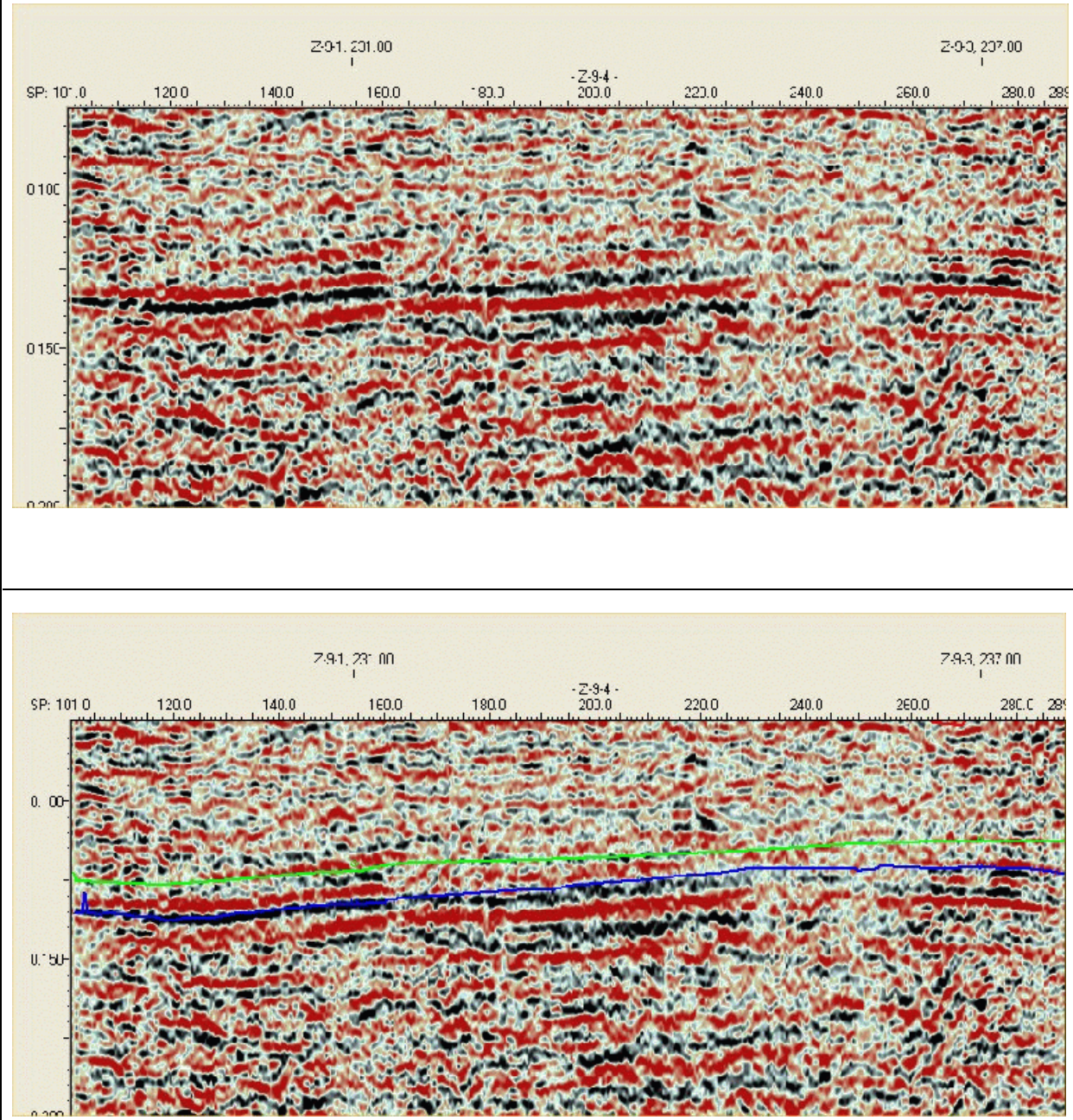

Figure 33. Color variable density display of seismic profile Z-9-4. The upper figure is without interpretation and the lower figure is with interpretation. The green line is the contact between the Hanford Fine and the Plio/Pleistocene. The blue line is the contact between the Plio/Pleistocene and the caliche layer. Black indicates the highest amplitude and red indicates the lowest amplitude. The light bluish-grey colors indicate negative or low amplitudes.

7.5 Top of Caliche Enhanced Amplitude Stacks

The modeling data (Figure 7) for the Plio/Pleistocene-caliche contact suggest that if CCl_4 is present in the pores either in the Plio/Pleistocene and or the caliche there will be an AVO response that is significantly different than the background response. If the Plio/Pleistocene pores are saturated with CCl_4 and the caliche pores are saturated with air, the model indicates the reflection coefficient response at small incident angles is negative. As incidence angles increase, the refection coefficient becomes less negative and at large angles of incidence the reflection coefficient becomes positive. If both the Plio/Pleistocene and caliche pores are saturated with CCl_4, the reflection coefficient is positive at small incidence angles and becomes more positive with increasing angles of incidence, but at a lesser rate than the background response. If the caliche pores are saturated with CCl_4 the critical angle is approximately 15^0 whereas all other scenarios reach critical angle at approximately 25^0, except for the the background response which reaches critical angle at 32^0.

At the Plio/Pleistocene-caliche contact two different methods of AVO analysis are applied to the seismic profiles. The first method is enhanced amplitude stack and the second method is offset range limited stacks. The reflection coefficient at large angles of incidence (long offsets) is sufficiently different than that at small angles of incidence (short offsets) so that stacking ranges of offsets will reveal the change in reflection coefficient if the contaminant is present. The range of angles used in the offset range limited stack is determined from the AVO modeling.

7.5.1 Z-9-1 Enhanced Amplitude Stack

Figure 34 is the enhanced amplitude stack for Z-9-1. Significant amplitude anomalies occur on line Z-9-1 along the top of the caliche event. An anomaly occurs between SP 379-426 at 121 ms, between SP 346-360 at 123 ms, and between SP 270 –306 at 125 ms. A minor anomaly is also found from SP 128-164 at 123 ms. Amplitude increases are seen in the interval between the Plio/Pleistocene (green event) and the caliche (blue event) boundaries.

According to Rohay and others (1994) well 299-W15-217 had the highest measured CCl_4 concentration (37,817 ppb) at a depth of 34.7 meters (114 ft.) in the Plio/Pleistocene (green event). This corresponds to the amplitude anomaly on line Z-9-1 from SP 346-360 (Enclosure 13).

7.5.2 Z-9-2 Enhanced Amplitude Stack

Figure 35 is the enhanced amplitude stack for Z-9-2. Significant amplitude increases exist on Z-9-2 between SP 120-152, SP 155-219, and SP 230-261 at approximately 127 ms. All these anomalies are along the top of caliche horizon. Amplitudes in general are significantly higher along this profile and are vertically more extensive than on Z-9-1. These amplitudes, along with the apparent areal extent, suggest that significant DNAPL is present along the caliche surface.

Well 299-W15-218 is projected into an amplitude anomaly on line Z-9-2 at SP 209 and well 299-W15-219 is projected into the end of an anomaly on Z-9-2 at SP 260. Wells 299-W15-218 and 299-W15-219 yielded CCl_4 concentrations of 15,794 ppb at 33.5 m (109.9 ft.) and 11,688 ppb at 34.9 m (114.5 ft.) respectively. These depths are in good agreement with line Z-9-2 for the interval between the Plio/Pleistocene and the top of caliche reflectors.

7.5.3 Z-9-3 Enhanced Amplitude Stack

Figure 36 is the enhanced amplitude stack for Z-9-3. Z-9-3 is located east of the crib area. A major increase in amplitude exists on Z-9-3 between SP 351-400 along the top of caliche reflector at approximately 140 ms. To the south along the line an amplitude increase exists from SP 114-204 within the Ringold Formation, but above the water table. The significance of this amplitude anomaly is not known at this time.

7.5.4 Z-9-4 Enhanced Amplitude Stack

Figure 37 is the enhanced amplitude stack for Z-9-4. The line is located to the south of the crib area. There appear to be high amplitudes between SP 120-150. West along the seismic profile, between SP 17-205, are non-continuous weak high amplitudes. These high amplitudes are attributed to lithology changes along the contact.

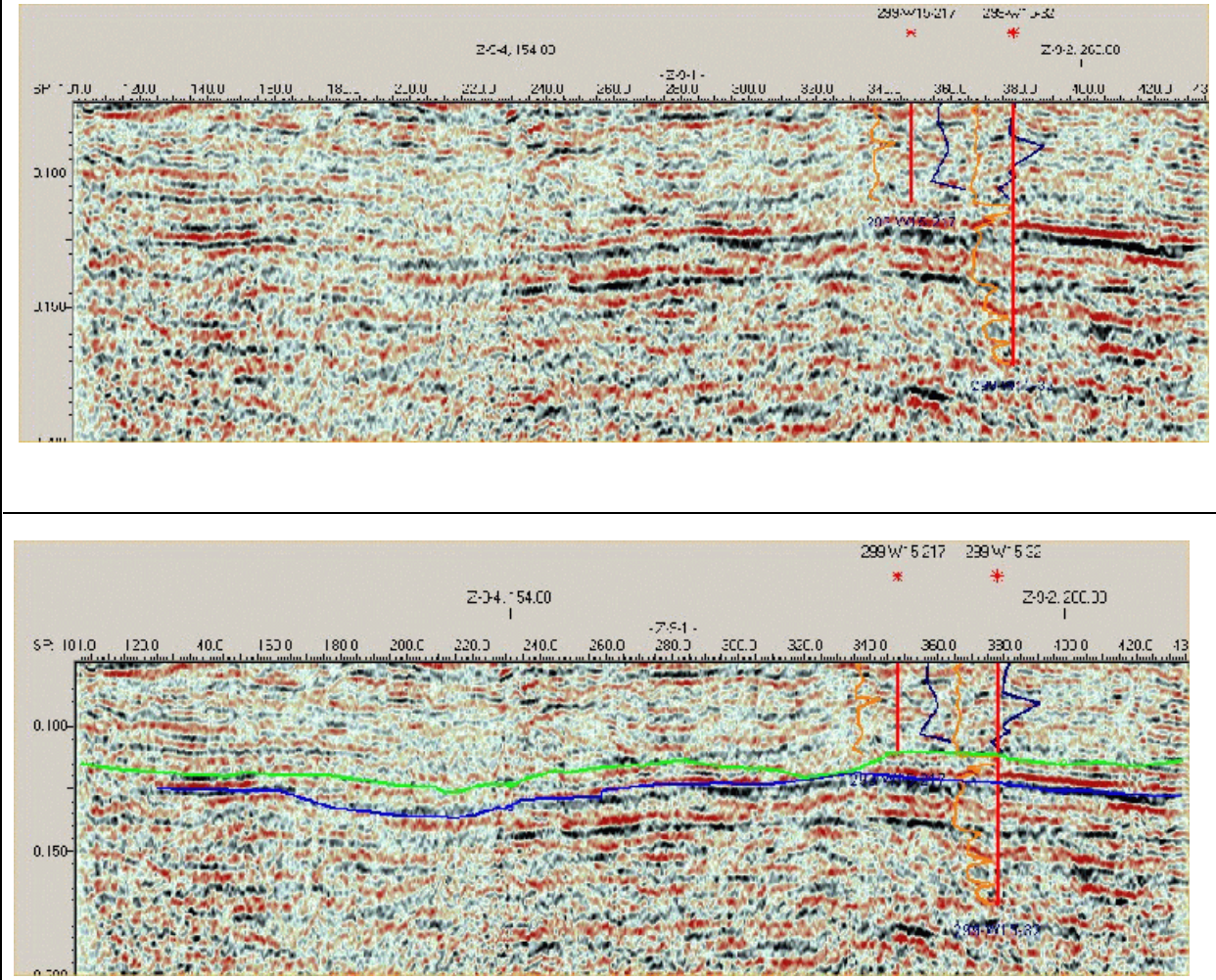

Figure 34. Enhanced amplitude stack of seismic profile Z-9-1. The upper figure is without interpretation and the lower figure is with interpretation. The green line is the contact between the Hanford Fine and the Plio/Pleistocene. The blue line is the contact between the Plio/Pleistocene and the caliche layer. Note the increase in amplitude of the black reflector at approximately 50 ms near SP 400.

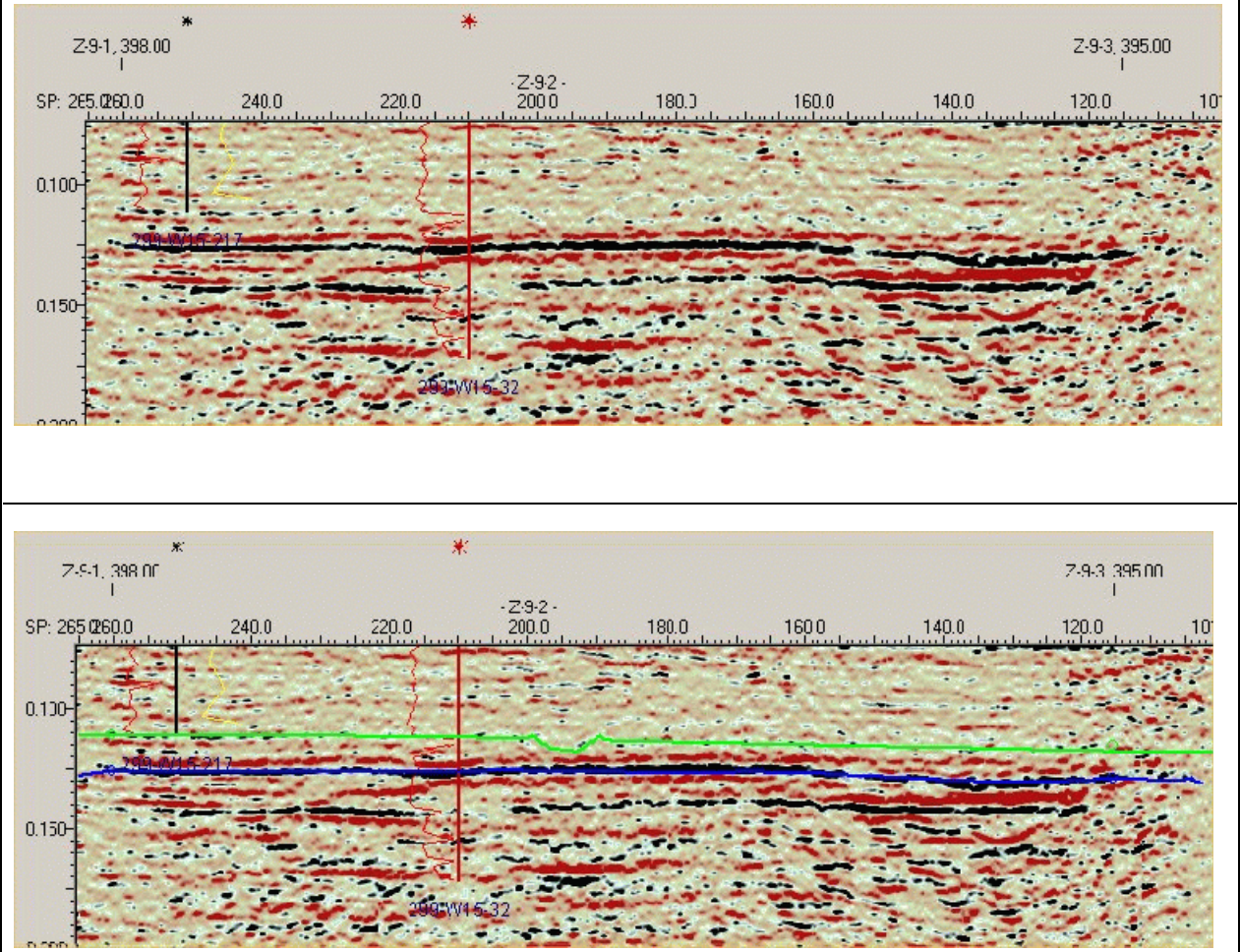

Figure 35. Enhanced amplitude stack of seismic profile Z-9-2. The upper figure is without interpretation and the lower figure is with interpretation. The green line is the contact between the Hanford Fine and the Plio/Pleistocene. The blue line is the contact between the Plio/Pleistocene and the caliche layer. Note the increase in amplitude of the black reflector at approximately 50 ms between SP 160-230.

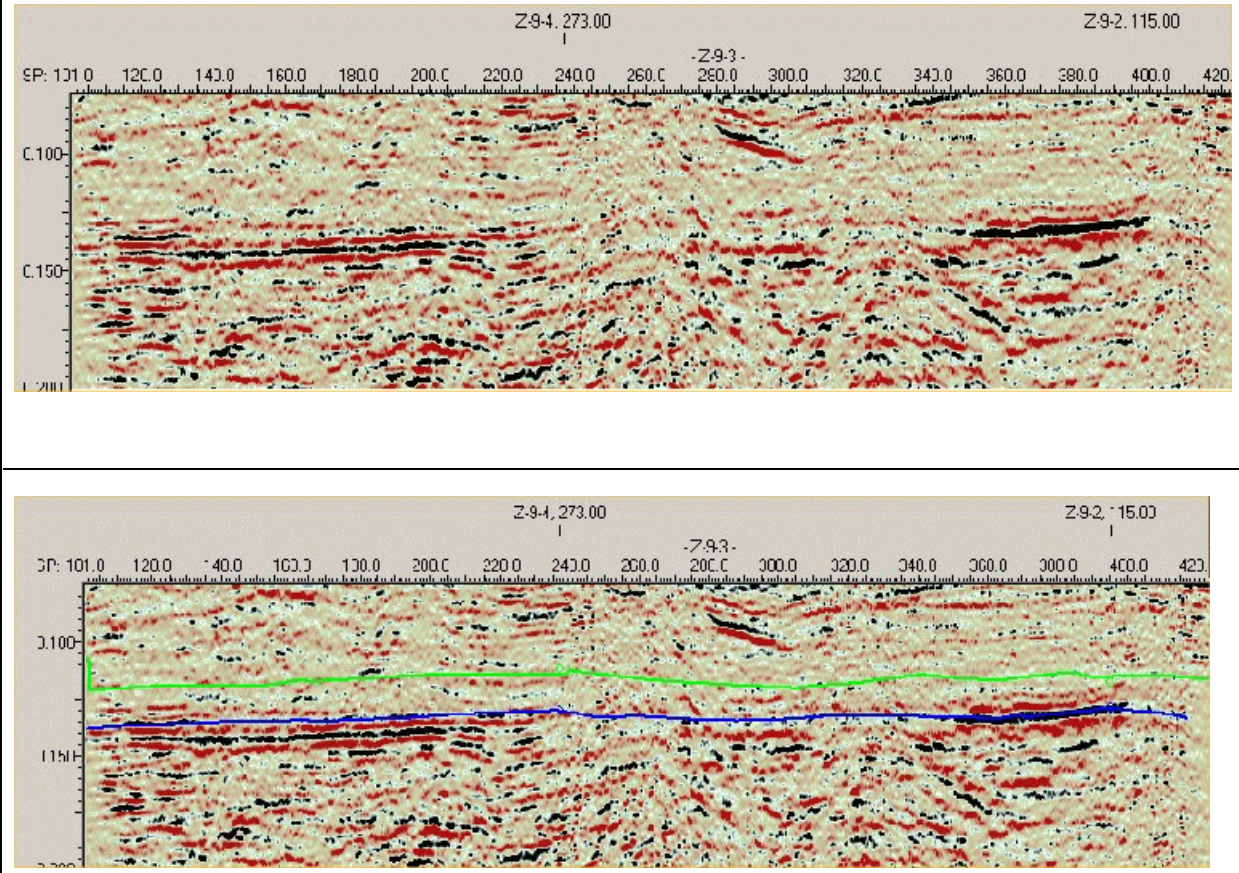

Figure 36. Enhanced amplitude stack of seismic profile Z-9-3. The upper figure is without interpretation and the lower figure is with interpretation. The green line is the contact between the Hanford Fine and the Plio/Pleistocene. The blue line is the contact between the Plio/Pleistocene and the caliche layer. Note the increase in amplitude of the black reflector at approximately 70 ms between SP 350-395.

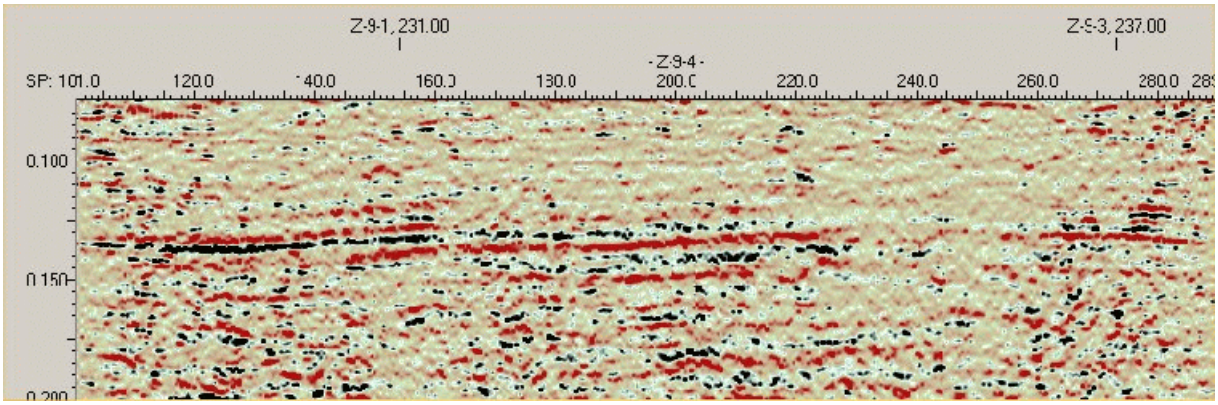

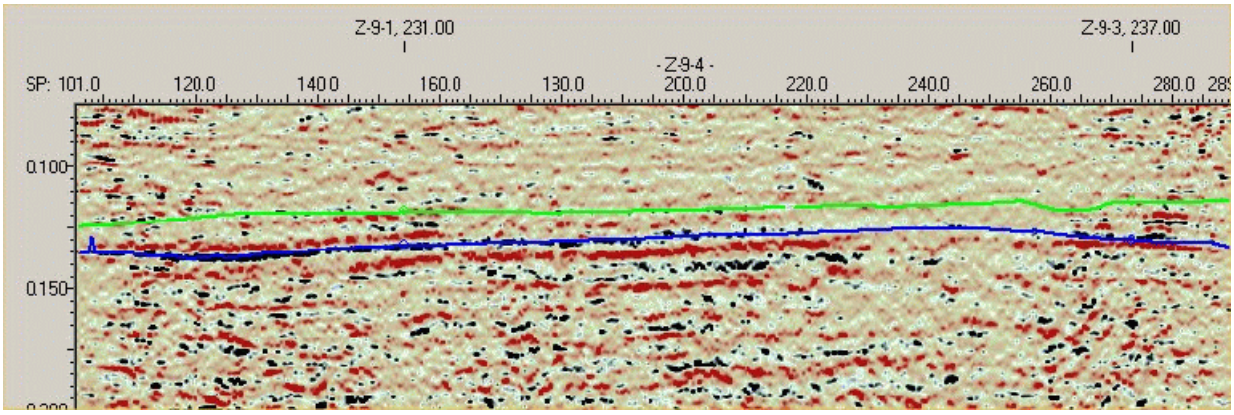

Figure 37. Enhanced amplitude stack of seismic profile Z-9-4. The upper figure is without interpretation and the lower figure is with interpretation. The green line is the contact between the Hanford Fine and the Plio/Pleistocene. The blue line is the contact between the Plio/Pleistocene and the caliche layer. Note the increase in amplitude of the black reflector at approximately 70 ms between SP 120-155.

7.6 Offset Range Limited Stacks

Based on the modeling (Figures 5 and 7) significant AVO effects can occur under certain conditions at the Hanford Fine-Plio/Pleistocene and the Plio/Pleistocene-caliche contacts. In this final report offset range limited stacking was used in conjunction with the enhanced amplitude stacks to detect AVO anomalies. Offset range limited stacks can be used to detect amplitude variation with offset if the reflection coefficient at large angles of incidence (long offsets) is significantly different than that at small angles of incidence (short offsets). In this situation, stacking ranges of offsets will reveal the change in reflection coefficient. The range of angles used in the offset range limited stack is determined from the AVO modeling.

7.6.1 Z-9-1 Offset Range Limited Stacks

Figure 38 shows offset range limited stacks for seismic profile Z-9-1. The angle ranges are $0\text{-}20^0$ (near offsets/angles), $20^0\text{-}40^0$ (intermediate offsets/angles), and $40^0\text{-}60^0$ (far offsets/angles). The angles are selected based on the modeling results (Figures 5 and 7) and the offsets corresponding to the angles are determined by the subsurface velocity field.

At the Hanford Fine-Plio/Pleistocene contact (Figure 38, green marker) there are weak negative amplitudes between SP 355-365 on the near offset stack (Figure 38, upper). On the intermediate offset stack (middle figure) the amplitudes become more negative between SP 345-365. According to the model (Figure 5), if the Hanford Fine pores are saturated with CCl_4 and the underlying Plio/Pleistocene pores are air-filled, the near offset amplitudes will be slightly negative and increase in negativity with increasing offset. The effect observed on the seismic data is so slight that it is inconclusive whether it is related to the presence of CCl_4 in the Hanford Fine.

In the Plio/Pleistocene there appears to be negative amplitudes on the near offset angle stack (Figure 38 lower) between SP 340-420. On the intermediate angles stack the amplitudes become less negative (Figure 34 middle). Recalling the model (Figure 7), if the Plio/Pleistocene is saturated with CCl_4 and the underlying caliche is air-filled, the amplitudes should become less negative with increasing incident angle. On the far offset angle stack (Figure 38 upper) the seismic data are spotty. If the model (Figure 7) is correct, the background response critical angle is about 30^0 and the curve representing the scenario where only the Plio/Pleistocene is saturated with CCl_4 has a critical angle of about 45^0. Thus, the data are consistent with the scenario of CCl_4 in the Plio/Pleistocene and air in the caliche.

7.6.2 Z-9-2 Offset Range Limited Stacks

Figure 39 shows offset range limited stacks for seismic profile Z-9-2. The upper figure is the near offset stack ($0\text{-}20^0$), the middle figure is the intermediate offset stack ($20^0\text{-}40^0$), and the lower

figure is the far offset stack (40^0-60^0). The top of the caliche is the blue marker. The green marker is top of the Plio/Pleistocene.

In the Plio/Pleistocene unit between SP 125-150, SP 155-170, and SP 210-235 are negative amplitudes. According to the model (Figure 5), the background response should be positive amplitude; however, if the Plio/Pleistocene is saturated with CCl_4 there should be negative amplitudes on all the offsets. Between SP 125 and 150 there are very strong negative amplitudes on the far offset stack directly below the Hanford Fine-Plio/Pleistocene contact. This result is consistent with the model for CCl_4 saturation of the Plio/Pleistocene.

Between SP 130-170 and SP 190 -210 the caliche event is a strong positive amplitude. This was not observed on seismic profile Z-9-1. If the model is correct, this suggests that there is CCl_4 in the caliche pores and/or in the Plio/Pleistocene pores directly above the caliche. On the far offsets (40^0-60^0) (lower figure) between SP 120-140 and SP 210-240 are moderate to strong positive amplitudes at the caliche event. Again according to the model (Figure 7), the moderate to strong amplitudes suggest either the caliche pores contain CCl_4 or both the caliche and the Plio/Pleistocene directly above the caliche contain CCl_4. Between SP 145-170 in the caliche and the portion of the Plio/Pleistocene directly above the caliche are very strong positive amplitudes that suggest the presence of CCl_4.

7.6.3 Z-9-3 Offset Range Limited Stacks

Figure 40 shows offset range limited stacks for seismic profile Z-9-3. On the near offset stack (Figure 40, upper) directly above the Hanford Fine and Plio/Pleistocene contact are strong positive amplitudes between SP 375-390. The model data indicates that this is the background response. However, according to the model the background response goes to critical angle at about 22^0 (Figure 5). On the immediate stack the positive amplitude is still present. This suggests that the Hanford Fine and the underlying Plio/Pleistocene pores are saturated with CCl_4. On the far offset stack the same anomaly is positive directly below a negative which could possibly be the result of the Hanford Fine pores saturated with air and the Plio/Pleistocene pores saturated with CCl_4. Also on the far offset stack between SP 360-375 the amplitudes directly above the Plio/Pleistocene are negative and are sandwiched between two positive amplitude events.

At the Plio/Pleistocene-caliche contact an amplitude anomaly is detected on the far offset stack between SP 130-165. This anomaly is a large negative amplitude which suggests that CCl_4 is in the Plio/Pleistocene. Between SP 360-380 on the far offset stack is large a positive event at the Plio/Pleistocene-caliche contact. Based on the model (Figure 7) this suggests that both the Plio/Pleistocene and the caliche are saturated with CCl_4. However, this anomaly is occurring where the data quality starts to deteriorate and thus may spurious rather than indicative of the presence of CCl_4.

7.6.4 Z-9-4 Offset Range Limited Stacks

Figure 41 is the offset range limited stacks for seismic profile Z-9-4. The only significant anomaly is located in the Plio/Pleistocene between SP 125-130. It appears to be present on the near offset stack (Figure 41 upper) and possibly as a very weak anomaly on the intermediate offset stack. The location of the anomaly is at the Plio/Pleistocene-caliche contact. In this case model 2 (Figure 7) applies. If the model is correct, this suggests that the anomaly may indicate that the Plio/Pleistocene is air-filled and the caliche is saturated with CCl_4.

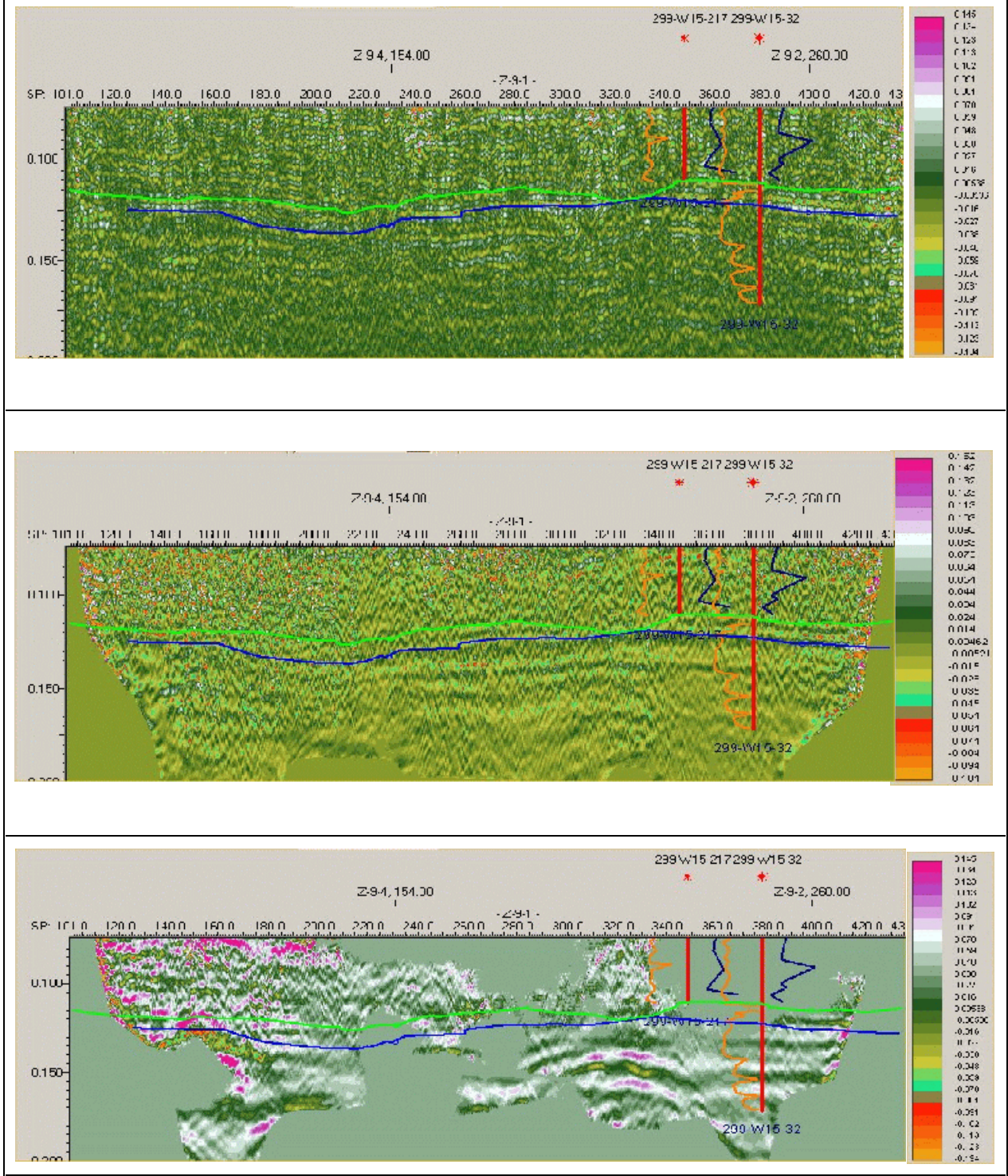

Figure 38. Seismic profile Z-9-1 offset range limited stacks. The upper figure shows the near offset stack (0-20^0). The middle figure is the intermediate angle stack (20^0-40^0). The lower figure shows the far offset stack (40^0-60^0).

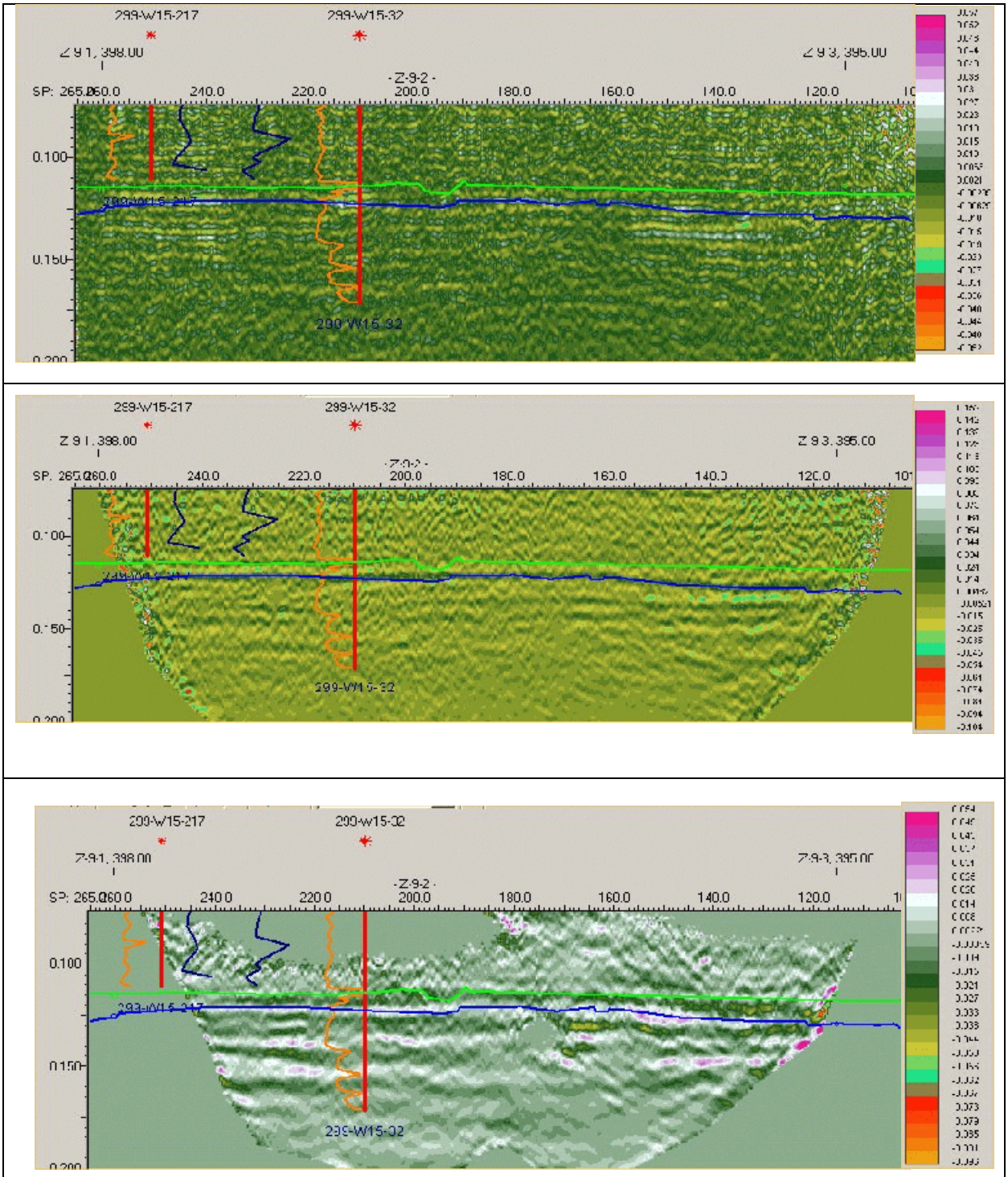

Figure 39. Seismic profile Z-9-2 offset range limited stacks. The upper figure is the near offset stack (0^0-20^0). The middle figure is the intermediate offset stack (20^0-40^0). The lower figure is the far offset stack (40^0-60^0).

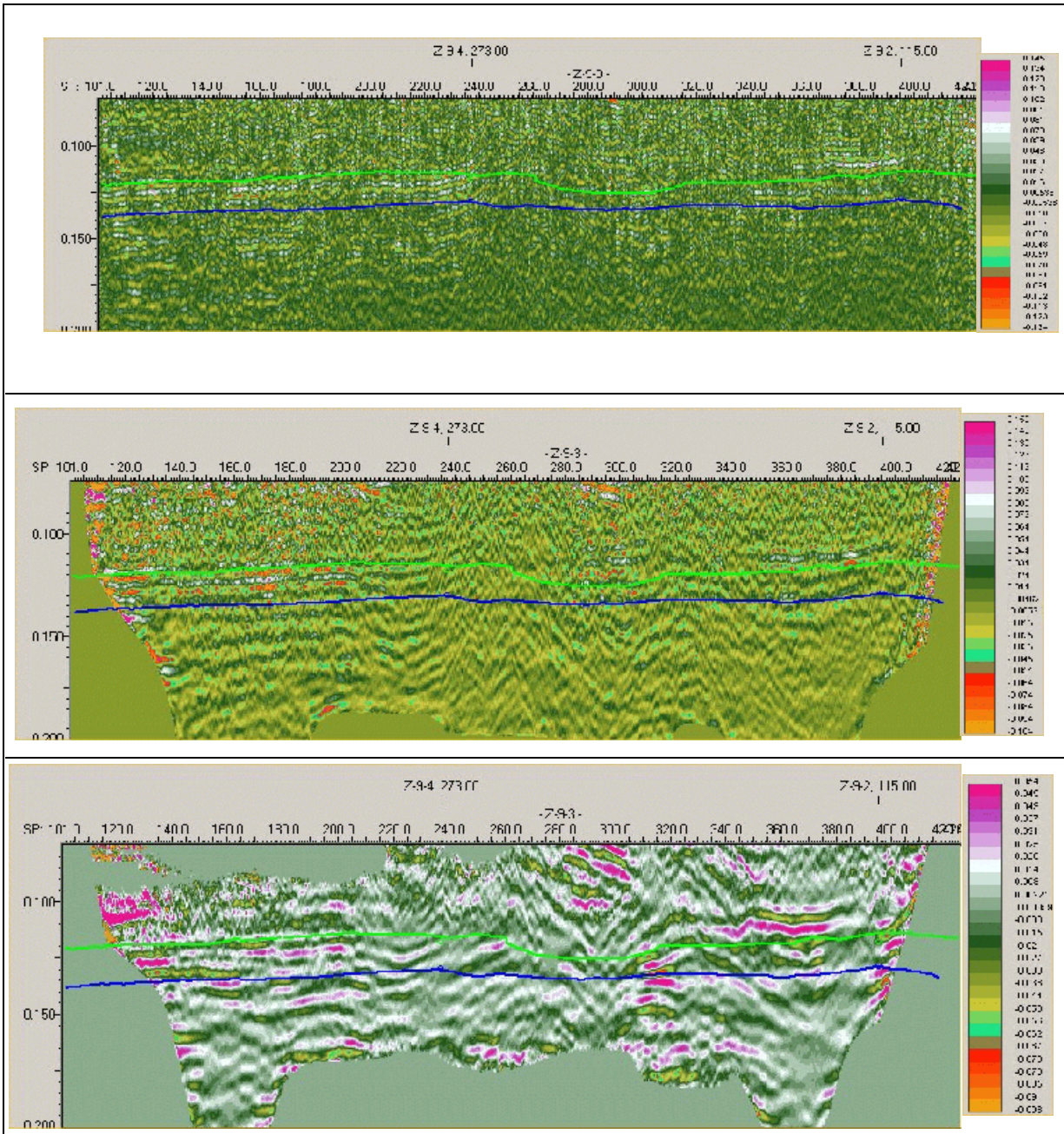

Figure 40. Seismic profile Z-9-3 offset range limited stacks. The upper figure is the near offset stack (0-40^0). The middle figure is the immediate offset stack (20^0-40^0). The lower figure is the far offset stack (40^0-80^0).

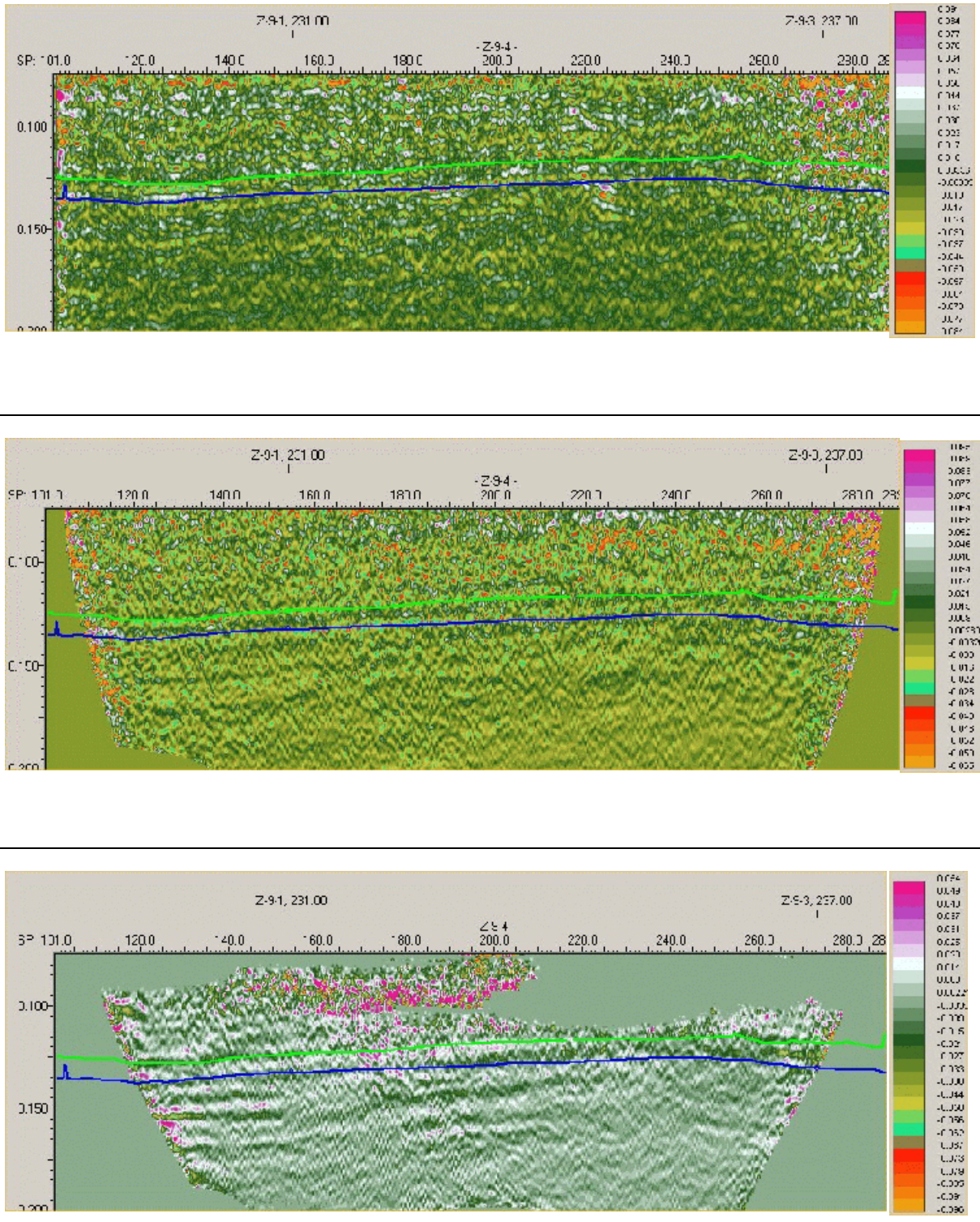

Figure 41. Seismic profile Z-9-4 offset range limited stacks. The upper figure is the near offset stack (0-40^0). The middle figure is the immediate offset stack (20^0-40^0). The lower figure is the far offset stack (40^0-80^0).

7.7 Gradient Stacks

7.7.1 Z-9-1 Gradient Stack

On seismic line Z-9-1 (Figure 42) there appear to be no gradient anomalies that can be attributed to CCl_4 accumulations. The absence of an anomaly in the Plio/Pleistocene could be attributed to the possibility that both the overlying Hanford Fine and Plio/Pleistocene are saturated with CCl_4. According to the model, if both units are saturated with CCl_4 the reflection coefficient is negative and becomes slightly more negative as offset increases - basically a flat response. If the response is flat there is no gradient. Another possible explanation is that there is not enough CCl_4 to cause anomaly, which we believe is the most likely explanation.

7.7.2 Z-9-2 Gradient Stack

On seismic line Z-9-2 (Figure 43) there are two prominent gradient anomalies at the Plio/Pleistocene-caliche contact. The first is between SP 125-165 and the second is between SP 190-210. According to the model (Figure 7), if the Plio/Pleistocene is saturated with CCl_4 and the caliche is air-filled, the amplitudes start off positive and become more positive with increasing offset. The other scenario is that both the Plio/Pleistocene and caliche are saturated CCl_4. In this case the amplitude starts off negative but becomes positive on the far offsets which would be a positive gradient. The two anomalies occur at the same locations where there are anomalies on the far offset range limited stacks (Figure 39). Both anomalies are positive gradients. If the model data are correct (Figure 7), these anomalies are associated with CCl_4.

7.7.3 Z-9-3 Gradient Stack

Figure 44 is a gradient stack of seismic line Z-9-3. Two prominent gradient anomalies are present on the seismic line. The first is between SP 145-165. This anomaly, which occurs in the Plio/Pleistocene unit, is very strong and weakens to the north to SP 230. The second anomaly is at the north end of the line between SP 375-390 near the intersection with seismic line Z-9-2. This anomaly occurs in the Hanford Fine directly above the Plio/Pleistocene. We believe both these anomalies are caused by CCl_4.

7.7.4 Z-9-4 Gradient Stack

Figure 45 is a gradient stack of seismic line Z-9-4. The gradient analysis preformed on these data revealed three weak gradient anomalies within the Plio/Pleistocene unit. The first anomaly is between SP 125-135. The second anomaly is at the Plio/Pleistocene-caliche contact between SP 165-195. The third is in the caliche layer at SP 225. Because these anomalies are weak, their origin is uncertain and could be attributed to either lithology change or the presence of CCl_4. Recent subsurface

sampling has found CCl_4 near these anomalies (Scott Peterson, Flour Hanford, personal communication, 2002).

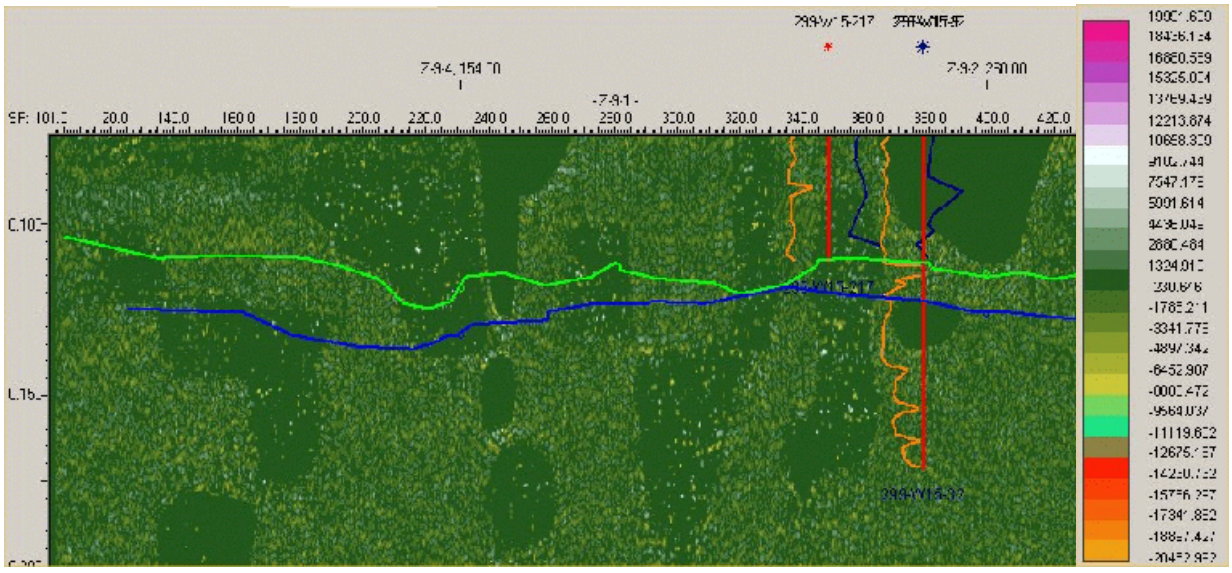

Figure 42. Gradient stack of seismic line Z-9-1. From the gradient analysis there appear to be no AVO anomalies either in the Plio/Pleistocene or the caliche.

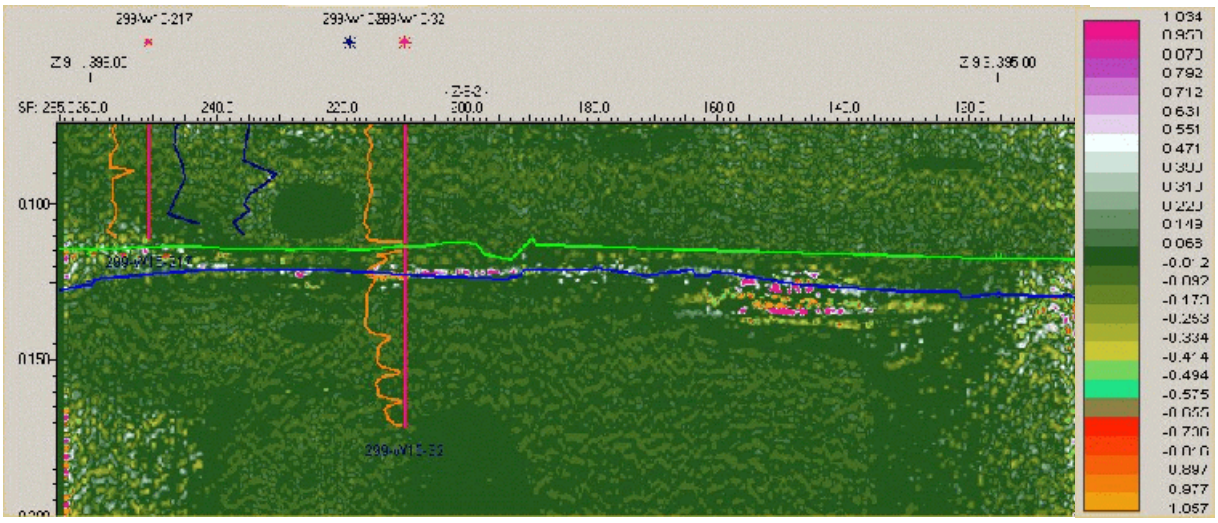

Figure 43. Gradient stack of seismic line Z-9-2. There are gradient anomalies between SP 125-165 and between SP 190-210. The anomaly between SP-125-165 appears to extend down into the Ringold Formation.

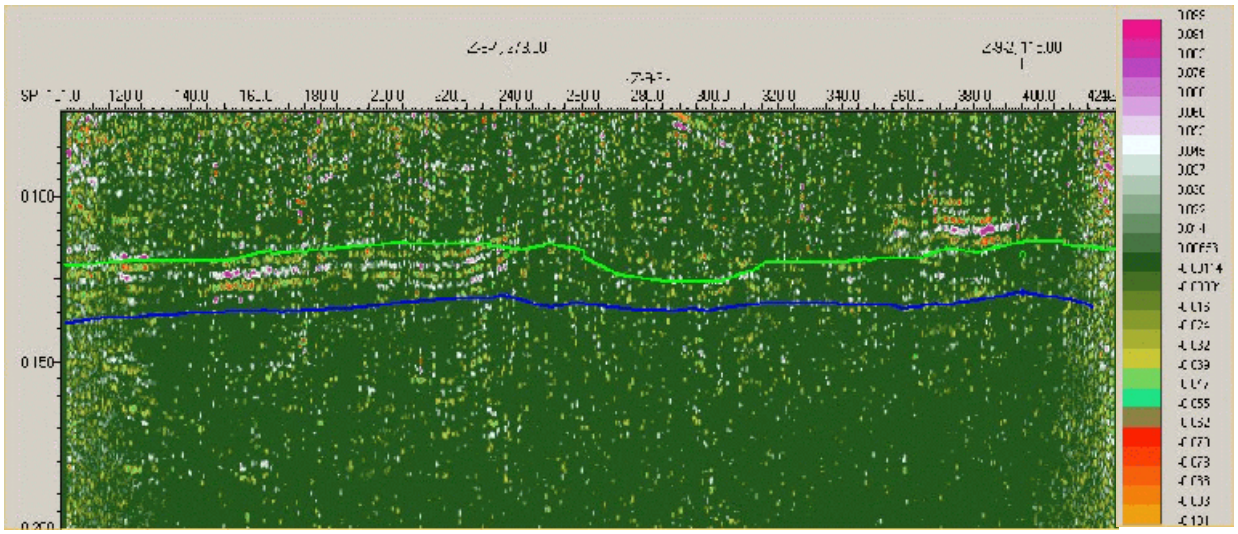

Figure 44. Gradient stack of seismic line Z-9-3. There is a strong gradient anomaly in the Plio/Pleistocene between SP 145-165 that weakens to SP 230. There is another strong gradient anomaly between SP 375-390 in the Hanford Fine near the contact with the Plio/Pleistocene.

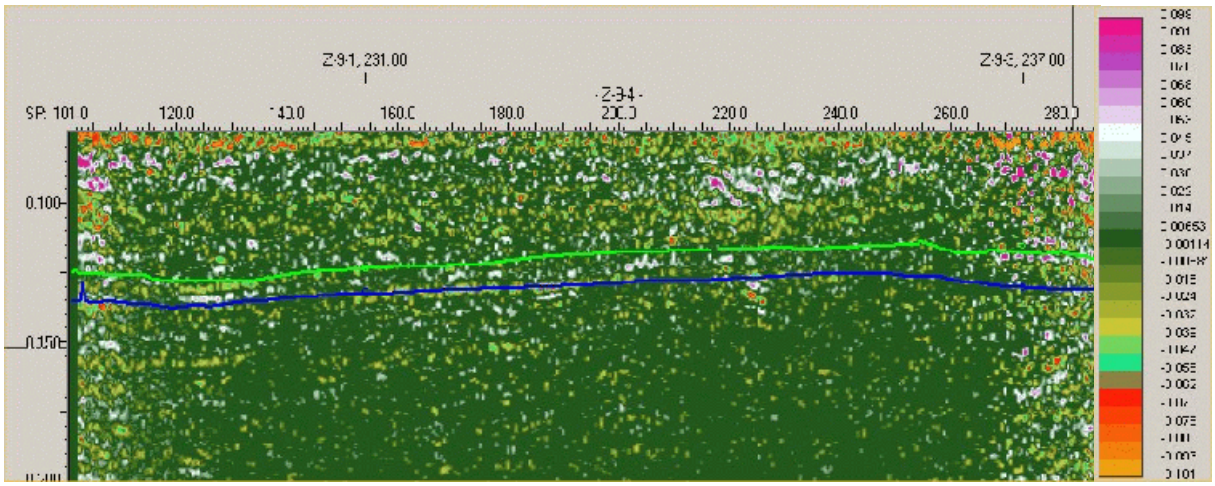

Figure 45. Gradient stack of seismic line Z-9-4. There is a weak gradient anomaly between SP 122-135 in the Plio/Pleistocene and another weak gradient anomaly between SP 160-195 at the Plio/Pleistocene-caliche contact. A third weak anomaly is at SP 225 in the caliche.

7.8 Integrated Interpretation

The project team used three methods of amplitude analysis to locate CCl_4 at the Z-9 crib area: enhanced amplitude stacks, offset range limited stacks, and gradient stacks. The gradient stack method was used because the models indicated that under certain circumstances there is an AVO gradient. According to the models, at the Hanford Fine-Plio/Pleistocene contact the background reflection coefficient is positive (Figure 5); however, if the Hanford Fine pores are saturated with CCl_4 and the underlying Plio/Pleistocene pores are saturated with air, there is a very substantial decrease in the reflection coefficients or "dim-out". Not only is there a dim-out, but the amplitudes become more negative with increasing incident angle (AVO gradient). If the Hanford Fine is air-filled and the underlying Plio/Pleistocene is saturated with CCl_4, the reflection coefficient at small angles of incidence is slightly positive and decreases with increasing incident angle. The reflection coefficient eventually flips polarity and becomes negative at the larger incident angles, i.e. there is also an AVO gradient. If both the Hanford Fine and the Plio/Pleistocene are saturated with CCl_4, the amplitude response starts off slightly positive and increases slightly with increasing in incident angle. In this case, however, the critical angle is reached after the background response, but before the other two scenarios; hence the need to examine intermediate offset range limited stacks.

A different range of amplitude responses occurs at the Plio/Pleistocene-caliche contact. The background amplitude response, i.e. both units are air-filled, starts off as slightly positive and increases with increasing incident angle (Figure 7). If CCl_4 saturates only the caliche pores, there is a substantial increase in reflection amplitude (bright spots). If CCl_4 saturates only the Plio/Pleistocene pores, the amplitude response starts off negative and becomes less negative with increasing incident angle and if both units are saturated with CCl_4 the amplitude response is initially positive and becomes more positive with increasing incidence angles. Under the preceding two scenarios the graphs of reflection coefficient versus incident angle show distinctive slopes, so gradient analysis can be used to determine the location of possible CCl_4 concentrations. Intermediate offset range limited stacks can also help separate the background response from the situation where both the Plio/Pleistocene and the caliche are saturated with CCl_4.

7.8.1 Hanford Fine-Plio/Pleistocene

Figure 46 is a map of reflection amplitude of the top of the Plio/Pleistocene (green line) horizon derived from the enhanced amplitude stacks and Figure 47 shows the locations of AVO amplitude anomalies identified on the offset range limited and gradient stacks. Modeling of this horizon shows that the presence of CCl_4 in the Hanford Fine should cause a dim-out. On the individual variable density stacks (Figures 30-33) it is difficult to detect areas of dim-out along the interface. On the amplitude map areas of dim-out are represented by the light blue and dark blue colored areas. The area of dark blue represents negative amplitudes which are believed to caused by of free-phase CCl_4. Comparison between the amplitude map and the anomalies identified from the offset limited and

gradient stacks shows that the dark blue areas to almost overlie the AVO anomalies on seismic profiles Z-9-1 and Z-9-2. The only exceptions are the dark blue anomaly adjacent to the intersection of profiles Z-9-1 and Z-9-4 and the dark blue area in the middle of seismic profile Z-9-3. This latter anomaly was not identified on either the offset range limited stacks or the gradient stack and may be caused by a lithology change.

At the Z-9 crib CCl_4 contamination is present in the vadose zone as well as in the groundwater south of the crib. The direction of groundwater flow is believed to be southward (Scott Peterson, Fluor Hanford, personal communication), yet the most pronounced AVO anomalies are on seismic line Z-9-2 north of the crib. The seismic data indicate a structural high directly under the crib. Presumably DNAPL would flow radially off the high and any preferential pathways should strongly influence the flow direction in the vadose zone. AVO analysis suggests there are "hot spots" to the north and northwest of the crib.

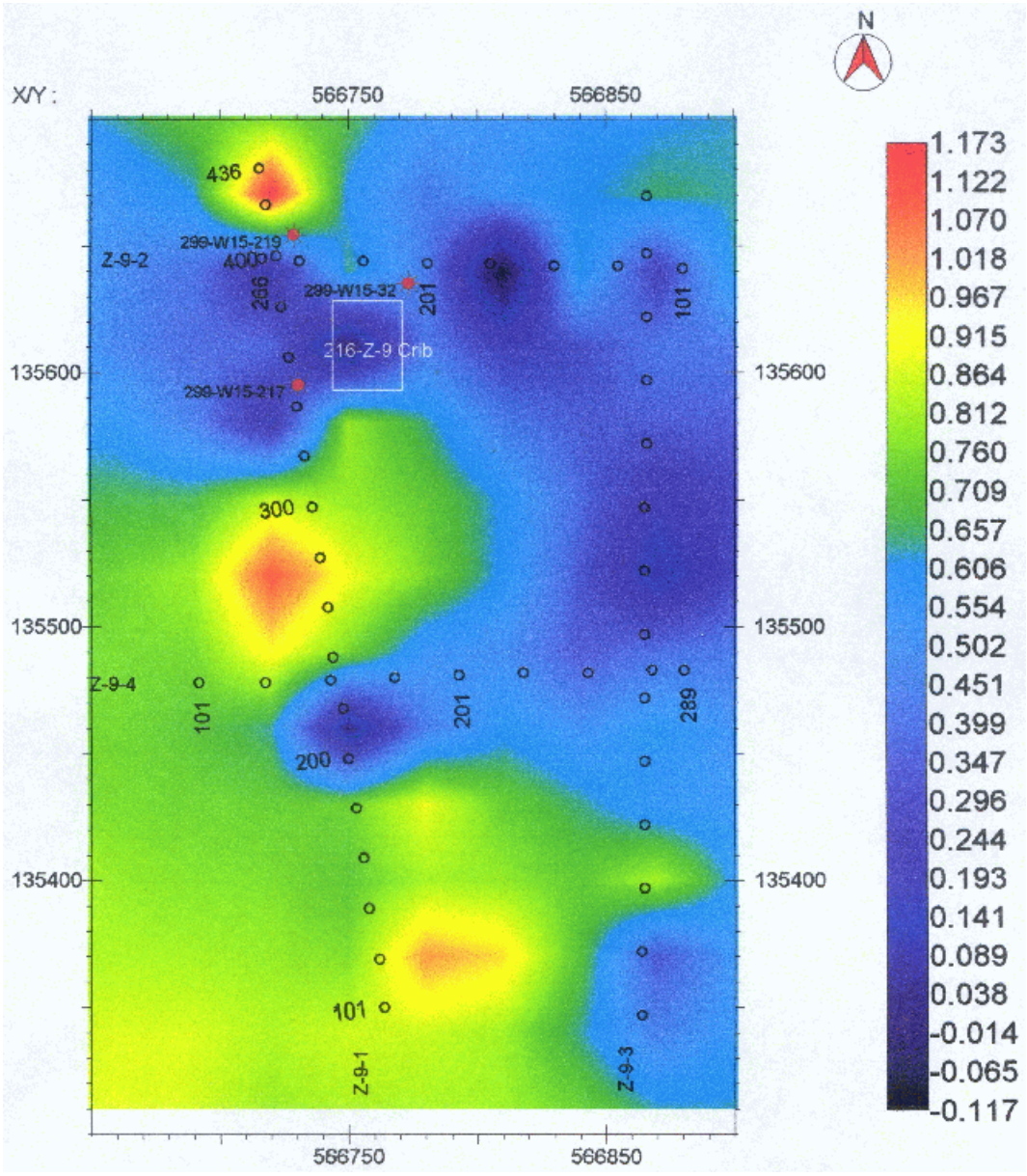

Figure 46. Amplitude map, top of Plio/Pleistocene. Amplitude values are relative.

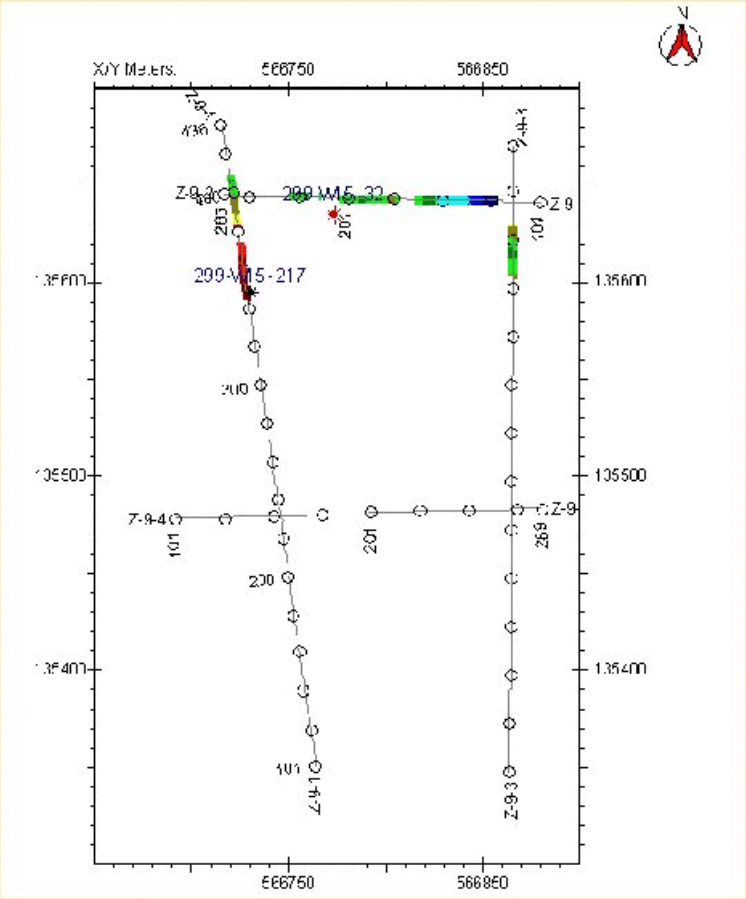

Figure 47. Location map of AVO anomalies at the Hanford Fine-Plio/Pleistocene contact. The areas highlighted in color are AVO anomalies identified on the offset range limited stacks and gradient stacks attributed to possible separate phase CCl_4 either in the Hanford Fine directly above the Plio/Pleistocene and/or in the Plio/Pleistocene.

7.8.2 Plio/Pleistocene-Caliche

Figure 48 is a reflection amplitude map of the top of the caliche reflection derived from the enhanced amplitude stacks. Figure 49 shows the location of AVO anomalies identified on the offset range limited and gradient stacks. According to the AVO models, a high amplitude event at the top of the caliche is associated with the presence of DNAPL. Amplitude values on the caliche surface represented by the red and yellow are the highest along line Z-9-2. Under assumption that an increase in amplitude indicates DNAPL, free-phase CCl_4 has collected along the top of caliche in this location. In addition, a large area represented by the area colored green also displays an increase in amplitude over background.

The most prominent AVO anomalies identified on the offset range limited and the gradient stacks are located on seismic line Z-9-2 (Figure 49). On seismic profile Z-9-1 there is an anomaly between 299-W15-217 north to the intersection with seismic profile Z-9-2 that was present only on the offset range limited offset stacks. On Figure 49 anomalies attributed to with free-phase CCl_4 appear to cover a larger area at the Plio/Pleistocene-caliche contact than the Hanford Fine-Plio/Pleistocene contact.

Figure 50 is a contour map of the average concentration of CCl_4 at the Plio/Pleistocene-caliche interval in the crib area. Information from five wells, 299-W15-216, 299-W15-217, 299-W15-218, 299-W15-219, and 299-W15-220 were averaged over the interval represented by the Plio/Pleistocene and mapped. Areas of high concentration of CCl_4 are red values and areas of low concentration are blue. The north/northwest area of the map (encompassing wells 299-W15-217, 299-W15-218, and 299-W15-219) falls within the zone of highest concentration. This agrees well with the amplitude anomaly maps of the top of Plio/Pleistocene (Figures 46 and 47) and the top of caliche (Figures 48 and 49). Modeling results also match well with the type of seismic AVO anomalies observed on both the enhanced amplitude stacks and the offset range limited offsets stacks.

Based on the close agreement between the seismic and the well data, a prediction of the location of free-phase CCl_4 can be made with reasonable confidence at the caliche event. This event, if the amplitudes are enhanced and identified using the range limited offset and gradient stacks, yields a distinctive anomaly that can be mapped with high confidence.

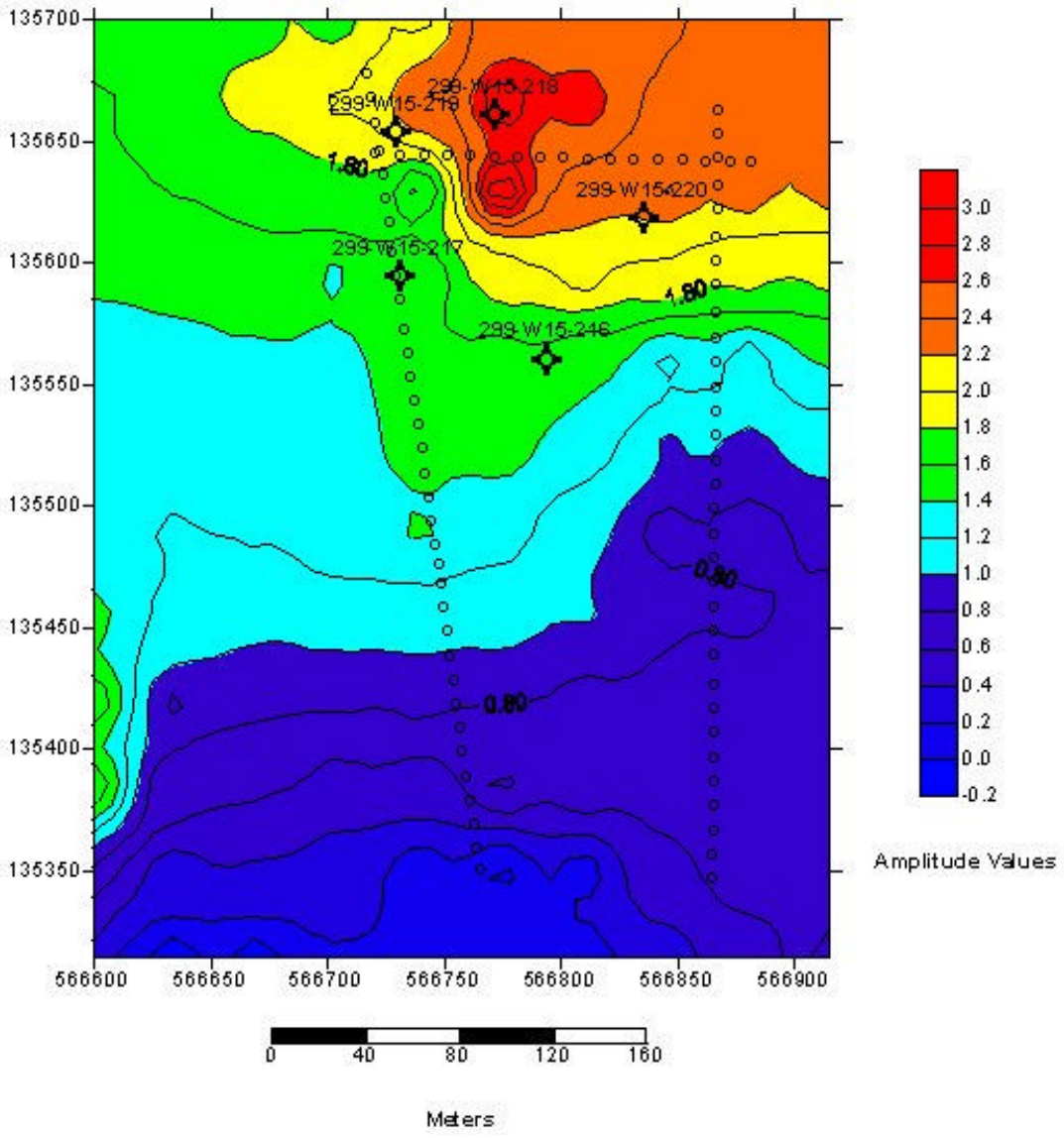

Figure 48. Amplitude map, top of caliche. Amplitude values are relative.

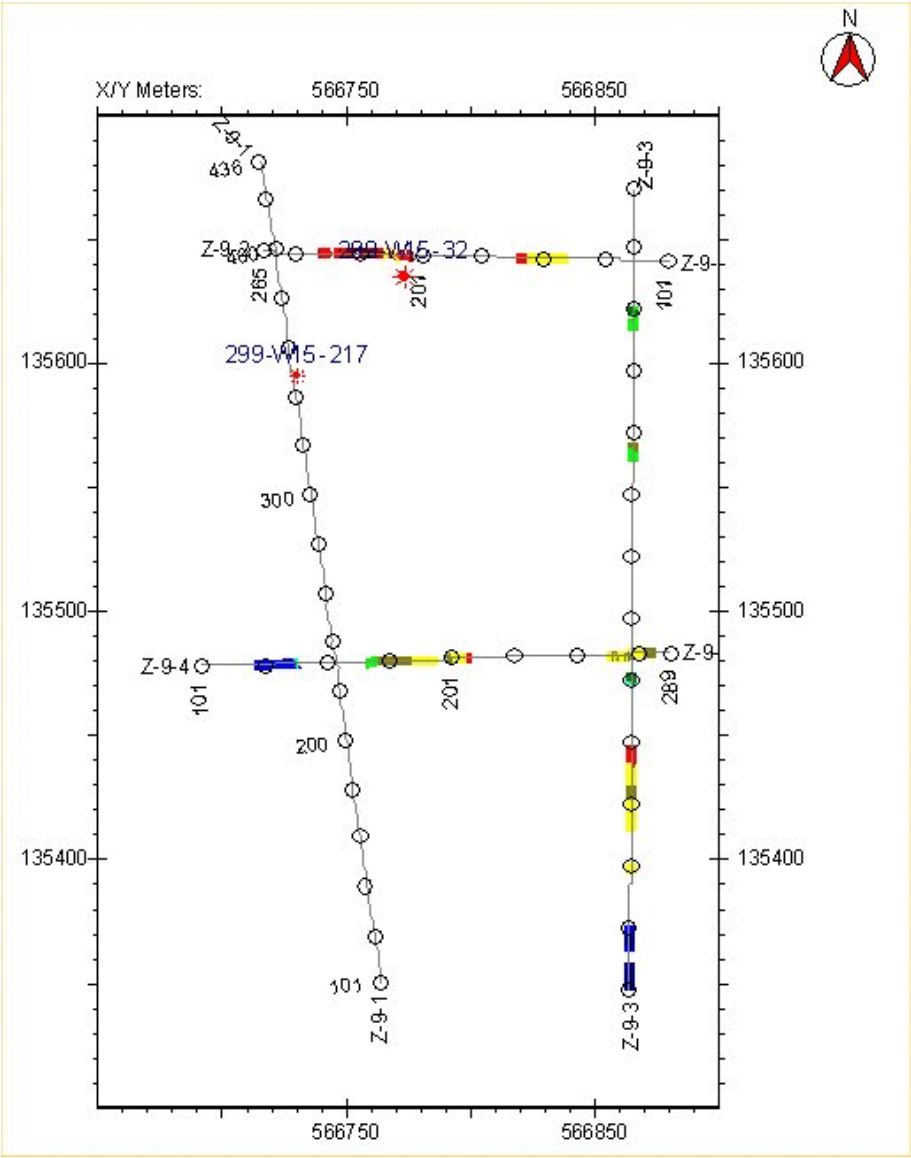

Figure 49. Location of AVO anomalies at the Plio/Pleistocene-caliche contact. The areas highlighted in color are AVO anomalies directly above the caliche and/or in the caliche identified on the offset range limited stacks and gradient stacks.

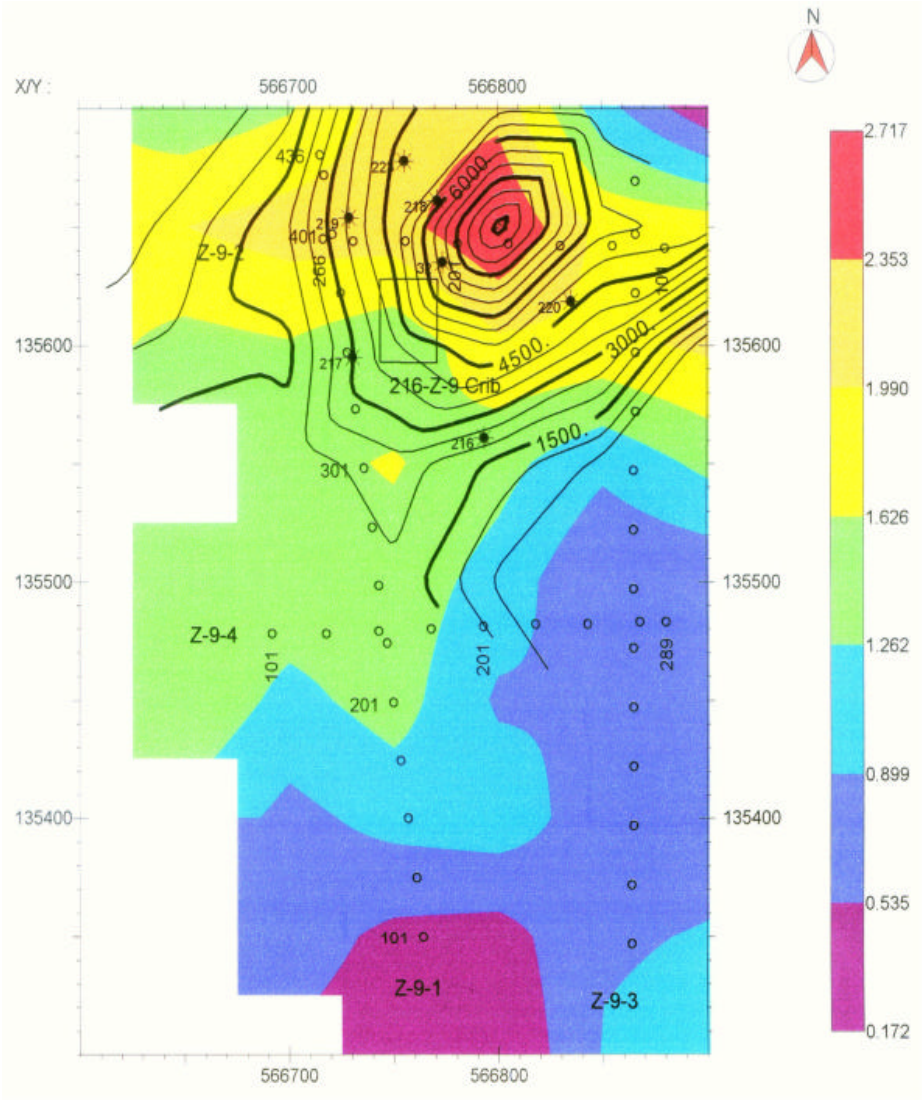

Figure 50. Carbon tetrachloride isoconcentration map. Concentration values in ppb.

8.0 Conclusions

- The results from Tasks 1,2, and 3 appear to be promising insofar as accomplishing the task objectives.
- The high-resolution reflection P wave seismic surveys provides continuous subsurface data between existing wells for the mapping of potential preferential pathways for carbon tetrachloride migration that had not been previously identified.

- The seismic data provides continuous data about the structural and stratigraphic features of the Hanford Fine-Plio/Pleistocene contact and the Plio/Pleistocene-caliche contact. The seismic data, even though it was not designed to image below the caliche, has provided some insight to the geology of the underlying Ringold Formation.

- It appears that the seismic amplitudes are responding to the presence of high concentration of carbon tetrachloride at the top of the Plio/Pleistocene. This is clearly evident from the similarity between the reflection amplitude map and the AVO anomaly map determined from the offset range limited and gradient stacks. At the Plio/Pleistocene-caliche contact the seismic data are consistent with the model for CCl_4 saturated Plio/Pleistocene. In this case, the offset range limited offsets and gradient stacks provided additional confirmation of the AVO anomalies identified on the enhanced amplitude stacks. The reflection amplitude map for the top of caliche indicates very high amplitudes in the area where there is high concentration of CCl_4 on seismic profiles Z-9-2 and Z-9-3. These high amplitude anomalies are also present on the offset range limited and gradient stack analyses.

- Even though the modeling results and the seismic data appear to correlate where there is indication of the presence or absence of high concentrations of CCl_4, the underlying assumption is that the seismic AVO models are correct. This assumption may not be valid. The velocities and densities for the fluid-filled layers were mathematically derived using Gassmann's equations.

- Suggested future work is to validate the models. The anomalies should be tested by drilling or direct push and sampled for the presence of CCl_4.

9.0 Acknowledgments

We thank Seismic Image Software Ltd. for support of the Vista for Windows software, Seismic Micro-Technology, Inc. for donation of the Kingdom Suite software, and Hampson-Russell Software Services Ltd. for donation of the AVO modeling software. The University of South Carolina-ESRI acknowledges support of this project by Landmark Graphics Corporation via the Landmark University Grant Program. We thank Ms. Arlene Tortoso (DOE Hanford), Mark Buckmaster and Joe Jimienez (Bechtel Hanford), Scott Peterson (Fluor Hanford), and Ms. Virginia Rohay (CH2M hill Hanford) for providing logistical support and for sharing their expertise on the 200 West area. Without their assistance this project could not have been completed.

10.0 References

Aki, K. and Richards, P.G., 1980, Quantitative Seismology: W.H. Freeman and Co., San Francisco, 932 p.

Allen, J.L. and Peddy, C.P., 1993, Amplitude variation with offset: Gulf Coast studies: SEG Geophysical Developments Series No. 4, Society of Exploration Geophysicists, Tulsa, OK, 111 p.

Balch, A.H. and Lee, M.W., eds., 1984, Vertical seismic profiling: Technique applications and case histories: IHRDC, Boston, 488 p.

Baker, V.R. and Bunker, R.C., 1985, Cataclysmic late Pleistocene flooding from glacial Lake Missoula; A review: Quaternary Science Reviews, v.4, p.1-41

Bortfield, R., 1961, Approximation to the reflection and transmission coefficients of plane longitudinal and transverse waves: Geophysical Prospecting, v. 9, p. 485-502.

Castagna, J.P. and Backus, M. M., eds., 1993, Offset-dependent reflectivity - Theory and practice: SEG Investigations in Geophysics No. 8, Society of Exploration Geophysicists, Tulsa, OK, 345 p.

Castagna, J.P., Batzle, M.L., and Eastwood, R.L., 1985, Relationships between compressional-wave and shear-wave velocities in clastic silicate rocks: Geophysics, v. 50, p. 571-581.

Gardner, G.H.F., Gardner, L.W., and Gregory, A.R., 1974, Formation velocity and density-the diagnostic basics for stratigraphic traps: Geophysics, v. 39, p. 770-780.

Graul, M. 2001, AVO seismic lithology: SEG Continuing Education, Society of Exploration Geophysicists, San Antonio, TX.

Koefoed, O., 1955, On the effect of Poisson's ratios of rock strata on the reflection coefficients of plane waves: Geophysical Prospecting, p. 381-387.

Mavko, G., Mukerji, T. and Dvorkin, J., 1998: The Rock Physics Handbook: Cambridge University Press, p. 1-220

Ostrander, W.J., 1984, Plane-wave reflection coefficients for gas sands at non-normal angles of incidence: Geophysics, v. 49, p. 1637-1648

Parker, D.L., 1995, DNAPL Investigation Report: BHI-DIS 9-25-95 GE7, Bechtel Hanford, Inc.

Rohay, V.J., Swett, K.J., and Last, G.V., 1994, Conceptual Model of the Carbon Tetrachloride Contamination in the 200 West Area at the Hanford Site: WHC-SD-EN-TI-248, Westinghouse Hanford Company.

Rutherford, S.S. and Williams, R.H., 1989, Amplitude-versus-offset variations in gas sands: Geophysics, v. 54, p. 680-688.

Sheriff, R.E., 1991, Encyclopedic Dictionary of Exploration Geophysics: SEG Geophysical Reference Series No. 1, Society of Exploration Geophysicists, Tulsa, OK, 376 p.

Shuey, R.T., 1985, A simplification of the Zoeppritz equations: Geophysics, v. 50, p. 609-614.

Smith, G.C. and Gidlow, P.M., 1987, Weighted stacking for rock property estimation and detection of gas: Geophysical Prospecting, v. 35, p. 993-1014.

Stone, D.G., 1994, Designing seismic surveys in two and three dimensions: SEG Geophysical References Series No. 8, Society of Exploration Geophysicists, Tulsa, OK, 244 p.

Telford, W.M., Geldart, L.P., Sheriff, R.E., and Keys, D.A., 1976, Applied Geophysics: Cambridge University Press, New York, 860 p.

Verm, R. and Hilterman, F., 1995, Lithology color-coded seismic sections: The calibration of AVO crossplotting to rock properties: The Leading Edge, v. 14, n. 8, p. 847-853.

Waddell, M.G, Temples, T.J., and Domoracki, W.J., 1997, Using high-resolution reflection seismic to image free-phase DNAPLs at the M-area, Savannah River Site (Abstract): Ann. Mtg. Am. Assoc. Petroleum Geologists, Dallas, TX.

Waitt, R. B., Jr., 1980, About forty last-glacial Lake Missoula jökulhlaups through southern Washington: Journal of Geology, v. 88, p 653-679

Waters, K.H., 1981, Reflection seismology: A tool for energy resource exploration: John Wiley and Sons, New York, 453 p.

White, J.E., 1985, Underground Sound: Elsevier, New York, 253 p.

Wright, J., Conca, J.L., and Chen, X, 1994, Hydrostratigraphy and Recharge Distributions From Direct Measurements of Hydraulic Conductivity Using the UFA™ Method: DE-ACo6-76RLO 1830, Pacific Northwest Laboratory.

Zoeppritz, K., 1919, Uber reflexion und durchgang seismischer wellen durch Unstetigkerlsflaschen: Berlin, Uber Erdbebenwellen VII B, Nachrichten der Koniglichen Gesellschaft der Wissenschaften zu Gottingen, math-phys. K1., p. 57-84.

Enclosures

Enclosure 1
Seismic Line Z-9-1
Variable Density Plot
Without Interpretations

Earth Sciences and Resources Inst.

Project: Hanford

Project Location: 200 West

Line Z-9-1
Variable Density Plot
Without Interpretations

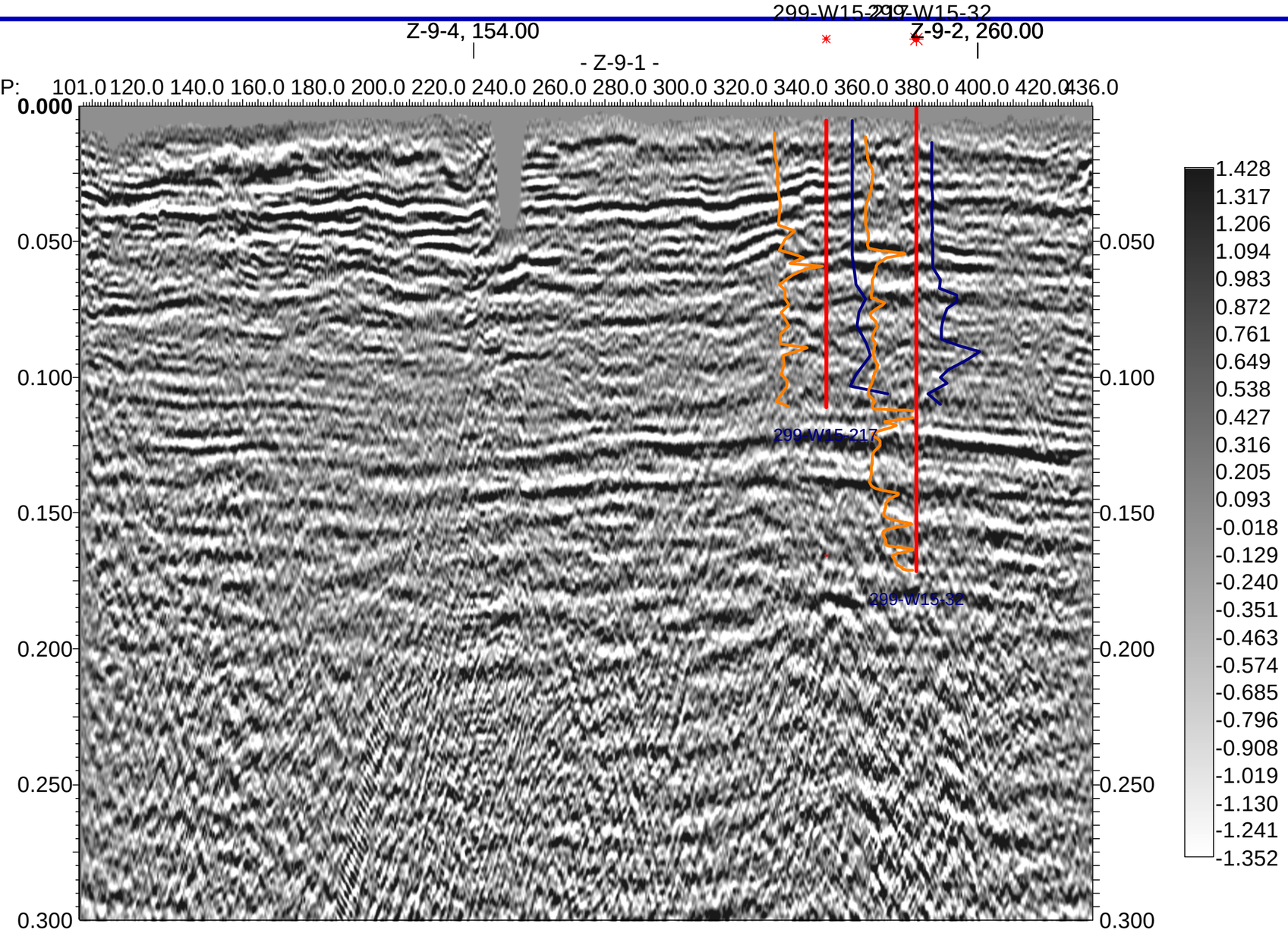

Enclosure 2
Seismic Line Z-9-1
Variable Density Plot
With Interpretations

Earth Sciences and Resources Inst.

Project: Hanford

Project Location: 200 West

Line Z-9-1
Variable Density Plot
With Interpretations

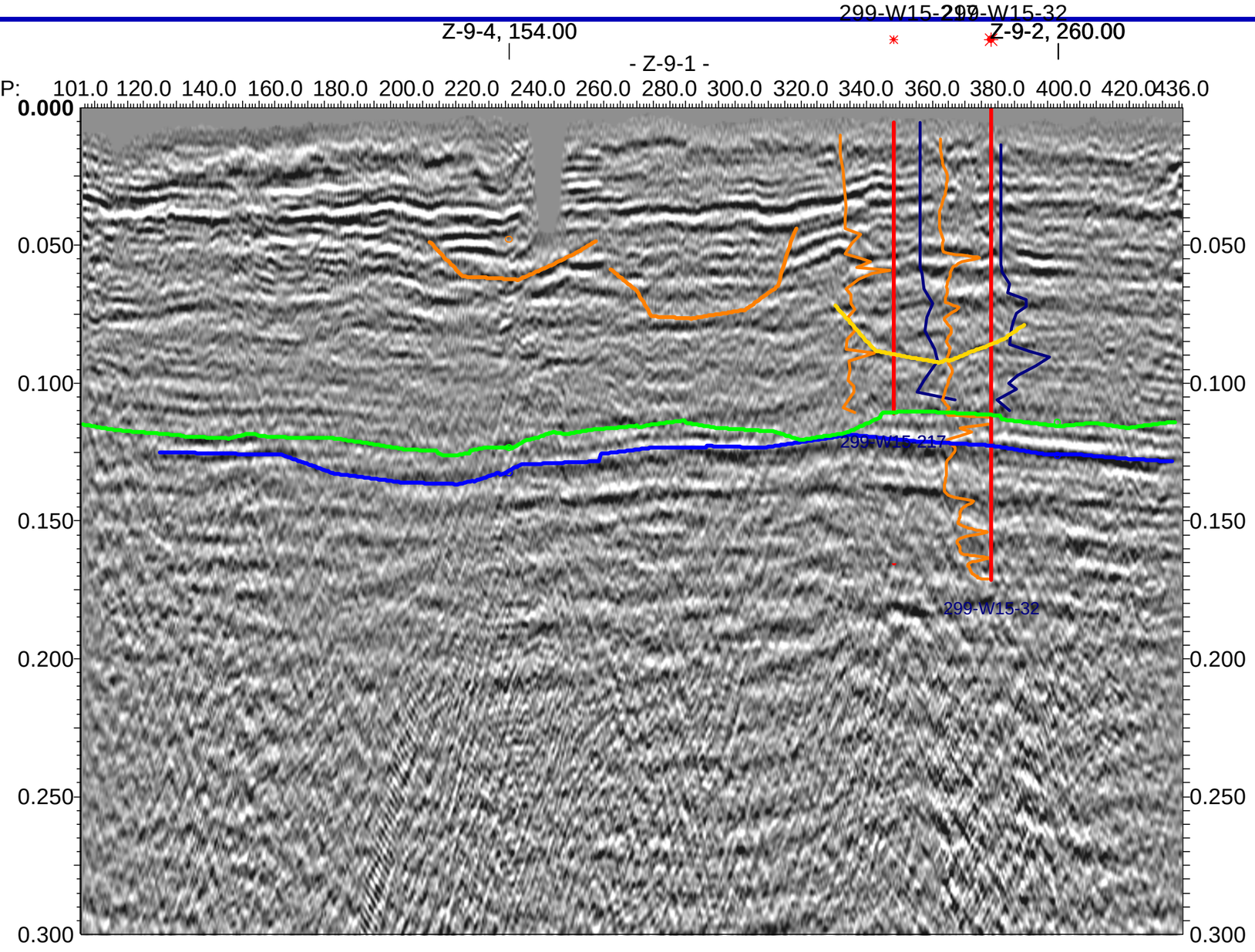

Enclosure 3
Seismic Line Z-9-2
Variable Density Plot
Without Interpretations

Earth Sciences and Resources Inst.

Project: Hanford

Project Location: 200 West

Line Z-9-2
Variable Density Plot
Without Interpretation

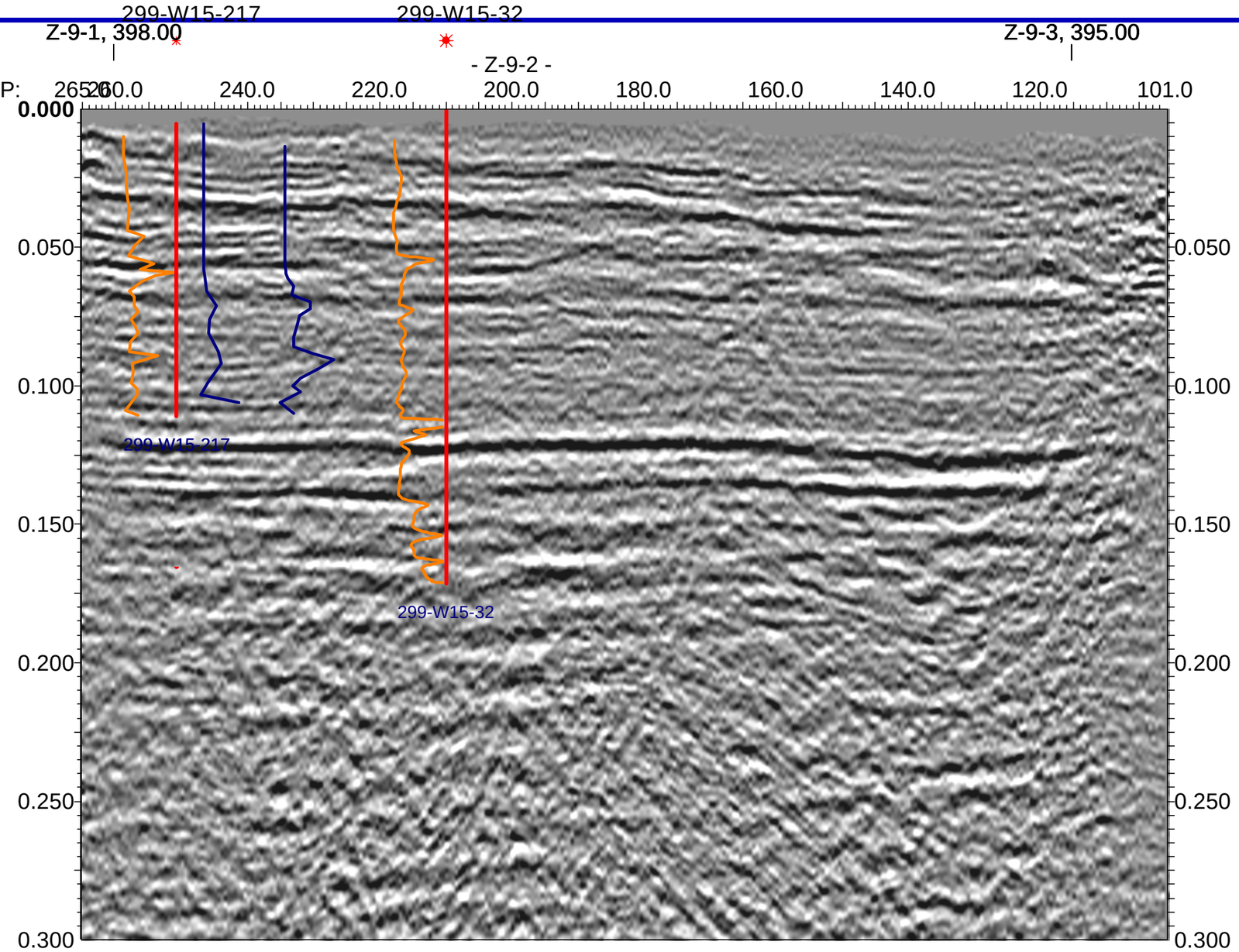

Enclosure 4
Seismic Line Z-9-2
Variable Density Plot
With Interpretations

Earth Sciences and Resources Inst.

Project: Hanford

Project Location: 200 West

Line Z-9-2
Variable Density Plot
With Interpretation

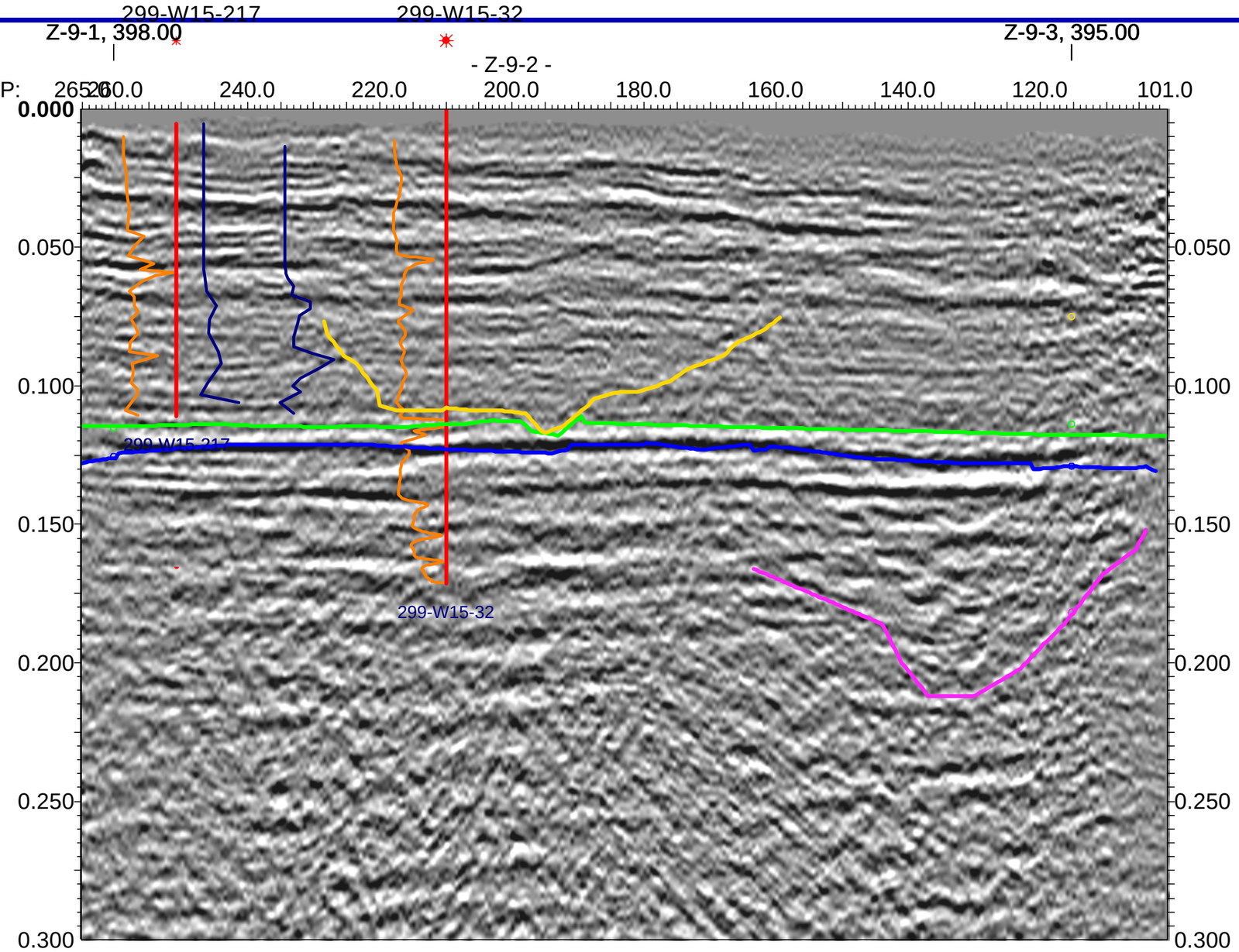

Enclosure 5
Seismic Line Z-9-3
Variable Density Plot
Without Interpretations

Earth Sciences and Resources Inst.

Project: Hanford

Project Location: 200 West

Line Z-9-3
Variable Density Plot
Without Interpretations

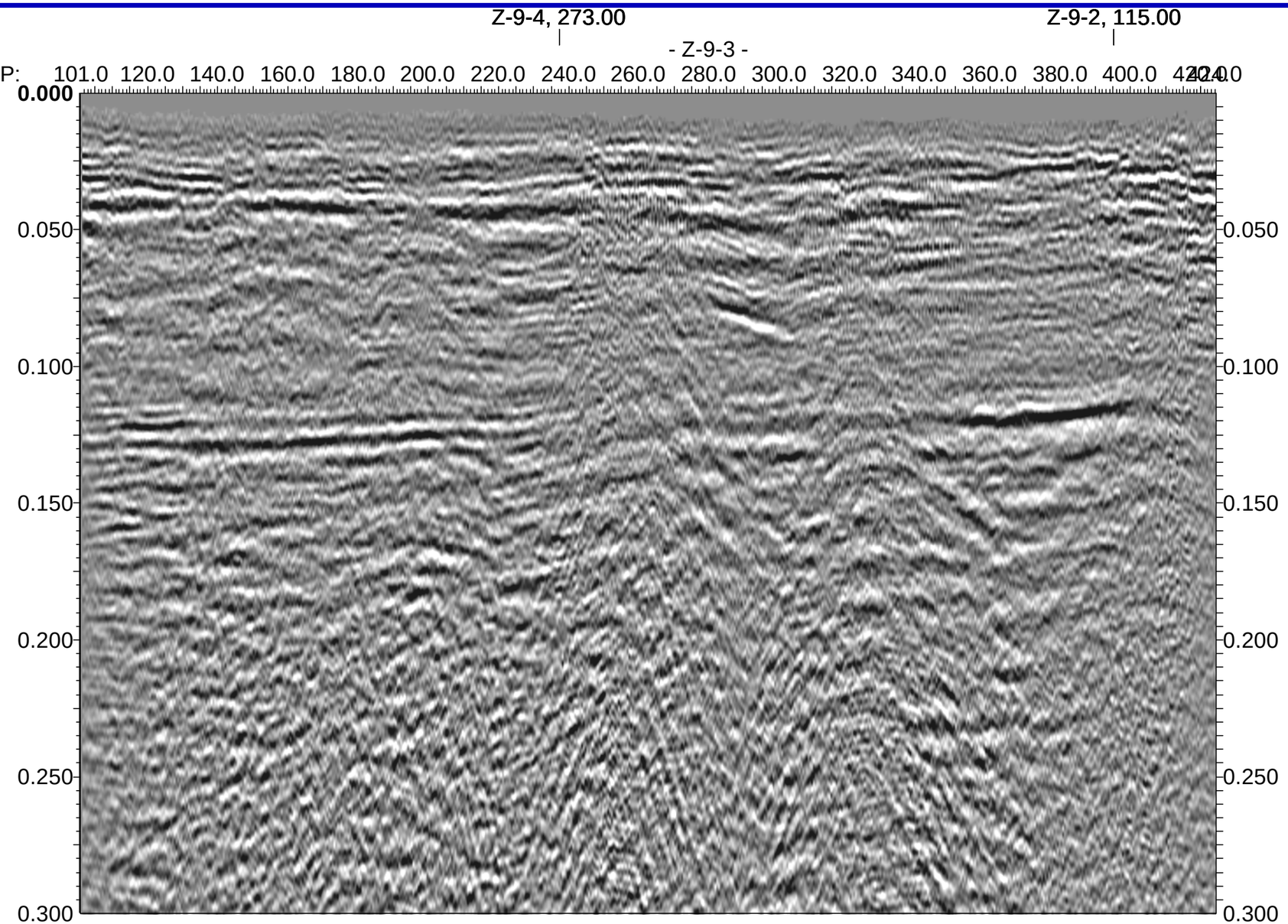

Enclosure 6
Seismic Line Z-9-3
Variable Density Plot
With Interpretations

Earth Sciences and Resources Inst.

Project: Hanford

Project Location: 200 West

Line Z-9-3
Variable Density Plot
With Interpretations

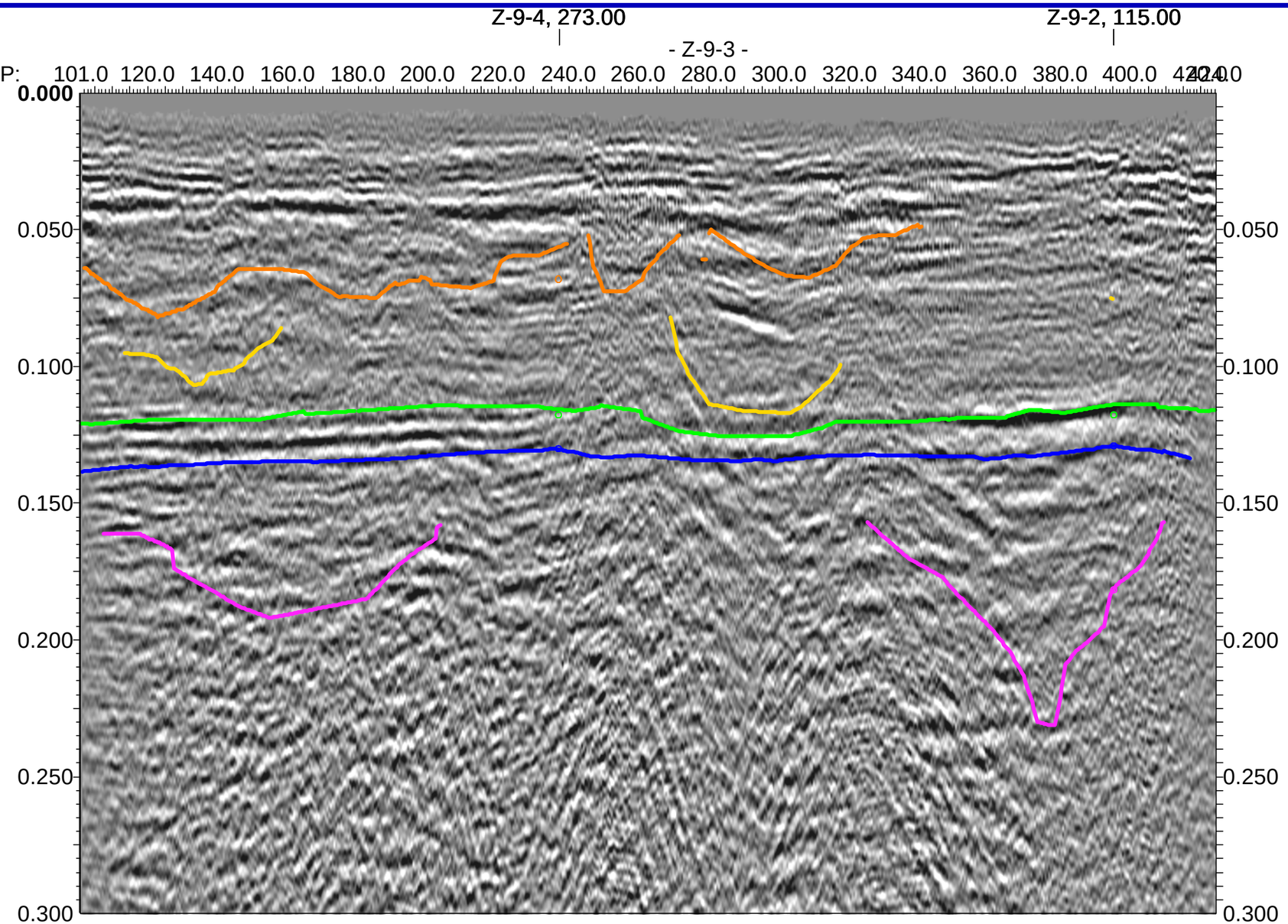

Enclosure 7
Seismic Line Z-9-4
Variable Density Plot
Without Interpretations

Earth Sciences and Resources Inst.

Project: Hanford

Project Location: 200 West

Line Z-9-4
Variable Density Plot
Without Interpretations

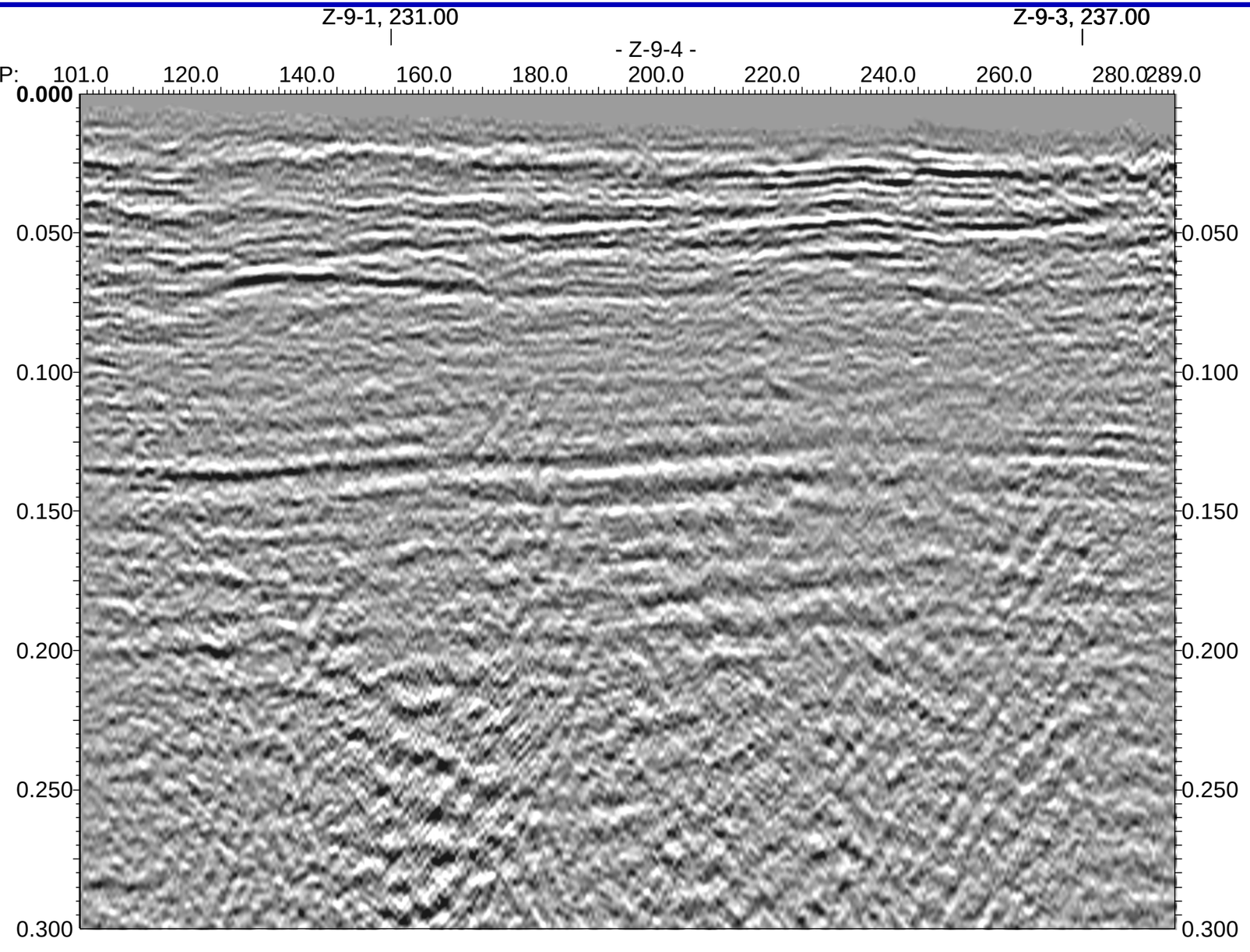

Enclosure 8
Seismic Line Z-9-4
Variable Density Plot
With Interpretations

Earth Sciences and Resources Inst.

Project: Hanford

Project Location: 200 West

Line Z-9-4
Variable Density Plot
With Interpretations

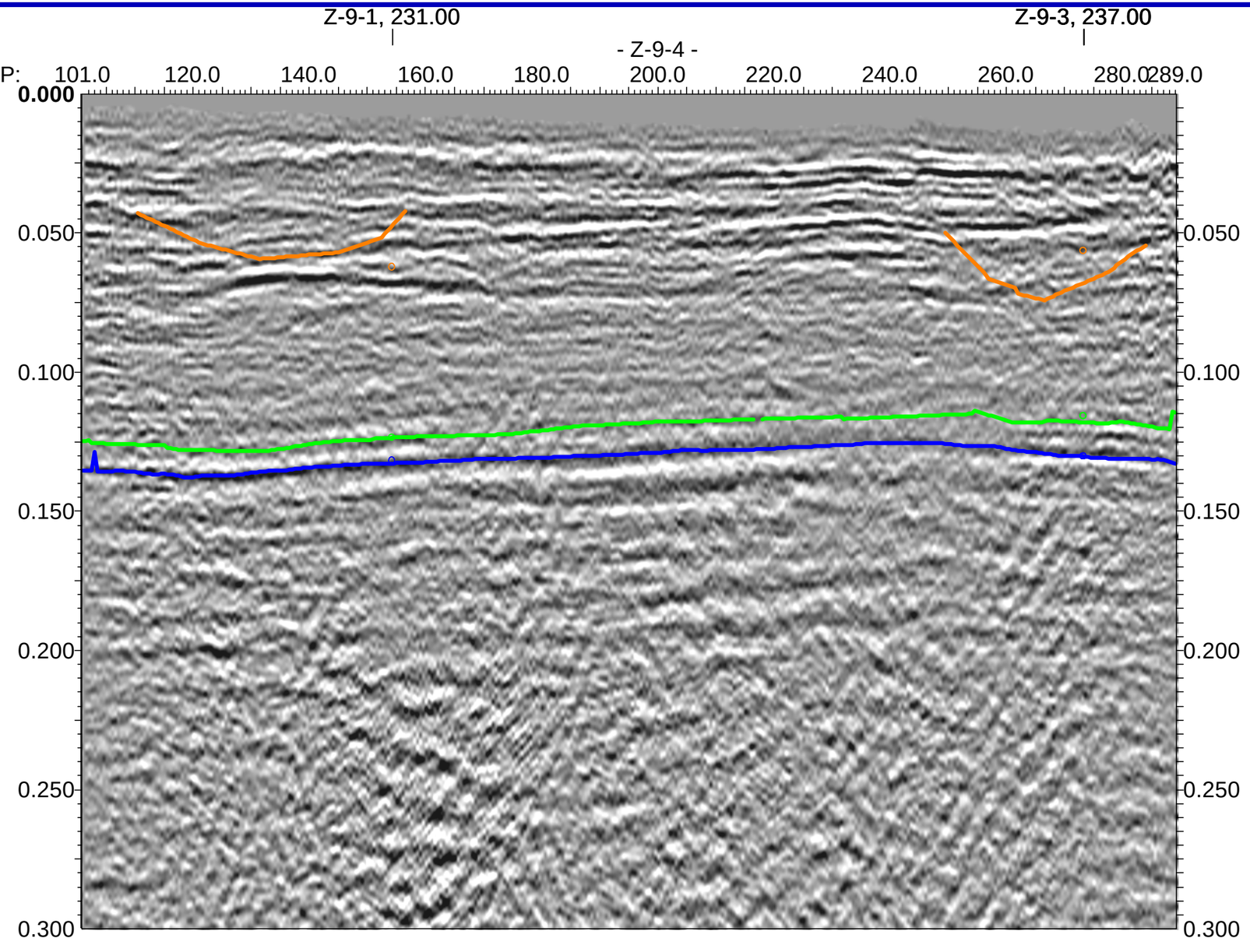

Enclosure 9
Seismic Line Z-9-1
Color Variable Density Plot
With Interpretations

Earth Sciences and Resources Inst.

Project: Hanford

Project Location: 200 West

Line Z-9-1
Color Variable Density Plot
With Interpretations

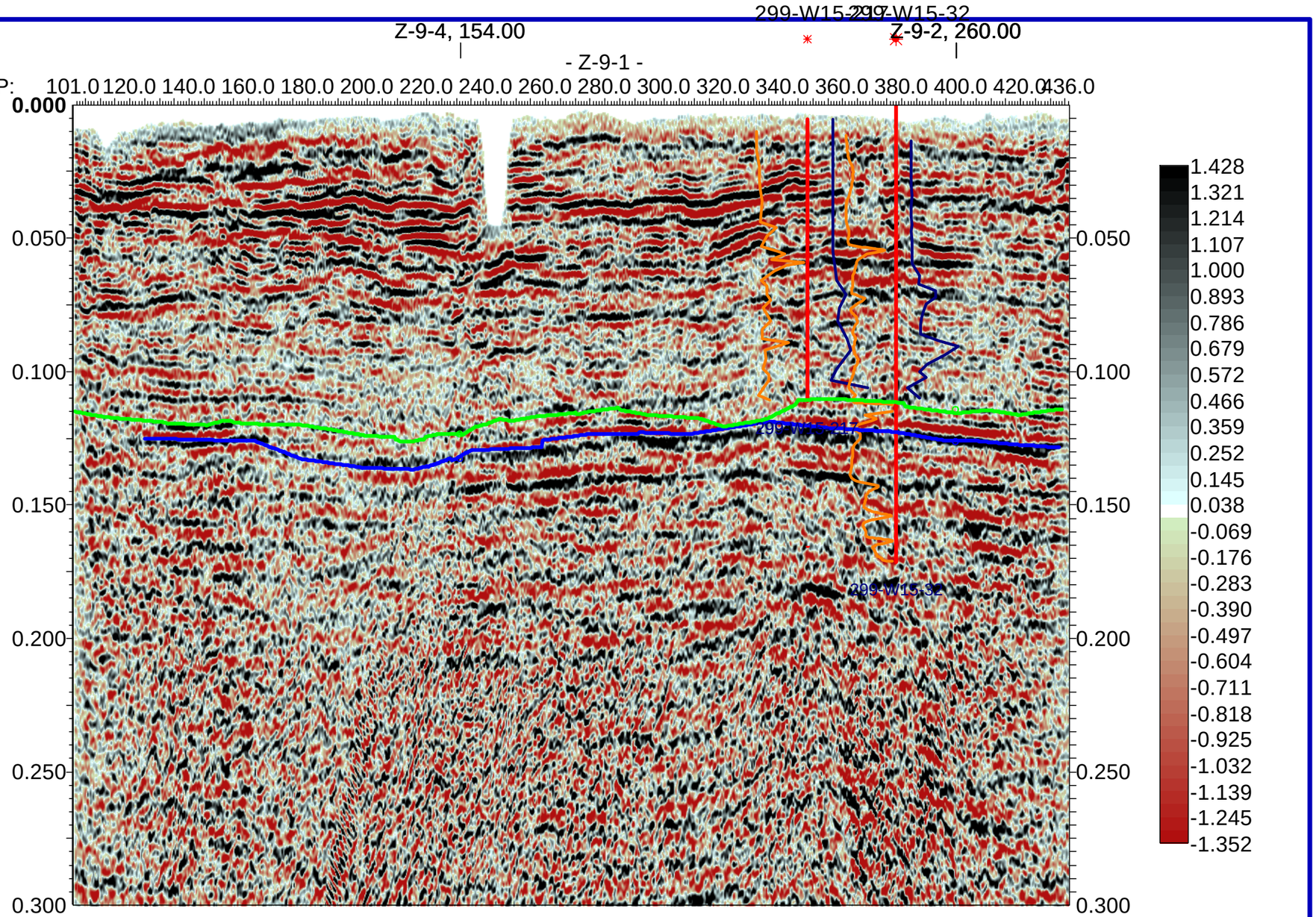

Enclosure 10
Seismic Line Z-9-2
Color Variable Density Plot
With Interpretations

Earth Sciences and Resources Inst.

Project: Hanford

Project Location: 200 West

Line Z-9-2
Color Variable Density Plot
With Interpretations

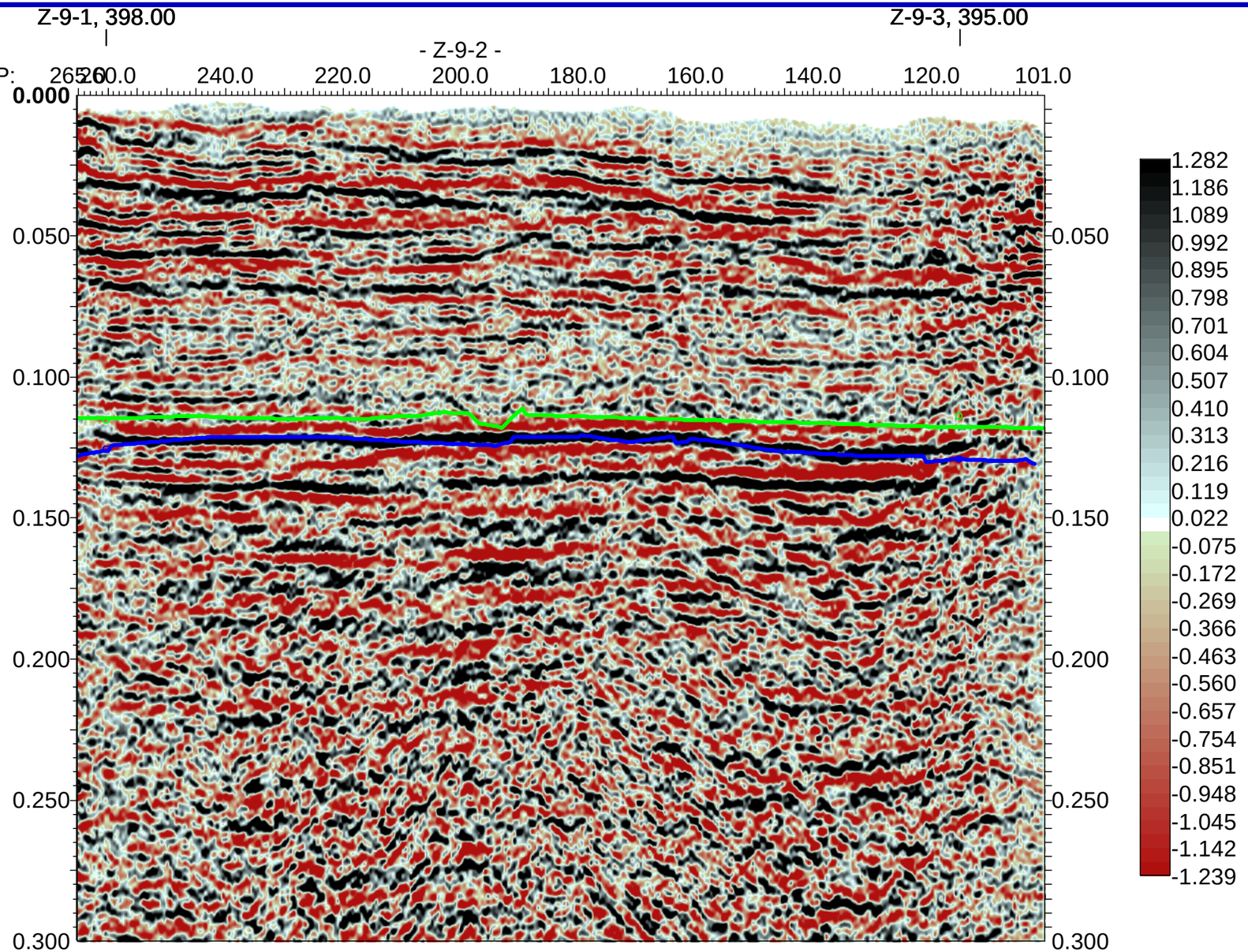

Enclosure 11
Seismic Line Z-9-3
Color Variable Density Plot
With Interpretations

Earth Sciences and Resources Inst.

Project: Hanford

Project Location: 200 West

Line Z-9-3
Color Variable Density Plot
With Interpretations

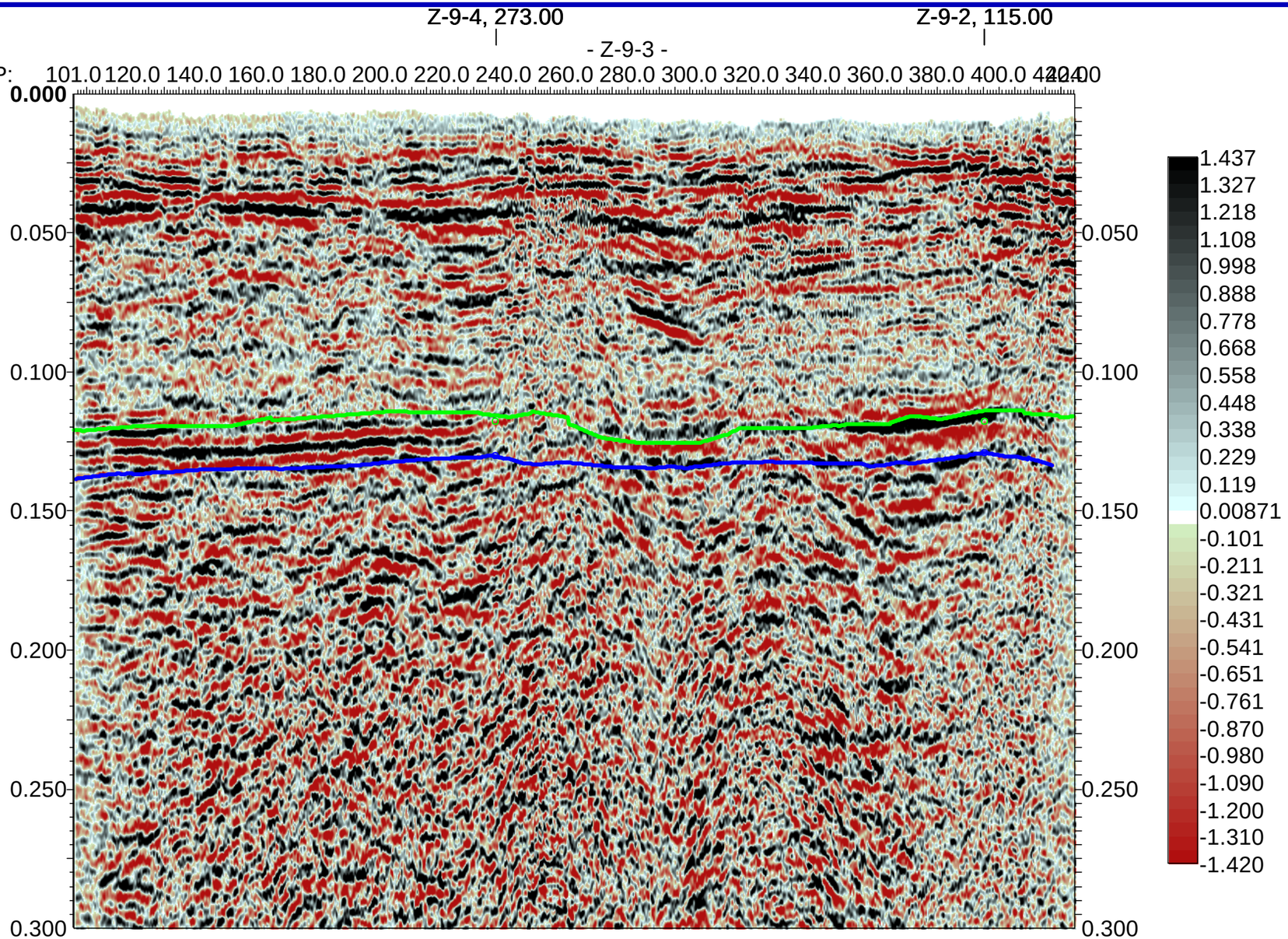

Enclosure 12
Seismic Line Z-9-4
Color Variable Density Plot
With Interpretations

Earth Sciences and Resources Inst.

Project: Hanford

Project Location: 200 West

Line Z-9-4
Color Variable Denisty Plot
With Interpretations

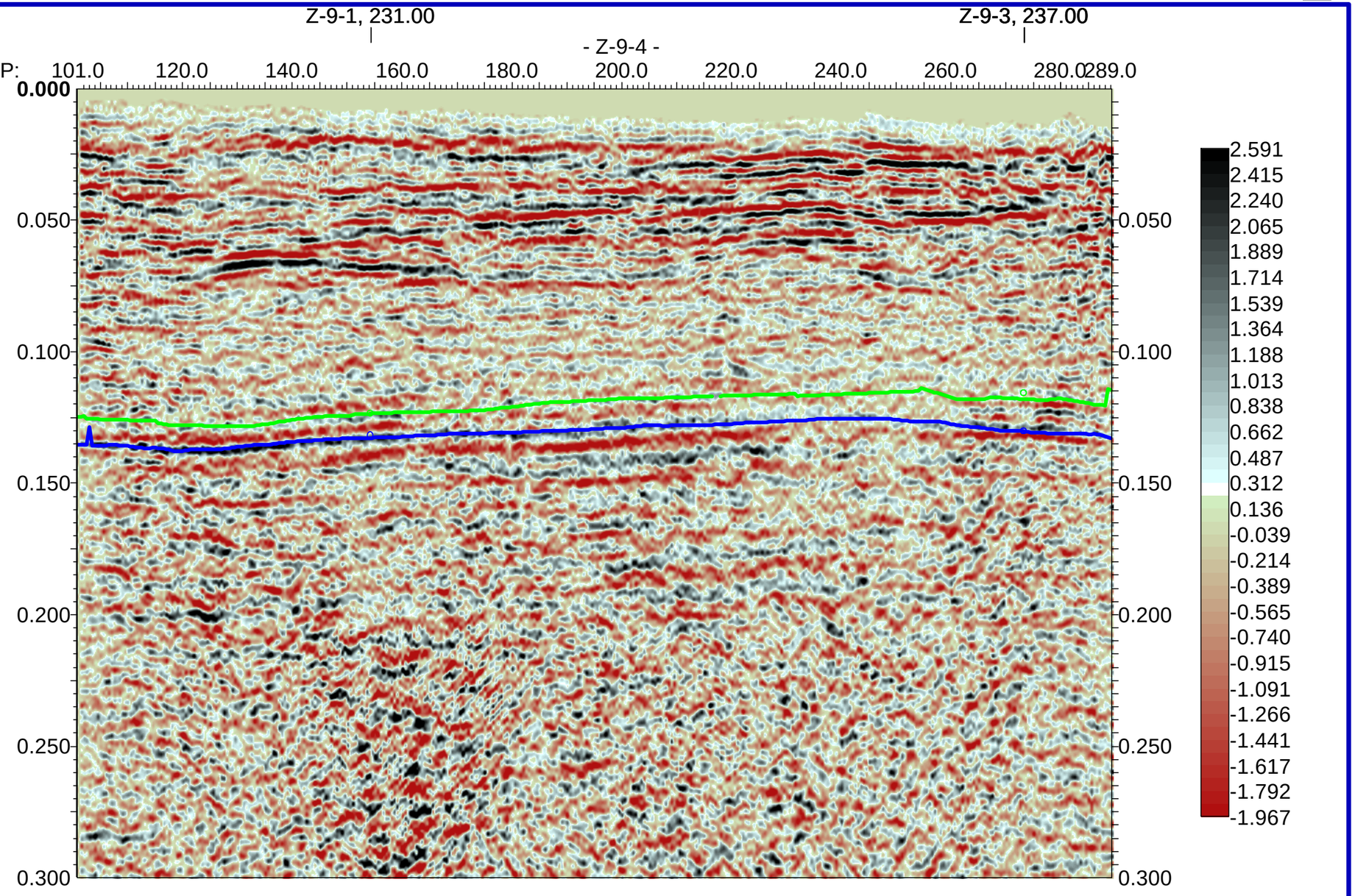

Enclosure 13
Seismic Line Z-9-1
Enhanced Amplitude Stack

Earth Sciences and Resources Inst.

Project: Hanford

Project Location: 200 West

Line Z-9-1
Enhance Stack

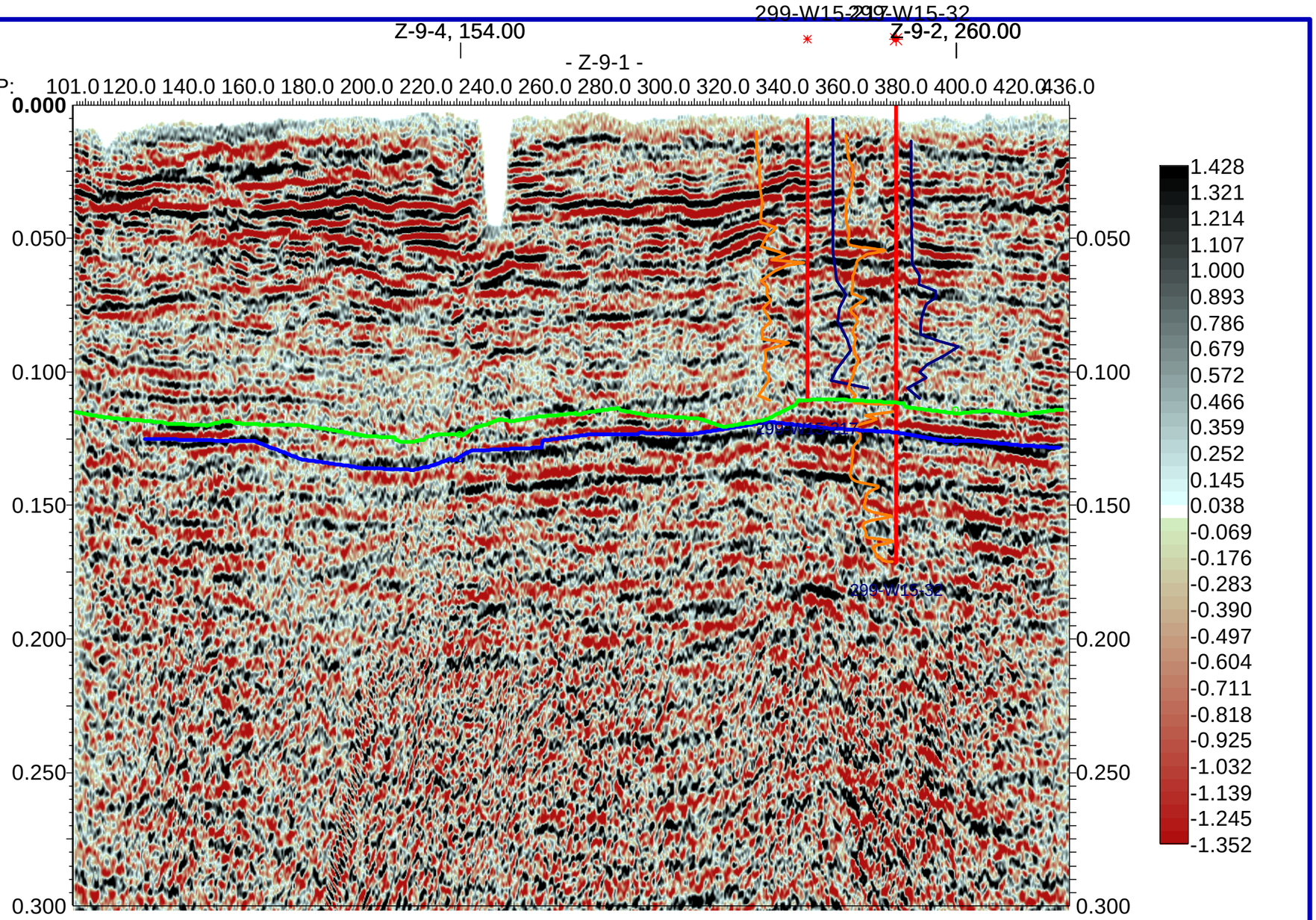

Enclosure 14
Seismic Line Z-9-2
Enhanced Amplitude Stack

Earth Sciences and Resources Inst.

Project: Hanford

Project Location: 200 West

Line Z-9-2
Enhance Stack

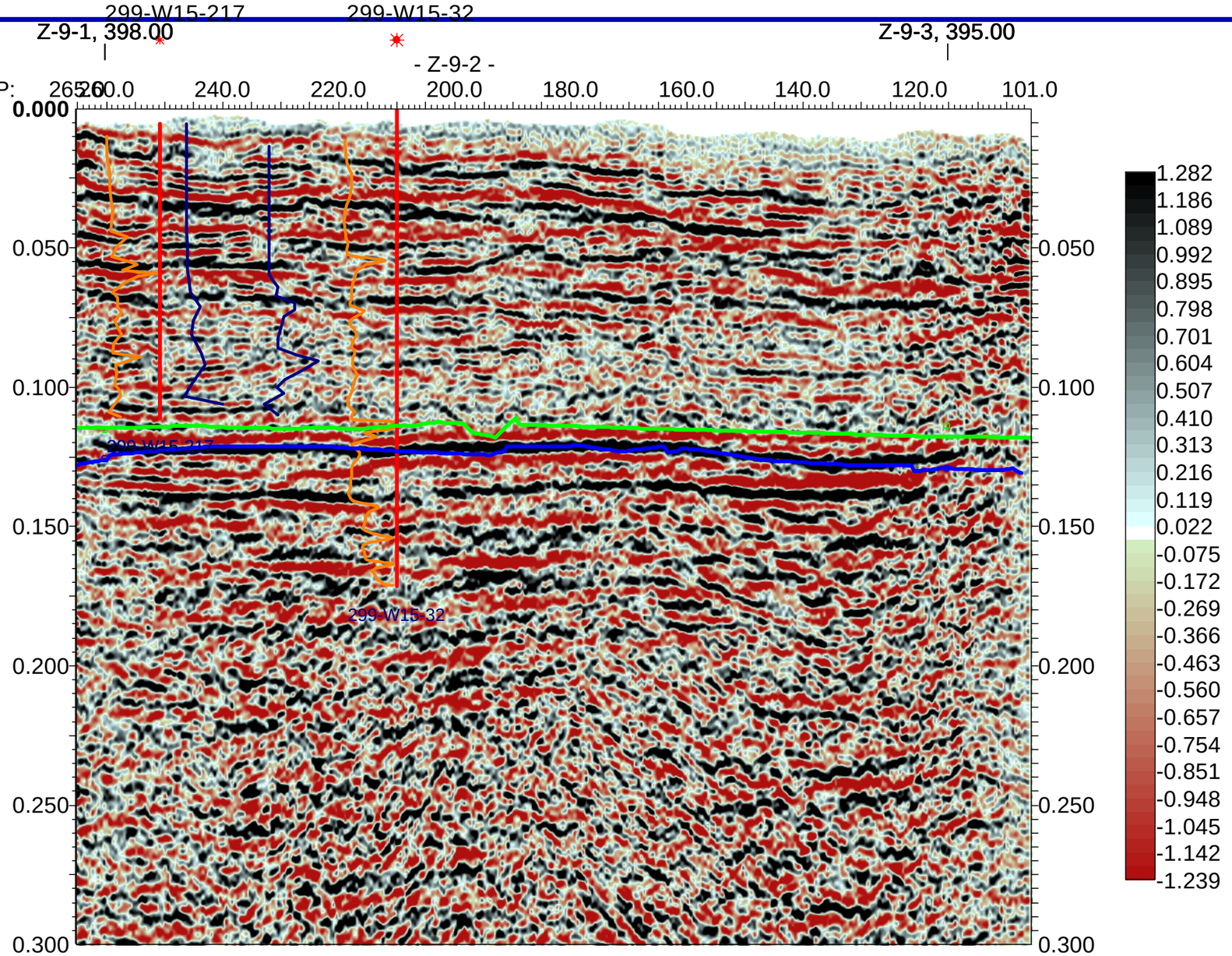

Enclosure 15
Seismic Line Z-9-3
Enhanced Amplitude Stack

Earth Sciences and Resources Inst.

Project: Hanford

Project Location: 200 West

Line Z-9-3
Enhance Stack

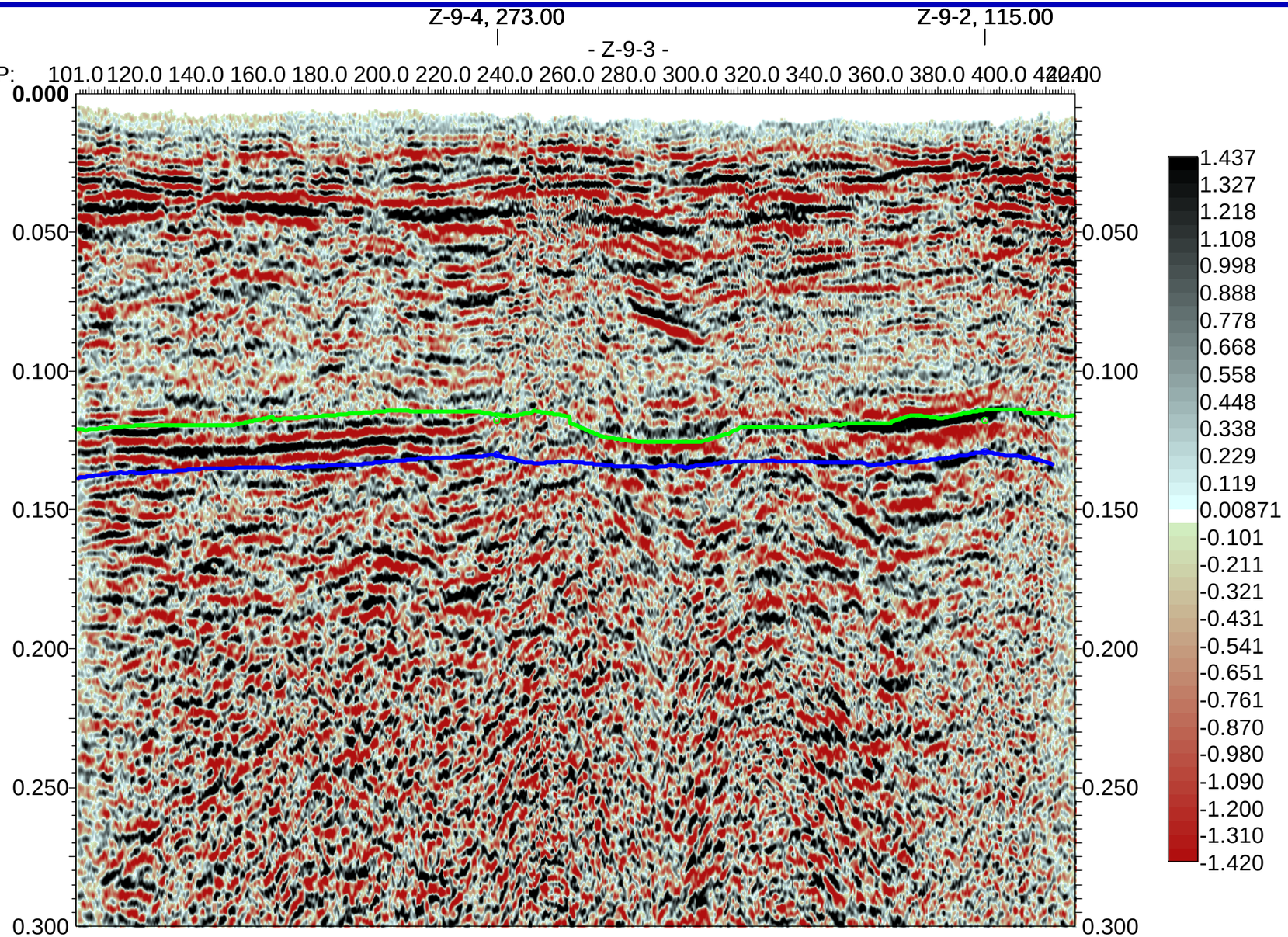

Enclosure 16
Seismic Line Z-9-4
Enhanced Amplitude Stack

Earth Sciences and Resources Inst.

Project: Hanford

Project Location: 200 West

Line Z-9-4
Enhance Stack

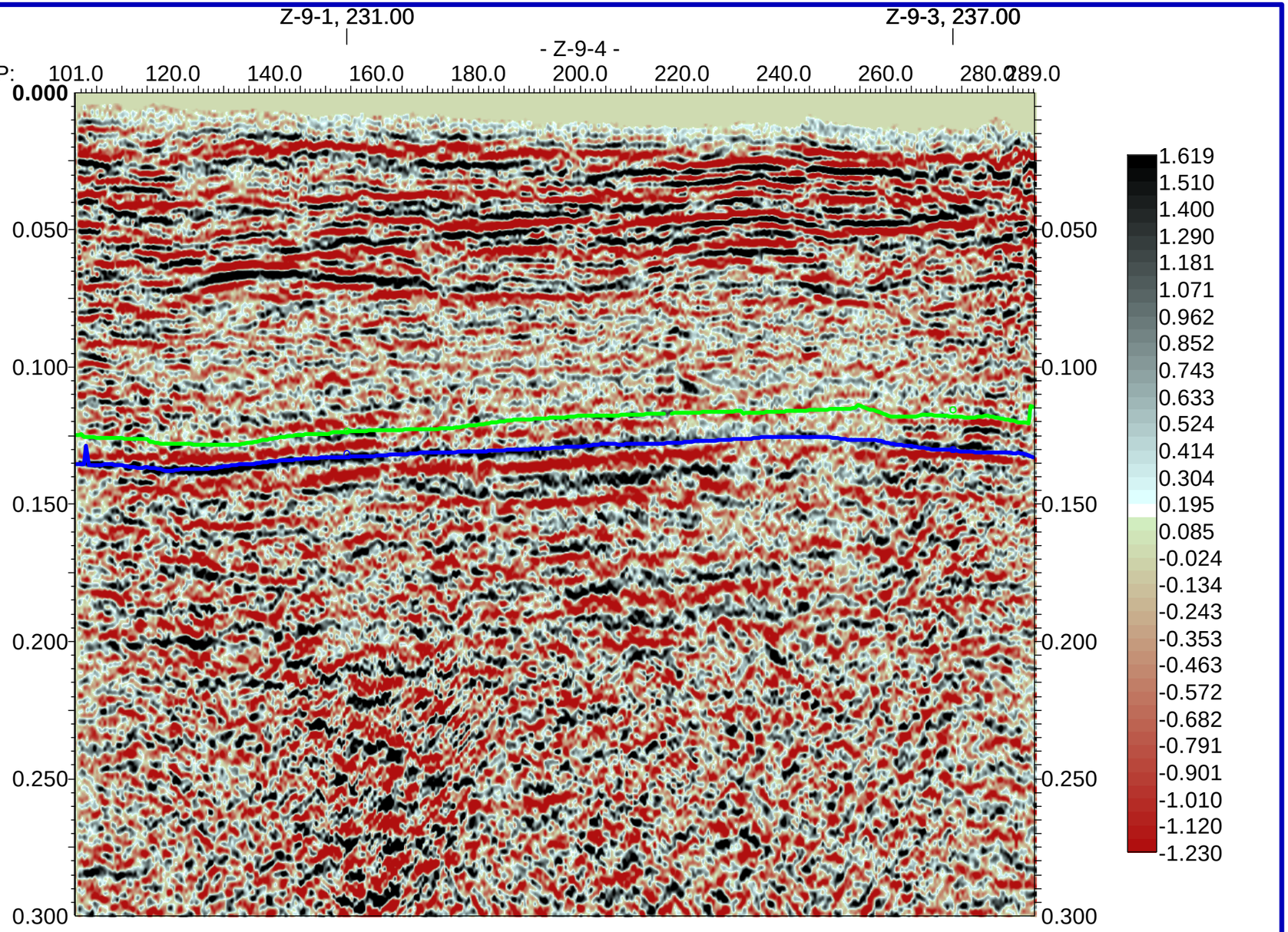

Enclosure 17
Seismic Line Z-9-1
Offset Range Limited Stack
0 - 20 Degrees

Earth Sciences and Resources Inst.

Project: Hanford

Project Location: 200 West

Line Z-9-1
Offset Range Limited Stack
0-20 Degrees

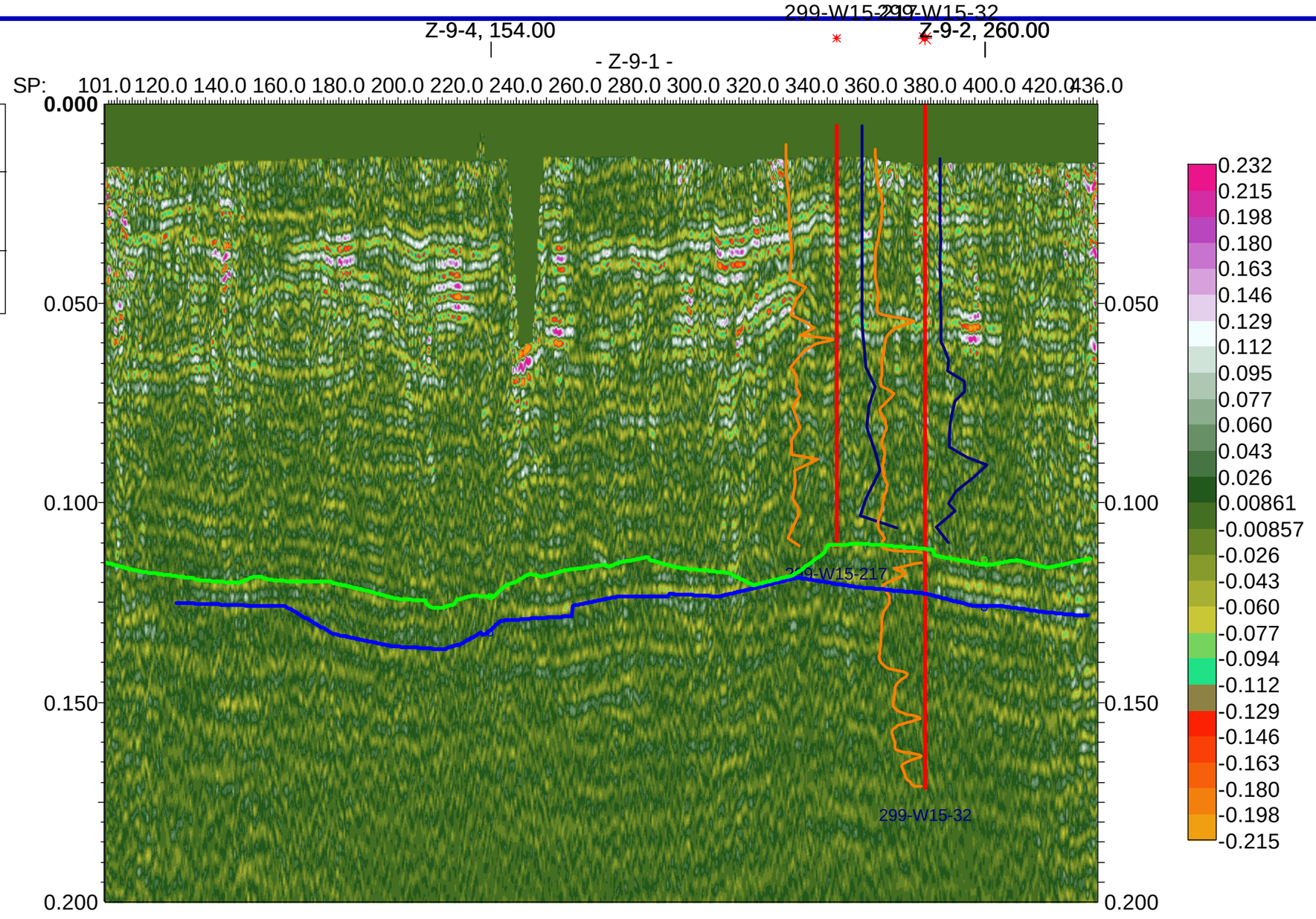

Enclosure 18
Seismic Line Z-9-1
Offset Range Limited Stack
20 - 40 Degrees

Earth Sciences and Resources Inst.

Project: Hanford

Project Location: 200 West

Line Z-9-1
Offset Range Limited Stack
20-40 Degrees

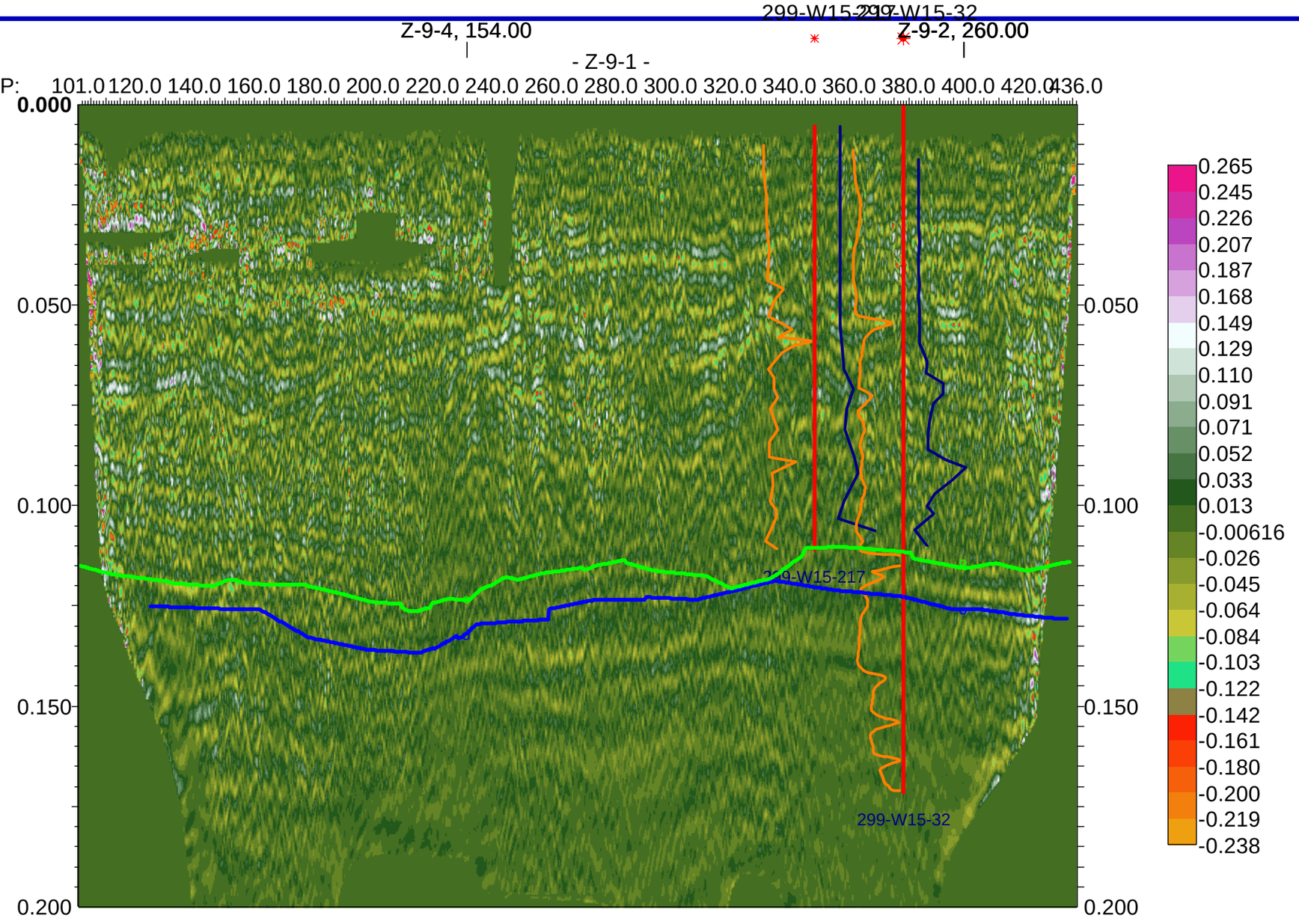

Enclosure 19
Seismic Line Z-9-1
Offset Range Limited Stack
40 - 60 Degrees

Earth Sciences and Resources Inst.

Project: Hanford

Project Location: 200 West

Line Z-9-1
Offset Range Limited Stack
40-60 Degrees

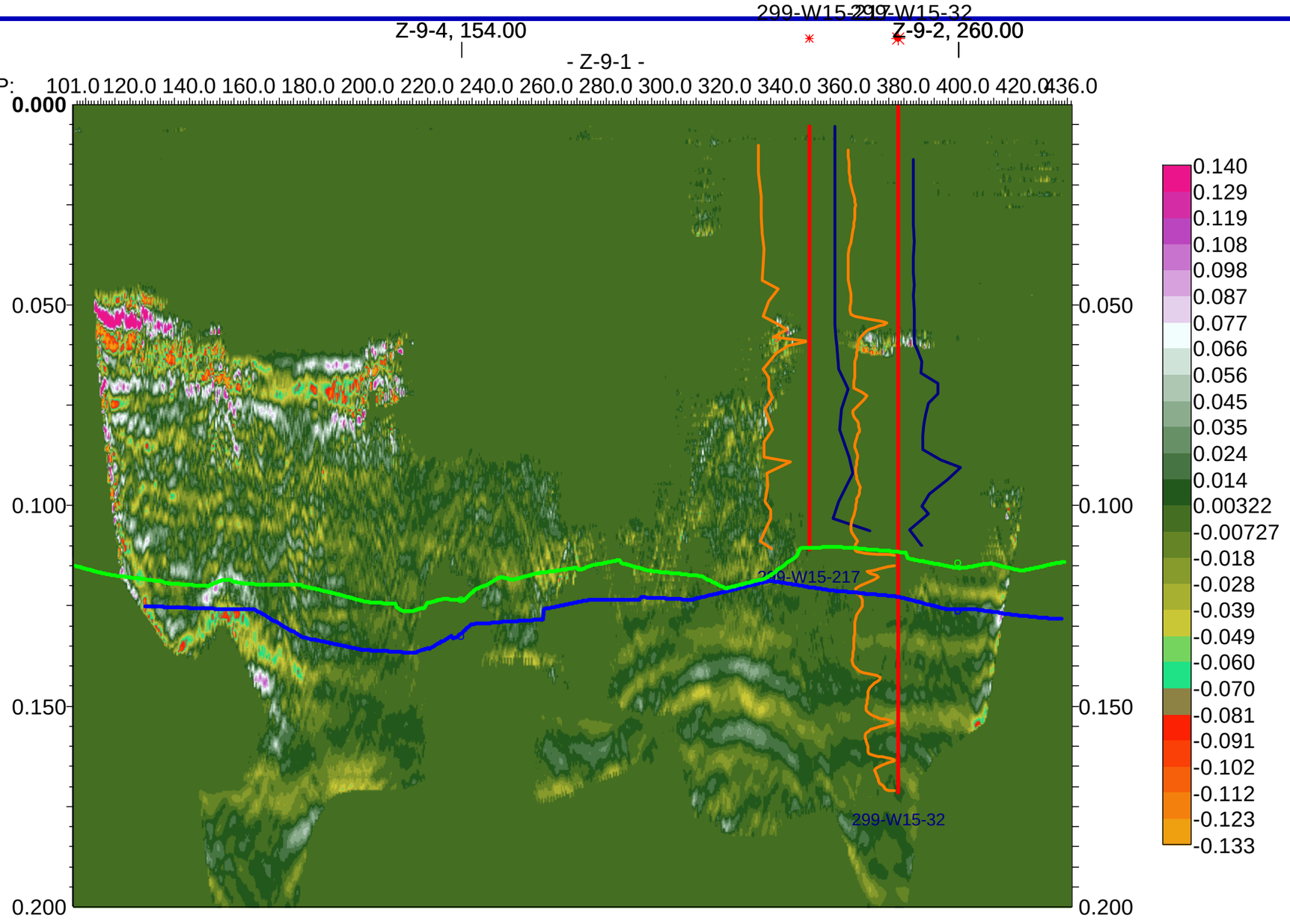

Enclosure 20
Seismic Line Z-9-2
Offset Range Limited Stack
0 - 20 Degrees

Earth Sciences and Resources Inst.

Project: Hanford

Project Location: 200 West

Line Z-9-2
Offset Range Limited Stack
0-20 Degrees

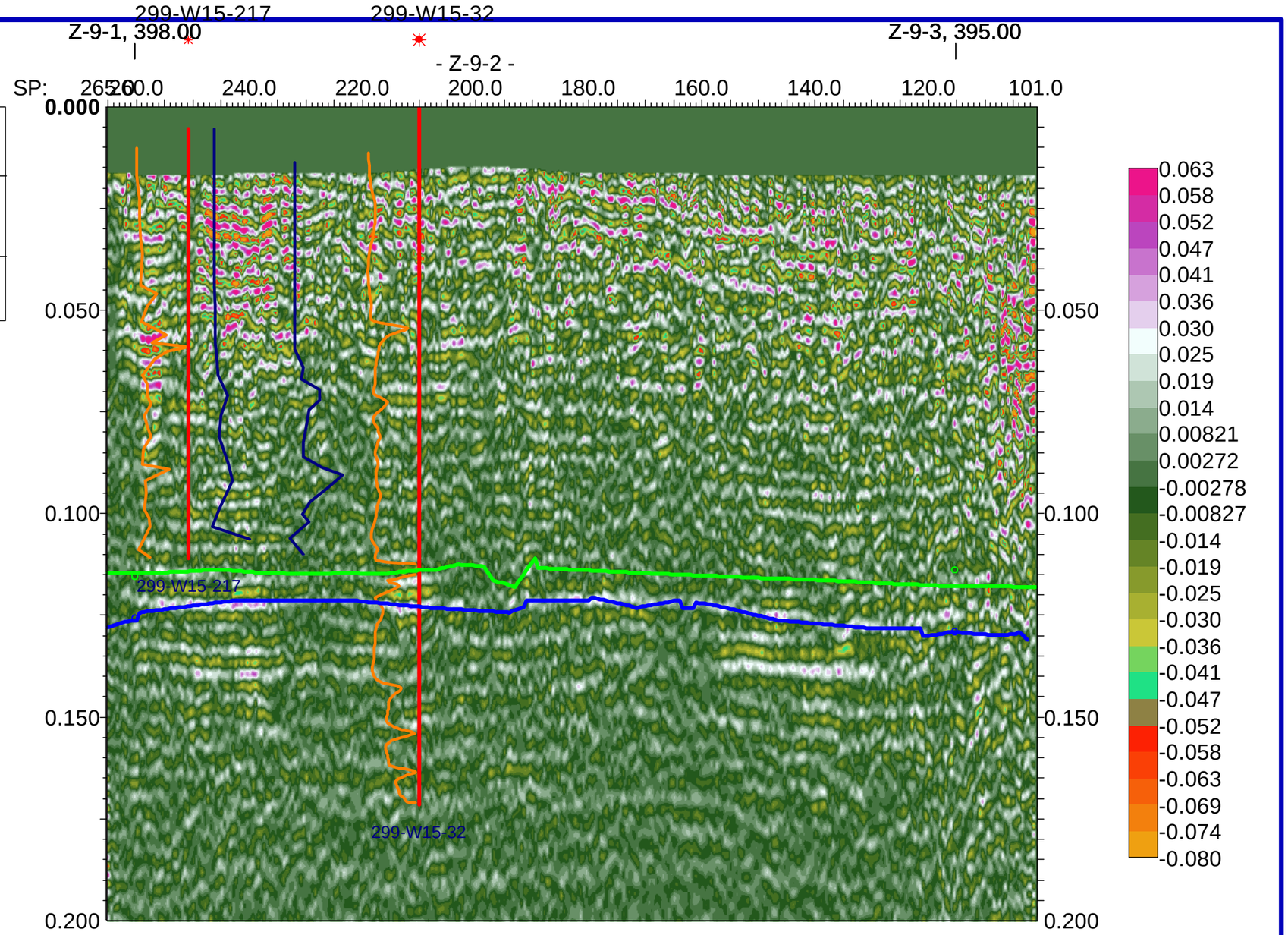

Enclosure 21
Seismic Line Z-9-2
Offset Range Limited Stack
20 - 40 Degrees

Earth Sciences and Resources Inst.

Project: Hanford

Project Location: 200 West

Line Z-9-2
Offset Range Limited Stack
20-40 Degrees

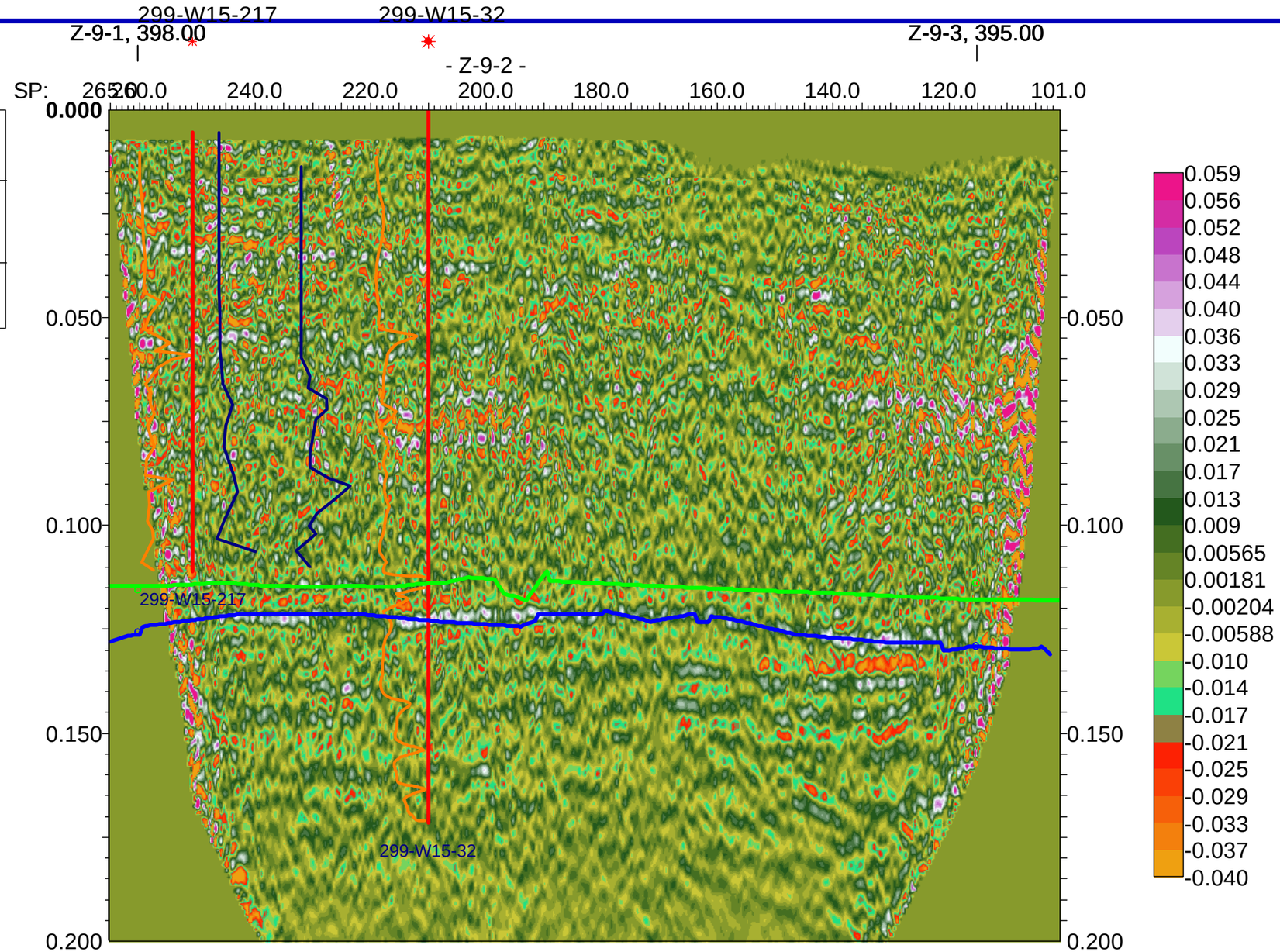

Enclosure 22
Seismic Line Z-9-2
Offset Range Limited Stack
40 - 60 Degrees

Earth Sciences and Resources Inst.

Project: Hanford

Project Location: 200 West

Line Z-9-2
Offset Range Limied Stack
40-60 Degrees

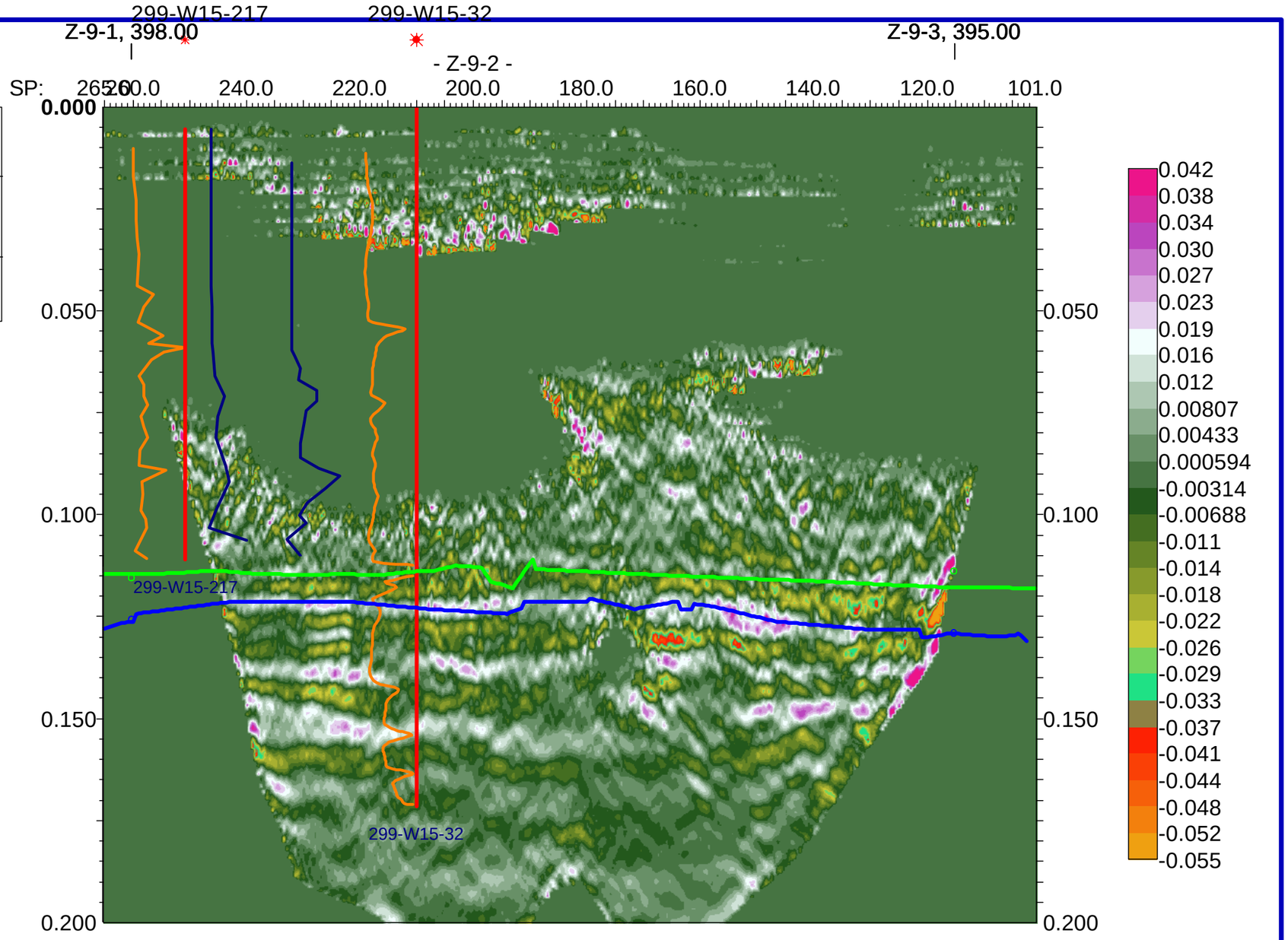

Enclosure 23
Seismic Line Z-9-3
Offset Range Limited Stack
0 - 20 Degrees

Earth Sciences and Resources Inst.

Project: Hanford

Project Location: 200 West

Line Z-9-3
Offset Range Limited Stack
0-20 Degrees

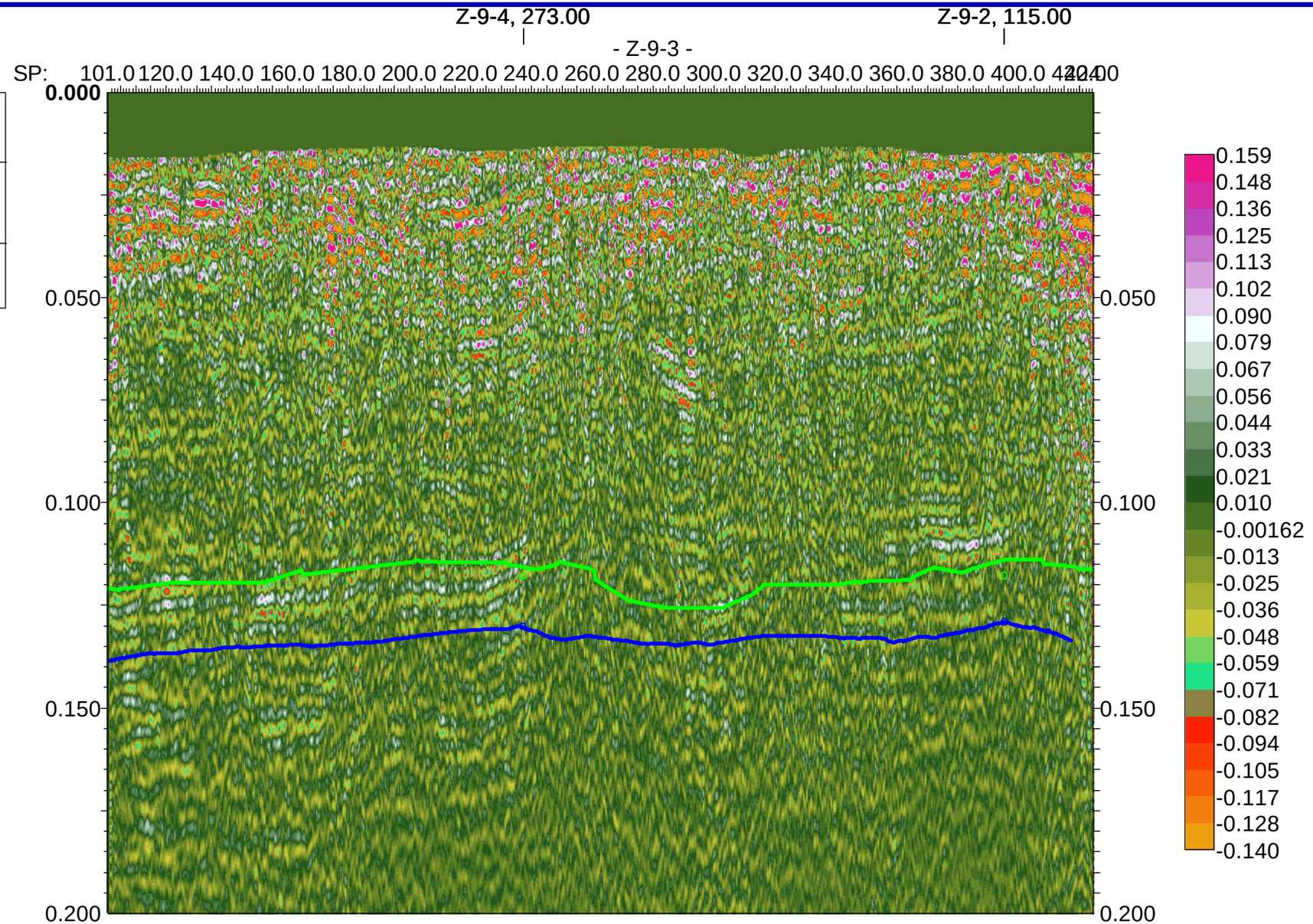

Enclosure 24
Seismic Line Z-9-3
Offset Range Limited Stack
20 - 40 Degrees

Earth Sciences and Resources Inst.

Project: Hanford

Project Location: 200 West

Line Z-9-3
Offset Range Limited Stack
20-40 Degrees

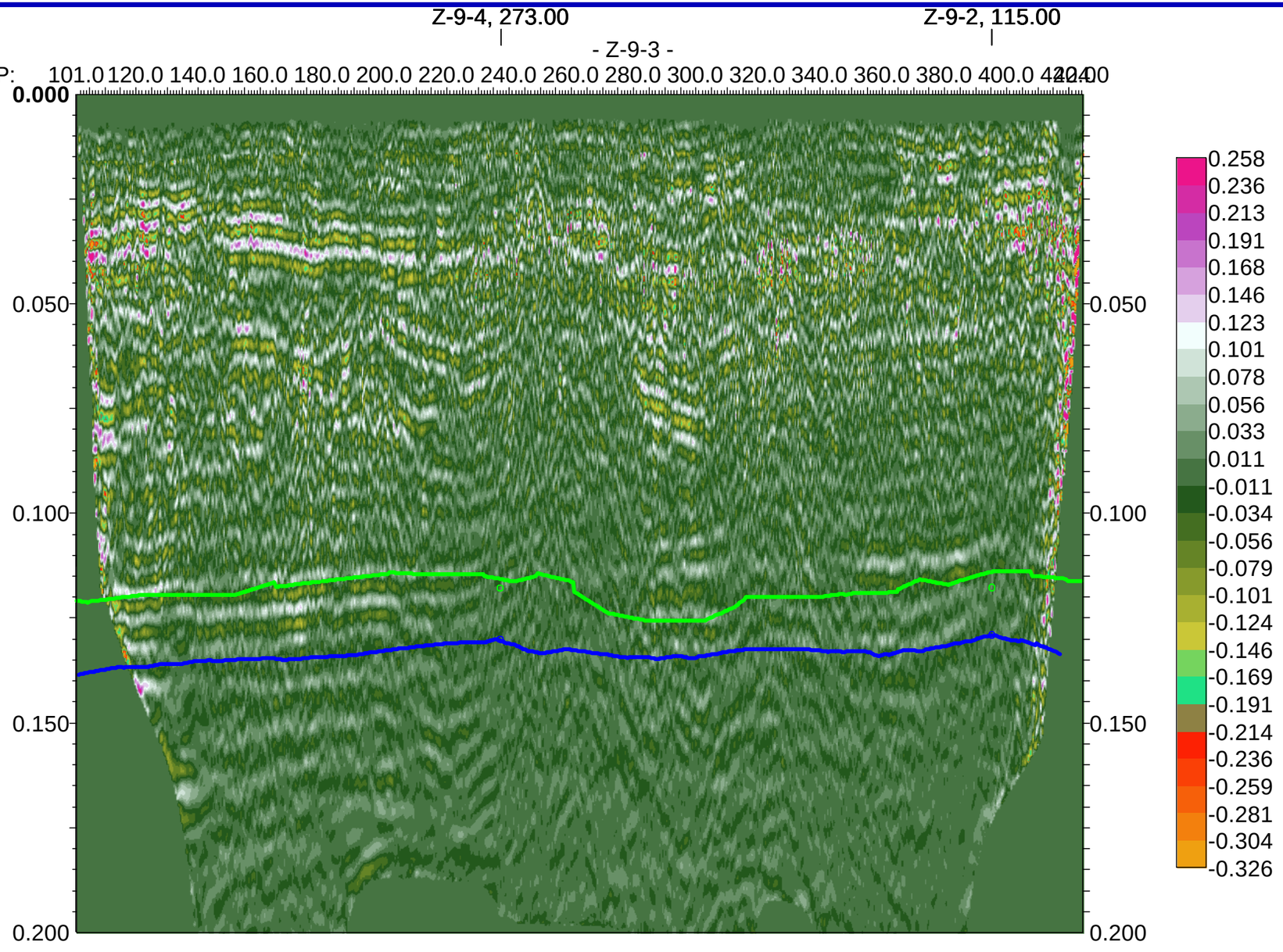

Enclosure 25
Seismic Line Z-9-3
Offset Range Limited Stack
40 - 60 Degrees

Earth Sciences and Resources Inst.

Project: Hanford

Project Location: 200 West

Line Z-9-3
Offset Range Limited Stack
40-60 Degrees

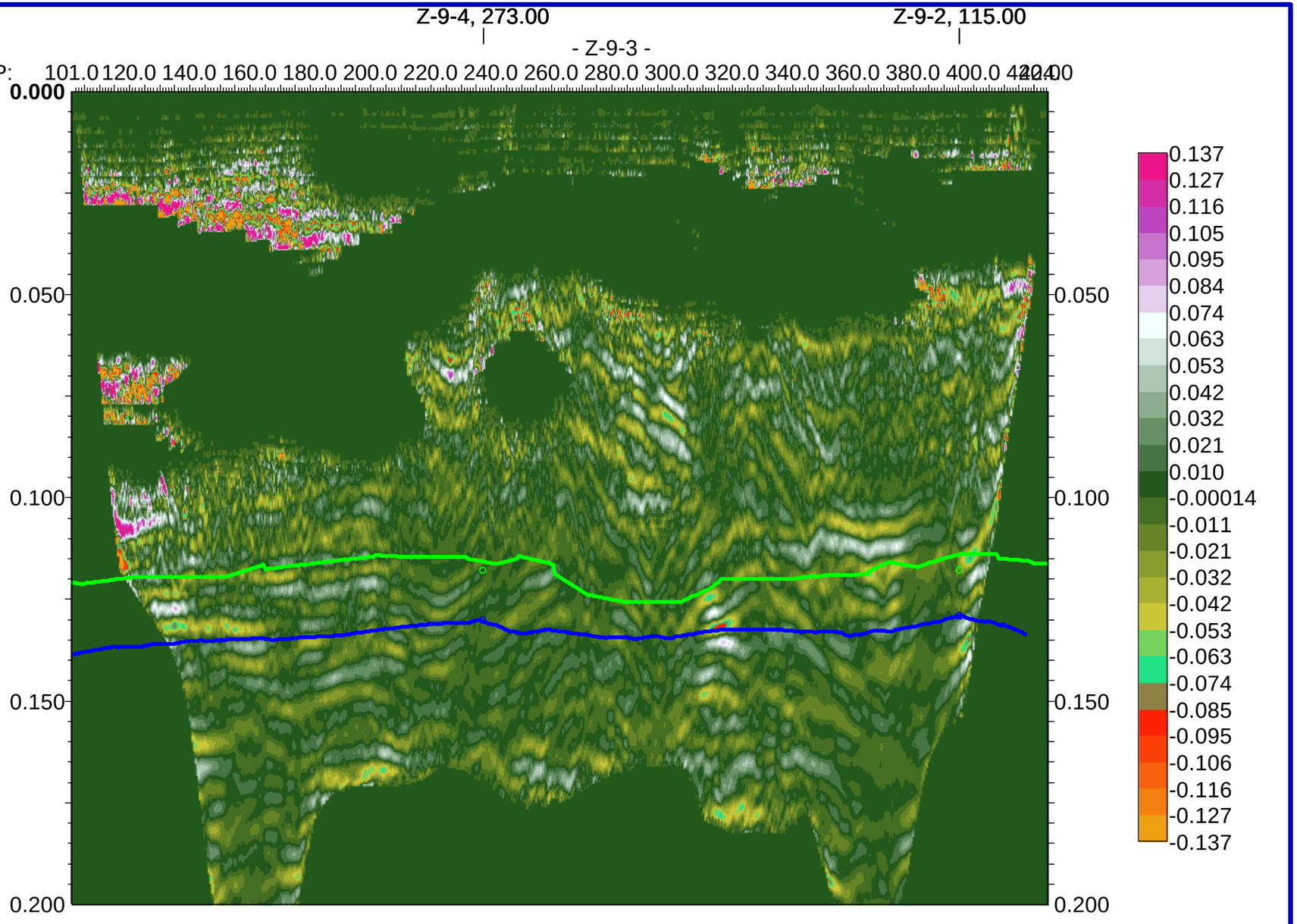

Enclosure 26
Seismic Line Z-9-4
Offset Range Limited Stack
0 - 20 Degrees

Earth Sciences and Resources Inst.

Project: Hanford

Project Location: 200 West

Line Z-9-4
Offset Range Limited Stack
0-20 Degrees

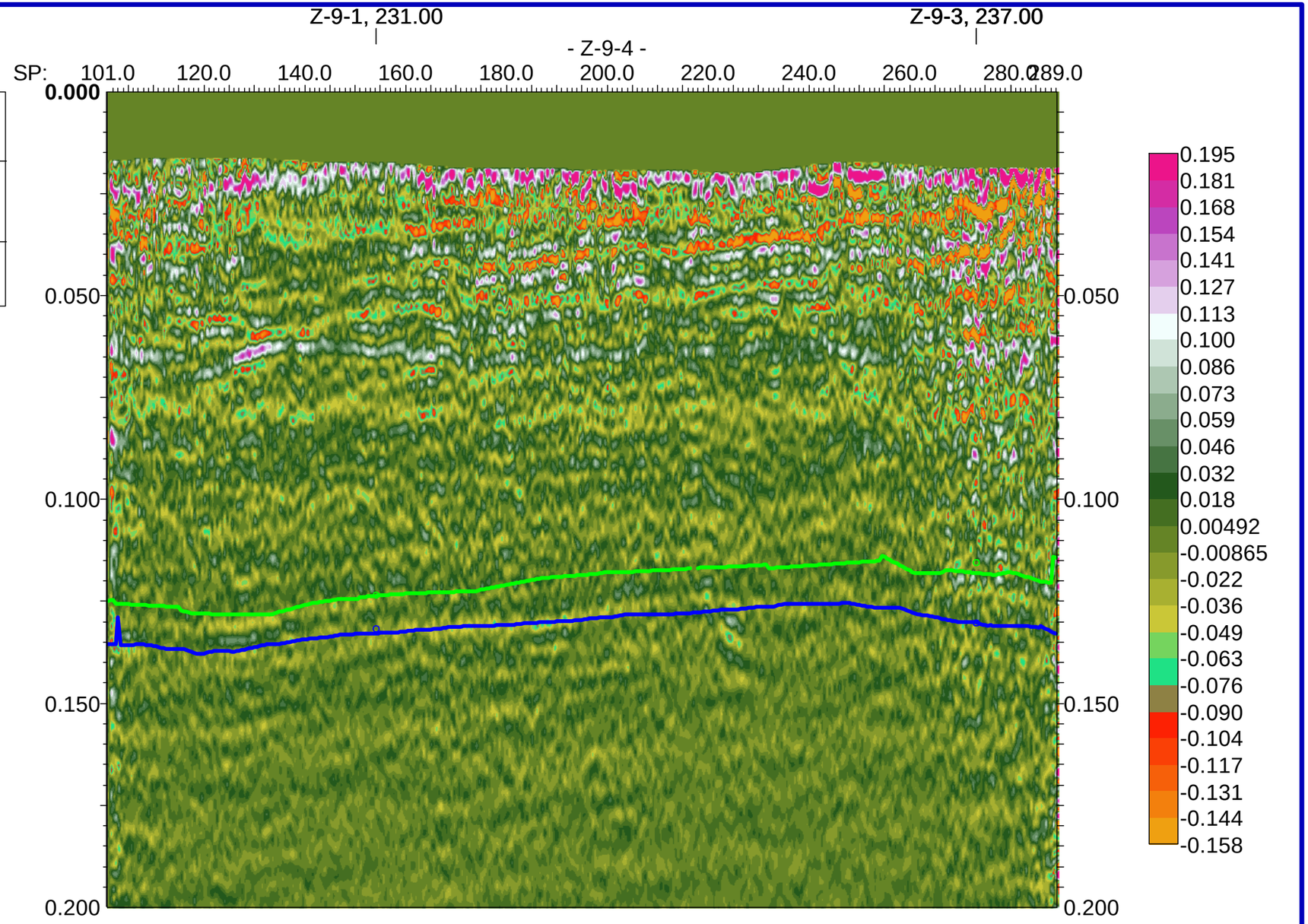

Enclosure 27
Seismic Line Z-9-4
Offset Range Limited Stack
20 - 40 Degrees

Earth Sciences and Resources Inst.

Project: Hanford

Project Location: 200 West

Line Z-9-4
Offset Range Limited Stack
20-40 Degrees

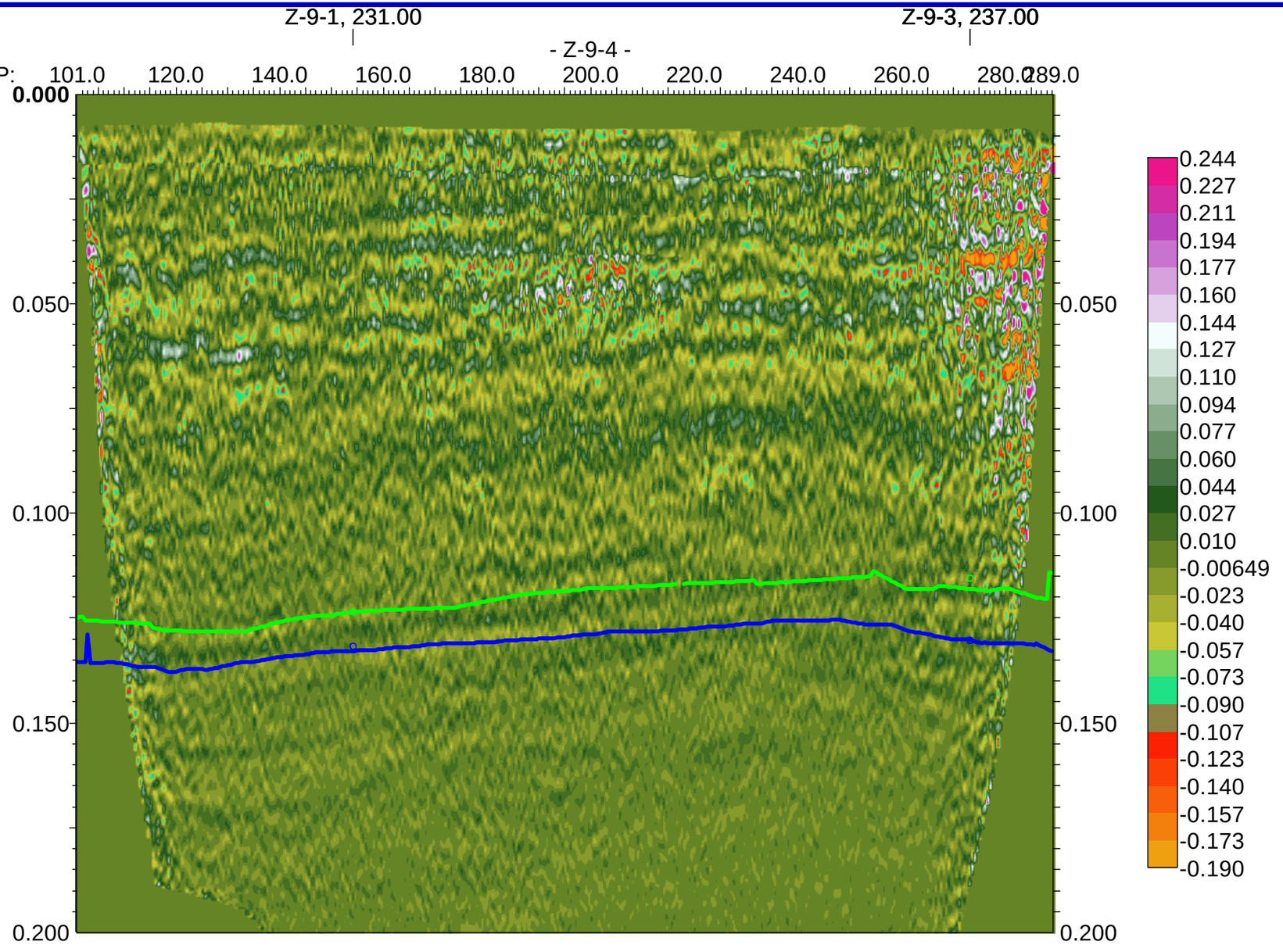

Enclosure 28
Seismic Line Z-9-4
Offset Range Limited Stack
40 - 60 Degrees

Earth Sciences and Resources Inst.

Project: Hanford

Project Location: 200 West

Line Z-9-4
Offset Range Limited Stack
40-60 Degrees

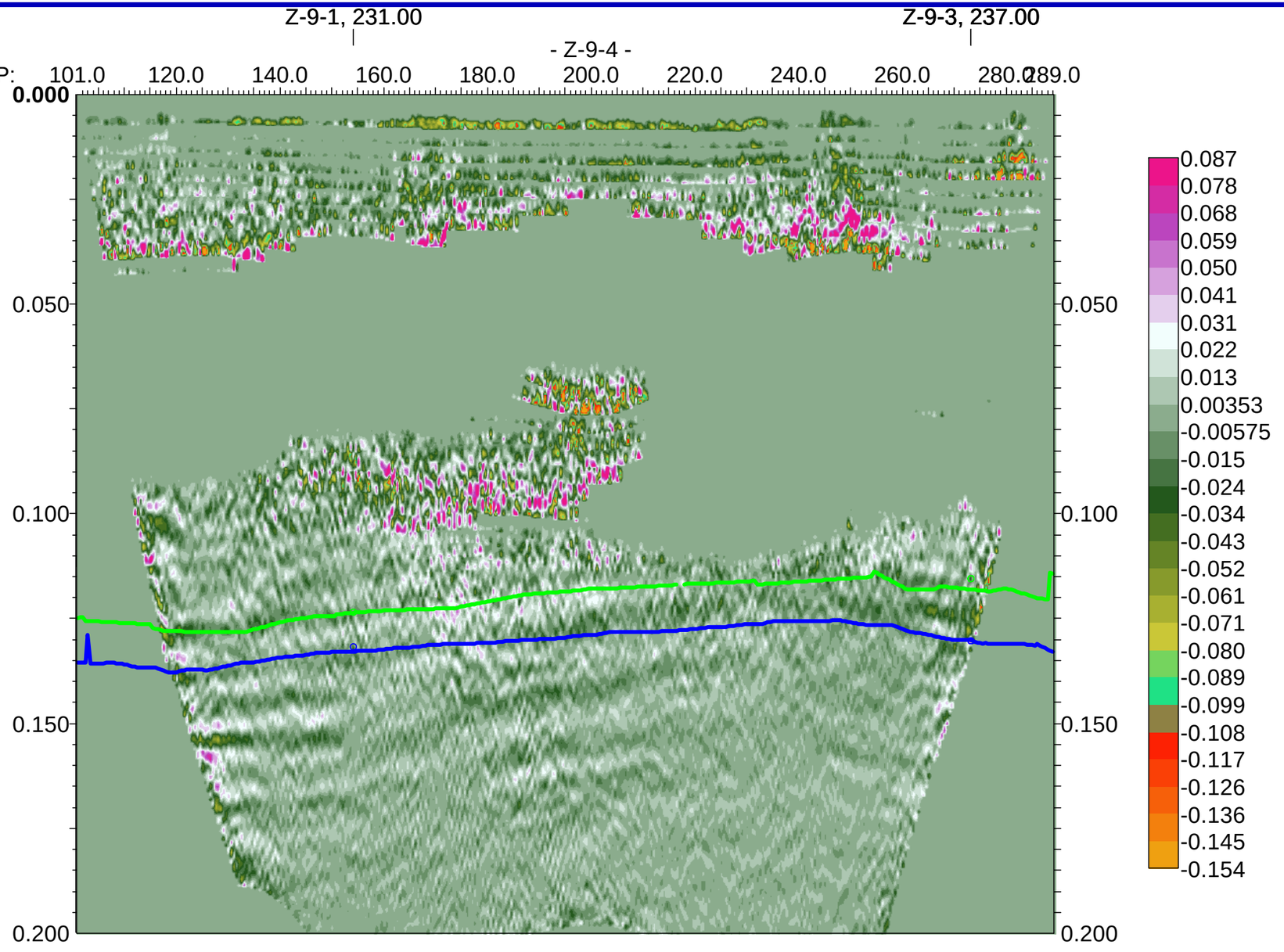

Enclosure 29
Seismic Line Z-9-1
Gradient Stack

Earth Sciences and Resources Inst.

Project: Hanford

Project Location: 200 West

Line Z-9-1
Gradient Stack

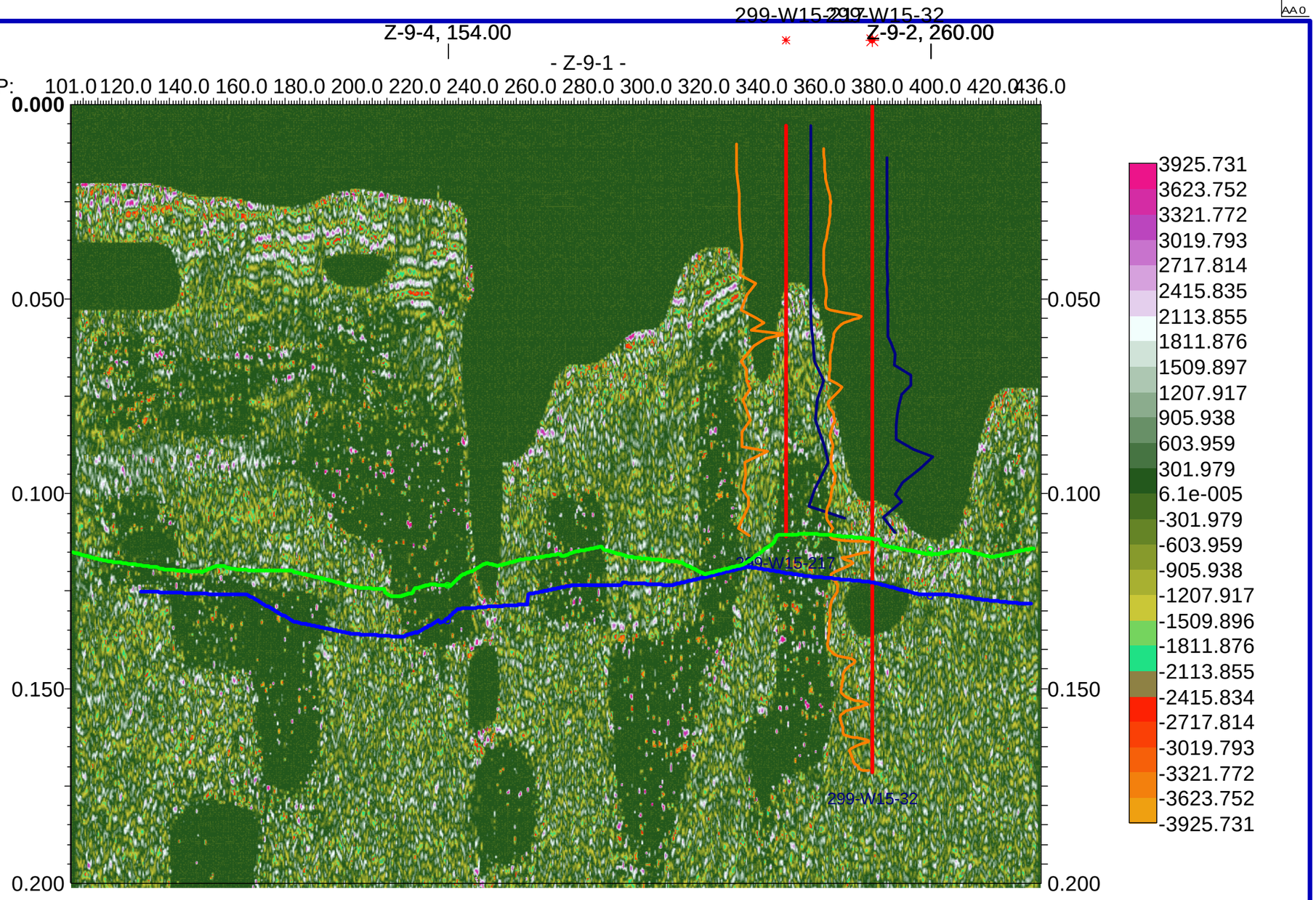

Enclosure 30
Seismic Line Z-9-2
Gradient Stack

Earth Sciences and Resources Inst.

Project: Hanford

Project Location: 200 West

Line Z-9-2
Gradient Stack

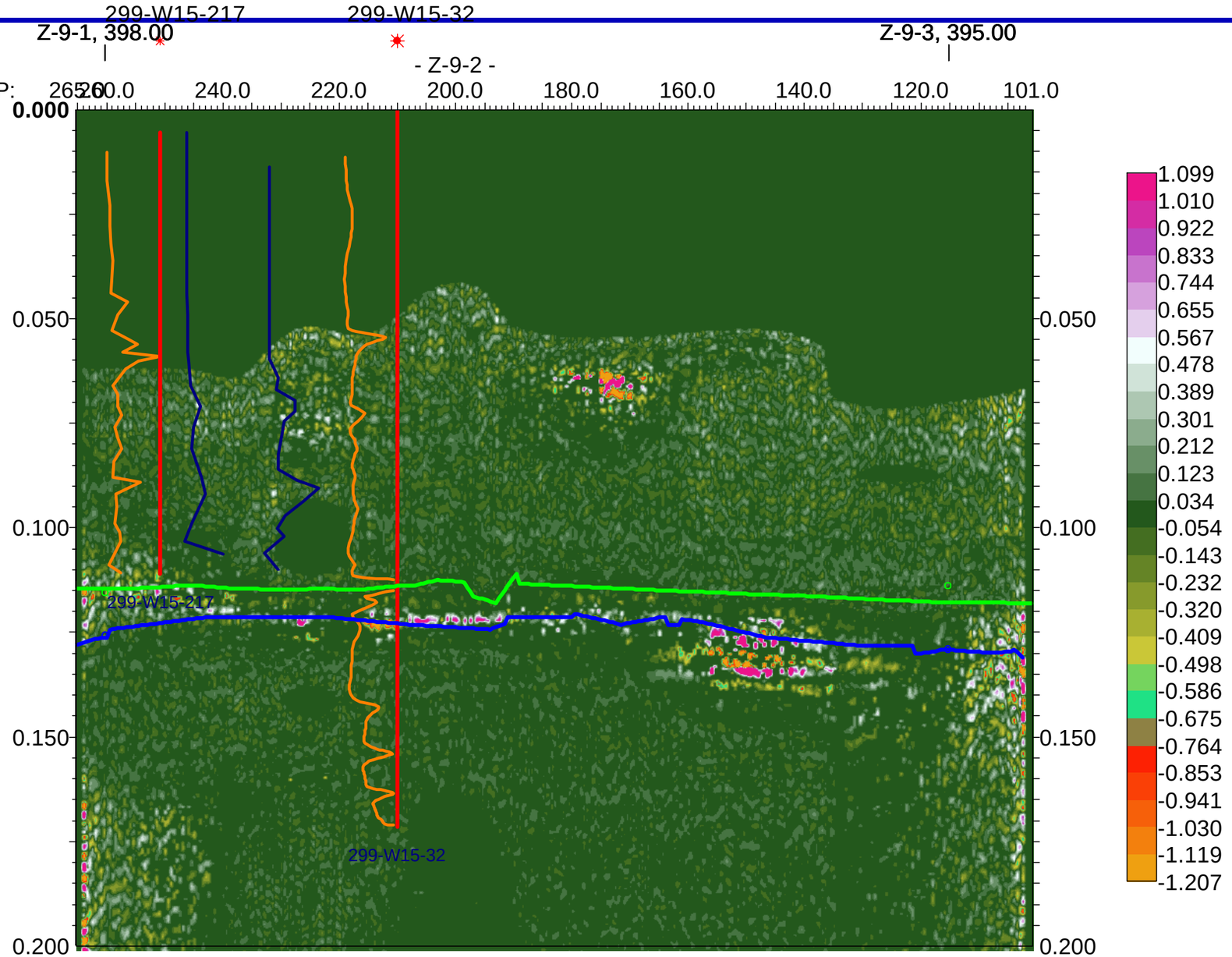

Enclosure 31
Seismic Line Z-9-3
Gradient Stack

Earth Sciences and Resources Inst.

Project: Hanford

Project Location: 200 West

Line Z-9-3
Gradient Stack

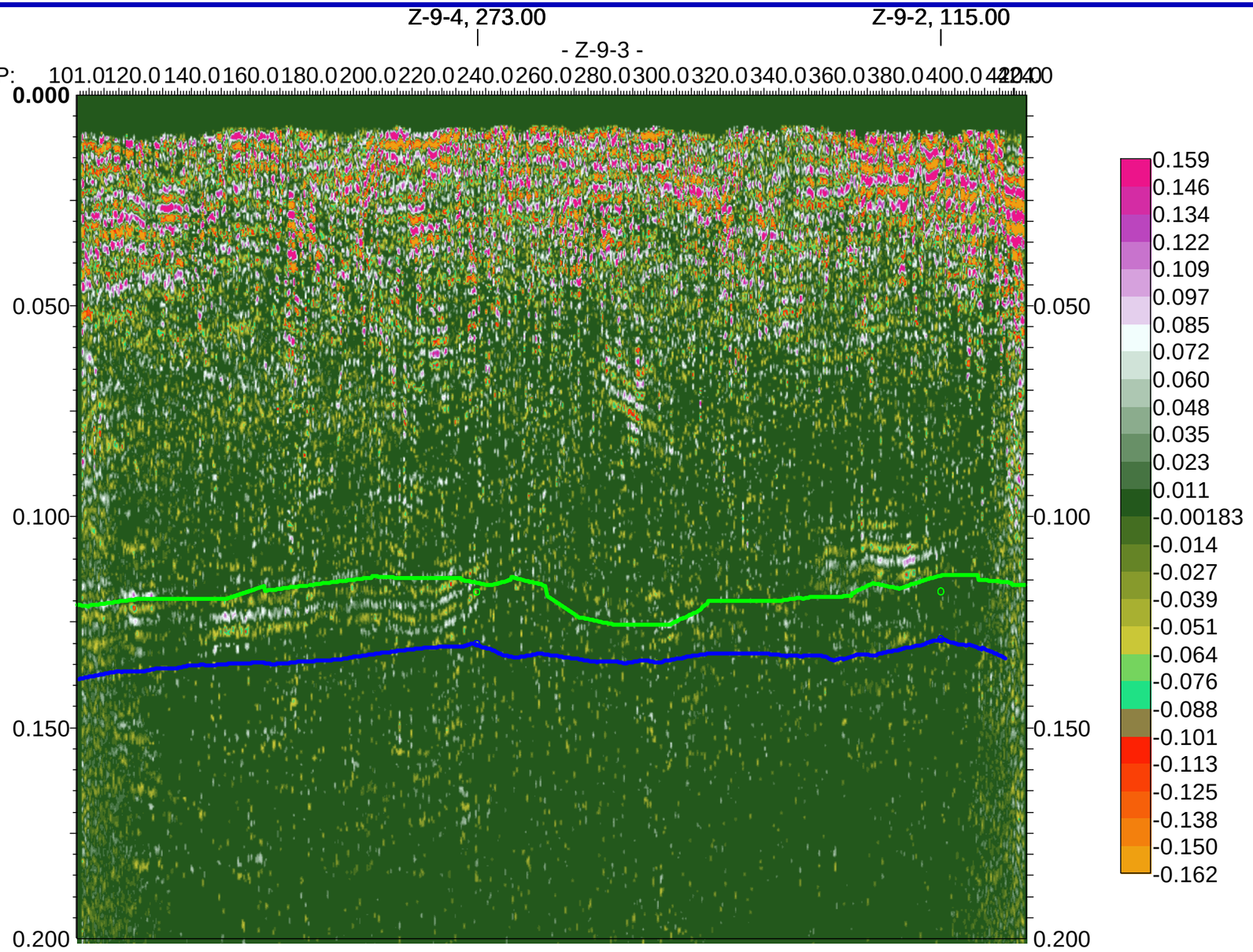

Enclosure 32
Seismic Line Z-9-4
Gradient Stack

Earth Sciences and Resources Inst.

Project: Hanford

Project Location: 200 West

Line Z-9-4
Gradient Stack

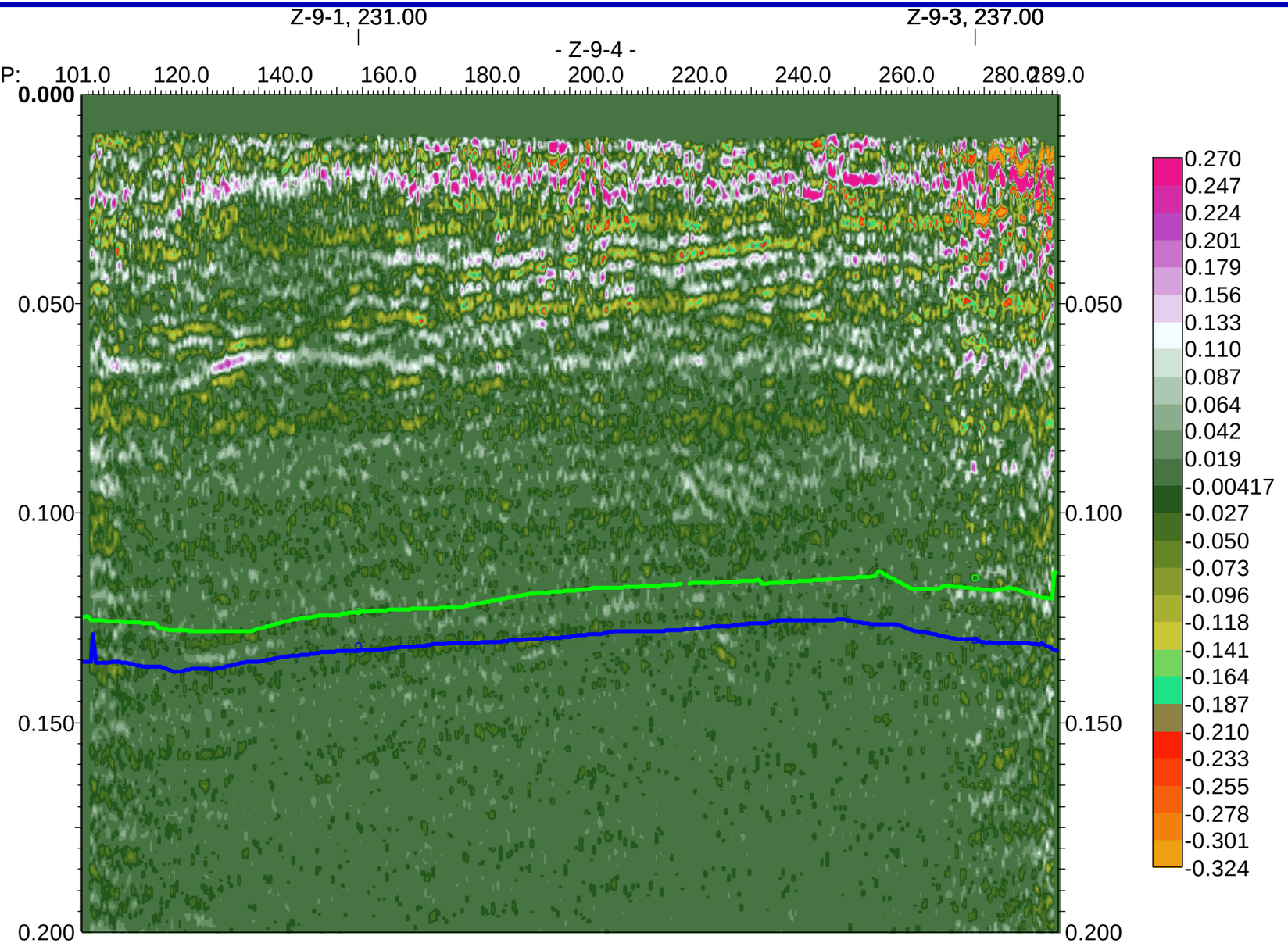

This page is intentionality blank

Non-Invasive Determination Of the Location and Distribution of Free-Phase Dense Nonaqueous Phase Liquids (DNAPL) By Seismic Reflection Techniques

Final Report

Tasks 4, 5, and 6

Reporting Period Starting Date: September, 1998

Reporting Period Ending Date: December, 2002

by

Michael G. Waddell
&
William J. Domoracki

Earth Sciences and Resources Institute
University of South Carolina
Columbia, South Carolina

January 2003

DOE Award Number DE-AR26-98FT40369

Disclaimer

Abstract

This document is the final report for Task 4 (site evaluation), Task 5 (2D seismic design, acquisition, and processing), and Task 6 (2D seismic reflection, interpretation, and AVO analysis) on DOE contact number DE-AR26-98FT40369. The project had planned one additional deployment to a site other than the Savannah River Site (SRS) or DOE Hanford Site. After the SUBCON midyear review in Albuquerque, NM (1999), it was decided that two additional deployments would be performed. The first deployment is to test the feasibility of using noninvasive seismic reflection and AVO analysis as a monitoring tool to assist in determining the effectiveness of Dynamic Underground Stripping (DUS) in removal of DNAPL at M-area Savannah River Site. The second deployment is to the Department of Defense (DOD) Charleston Naval Weapons Station Solid Waste Management Unit 12 (SWMU-12) Charleston, SC to further test the technique to detect high concentrations of DNAPL.

The Charleston Naval Weapons Station SWMU-12 site was selected in consultation with National Energy Technology Laboratory (NETL) and DOD Naval Facilities Engineering Command Southern Division (NAVFAC) personnel. Based upon the review of existing data and due to the shallow target depth, the project team collected three Vertical Seismic Profiles (VSP) and an experimental p-wave seismic reflection line. After preliminary data analysis of the VSP data and the experimental reflection line data, it was decided to proceed with Task 5 and Task 6. Three high resolution p-wave reflection profiles were collected with two objectives: 1) design the reflection survey to image a target depth of 20 feet below land surface to assist in determining the geologic controls on the DNAPL plume geometry, and 2) apply AVO analysis to the seismic data to locate the zone of high concentration of DNAPL.

Based upon the results of the data processing and interpretation of the seismic data, the project team was able to map a buried channel that is controlling the DNAPL plume geometry. The AVO analysis located a major amplitude anomaly, which was tested using a Geoprobe™ direct push system. The Geoprobe™ was equipped with a membrane interface probe (MIP) that was interfaced with a sorbent trap/gas chromatograph (GC) system. Both the Photo Ionization Detector (PID) and Electron Capture Detector (ECD) on the GC exceeded the maximum measurement values through the anomaly. A well was drilled to collect a water sample. The concentration of chlorinated solvents in the water sample was in excess of 500 ppm. Other amplitude anomalies located directly under an asphalt road were also tested. In these cases both the PID and ECD were zero. Further analysis was able to attribute the asphalt road anomalies to data processing artifacts. Based upon the water samples and MIP probes, it appears that surface seismic and AVO analysis were able to detect the area of highest concentration of DNAPL.

At the Dynamic Underground Stripping (DUS) demonstration project steam was injected into a zone between 20 feet and to 165 feet below the surface. The base of this zone is the top of the "green clay" confining unit. The steam vaporized the PCE and TCE contaminants and the vapors were extracted though an extraction well. The objective of this phase of the project is to determine if surface seismic can be used to assist in monitoring the effectiveness of DUS in removal of DNAPL. To test this objective two deployments of Task 5 (seismic design, acquisition, processing) and Task 6 (seismic

interpretation and AVO analysis) are required - one before steam injection and one after steam injection and vapor extraction have been completed. The first deployment has been completed at the DUS site. The first deployment of Task 5 involved collecting 522 feet of p-wave reflection seismic data across the location where the DNAPL is accumulating. Acquisition and processing parameters were based on previous work the project team completed at the adjacent M-Area seepage basin. AVO analysis of the seismic data revealed an AVO anomaly in a location where there is suspected DNAPL. At this time no second deployment to DUS has been done.

Table of Contents

List of Figures

List of Tables

1.0 Introduction

This document is the final report for Task 4, 5, and 6 (site evaluation, 2D seismic design and acquisition, and data interpretation) under DOE contact DE-AR26-98FT40369. This report pertains to only Tasks 4, 5, and 6 at the Solid Waste Management Unit-12 (SWMU-12) at the Charleston Naval Weapons Station (Figure 1). This site offers some unique technical challenges in that the target depth for the seismic surveys is less than 20 feet below land surface. A second deployment of Tasks 5 and 6 was also to have been completed for this report at the Dynamic Underground Stripping (DUS) site at Savannah River Site (Figure 2). Steam injection has been completed, but the equipment has not been removed from the site; therefore we could not deploy and reshoot the seismic line DUS-1.

At the SWMU-12 site the greatest concentration of DNAPL is located in the upper 20 feet within the surficial aquifer (Figure 3) (Tetra Tech, NUS Inc, 2000). In the lower aquifer there appears to be very low concentrations of dissolved chlorinated solvents, so consequently the emphasis is to image the DNAPL in the upper surficial aquifer. Based upon review of existing data and due to the shallow target depth, the project team collected two vertical seismic profiles (VSP) and an experimental p-wave seismic reflection line. After analysis of the VSP velocities and processing of the experimental reflection line, it was decided to proceed with Task 5 (design, acquire, and process the 2D seismic data) and Task 6 (interpretation of the 2D reflection data). Three high-resolution reflection seismic profiles were acquired, processed, and interpreted (Figure 1). AVO analysis was applied to each seismic profile.

At the Dynamic Underground Stripping (DUS) demonstration project steam was injected into a zone between 20 feet and 165 feet below the surface. The base of the zone is the top of the "green clay" confining unit. The PCE and TCE contaminants were vaporized and the vapors were extracted through an extraction well. The objective of this phase of the project is to determine if surface seismic can be used to assist in monitoring the effectiveness of DUS in removal of DNAPL. To test this objective two deployments of Task 5 (seismic design, acquisition, processing) and Task 6 (seismic interpretation and AVO analysis) are required - one before steam injection and one after steam injection and vapor extraction are completed. The first deployment has been completed at the DUS site. The first deployment of Task 5 involved collecting 522 feet of p-wave reflection seismic data across the location where the DNAPL is accumulating. Acquisition and processing parameters were based on previous work the project team completed at the adjacent M-Area seepage basin. AVO analysis of the seismic data revealed an AVO anomaly in a location where there is suspected to be DNAPL.

2.0 Executive Summary

This final report concerns Task 4 (site evaluation), Task 5 (design, acquire, and process 2D seismic data), and Task 6 (interpretation and AVO analysis of the 2D reflection data) for the Solid Waste Management Unit 12 (SWMU-12) at the Charleston Naval Weapons Station under DOE contact number DE-AR26-98FT40369. After the SUBCON midyear review in Albuquerque, NM (1999) and recommendations from the peer review, it was decided that two additional deployments would be performed on this

project. The first deployment is to test the feasibility of using non-invasive seismic reflection and AVO analyses as a monitoring tool in determining the effectiveness of Dynamic Underground Stripping (DUS) in removal of DNAPL. The site selected for this feasibility study is the solvent storage area at M-Area Savannah River Site. The second site is to test the AVO analysis method under a different set of geologic conditions than those investigated previously. The site selected is the DOD Charleston Naval Weapons Station SWMU-12 site Charleston, SC. This site was selected in consultation with NETL and DOD NAVFAC Southern Division personnel. Tasks 4, 5, and 6 were performed at the Charleston Naval Weapons Station. The Charleston site offers some unique technical challenges in that the target depth to image is very shallow, less than 20 feet below land surface.

At the SWMU-12 site the greatest concentration of DNAPL is located in the upper 20 feet within the surficial aquifer (Figure 2). In the lower aquifer there appears to be very low concentrations of dissolved chlorinated solvents, therefore, the emphasis is to image the DNAPL in the upper surficial aquifer. After review of existing data and considering the shallow target depth, the project team collected three vertical seismic profiles (VSP) and an experimental reflection line. Analysis of the experimental reflection seismic profile demonstrated that reflections could be obtained from the shallow depth where the DNAPL is occurring.

The next step was generating a series of reflection coefficient versus offset (AVO) models to determine whether there will be a detectable change in seismic amplitude if DNAPL replaces water in the pore spaces. The results of the modeling suggested that there would be an amplitude anomaly if DNAPL replaced water in the pore spaces (Figure 9). The modeling results also indicated that more sophisticated AVO analysis would be required to detect DNAPL than using only range limited stacking techniques (employed at Savannah River Site) or enhancing the amplitudes to look for bright spots or dim-outs (employed at Hanford Site).

Three high-resolution p-wave reflection profiles were collected with two objectives: 1) to design the reflection survey to image a target depth of 20 feet below land surface and to assist in mapping the geologic conditions that control the DNAPL plume geometry, and 2) to apply AVO analysis to the seismic data to locate the zone(s) of high concentration of DNAPL (Figure 1).

Based on the results of the data processing and interpretation of the seismic data, the project team was able to map the buried channel that is controlling the DNAPL plume geometry. The AVO analysis located a major amplitude anomaly that was tested using a Geoprobe™ equipped with a membrane interface probe (MIP) interfaced with a sorbent trap/GC system. When the MIP penetrated the AVO anomaly both the Photo Ionization Detector (PID) and Electron Capture Detector (ECD) on the GC exceeded the maximum values throughout the anomaly. Subsequently, a well was drilled to collect a water sample. The concentration of chlorinated solvents in the water sample was in excess of 500 ppm. Other amplitude anomalies were tested that were located directly under an asphalt road. In these cases both the PID and ECD were zero. Upon further examination of the unstacked data, it appears that the false AVO anomaly was a data processing artifact. Based upon the water samples and MIP probes, it appears that surface seismic and AVO analysis was able to detect the area of highest concentration of DNAPL.

3.0 Project Objectives

The research as initially proposed was a 14 month proof of concept study to determine the location and distribution of subsurface DNAPL contamination at the 200 West area, DOE Hanford Site by the use of two and three dimensional high-resolution seismic reflection data and borehole geophysical surveys. The major change in the project objectives during this proof of concept phase is testing the feasibility of using this technique as a monitoring tool at the DUS project at the M-Area solvent tanks area, Savannah River Site and adding the Charleston Naval Weapons Station, Charleston SC as an additional site. The specific objectives of the research at these sites are:

- Subsurface imaging of geologic sinks where DNAPL can pool.
- Direct detection of DNAPL by use of seismic reflection amplitude versus offset (AVO) method in the very near surface.
- Testing the feasibility of using high-resolution seismic techniques and AVO analysis as a monitoring tool in evaluating the effectiveness of the DUS technique at the M-Area solvent tank area (SRS only).

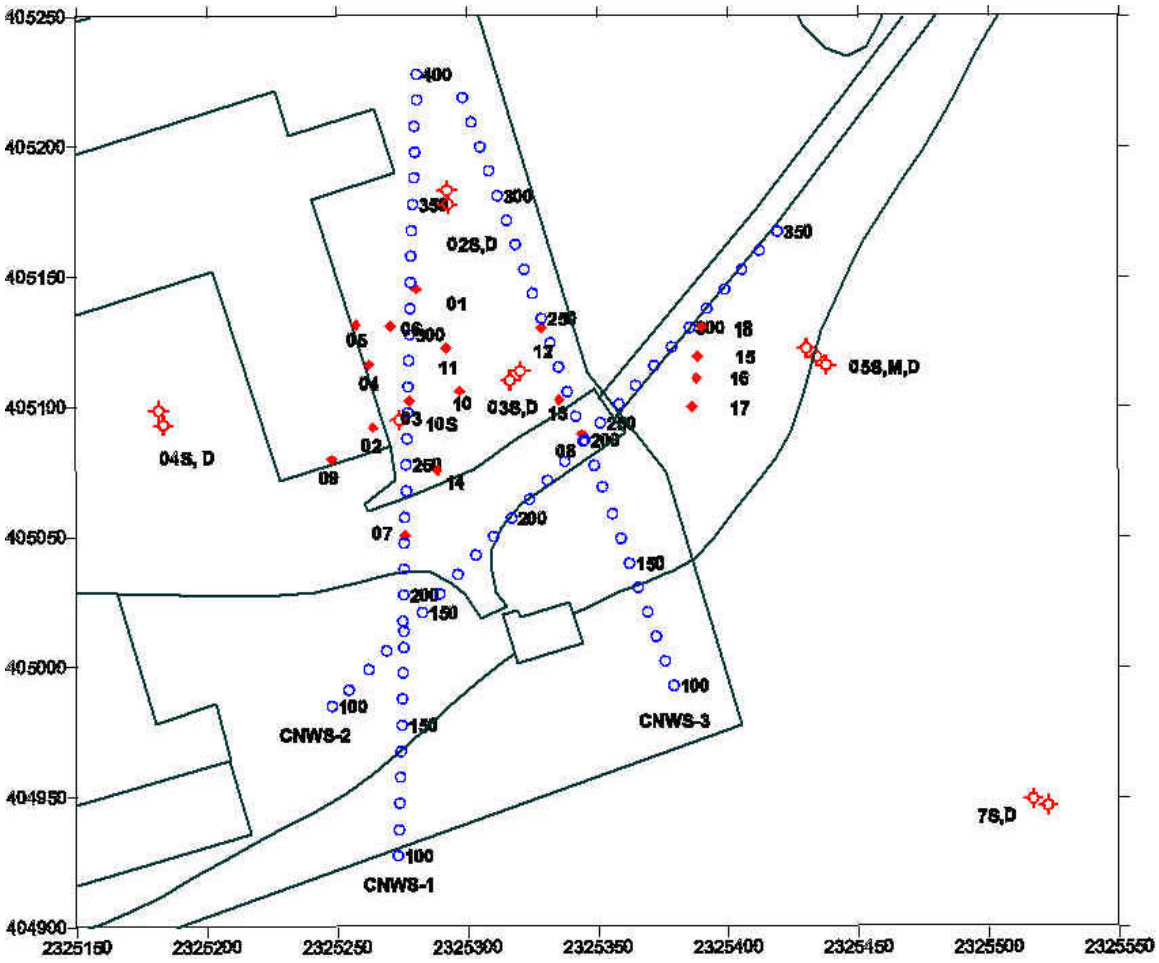

Figure 1. Location map of the Solid Waste Management Unit 12 (SWMU) site at the Charleston Naval Weapons Station. The blue circles are the location of every 50th shot point. The circles with hash lines on the outside are well locations, the designation after the number indicates if the well is screened in the shallow zone (S) or the intermediate zone (M) or the deep zone (D). The diamonds represent Membrane Interface Probe (MIP) locations. Grid is South Carolina state plane in feet.

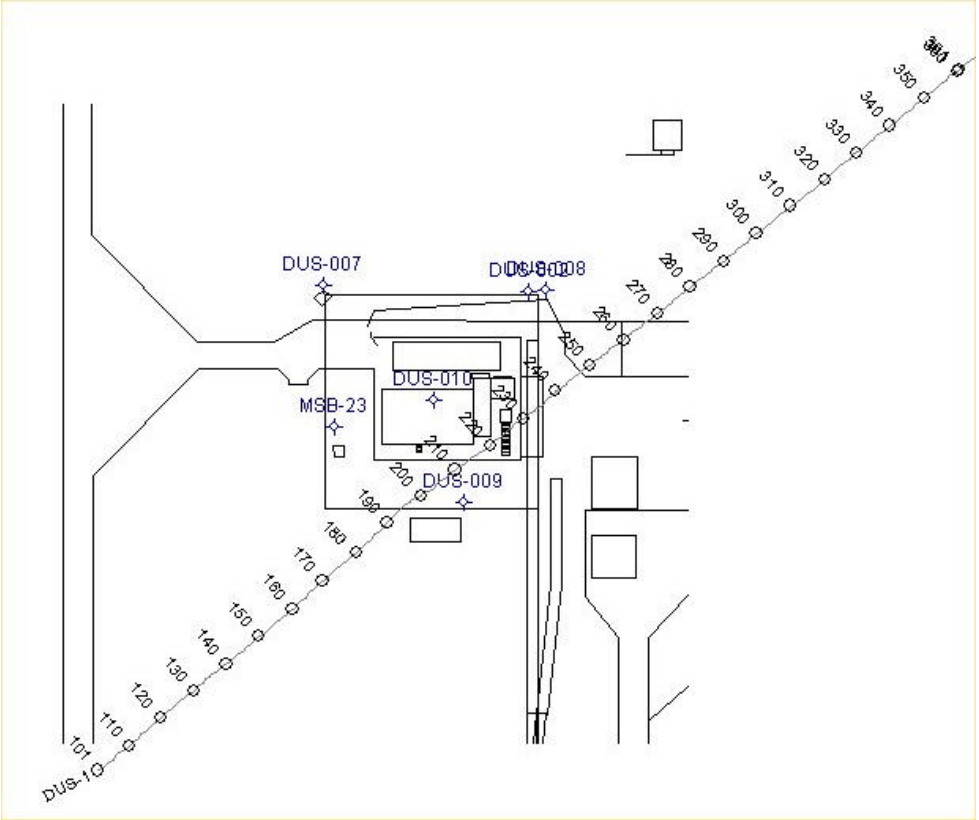

Figure 2. Location map of wells and seismic profile DUS-1 at the DUS site. Well DUS-10 is the extraction well and the location of p-wave VSP. Wells DUS- 7, 8, and 9 are steam injection wells at the M/A area, Savannah River Site. Shotpoints are at every 2 feet.

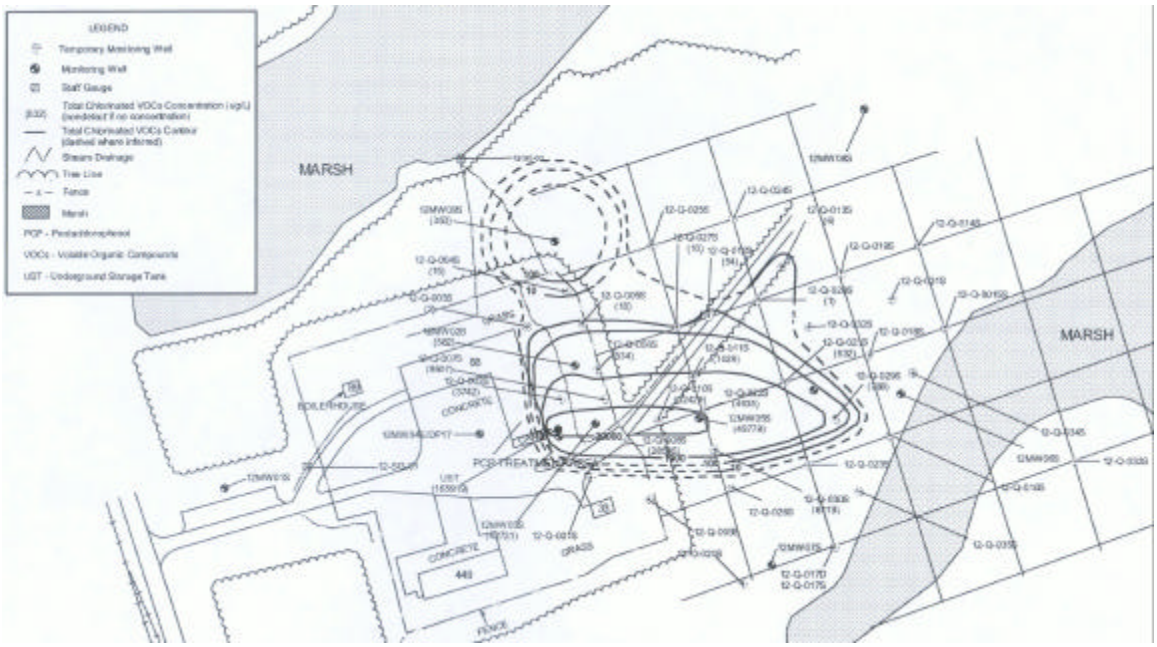

Figure 3. Concentration map of total chlorinated solvents in the upper surficial aquifer at the SWMU-12 site. The outer dashed contour line is zero concentration and the inner contour line is 30,000 micrograms per liter.

4.0 Experimental (CNWS)

The Solid Waste Management Unit 12 (SWMU-12) at the Charleston Naval Weapons Station offers some unique technical problems for applying the AVO technique to directly detect DNAPL. The site is located in a low swampy area where the water table is almost at land surface. Based on results from both the vertical seismic profiles (VSP) and a short experimental seismic reflection profile, it was determined by the project team that the shallow target could be imaged. The preliminary AVO models using velocities from the VSPs indicated that there would be an amplitude versus offset anomaly (AVO) if dense non-aqueous phase liquids (DNAPL) either completely or partially replaced the water within the pore spaces. Using the plume map (Figure 3) as a guide, three seismic profiles were located in such a manner so as to accomplish the two objectives (Figure 1).

4.1 Seismic Reflection Data (CNWS)

4.1.1 Vertical Seismic Profile (VSP) Data Acquisition

Vertical seismic profiles were collected in wells 12MW-01D, 12MW-05D, and 12MW-10S at the Charleston Naval Weapons Station (SWMU-12). These data include both compressional wave (p) (12MW-01D, 12MW-05D, 12MW-10S) and shear wave (s) (12MW-01D) recordings. The VSPs were collected to provide information on the subsurface p and s-wave velocity field of the geologic strata at and above the known

DNAPL contamination (Figures 5-8). The velocity information was used to construct seismic models to investigate the probable amplitude versus offset (AVO) response that would be recorded by the surface seismic survey. In addition, the subsurface velocity information is needed to perform high-fidelity ties between the surface seismic profiles and the borehole lithology picks. The velocity versus depth information obtained from the VSPs can be used to convert interpretations made on the seismic data to depth.

Seismic recordings were made at 1 meter increments from the bottom of the borehole to approximately 1 meter below land surface using a three geophone (1 vertical, 2 horizontal) Geostuff sonde and an 8 lb. sledgehammer source. For p-wave acquisition a vertical steel cylinder was placed on the ground and struck four to eight times. Each hit was vertically summed to the preceding hits in the seismograph and written to disk as a single record for each level. For s-wave acquisition strike plates were mounted on the ends of an 8 ft horizontal plank and a truck was driven on to the plank to couple the plank to the ground. Each end of the plank was struck six to eight times, first from one side of the vehicle and then the other. The summed records for each source orientation were written to disk separately for each level.

Because of the relatively shallow depths of investigation and the critical need to have reliable subsurface velocity information, the p-wave VSPs from wells 12MW-01D, and 12MW-05D were logged multiple times with different seismographs and slightly different recording parameters. The recording parameters for each VSP are summarized in the Table 1.

Table 1. Summary of VSP recording parameters (CNWS).

	12MW-01D	**12MW-05D**	**12MW-10S**	**18CC-Q1**
No. of VSP runs	3 P, 1 S	2 P, 0 S	2 P, 0 S	3 P, 1 S
Recorded depth p-wave (m from TOC)	1-12	1-14	1-5	1-31, 1-51,1-15
Recorded depth s-wave (m from TOC)	1-12	.	.	1-31
Source offset p-wave (m)	2.0-0.55, 2.0-0.55, 2.0	2.0-0.55, 2.0	0.55, 1.0-0.55	2.5-1.5, 2.0,2.0
Source offset s-wave (m)	1.82	.	.	2.5
No. of source hits p-wave	4, 8, 8	8	8	8
No. of source hits s-wave	(6,6)	.	.	(8,8)
Depth increment (m)	1	1	1	1
Sample rate p-wave (ms)	0.125, 0.125, .02833	0.125, 0.021	0.125, 0.125	0.125,0.0283,0.02833
Sample rate s-wave (ms)	0.125	.	.	0.125
Record length p-wave (ms)	200	200	200	200
Record length s-wave (ms)	200	.	.	400
Seismograph	Seistronix RAS-24 (P 1, 2 & S) Geometrics Geode (P 3)	Seistronix RAS-24 (P 1) Geometrics Geode (P 2)	Seistronix RAS-24	Seistronix RAS-24 (P 1 & S) Geometrics Geode (P 2, 3)

4.1.2 Vertical Seismic Profile (VSP) Data Processing

The generalized data processing flow for the VSP data appears below (Figure 4). The PC-based VISTA seismic processing software (Seismic Image Software, Ltd.) was used to process the data. In the field some rudimentary data processing was performed for QA/QC purposes using VISTA. The field QA/QC ensured that usable data were recorded. The field data processing also revealed that no usable VSP data could be obtained from borehole 12MW-10S.

First arrival times were picked on the p-wave records and the better of the two channels on the s-wave records. These times were corrected for source offset from the borehole to true vertical travel time (TVT), or zero-offset time, using a straight raypath assumption. The velocity profile, average velocity, and interval velocity for each borehole was computed (Figures 5 through 8) using the data presented in Tables 2 through 5. The average velocity (total depth divided by total time) from the surface to the recording depth was used to convert recording time to depth. The interval velocity, or velocity of the material between recording levels, is an approximate indicator of lithologic changes in the borehole.

For correlation to the surface seismic data displays of the up-going wavefield data were shifted to two-way reflection time (twice TVT) and narrow (3-10 trace) front corridor stacks were produced. Because the time-depth relationship for the front corridor stack is known, the depth to the reflectors in the subsurface can be determined.

On the following pages are the data tables and interval velocity curves from the best VSP profiles, p-wave and s-wave, recorded in wells 12MW-01D and 12MW-05D. Near the surface the pick times are unreliable because the seismic raypath is not favorably oriented with respect to the geophone. Thus, no velocity information is reported for the upper few meters of the borehole.

In well 12MW-05D it was possible to obtain s-wave information by processing first arrival information recorded on the shear wave geophones during the p-wave VSP. The s-wave velocities found were compared to those obtained in 12MW-01D to verify that valid s-wave velocities were computed.

Generalized Vertical Seismic Profile Data Processing Flow

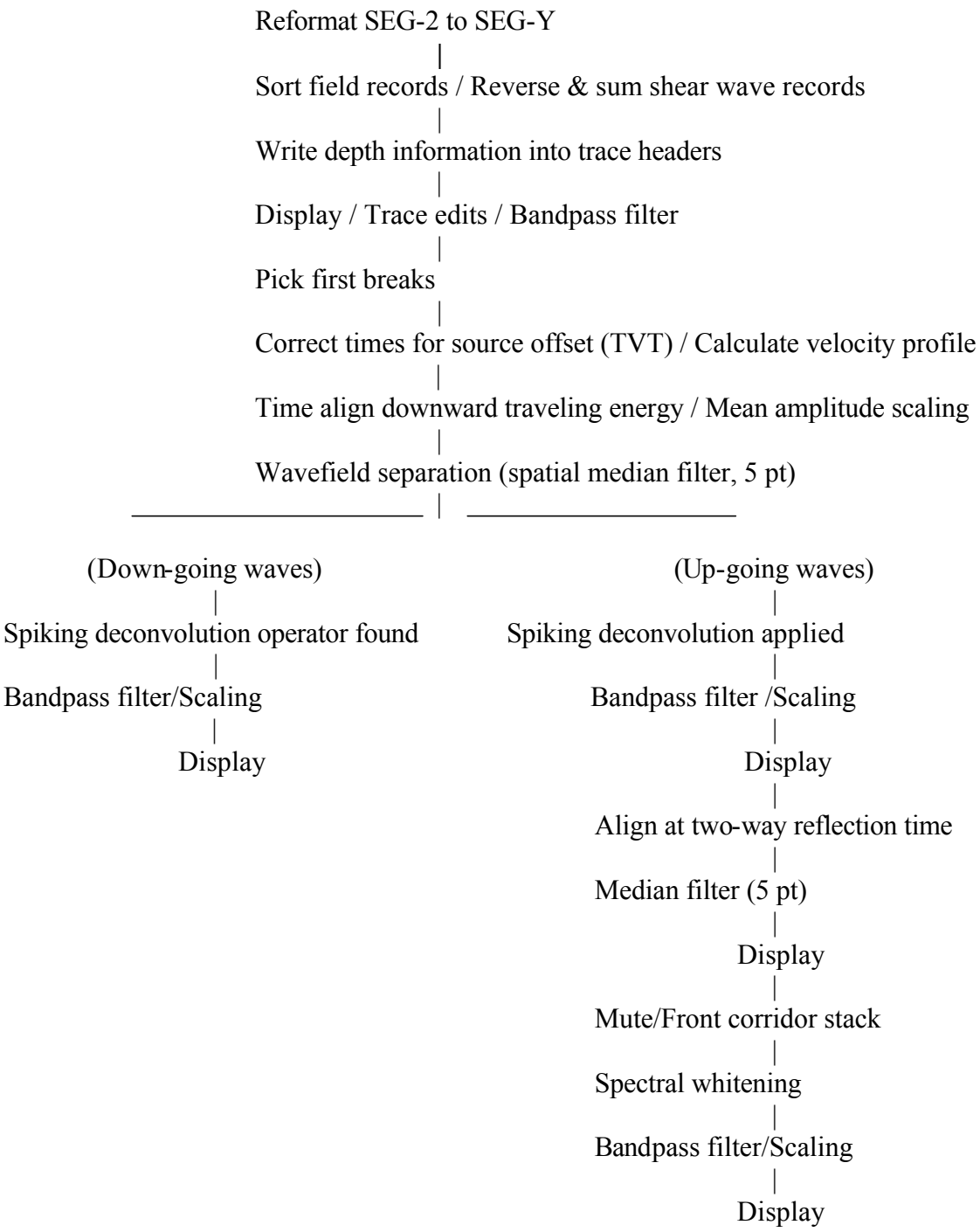

Figure 4. VSP data processing flow (CNWS).

Table 2. P-wave velocity table from well 12MW-01D

Well 12MW-01D

P-Wave Vertical Seismic Profile

GL = 2.52 m TOC = .60 m

(Offset = 2 m)

Seq. No.	Depth (TOC) (m)	Pick Time (ms)	Depth (GL) (m)	True Vertical Time (ms)	Average Velocity (ft/s)	Interval Velocity (ft/s)	Two-way Time (ms)	Gardner's Density (g/cc)
13	1	3.69	0.37	0.67	1808	1808	1.34	1.50
12	2	4.00	1.37	2.26	1988	2064	4.52	1.55
11	3	4.46	2.37	3.41	2281	2858	6.82	1.68
10	4	4.65	3.37	4.00	2765	5558	8.00	1.99
9	5	5.06	4.37	4.60	3116	5448	9.20	1.98
8	6	5.98	5.37	5.60	3144	3271	11.21	1.74
7	7	6.75	6.37	6.44	3245	3924	12.88	1.82
6	8	8.40	7.37	8.11	2983	1968	16.21	1.53
5	9	8.81	8.37	8.57	3205	7102	17.14	2.11
4	10	9.25	9.37	9.05	3398	6872	18.09	2.09
3	11	10.06	10.37	9.88	3444	3945	19.76	1.82
2	12	10.33	11.37	10.17	3667	11090	20.35	2.36

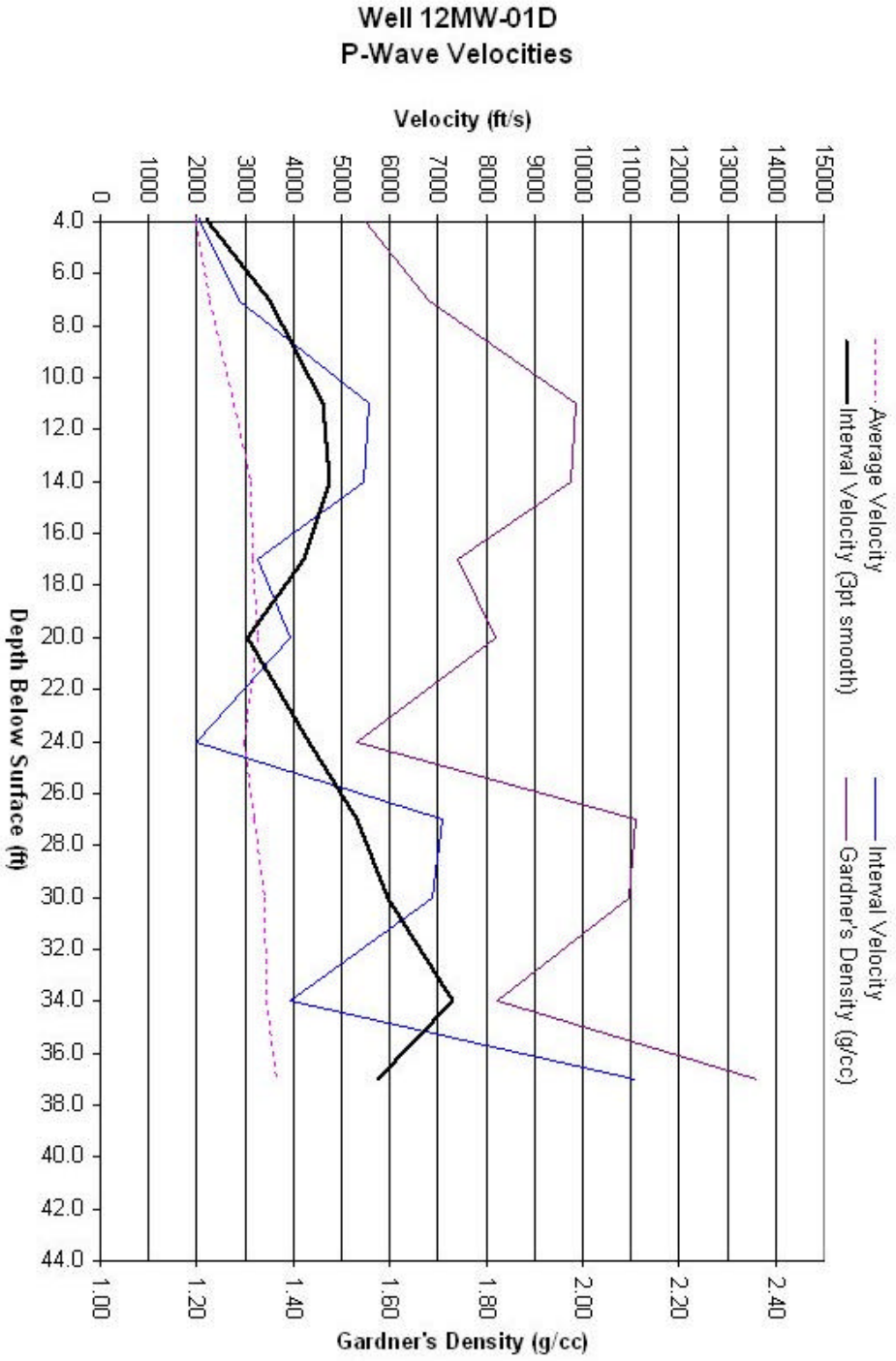

Figure 5. Graph of p-wave interval velocity, smoothed interval velocity, average velocity and Gardner's density derived from the p-wave velocity versus depth in well 12MW-01D.

Table 3. S-wave velocity table from well 12MW-01D

Well 12MW-01D

S-Wave Vertical Seismic Profile

GL 2.52 m TOC = 0.6 m

(Offset = 1.82 m)

Seq. No.	Depth (TOC) (m)	Pick Time (ms)	Depth (GL) (m)	True Vertical Time (ms)	Average Velocity (ft/s)	Interval Velocity (ft/s)	Two-way Time (ms)
12	1	14.85	0.40	3.19	412	412	6.38
11	2	15.00	1.40	9.15	502	551	18.29
10	3	16.00	2.40	12.75	618	911	25.50
9	4	20.50	3.40	18.07	617	616	36.15
8	5	29.85	4.40	27.58	523	345	55.17
7	6	37.25	5.40	35.30	502	425	70.60
6	7	43.40	6.40	41.74	503	509	83.49
5	8	49.90	7.40	48.46	501	489	96.91
4	9	55.95	8.40	54.68	504	527	109.36
3	10	61.40	9.40	60.28	512	586	120.56
2	11	65.10	10.40	64.13	532	853	128.25
1	12	70.35	11.40	69.47	538	614	138.94

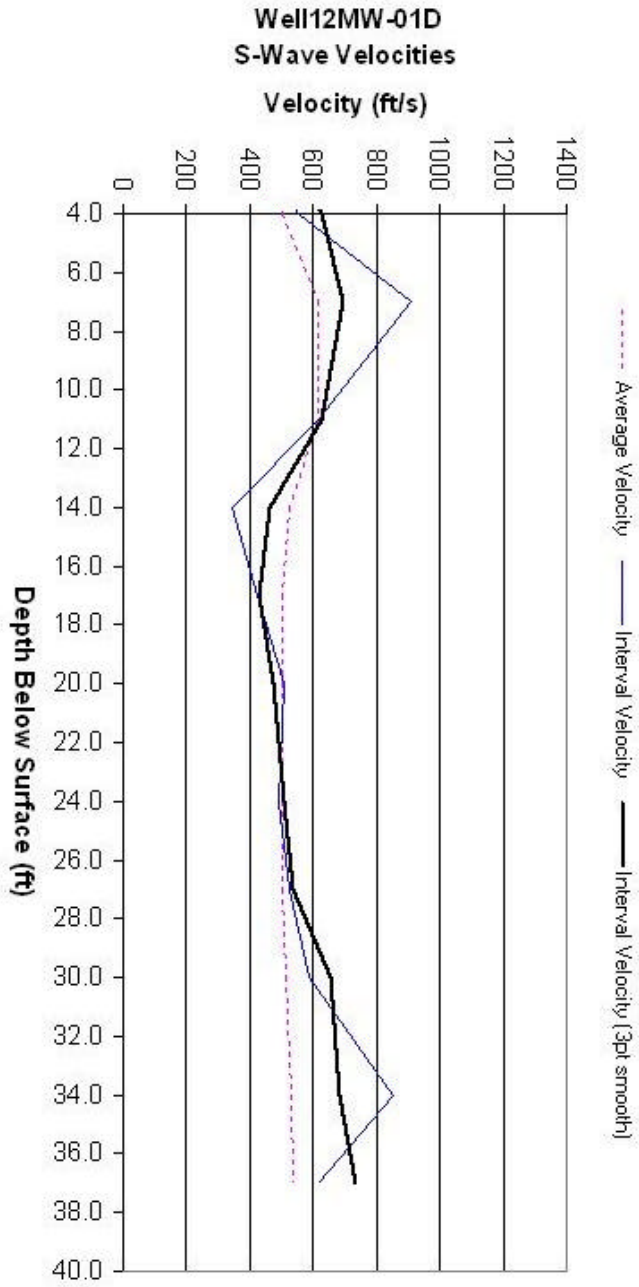

Figure 6. Graph of s-wave interval velocity, smoothed interval velocity, and average velocity versus depth in well 12MW-01D.

Table 4. P-wave velocity table from well 12MW-05D

Well 12MW-05D

P-Wave Vertical Seismic Profile

GL = 1.79 m TOC = 0.43 m

(Offset = 2 m)

Seq. No.	Depth (TOC) (m)	Pick Time (ms)	Depth (GL) (m)	True Vertical Time (ms)	Average Velocity (ft/s)	Interval Velocity (ft/s)	Two-way Time (ms)
10	5	8.750	4.57	8.02	1870	1870	16.03
9	6	9.750	5.57	9.18	1991	2827	18.35
8	7	10.250	6.57	9.81	2198	5213	19.61
7	8	10.630	7.57	10.28	2417	6956	20.55
6	9	11.500	8.57	11.20	2511	3559	22.40
5	10	12.250	9.57	11.99	2618	4143	23.98
4	11	13.130	10.57	12.90	2688	3605	25.80
3	12	13.880	11.57	13.68	2775	4227	27.35
2	13	14.630	12.57	14.45	2854	4255	28.90
1	14	15.130	13.57	14.97	2974	6309	29.94

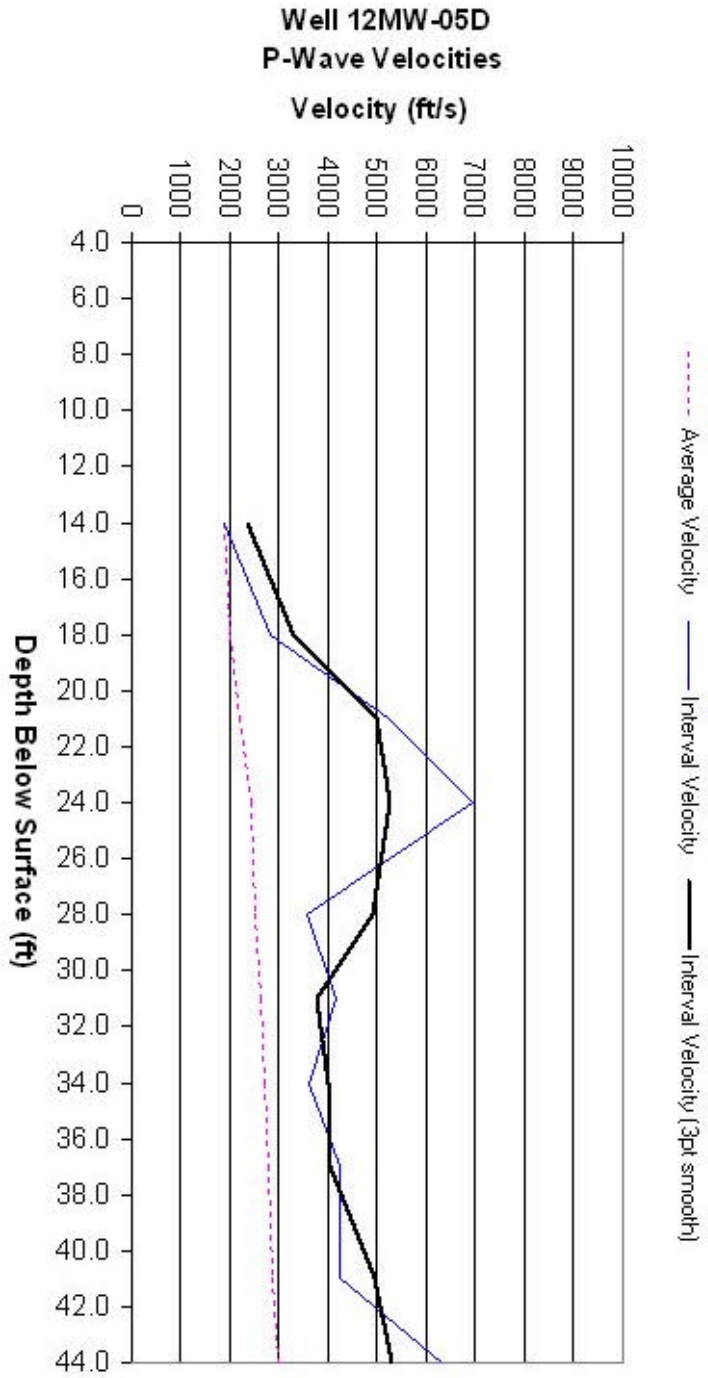

Figure 7. Graph of p-wave interval velocity, smoothed interval velocity, and average velocity versus depth in well 12MW-05D.

Table 5. S-wave velocity table from well 12MW-05D

Well 12MW-05D

S-Wave Vertical Seismic Profile

GL = 1.795 m TOC = 0.43 m

(Offset = 2 m, (5-14 m))
(Offset = 1 m, (3-4 m))
(Offset = 0.55 m, (1-2 m))

Seq. No.	Depth (TOC) (m)	Pick Time (ms)	Depth (GL) (m)	True Vertical Time (ms)	Average Velocity (ft/s)	Interval Velocity (ft/s)	Two-way Time (ms)
14	1	22.71	0.52	5.71	299	299	11.43
13	2	20.31	1.52	12.29	406	499	24.58
12	3	25.08	2.52	19.65	421	446	39.29
11	4	29.99	3.52	26.08	443	510	52.17
10	5	35.92	4.52	32.84	452	485	65.69
9	6	46.10	5.52	43.35	418	312	86.69
8	7	54.85	6.52	52.44	408	361	104.88
7	8	63.27	7.52	61.14	404	377	122.29
6	9	70.42	8.52	68.55	408	443	137.10
5	10	75.04	9.52	73.44	425	672	146.87
4	11	80.48	10.52	79.06	437	583	158.12
3	12	86.42	11.52	85.14	444	540	170.28
2	13	92.75	12.52	91.59	448	509	183.17
1	14	97.48	13.52	96.43	460	678	192.86

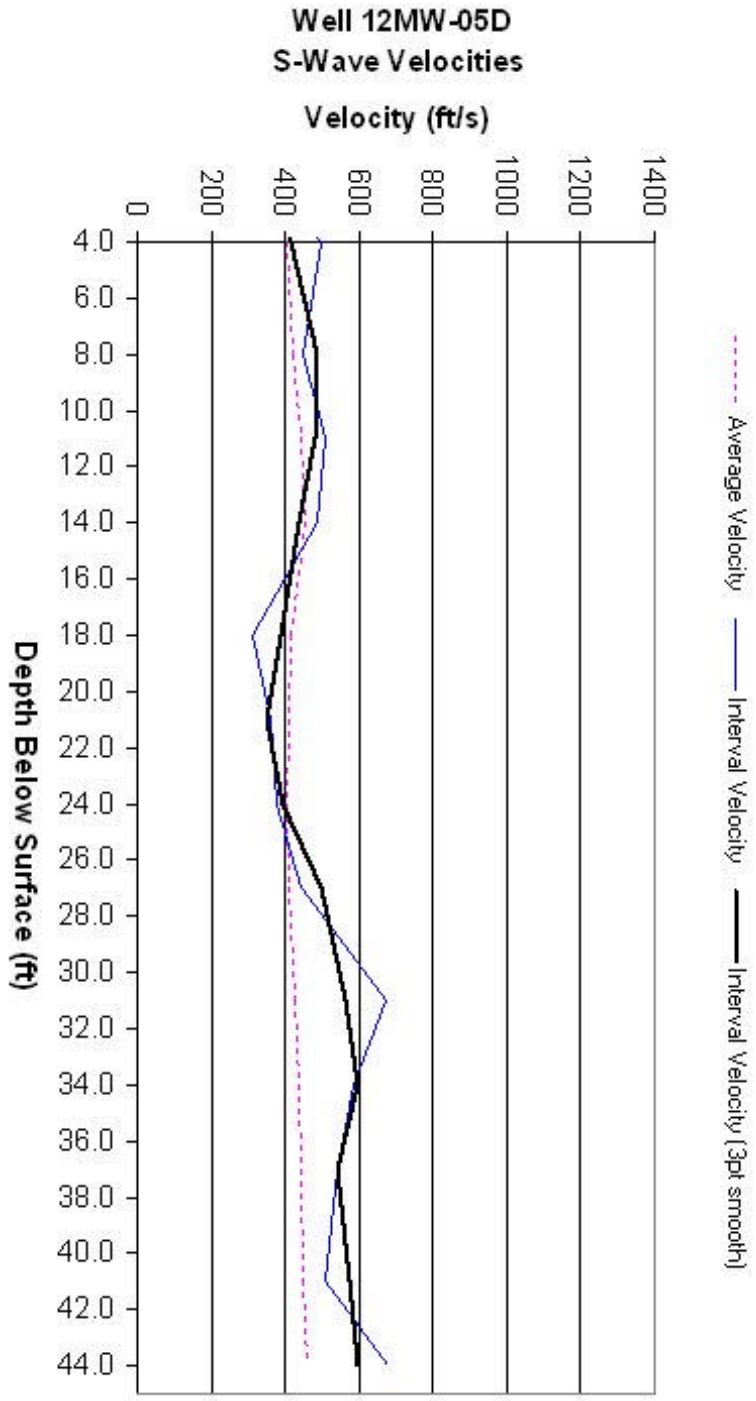

Figure 8. Graph of s-wave interval velocity, smoothed interval velocity, and average velocity versus depth in well 12MW-05D.

4.2 Amplitude Variation with Offset (AVO) Modeling (CNWS)

One of the most important aspects of AVO analysis to detect DNAPL is the AVO modeling. The modeling determines the background seismic amplitude response along an interface and the expected change, if any, in the reflection amplitude if the pore space fluid type or lithology changes along the interface.

The modeling conducted in this study is a two layer one-dimensional model of reflection coefficient versus incident angle. The p-wave reflection coefficients were calculated using the full Zoeppritz equations (1919) as modified by Graul, 2001. The input into the Zoeppritz equations were p-wave and s-wave velocities calculated from the VSPs and modified using the Gassmann (1951) theory of fluid saturated rocks and densities derived from calculations using the empirical Gardner and others (1974) relationship between p-wave velocity and density.

Based upon existing geologic and concentration data (Tetra Tech NUS, 2000), the DNAPL is accumulating and confined to a sand layer (referred to as Unit 2) overlying a sandy clay unit (referred to as Unit 3). Using the physical parameters listed in Table 6 three scenarios were modeled (Figure 9). Fluid saturation in the pores is assumed to be 100 percent and porosity 35 percent.

The first scenario was to determine the background characteristic of the reflection coefficient versus offset if the pore spaces of both units are water filled (long dashed line, Figure 9). The second scenario is to replace water in the pore spaces in the Unit 1 sand with DNAPL (solid line, Figure 9). The third scenario is to replace the water in the pore spaces in both units with DNAPL (short dash line, Figure 9).

It appears that if the pore spaces are water filled, the reflection coefficient is slightly negative until approximately 60^0 of incident angle where it becomes more negative (Figure 9). Based upon the two scenarios where DNAPL replaces water in the pore spaces there appears to be an AVO anomaly (Figure 9). Scenario one: if DNAPL is present only in Unit 1 sand the reflection coefficient is slightly negative on the near offsets until approximately 30^0 of incident angle at which point the reflection coefficient becomes positive. Scenario two: if both the Unit 1 sand and the underlying Unit 2 sandy clay have DNAPL replacing water in the pore spaces the reflection coefficient begins negative, well below that of the water filled case, and becomes more negative at about 20^0 of incident angle.

Table 6. List of parameters used in the AVO modeling (CNWS).

Lithology	Density (g/cc)	P-Wave m (ft/sec)	S-Wave m (ft/sec)
Unit 1 Sand	1.99	1694 (5558)	188 (616)
Unit 1 Sand with DNAPL	2.36	1450 (4755)	172 (564)
Unit 2 Sandy Clay	1.98	1661 (5448)	105 (345)
Unit 2 Sandy Clay with DNAPL	2.36	1419 (4655)	96 (315)

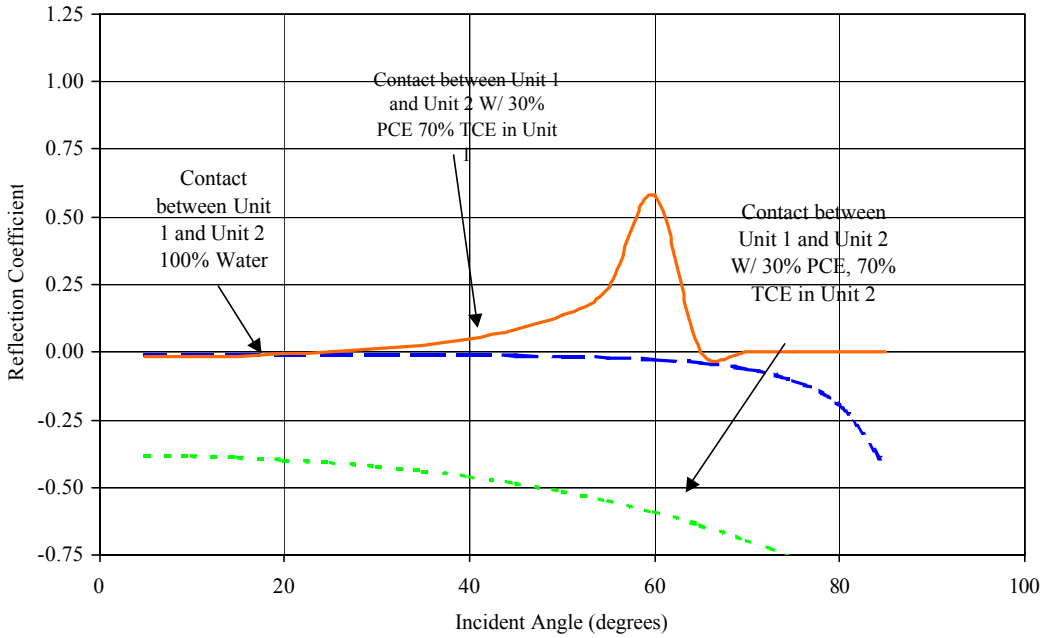

Figure 9. Amplitude variation with offset models (CNWS). AVO models generated using the full Zoeppritz equations.

4.3 Seismic Reflection Profiles (CNWS)

4.3.1 Seismic Reflection Acquisition

To evaluate the recording parameters needed to optimally image the target geologic horizons at the Charleston Naval Weapons Station SWMU-12, a test seismic reflection profile was recorded. Because target depths are shallow, 10-40 feet, adequate spatial sampling of the seismic wave field is critical. In addition, high frequency seismic wave energy must be generated and recorded to be able to resolve closely spaced reflectors.

The test line was recorded using a 24 channel recording system utilizing single 100 Hz geophones at two foot station spacing. The recording geometry was off-end with a 1 or 2 foot near offset. Source points were positioned at one foot station spacing on the half station so that tests could be done to process the data as either one foot or half foot CMP spacing to evaluate spatial resolution requirements. The line was first recorded using an 8 lb. sledgehammer source, then partly re-recorded using a 4 lb. sledgehammer source. This later test was done because a smaller seismic source can generate higher frequency waves needed for high resolution.

The results of the test profile indicated that quality seismic reflection data could be obtained from the target horizons. Ambient noise was not a problem, although acoustic echoes were recorded off of buildings and infrastructure. Ground roll was a concern, but could be adequately dealt with via two dimensional filtering techniques. Furthermore, to image the shallow reflectors of interest with sufficient subsurface redundancy for structural

mapping and AVO analysis, source and receiver spacing of one foot was indicated. In addition, the smaller 4 lb. hammer yielded higher frequency data without loss of imaging the horizons of interest.

Based upon the results of the test profile and seismic AVO modeling, the parameters for acquisition of the production seismic lines were determined. The seismic lines were recorded using a 60 channel recording system utilizing single 100 Hz geophones at one foot station spacing. The recording geometry was off-end with 1.5 feet near offset and 60.5 feet far offset. Source points were positioned at one foot station spacing on the half station to yield nominal 30 CMP fold data. A 4 lb. Sledgehammer was used for a seismic source and six blows per source point were stacked and recorded. The parameters used to record the seismic data are listed in the table below.

Table 7. Seismic reflection profile recording parameters (CNWS)

Type of survey	P-wave seismic reflection
Date recorded	March 26-30, 2001
Station interval	1 foot
Source	4 lb. Hammer, 6 hits per station
Source interval	1 foot on half stations
Record Length	500 milliseconds
Recording instrument	Geometrics Strataview 24 bit A/D resolution
Number of channels	60
Instrument Gain	24 dB fixed
Sample interval	0.25 millisecond
Data format	SEG-2
Data redundancy	30 fold max
Geophones	Geospace 100 Hz vertical one per station
Near offset	1.5 feet
Far offset	60.5 feet
Cable Geometry (ft)	SP------1.5'------60.5'

4.3.2 Seismic Reflection Data Processing

After completion of the field survey extensive detailed seismic data processing was performed at ESRI-USC's Environmental Geophysics Laboratory on the campus of the University of South Carolina. To process the data the Landmark Graphics Corp. ProMAX software operational on a Sun Microsystems Ultra-60 workstation was used. The generalized flow used to process the data is shown in Figure 10. Overall data quality is excellent with a dominant frequency after data processing of approximately 500 Hz (Figure 11). For study of AVO effects, additional sets of CMP gathers were generated without scaling.

Two of the data processing steps deserve special mention. Although the water table is very shallow at the site, it was found that the near surface has considerable lateral velocity variation. Application of refraction statics was absolutely essential to account for the velocity variation. Without refraction statics it is doubtful whether the shallowest reflections would have stacked coherently and the stacked data overall would have had the high frequency content that it ultimately did.

The other data processing step that had significant impact on the data quality is the application of long-offset NMO corrections to the data. These corrections are not commonly applied to shallow data. The NMO correction commonly applied to seismic reflection data is derived from a two term mathematical formula that describes a hyperbolic travel-time curve. This correction is valid only for short offsets where the reflector depth is less than the source to receiver offset. In addition, there is an implicit assumption of an isotropic medium. At larger offsets and with the addition of anisotropy (multi-layering) the travel-time curve deviates from a hyperbola. In this case the application of conventional NMO corrections can lead to loss of effective fold (via larger mutes than necessary) and a degraded stack (less fold and incomplete moveout correction). The vast majority of seismic data are collected so that the "short offset" assumption is valid.

The seismic survey at CNWS recorded offsets to 60.5 feet. This maximum offset was needed to record AVO responses. For reflections from reflectors shallower than 18.4 m (60.5 feet) and particularly for those reflectors shallower than about 30 feet, the small offset assumption is not valid. Application of conventional NMO and stretch mute truncates the number of traces to be stacked in the CMP gather more than necessary.

Within the ProMAX software modules exist to apply "third-term" or "long-offset" NMO corrections. The method developed by Tsvankin and Thomsen (1994) was applied to the CNWS data set. The application of the long-offset NMO correction improved the imaging of shallow reflections occurring 20 ms and earlier.

For interpretation purposes the sections are displayed at a datum of 7 feet .

SEISMIC DATA PROCESSING FLOW

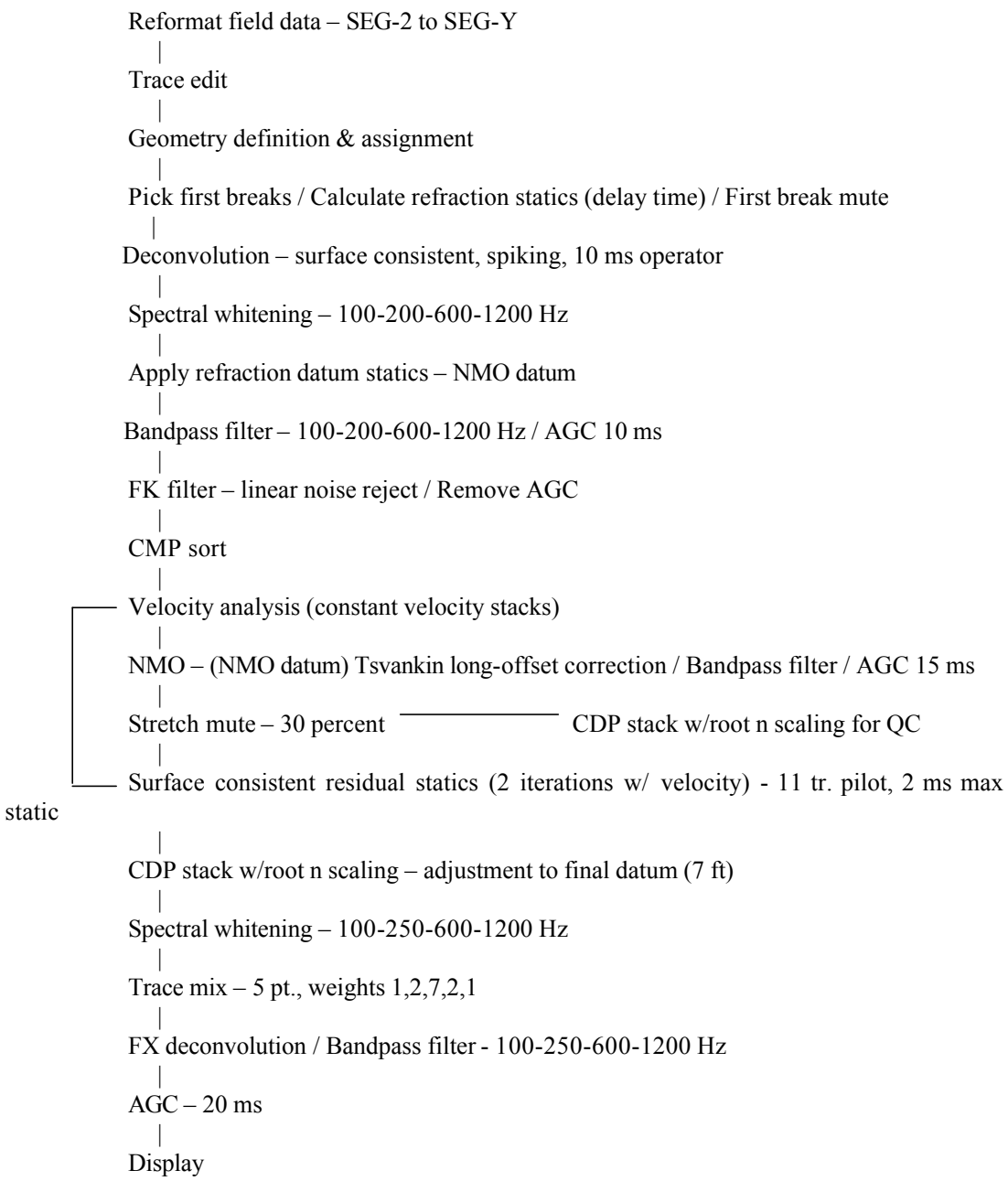

Figure 10. Data processing sequence for CNWS seismic lines.

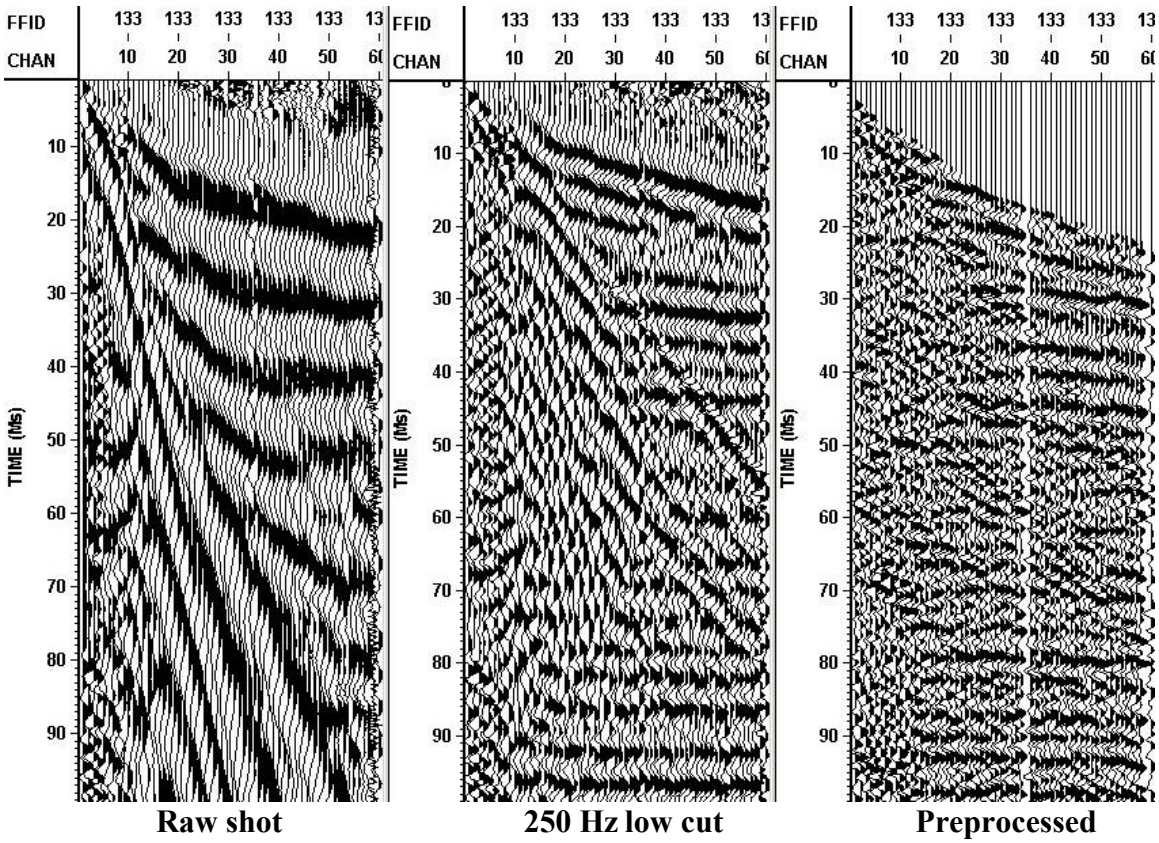

Figure 11. Shot record from line CNWS-1. Note frequency content of the data. AGC 15 ms.

4.4 Seismic Reflection Data (DUS)

4.4.1 Vertical Seismic Profile (VSP) Data Acquisition

A compressional wave (p) vertical seismic profile was collected in well DUS-10 to obtain information on the subsurface velocity field of the geologic strata at and above the known DNAPL contamination. These data were used to construct seismic models to investigate the probable amplitude versus offset (AVO) response that would be recorded by the surface seismic survey. In addition, the subsurface velocity information was needed to perform high-fidelity ties between the surface seismic profile and the borehole lithology picks. The velocity versus depth information obtained from the VSPs was used to convert interpretations made on the seismic data to depth.

Seismic recordings were made at one meter increments from near the bottom of the well (49 m) to approximately two meters below land surface using a three geophone (1 vertical, 2 horizontal) Geostuff sonde and an 8 lb. sledge hammer source. A Geometrics seismograph recorded 500 ms of data at a 0.25 ms sample rate. For data acquisition a vertical steel cylinder was placed on the ground 6.4 meters from the borehole and struck eight times. Each hit was vertically summed to the preceding hits in the seismograph and written to disk as a single record for each level. The recording parameters for the VSP are summarized in Table 8.

Table 8. Summary of VSP recording parameters (DUS).

	DUS-10
Date recorded	5/25/2000
VSP type	P-wave
Recorded depth (m from TOC)	2-49
Sonde	Geostuff 3-component borehole geophone
Source offset P wave (m)	6.4
Source	8 lb. hammer
No. of hits	8
Depth increment (m)	1
Sample rate (ms)	0.25
Record length (ms)	500
Seismograph	Geometrics Strataview RX

4.4.2 Vertical Seismic Profile (VSP) Data Processing

The generalized data processing flow of the VSP data appears in Figure 12. Examination of the raw VSP data shows good p-wave first arrivals and clear shear wave shear (s) arrivals on the horizontal geophone channels even though a shear wave source was not used (Figure 13).

P-wave first arrival times were picked on the vertical geophone records and s-wave first arrivals were picked on the better of the two horizontal geophone channels. These times were corrected for source offset from the borehole to true vertical travel time (TVT), or zero-offset time, using a straight raypath assumption. The velocity profile, average velocity and interval velocity, was computed (Figures 14 and 16). The s-wave velocities computed are comparable to shear wave velocities determined elsewhere in M-Area, which supports their identification.

The average velocity (total depth divided by total time) from the surface to the recording depth is used to convert recording time to depth. The interval velocity, or velocity of the material between recording levels, is an approximate indicator of lithologic changes in the borehole. For correlation to the surface seismic data a display of the up-going wavefield data shifted to two-way reflection time (twice TVT) and a front corridor stack was produced (Figure 15). Because the time-depth relationship for the front corridor stack is known, the depth to the reflectors in the subsurface can be calculated.

Generalized Vertical Seismic Profile Data Processing Flow

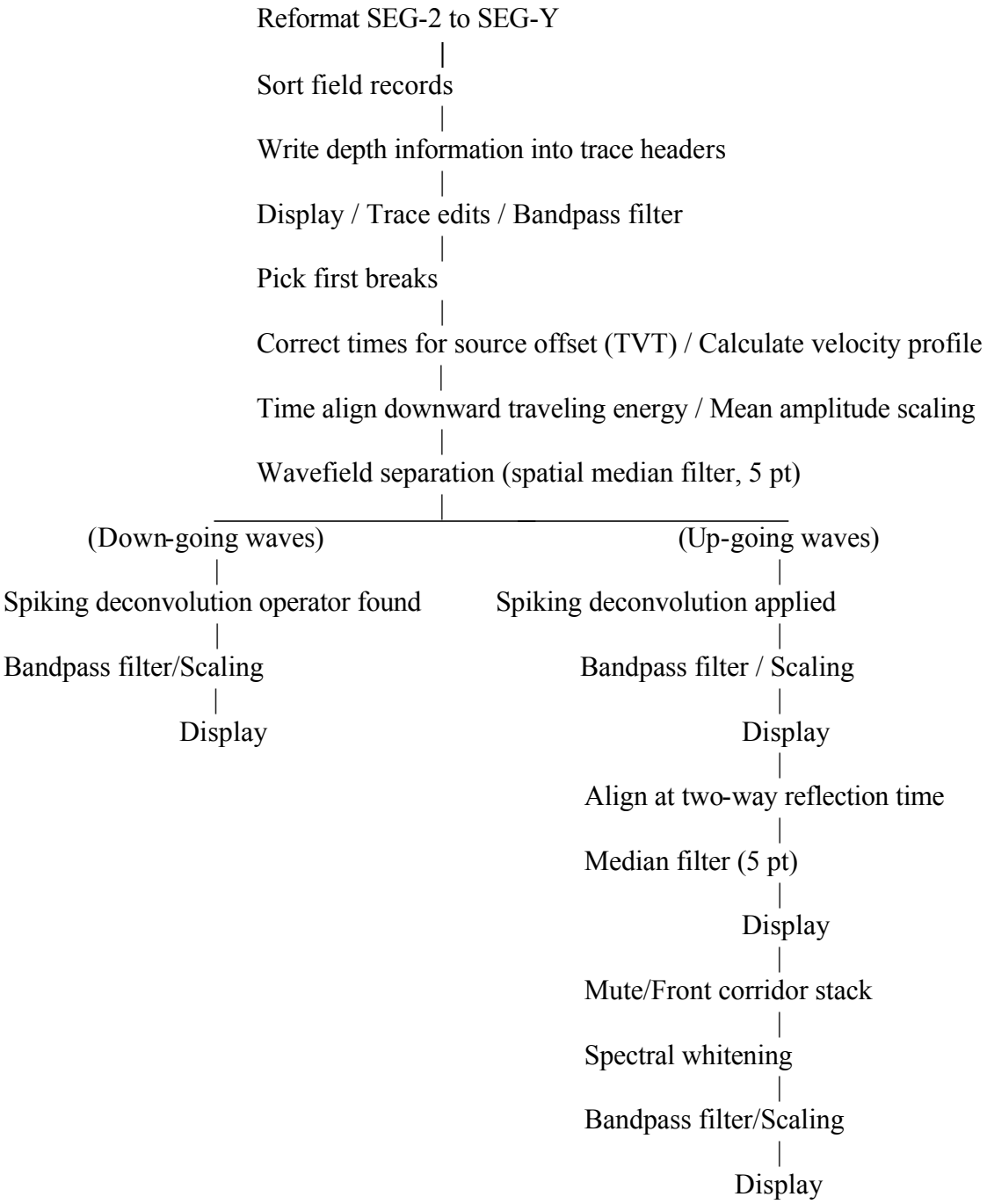

Figure 12. VSP data processing flow.

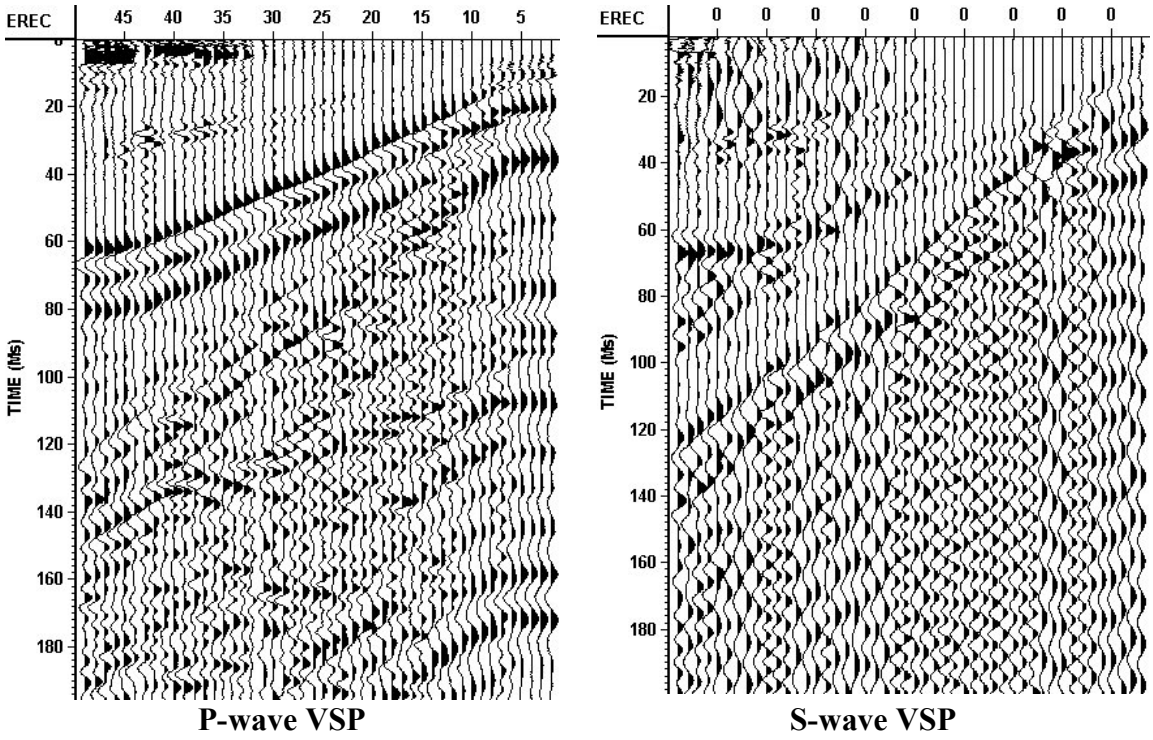

Figure 13. Raw vertical seismic profile data from well DUS-10. Note that the first arrival times of the P-wave VSP flatten near the bottom of the borehole indicating high interval velocity of the saturated zone. The depth where the break in slope occurs is the top of the water table. The S-wave VSP shows no corresponding slope break because S-waves are mostly unaffected by pore fluids. Display gain 50 ms AGC.

Table 9. P-wave velocity table from well DUS-10.

Well DUS-010

P-Wave Vertical Seismic Profile

GL = - m TOC = .72 m

(Offset = 6.4 m)

Seq. No.	Depth (TOC) (m)	Pick Time (ms)	Depth (GL) (m)	True Vertical Time (ms)	Average Velocity (ft/s)	Interval Velocity (ft/s)	Two-way Time (ms)
48	2	14.10	1.28	2.76	1519	1519	5.53
47	3	14.10	2.28	4.73	1581	1668	9.46
46	4	14.10	3.28	6.43	1674	1931	12.86
45	5	14.20	4.28	7.89	1779	2243	15.79
44	6	14.10	5.28	8.97	1931	3040	17.94
43	7	14.40	6.28	10.08	2043	2949	20.17
42	8	15.00	7.28	11.26	2120	2780	22.53
41	9	16.00	8.28	12.66	2146	2354	25.32
40	10	17.60	9.28	14.49	2101	1793	28.98
39	11	19.10	10.28	16.21	2080	1901	32.43
38	12	21.40	11.28	18.61	1988	1368	37.22
37	13	22.50	12.28	19.95	2019	2448	39.90
36	14	23.60	13.28	21.26	2049	2510	42.52
35	15	25.30	14.28	23.09	2029	1795	46.17
34	16	26.70	15.28	24.63	2036	2131	49.25
33	17	27.80	16.28	25.87	2064	2634	51.74
32	18	29.10	17.28	27.29	2078	2317	54.58
31	19	30.40	18.28	28.69	2090	2337	57.38
30	20	31.10	19.28	29.52	2143	3982	59.03
29	21	33.50	20.28	31.95	2083	1350	63.89
28	22	34.90	21.28	33.42	2089	2225	66.84
27	23	36.20	22.28	34.79	2101	2392	69.59
26	24	37.30	23.28	35.97	2124	2798	71.93
25	25	38.70	24.28	37.42	2129	2253	74.84
24	26	39.90	25.28	38.68	2144	2608	77.36
23	27	41.00	26.28	39.84	2164	2838	79.67
22	28	42.20	27.28	41.08	2178	2627	82.17
21	29	43.20	28.28	42.13	2202	3125	84.27
20	30	44.20	29.28	43.18	2225	3136	86.36
19	31	45.50	30.28	44.52	2232	2456	89.03
18	32	46.70	31.28	45.75	2243	2655	91.50
17	33	48.00	32.28	47.08	2249	2464	94.17
16	34	48.90	33.28	48.02	2274	3503	96.04
15	35	50.40	34.28	49.54	2270	2153	99.09
14	36	51.80	35.28	50.97	2271	2304	101.94

13	37	53.10	36.28	52.29	2276	2477	104.58
12	38	54.30	37.28	53.52	2285	2679	107.03
11	39	55.40	38.28	54.64	2298	2918	109.28
10	40	56.30	39.28	55.57	2319	3544	111.13
9	41	57.30	40.28	56.59	2335	3207	113.18
8	42	58.70	41.28	58.01	2335	2316	116.01
7	43	59.40	42.28	58.73	2362	4532	117.46
6	44	60.90	43.28	60.24	2357	2167	120.49
5	45	.	44.28	.	.	.	.
4	46	62.10	45.28	61.49	2416	5275	122.98
3	47	62.50	46.28	61.91	2453	7775	123.82

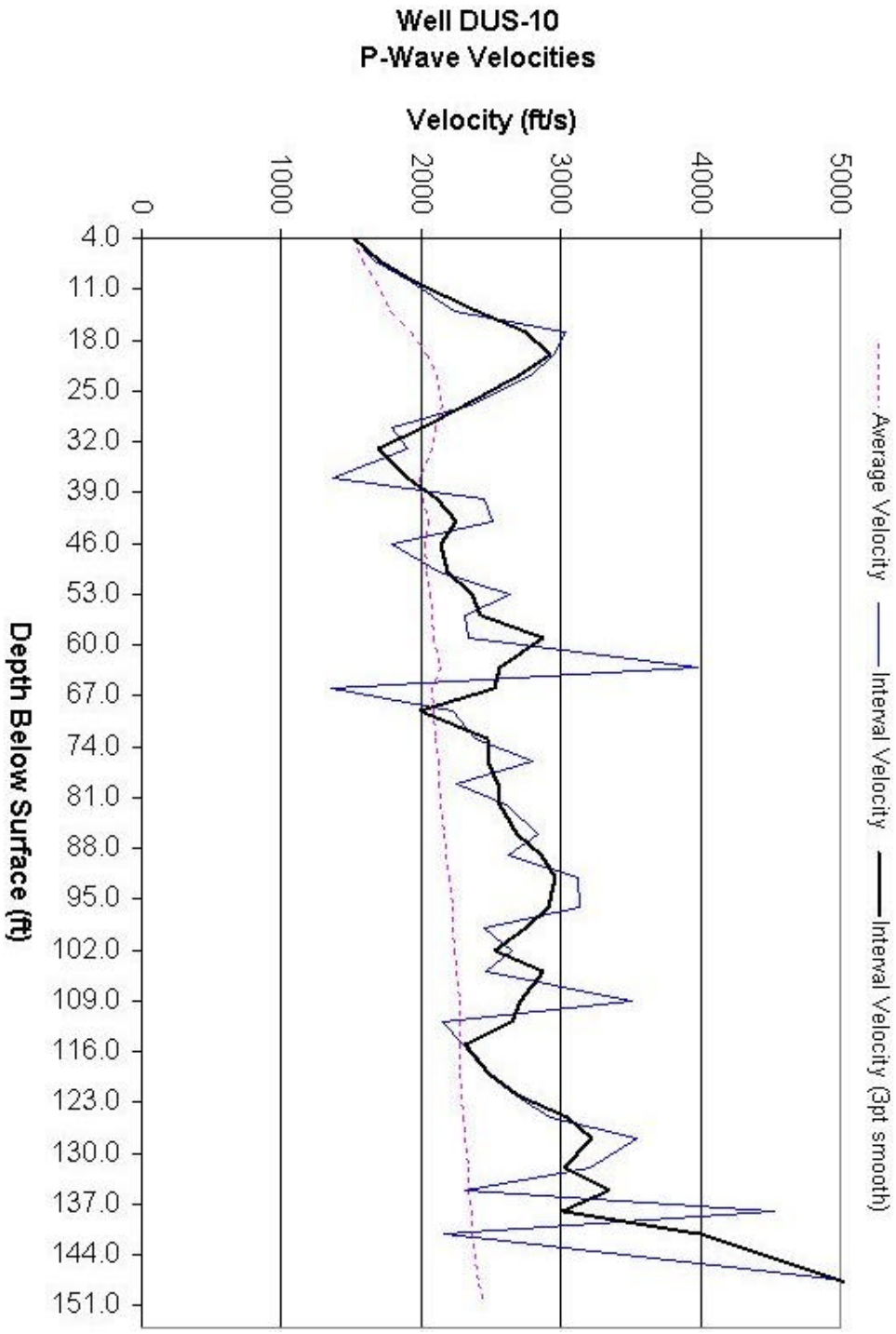

Figure 14. Graph of p-wave interval velocity, smoothed interval velocity and average velocity versus depth in borehole DUS-010.

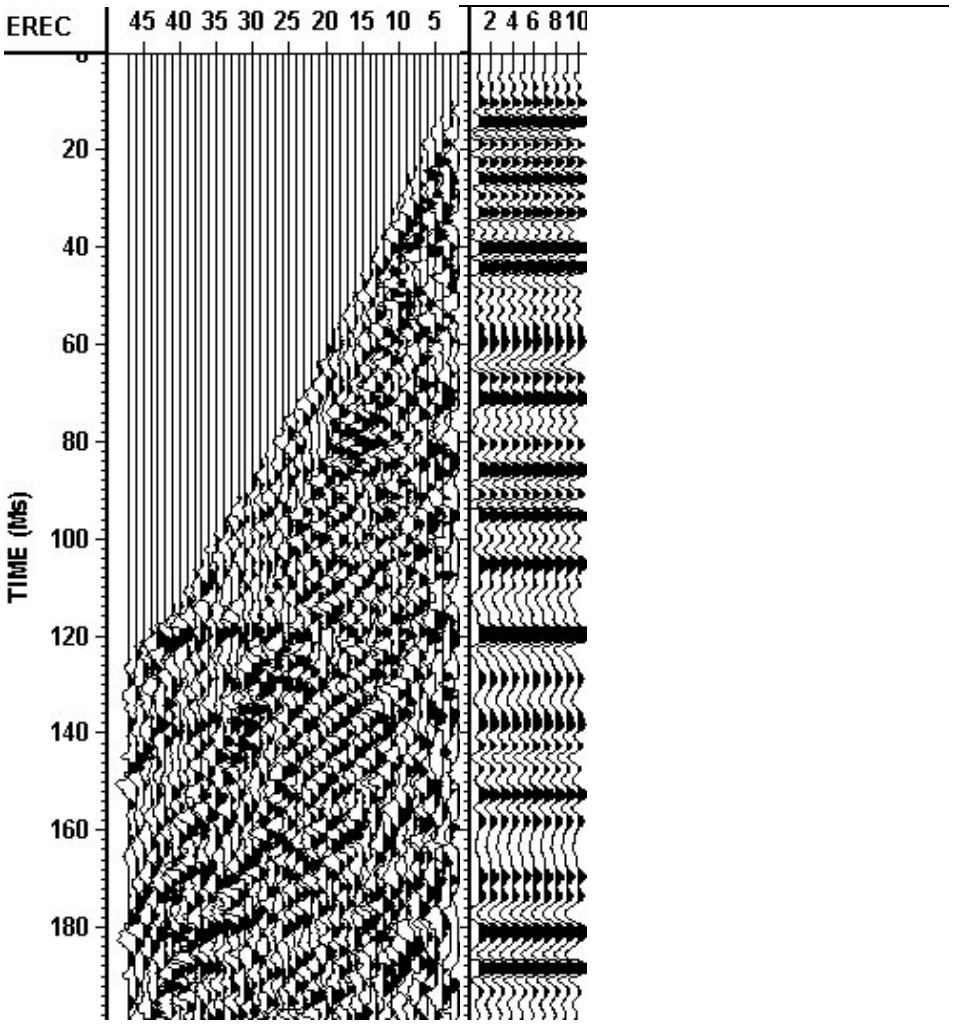

Figure 15. Display of upgoing wavefield and front corridor stack well DUS-10. The front corridor stack can be correlated to the surface seismic data to find the depth to the reflector.

Table 10. S-wave velocity table from borehole DUS-10.

Well DUS-010

S-Wave Vertical Seismic Profile

GL = 0 m TOC = .72 m

(Offset = 6.4 m)

Seq. No.	Depth (TOC) (m)	Pick Time (ms)	Depth (GL) (m)	True Vertical Time (ms)	Average Velocity (ft/s)	Interval Velocity (ft/s)	Two-way Time (ms)
48	2	12.70	1.28	2.49	1686	1686	4.98
47	3	13.10	2.28	4.40	1702	1722	8.79
46	4	14.40	3.28	6.57	1639	1511	13.13
45	5	14.60	4.28	8.12	1730	2119	16.23
44	6	16.70	5.28	10.63	1630	1306	21.25
43	7	17.40	6.28	12.19	1691	2104	24.37
42	8	18.60	7.28	13.97	1710	1840	27.94
41	9	20.90	8.28	16.54	1643	1278	33.07
40	10	24.00	9.28	19.76	1541	1019	39.51
39	11	27.10	10.28	23.01	1466	1010	46.01
38	12	31.40	11.28	27.31	1355	762	54.62
37	13	34.90	12.28	30.95	1302	902	61.90
36	14	37.90	13.28	34.14	1276	1028	68.28
35	15	40.90	14.28	37.32	1255	1031	74.64
34	16	43.50	15.28	40.12	1249	1172	80.24
33	17	45.40	16.28	42.25	1264	1541	84.50
32	18	48.20	17.28	45.20	1254	1113	90.40
31	19	50.90	18.28	48.04	1248	1155	96.08
30	20	53.10	19.28	50.40	1255	1393	100.79
29	21	56.00	20.28	53.40	1246	1091	106.81
28	22	58.60	21.28	56.12	1244	1209	112.23
27	23	61.00	22.28	58.63	1247	1306	117.26
26	24	63.30	23.28	61.04	1251	1363	122.07
25	25	66.60	24.28	64.40	1237	975	128.80
24	26	68.50	25.28	66.40	1249	1637	132.81
23	27	70.50	26.28	68.50	1259	1568	137.00
22	28	73.10	27.28	71.17	1258	1229	142.33
21	29	74.60	28.28	72.76	1275	2060	145.52
20	30	76.50	29.28	74.74	1285	1661	149.47
19	31	.	30.28	.	.	.	.
18	32	82.70	31.28	81.02	1267	1044	162.04
17	33	84.50	32.28	82.89	1278	1759	165.77
16	34	86.90	33.28	85.34	1279	1339	170.67
15	35	89.70	34.28	88.18	1275	1155	176.35
14	36	91.80	35.28	90.33	1281	1526	180.65

13	37	.	36.28	.	.	.	.
12	38	96.70	37.28	95.31	1283	1318	190.61
11	39	98.70	38.28	97.35	1290	1606	194.70
10	40	100.50	39.28	99.19	1299	1780	198.38
9	41	102.00	40.28	100.74	1312	2124	201.47
8	42	105.20	41.28	103.96	1303	1018	207.92
7	43	107.80	42.28	106.59	1301	1249	213.17
6	44	110.30	43.28	109.11	1301	1298	218.23
5	45	112.90	44.28	111.74	1300	1250	223.48
4	46	115.30	45.28	114.16	1301	1352	228.33
3	47	118.00	46.28	116.89	1299	1205	233.77
2	48	120.50	47.28	119.41	1299	1300	238.82
1	49	122.10	48.28	121.04	1309	2013	242.08

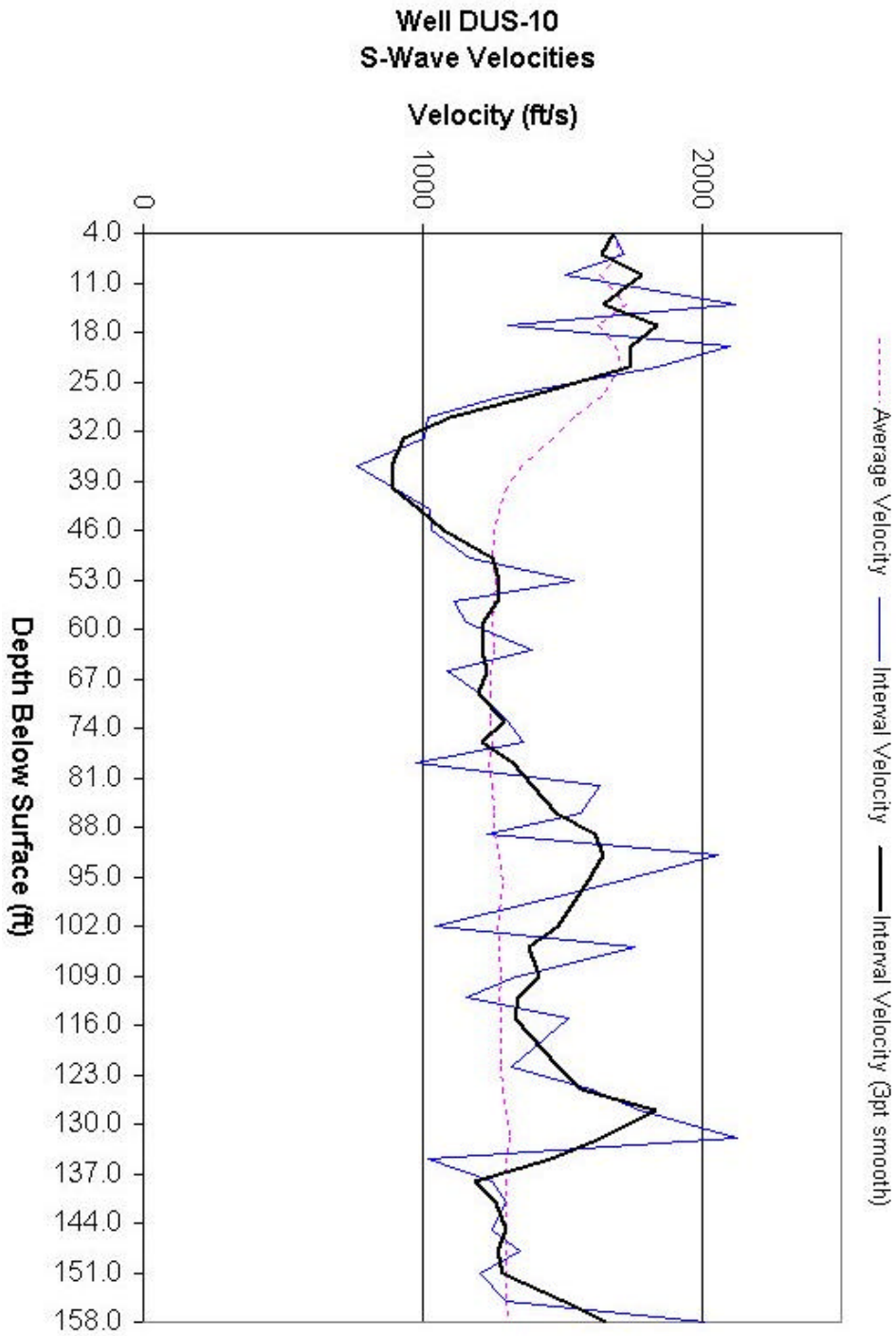

Figure 16. Graph of s-wave interval velocity, smoothed interval velocity, and average velocity versus depth in well DUS-10.

4.5 Amplitude Variation with Offset (AVO) Modeling DUS

The most important aspect to this study is the AVO modeling, which was used to design the field acquisition parameters for seismic profile DUS-1. The models are adapted from the models generated for AVO analysis at the M-Area seepage basin, which is adjacent to the DUS site. The AVO curves were generated using the Zoeppritz equations (Graul 2001) (Table 11) (Figure 17). The first scenario is a sand wedge saturated with water overlying a clay layer "green clay," which is considered the normal background response. The second scenario is sand saturated with 100% TCE overlying the clay. The third scenario is water filled sand overlying sand saturated with 100% TCE.

Because the project team did not know what the sensitivity of the amplitude response of the surface seismic data to DNAPL concentration would be, the curves were generated assuming 100% saturation of TCE in the pore spaces. Porosity is assumed to be 30 percent.

Using the parameters in Table 11, the results of the modeling suggested that there would be an AVO effect caused by the presence of DNAPL (Figure 17). Furthermore, these results indicated that changes in the reflection coefficient would begin to occur at approximately 25^0 angle of incidence. Using this information the seismic lines were designed such that half the receivers would be below this incident angle and half would be above.

Table 11 List of AVO modeling parameters at the DUS site.

Lithology	Vp	Vs	Density
	m/s (ft/s)	m/s (ft/s)	g/cc
Wedge			
Water Sand	1768 (5800)	422 (1450)	1.9
TCE Sand	1515 (4968)	498 (1634)	2.07
Substrate			
Clay	1707 (5600)	396 (1300)	1.85
Water Sand	1768 (5800)	422 (1450)	1.89

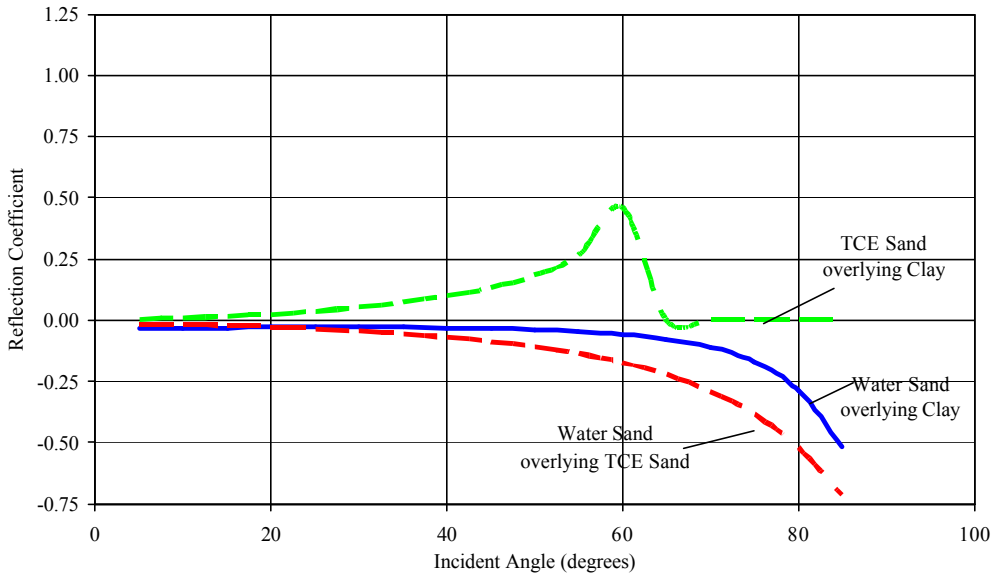

Figure 17. Amplitude variation with offset models (DUS). AVO models showing changes in reflection coefficients versus angle of offset using the full Zoeppritz equations. The solid blue line is the expected background response with water saturated sand overlying the "green clay". The long dashed green line is the expected response if the overlying sand pores are saturated with 100% TCE. The red dashed line is the expected response if water saturated sand is overlying a TCE saturated sand.

4.6 Seismic Reflection Profiles (DUS)

4.6.1 Seismic Reflection Acquisition (DUS)

A single seismic reflection profile was collected through the DUS project area. This line, designated DUS-1, was located to pass through the area with the greatest amount of subsurface contamination and begins and ends in areas that are relatively contaminant free (Figure 2). A 120 channel Geometrics seismograph and an 8 lb. sledge hammer source were used to collect the data. The seismic acquisition parameters were chosen based on the results of previous seismic surveys collected nearby and the results of preliminary AVO seismic modeling. Other considerations were to have adequate temporal and spatial sampling necessary for high-resolution recording and to attenuate acoustic noise. The parameters used to record the 2-D seismic profiles are listed in Table 12.

The receiver group spacing and shot interval were set at two feet and three geophones were bunched at each recording station. This arrangement resulted in 60 CMP fold data nominally. An asymmetric split spread recording geometry of pushing 100 channels and pulling 20 channels was used. This geometry ensured sufficient source-to-receiver offset so that any seismic AVO amplitude effects that might exist were recorded.

Table 12. Summary of seismic reflection recording parameters (DUS).

Type of survey	P wave seismic reflection
Date recorded	May 19-20, 2000
Station interval	2 ft
Source	Hammer, 8 lb.
Source interval	2 feet on half stations
Reptitions/SP	8
Record Length	500 milliseconds
Recording instrument	Geometrics RX 24 bit A/D resolution
Number of channels	120
Instrument Gain	48 dB fixed
Sample interval	0.5 millisecond
Data format	SEG-2
Data redundancy	60 Fold
Geophones	Geospace 40 Hz vertical 3/ station bunched
Near offset	1 foot
Far offset	39 ft, 199 ft
Cable Geometry	TR 1 TR 20 TR 21 TR 120
Cable Geometry (ft)	39′--------1′-----VP-----1′---------199′

4.6.2 Seismic Reflection Data Processing

After completion of the field survey, extensive detailed seismic data processing was performed at ESRI's Environmental Geophysics Laboratory on the campus of the University of South Carolina. To process the data the Landmark Graphics Corp. ProMAX software operational on a Sun Microsystems Ultra-60 workstation was used. The generalized flow used to process the data is shown in Figure 18.

The main goal of the data processing was to enhance as much as possible any reflections emanating from reflectors in the vadose zone and at the water table where most of the DNAPL contamination was expected to be found. Also, efforts were made to preserve the amplitude of the reflected waves so that AVO analysis could be performed.

The DUS-1 raw field records exhibit poor signal-to-noise ratio uniformly. What reflection signal exists is confined to a narrow frequency band of approximately 70-200 Hz. Surface wave energy and scattered waves dominate the records to the extent that few or no reflections are visible in the records. Much of the poor data quality is attributed to attenuation and scattering caused by poorly consolidated near surface gravel deposits that cover the study area. Also, the water table is over 40 m deep, which exacerbates the problem of near surface velocity variation.

To attenuate surface waves various two-dimensional filtering techniques were tried including frequency-wave number (FK), Tau-p, and Karhunen-Loeve (KL). The FK and Tau-p methods were unsuccessful and merely resulted in lower frequency content and smeared waveforms. Both of these methods are known to perform poorly on low signal-to-noise ratio data (Liu and Goulty, 1999). The KL transform method yielded somewhat better results and was used to process the DUS data.

In brief, the Karhunen-Loeve transform works by treating a seismic record as a matrix and performing principal component decomposition on it. The data are then reconstructed omitting large eigen values, which are presumably associated with noise. The result is that noise trains are attenuated and relative amplitude is preserved (Liu, 1999).

To apply this technique to the DUS data the surface wave trains were digitized and the data flattened on them followed by application of the KL transform. Because the aligned surface waves dominate the record, this noise was associated with the largest eigen values in the decomposition. In the reconstruction, the largest two eigen values were eliminated. The result, while not perfect, was better than any of the other methods tried (Figure 19). After application of the KL transform, surface consistent spiking deconvolution, spectral whitening, and a mild 3 pt spatial mix were applied to the data followed by computation and application of surface consistent residual statics.

To enhance the continuity of the stacked data, a 5 pt trace mix and FX deconvolution were applied. The data were migrated using a finite difference technique and filtered to a 70-250 Hz passband in the area of the interest. For interpretation purposes the sections are displayed at a datum of 372 feet using a datum correction velocity of 2953 ft/s.

Seismic Data Processing Flow

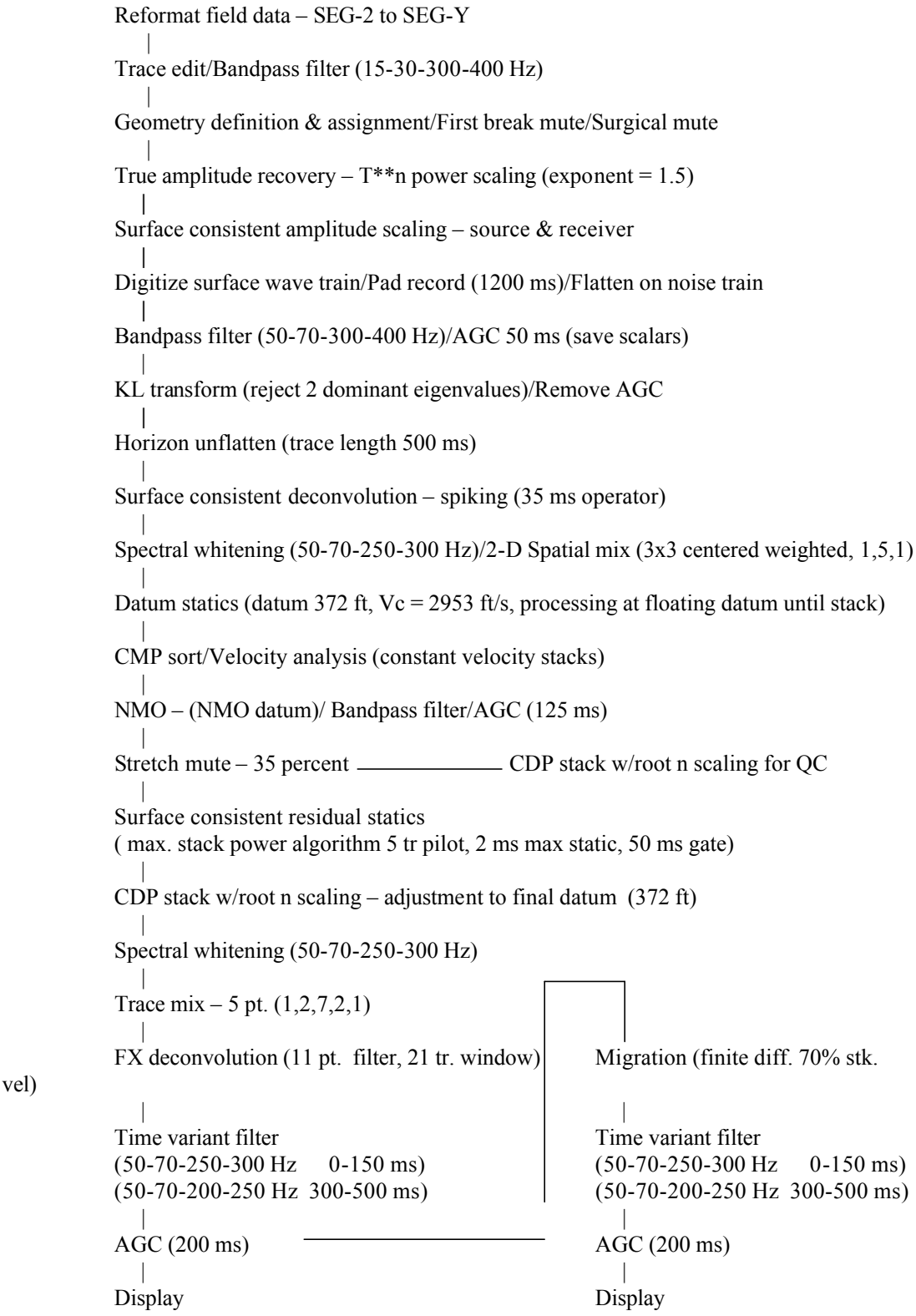

Figure 18. Data processing sequence for line DUS-1.

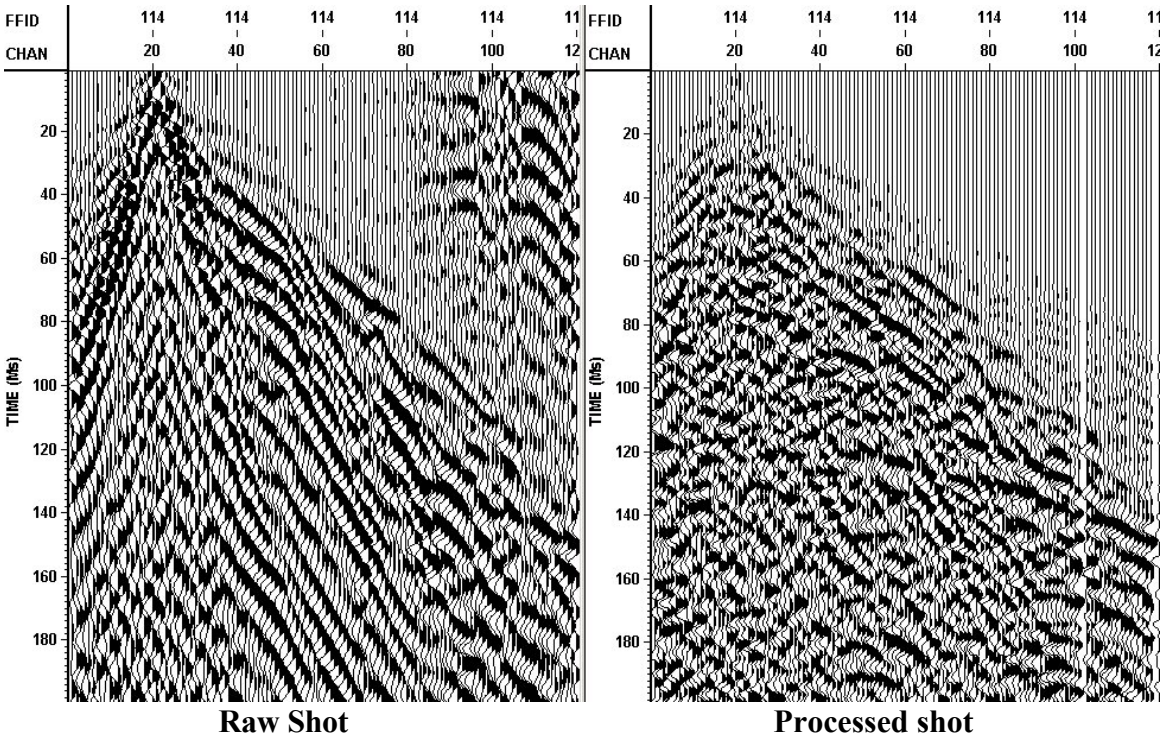

Figure 19. Shot record before and after data processing. Note the presence of reflections at 120 ms, 60 ms, and 30 ms revealed by the data processing. Both records: filter (50-70-250-300 Hz), AGC 125 ms

5.0 Results and Discussion (CNWS)

The Navy had two objectives for the project. The first was to locate the high concentrations of DNAPL using nonintrusive seismic techniques and AVO analysis, and second to use the seismic data in conjunction with existing well data to determine the geologic controls on the plume geometry. Therefore, the first section discussed here concerns the geology and second section concerns the AVO analysis for DNAPL detection.

5.1 Geology (CNWS)

The project team was able to extract 500 Hz data from the shallow subsurface. This high frequency data allows a vertical resolution of approximately 1.5 to 2 feet. The data has a subsurface horizontal resolution of 0.5 feet as a consequence of the one foot geophone spacing. With this high frequency data the project team was able to map not only the gross features such as lithologic boundaries and channels features, but features within the individual channels. In Figures 20 though 22 are seismic profiles CNWS-1, 2, and 3 plotted as amplitudes. On each of the seismic lines are two interpreted horizons. The purple line is the base of a channel described as a channel scour, and the green line is the base of a younger channel that has incised into the older channel. In Figure 20, (CNWS-1) it appears that the seismic profile crossed both channels apparently perpendicular to the strike of the channel.

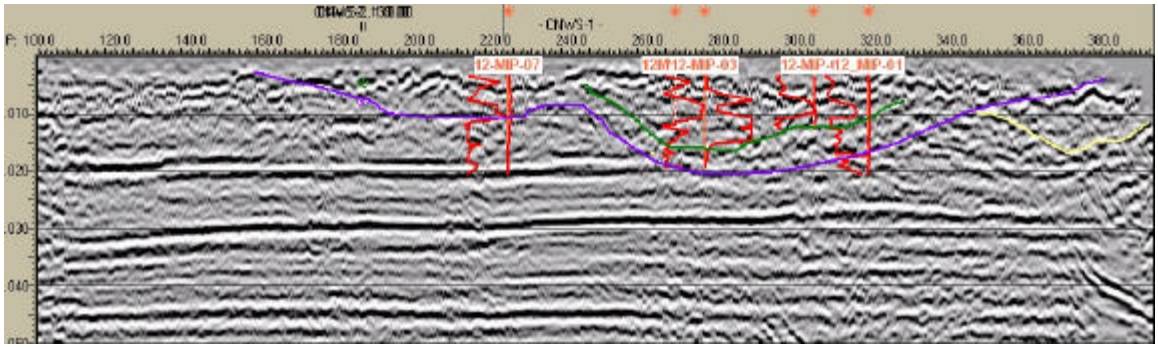

Figure 20. Seismic profile CNWS-1. The purple line is interpreted as a major channel, the green line is a second channel within the older channel complex, and the yellow line is yet a third channel complex. The red log to the left of the vertical red line denoting the Geoprobe™ MIP test location is electrical conductivity and the log to the right is the ECD. On the conductivity log deflections to the right indicates conductive soil such as clays. The ECD log deflections to the right indicate an increase in compounds containing chlorine. The blocky pattern on the ECD indicates that the amount of chlorine compounds has exceeded the maximum resolution of the probe.

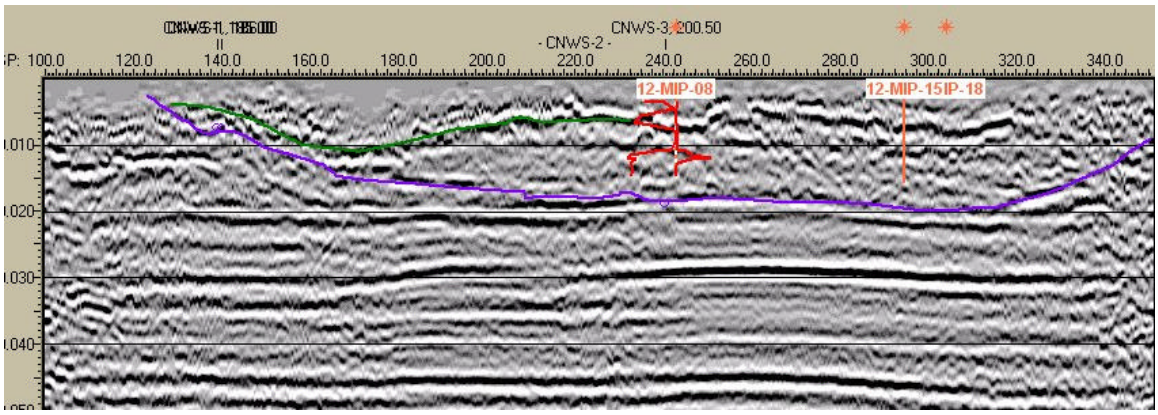

Figure 21. Seismic profile CNWS-2. CNWS-2 was acquired from southwest to northeast. As in Figure 20 the two prominent features are the purple line, which is the base of a major channel scour, and the green line, which is the smaller and younger channel scour that incised into the older channel.

In Figure 21 (CNWS-2) the two prominent features are 1) the large older purple channel scour and 2) the smaller and younger green channel scour. These two features correlate with the same channel scours observed on seismic profile CNWS-1. It appears from the geometry of the lower scour (purple) that the seismic profile has crossed this feature at an oblique angle almost parallel with the depositional dip of the channel. The upper channel feature (green) also appears to be more elongated, in the cross-section view, on seismic profile CNWS-2 than on profile CNWS-1. It appears that this younger channel is also intersected at a slight oblique angle. Based upon the DNAPL concentration data, the green channel scour is controlling the spatial geometry of the contaminant plume and, even though the base of the channel is sandy clay, it is retarding downward migration of the DNAPL plume.

Figure 22 is an amplitude presentation of seismic line CNWS-3. The two major features on this seismic profile are the lower major channel scour (purple) and a smaller channel scour within the larger channel feature (green). The green channel is not the only channel feature within the larger channel. However, based upon the DNAPL concentration data, the green channel is controlling the plume geometry. Also note on Figure 22 the location of 12-MIP-12. A substantial increase in the ECD (right side) occurs at about 10 ms, which is located at the base of the small sand layer at the base of the green channel.

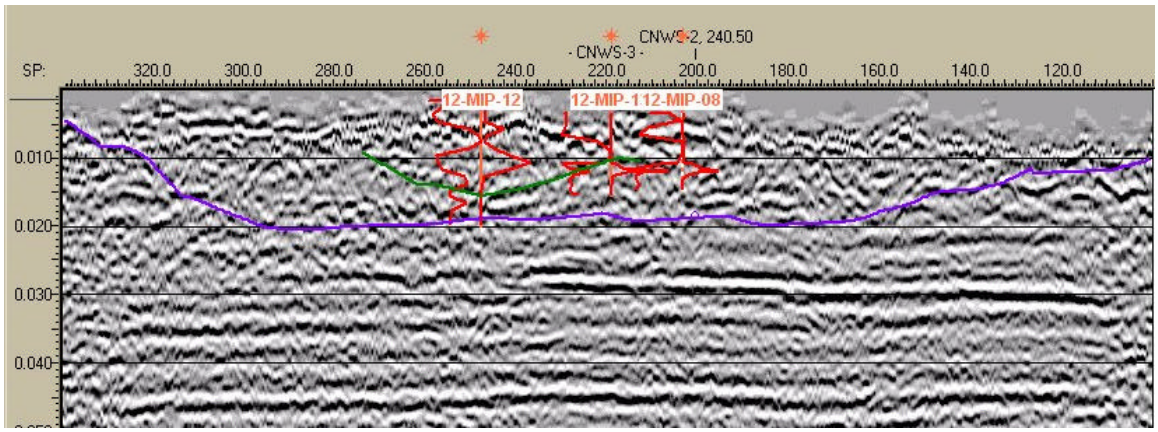

Figure 22. Seismic profile CNWS-3. CNWS-3 was acquired from southeast to northwest. The two major events are the purple line interpreted to be the base of a major channel and the green line a smaller secondary channel.

5.2 AVO Interpretation (CNWS)

Amplitude variation with offset (AVO) analysis can be as simple as processing the seismic data into offset range stacks such as the project team used at the M-Area seepage basin and at the Dynamic Underground Stripping (DUS) site at the M-Area solvent tank area, Savannah River Site. Other techniques such as gradient stacks (Castagna et al., 1998) and Poisson's Ratio stack (Vern and Hilterman, 1995) are used extensively in the petroleum industry for direct hydrocarbon detection. At the Charleston Naval Weapons Station the modeling data (Figure 9) suggest that if DNAPL is present in both the lower part of Unit 1 sand and the upper part of Unit 2 sandy clay, the amplitude response would be a bright spot, i.e. a negative amplitude becoming more negative with increase in offset. A bright spot is also indicative of lithology change as well as change in fluid type within the pore spaces. Therefore, a bright spot would not necessarily mean a change in fluid type along an interface.

Castagna and others (1998) stated that AVO interpretation could be enhanced by crossplotting the AVO intercept (A) and gradient (B) provided that reasonable petrophysical parameters are used so that a well defined background trend in the A-B plane is present. The B term (gradient) is the second term from the Shuey (1985) approximation of the Zoeppritz equations, which describes the amplitude characteristics from 15 degrees of offset to 30 degrees of offset (immediate angles of offset). In the shallow subsurface the background trend is generally positive. Any deviation from the background trend is a very good indicator of the presence of DNAPL or a change in the lithology with non-normal elastic properties. Simply put, the AVO gradient is the change in slope of the reflection coefficient with increase in offset (Graul, 2001). In Figure 9 the slope of the line on each of the graphs (reflection coefficient versus offset) is the gradient. At the CNWS, there is excellent control of the geology in the area of contamination. Therefore, any change in background is believed to be attributed to a change in fluid in the pore spaces, such as DNAPL and not because of changes in the geologic strata or structure.

The other AVO interpretation technique used in this study is the Poisson's ratio stack, which is a stack generated from the product of Poisson reflectivity and the (NI) normal incidence reflectivity (Vern and Hilterman, 1995). This is the change of Poisson's ratio across an acoustic interface with offset. The scaled Poisson's Ratio stack is derived from Shuey's approximation of Zoeppritz equations and represents angles of offset greater than 30 degrees. Any changes observed on the Poisson's stack would suggest a change in fluid type since there is no indication there is a change in the geology.

5.2.1 Seismic Profile CNWS-1

In Figure 23, Figures 23A and 23B are the gradient stack (upper, middle) and Figure 23C (lower) is a scaled Poisson's ratio stack. On the gradient stack there are several bright anomalies. The first starts at CDP 211 and extends to CDP 373, the second starts at CDP 410 to CDP 470, the third CDP 500 to CDP 643, and the fourth starts at CDP 660 and extends to the end of the line.

In conducting AVO analysis on shallow near surface data, the project team has observed that there is an edge effect when performing near and far range limited stacks, gradient stacks, and Poisson's ratio stacks. It appears that when there are not enough offsets, such as in the beginning of the data and at the end of the data, erroneous amplitude anomalies occur (examples Figures 23A, 23B, and 23C, the first and fourth anomalies described in the preceding paragraph). During field operations, the shot is "walked" into the spread until the shot reaches full spread and the spread begins to roll-along. Until the shot location has moved a number of stations equal to the half the recording spread length the CDP gathers are not populated with the full complement of source-receiver offsets. At the end of the line, the same is also true as the shot is "walked" off the spread.

The second anomaly between CDP 410 and 470 occurs below an asphalt road. This phenomenon is also observed on lines CNWS-2 and 3 where the seismic profiles cross the asphalt road. The anomaly may be the result of not having the full set of offsets in the CDP gather. This occurs because the data beneath the road was of poor quality and some of the shots were edited prior to final processing of the gathers. Another possibility is that the asphalt composition might have caused the anomaly.

The anomaly between CDP 500 and 643 on Figure 23A and between shot points 250 and 320 on Figure 23C is interpreted to be not the result of an edge effect or asphalt, but the result of a change in the pore fluids. Based upon the models (Figure 9), if DNAPL replaces water in either Unit 1 or replaces water at the base of Unit 1 and the top of Unit 2 there would be an AVO anomaly and consequently a change in the AVO gradient. In the area of CDP 550 (shot point 275, Figure 23B) there is a pronounced AVO anomaly even though it appears to be faint on the Figures 23A and 23C. This particular anomaly is well out of the influence of the edge effect at the end of the survey caused by the asphalt road. Therefore, it appears that it is the result of DNAPL either partially replacing or completely replacing the pore waters. This particular area is adjacent to well 12MW-10S, which has high concentrations of DNAPL. Note that at the location of 12MIP-03 (Figure 23), the ECD curve has a blocky appearance, which is due to chlorinated solvent concentration exceeding the maximum range of the probe.

In addition to the AVO gradient and Poisson's ratio stacks, another robust AVO interpretation technique is range limited offset stacks (Graul, 2001). In Figure 24 are the

near and far offset range limited stacks for seismic profile CNWS-1. Based upon the model (Figure 9) if there is no DNAPL present, the amplitudes should be negative on the near offsets and positive on the far offsets. In Figure 24 the upper figure is the range limited offset stack for the offset range from 0 degrees to 30 degrees. At approximately 10 ms, between CDPs 535 and 689 the amplitudes are all negative, which is what the model indicates for the absence of DNAPL. However, according to the model if both units 1 and 2 have DNAPL, then the amplitudes become more negative which is perhaps influencing the amplitudes on the near offset stack. On the far offset stack at the same intervals, the amplitudes become positive. Because the interpretation of range limited stacks is not clear, gradient and scaled Poisson's ratio analysis were performed on the data sets.

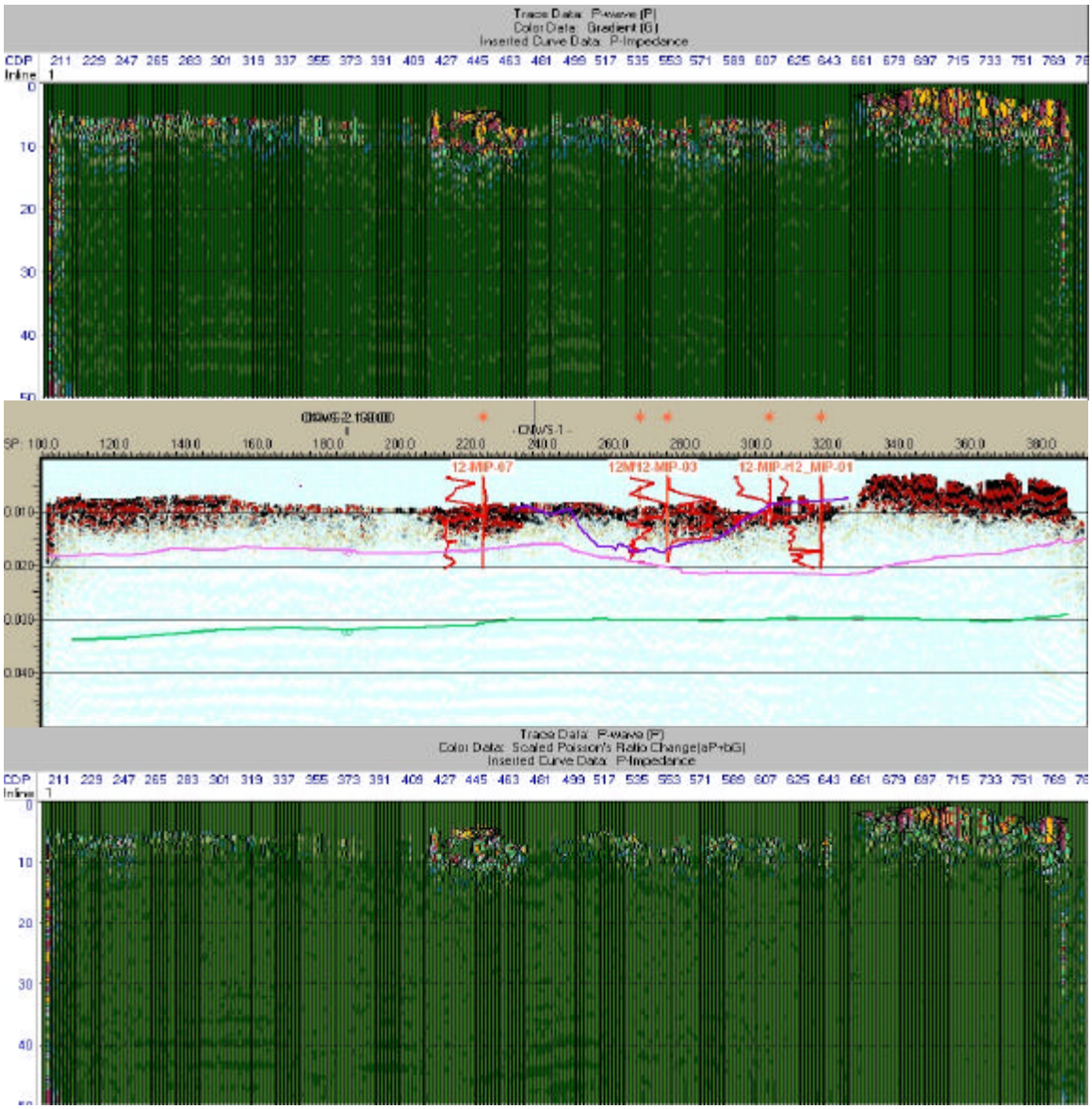

Figure 23. Seismic profile CNWS-1 AVO gradient and scaled Poisson's ratio stacks. The upper (Figure 23A) and middle figure (Figure 23B) is the gradient stack for seismic profile CNWS-1. Figure 23B is the gradient stack plotted in another software package with the geologic interpretations and MIP probe data added. The left curve is conductivity and the right curve is ECD. Figure 23C is the scaled Poisson's ratio stack.

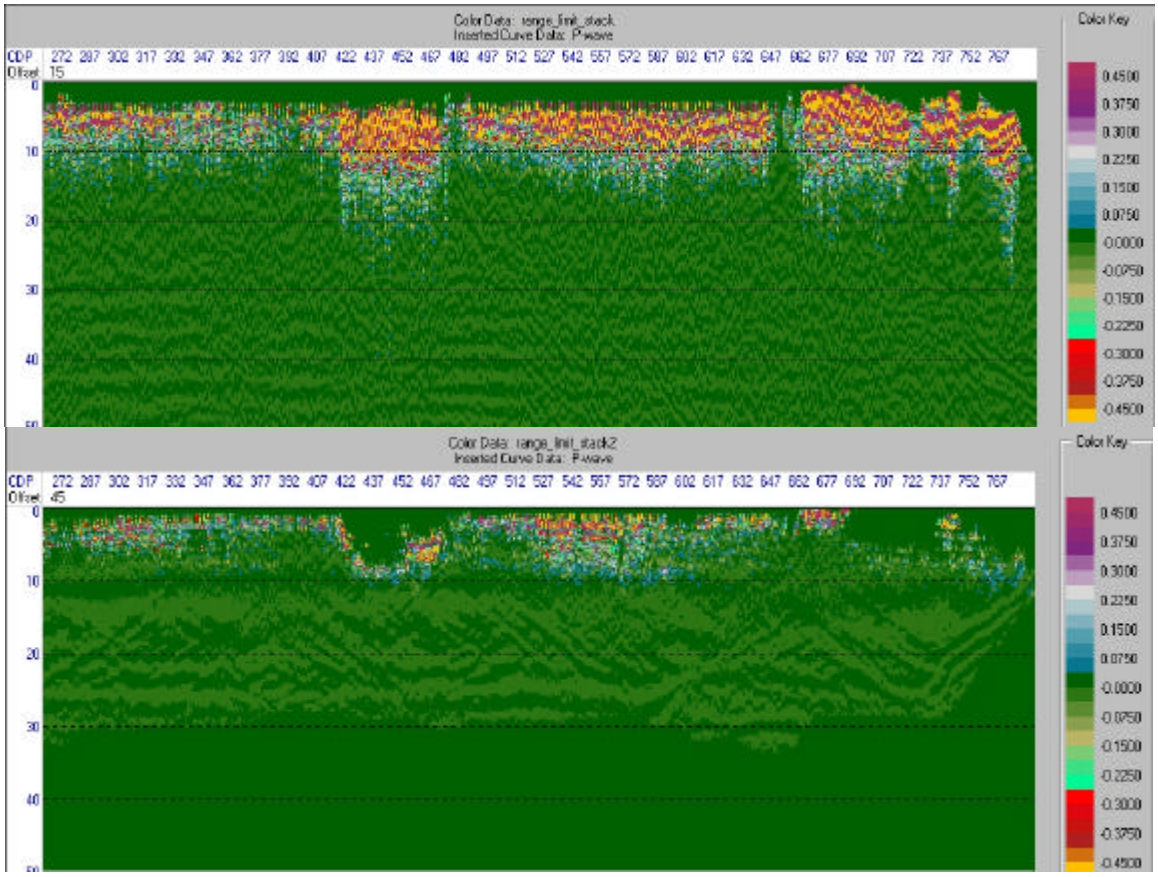

Figure 24. Seismic profile CNWS-1 AVO range limited stacks. Figure 24A (upper figure) is the range limited stack with offset ranges from 0 degrees to 30 degrees and Figure 24B (lower figure) is range limited stack with offset ranges from 30 degrees to 60 degrees.

5.2.2 Seismic Profile CNWS-2

Figure 25 displays gradient stacks (A and B) and scaled Poisson's ratio stack for seismic line CNWS-2. Seismic line CNWS-2 is similar to seismic line CNWS-2 in that the edge effects produce anomalous features at the beginning and end of the seismic line. As on CNWS-1, the edge effect is more prominent on the end of the line than at the beginning of the line. If the anomalies at the beginning and at the end of the seismic line are discarded, there appears to be no amplitude variations that can be associated with DNAPL. At the top of the data, occurring at approximately 10 ms, there is a thin zone that is visible across the entire line, but is believed to be an artifact from the AVO analysis. There is one anomaly between CDP 320 and 370 (Figures 25A and 25C) (between shotpoints 160 and 185, Figure 25B) that occurs where the seismic line crosses an asphalt road. This anomaly, like the anomaly similarly located on CNWS-1 is believed to be spurious. MIP 12-MIP-18 is located slightly off the seismic line (Figure 25B) and the ECD did not give a significant response.

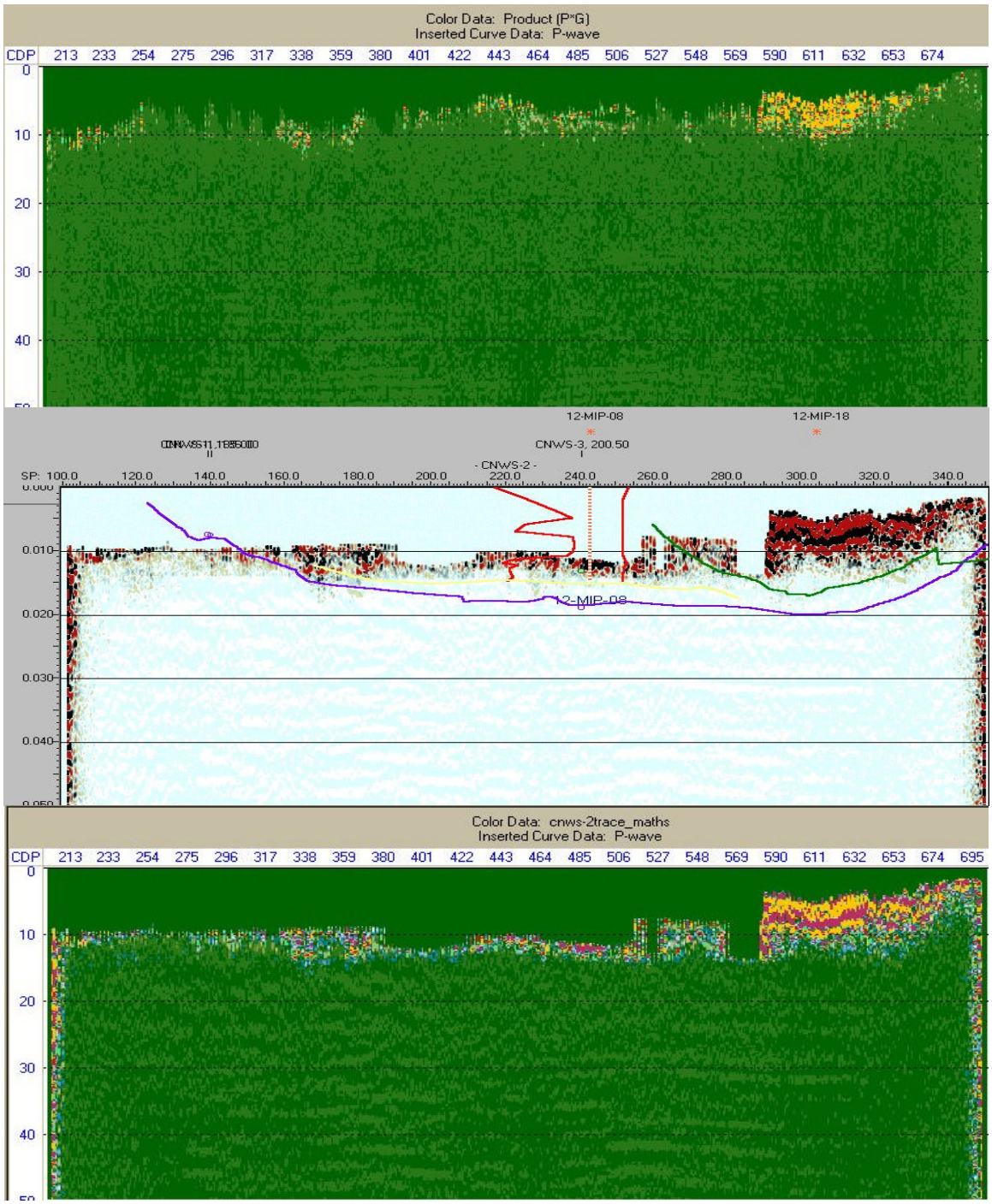

Figure 25. Seismic profile CNWS-2 AVO gradient and scaled Poisson's ratio stacks. Figure 25A is gradient stack of seismic line CNWS-2. Figure 25B is gradient stack with geologic interpretations and conductivity log (left) and MIP ECD curve (right) for MIP 12MIP-08. Figure 25C is scaled Poisson's ratio stack..

5.2.3 Seismic Profile CNWS-3

Figure 26 shows a series of AVO analyses preformed on seismic line CNWS-3. The AVO analysis consists of gradient stacks (Figures 26A and 26B) and scaled Poisson's ratio stack (Figure 26C). The only AVO anomaly, besides the artifacts generated from edge effect, is located between CDPs 400 and 402 (Figures 26A and 26C) and between shot points 200 and 210 (Figure 26B). The anomaly is mostly attributed to an artifact caused by editing traces where the seismic line crossed an asphalt road. On Figure 26B MIP location 12-MIP-08 was drilled in the middle of the anomaly and there was no significant response from the ECD probe.

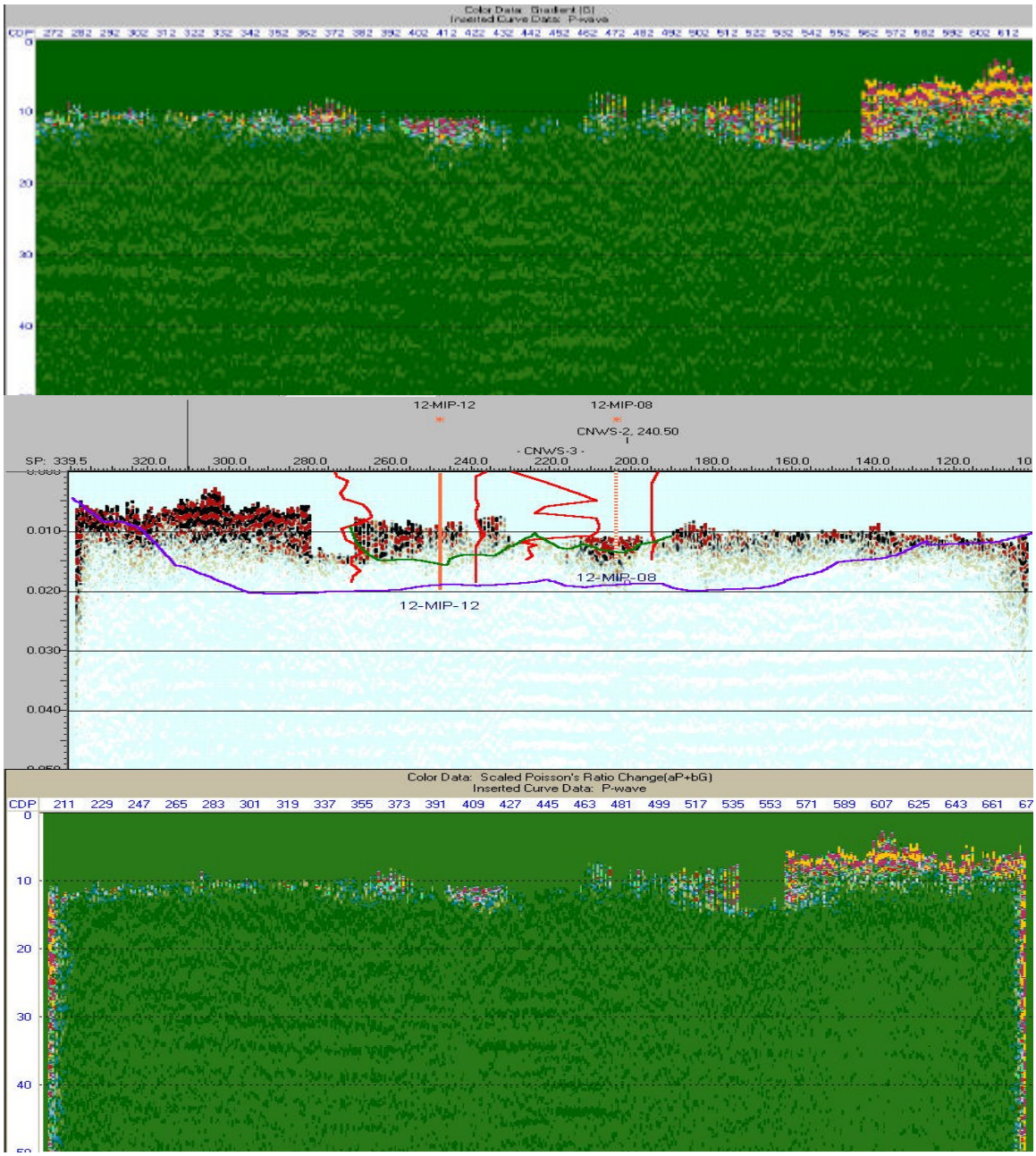

Figure 26. Seismic profile CNWS-3 AVO gradient and scaled Poisson's ratio stacks. Figure 26A is gradient stack of seismic line CNWS-3. Figure 26B is also a gradient stack with the geologic interpretations, conductivity log (left curve), and MIP-ECD (right curve). Figure 26C is a scaled Poisson's ratio stack..

5.2.3 Validation (CNWS)

In all the previous studies conducted by the project team, criticism has been expressed regarding the validation of the results. At Savannah River Site, M-Seepage Basin, the project team believes there are enough existing wells to validate the results of the study. However, critics have expressed concern that there were no wells drilled in areas where anomalies were absent to demonstrate that the absence of any anomaly signifies the absence of DNAPL.

The Charleston Naval Weapons Station site offered a unique opportunity for the project team to drill wells in and out of anomalous areas. Several locations were drilled where AVO anomalies were present and where AVO anomalies were absent (Figure 1 solid diamonds and Figure 27). In some instances the anomalies investigated were found to be spurious (the asphalt road anomalies). In Table 13 are the MIP locations selected by the project team and their predictions based upon the AVO analysis. Figures 28 and 29 shows the concentration data of different solvents and daughter products from the water samples.

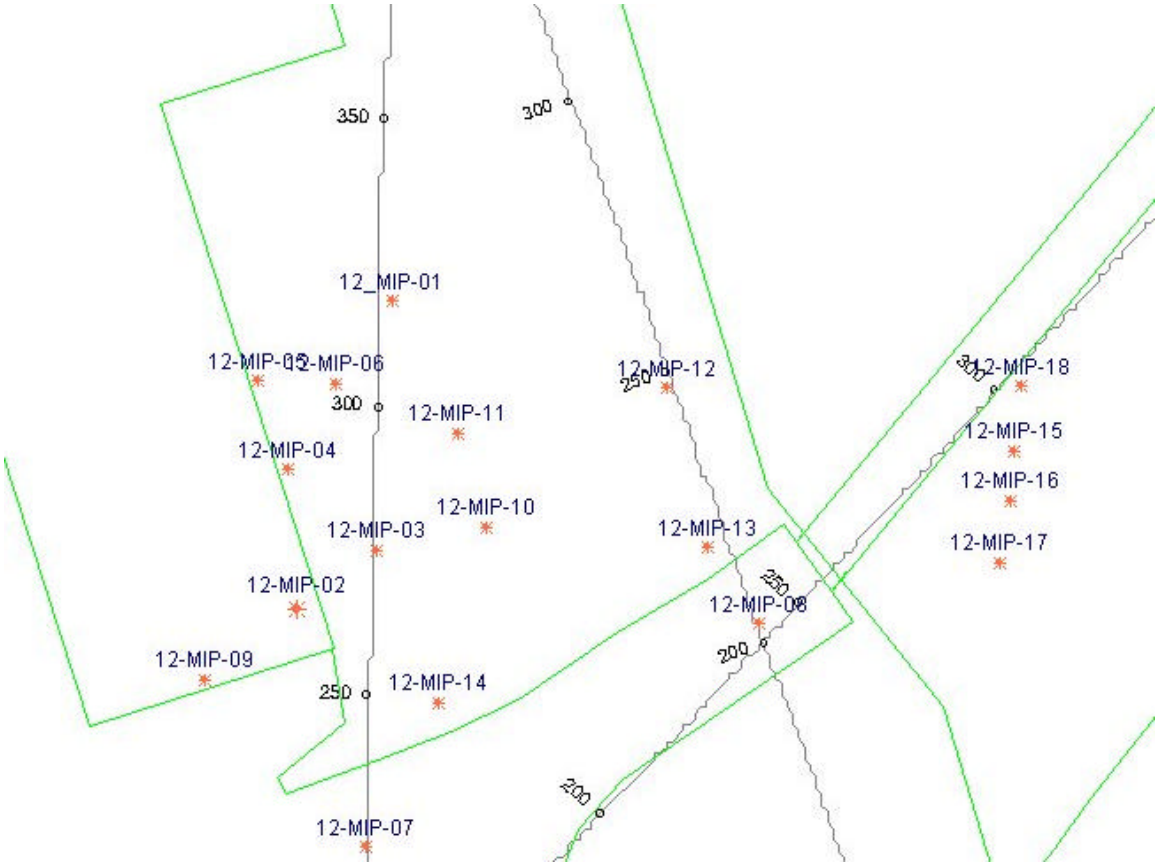

Figure 27. Location map of wells and MIP tests at the SWMU-12 site. Figure 27 is an enlargement of Figure 1. The MIP names are easily recognizable.

Table 13. Selected MIP locations for validation and predicted results

MIP ID	Line Number	Shot Pt. Number	Prediction
12-MIP-01	1	318	No high concentration
12-MIP-03	1	273	High concentration
12-MIP-07	1	223	No high concentration
12-MIP-08	3	203	No high concentration
12-MIP-12	3	247	No high concentration

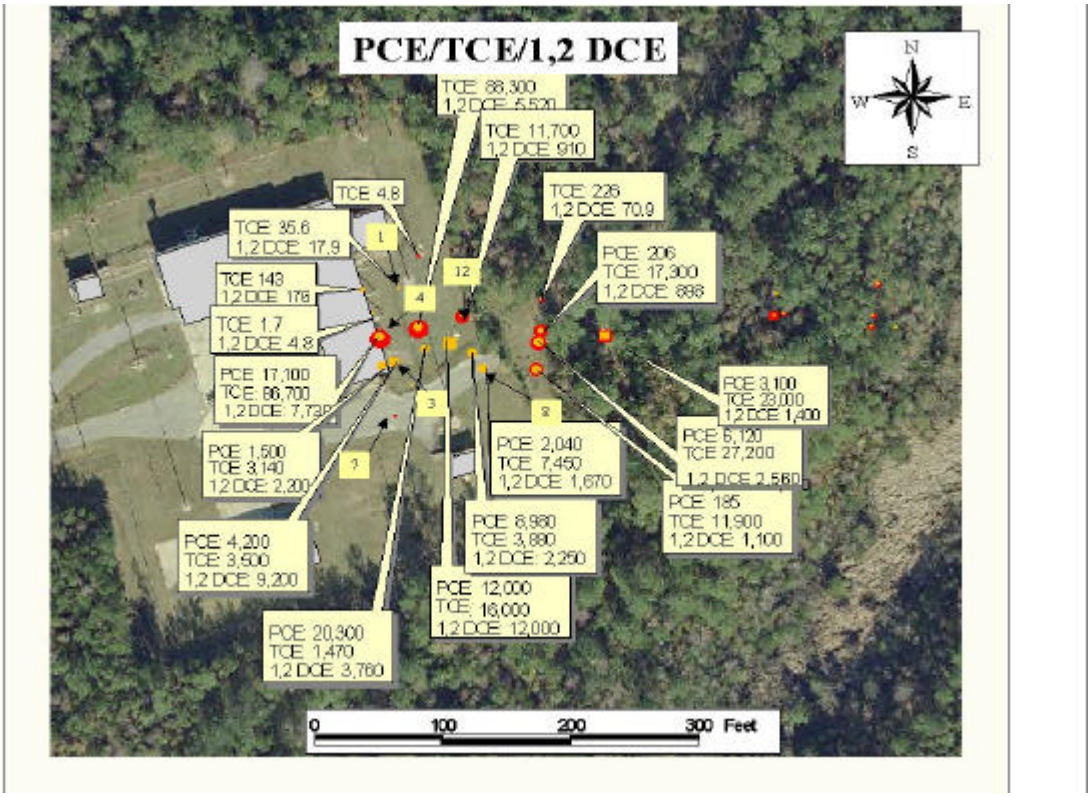

Figure 28. Location of water samples that were analyzed for PCE, TCE, and 1,2 DCE and the concentrations of contaminants found. The yellow squares with a number are the MIP locations and the magenta and yellow circles are the locations where water samples were taken. Note that the water samples were taken within 2 feet of the MIP locations. Diagram provided by Naval Facilities Engineering Command Southern Division.

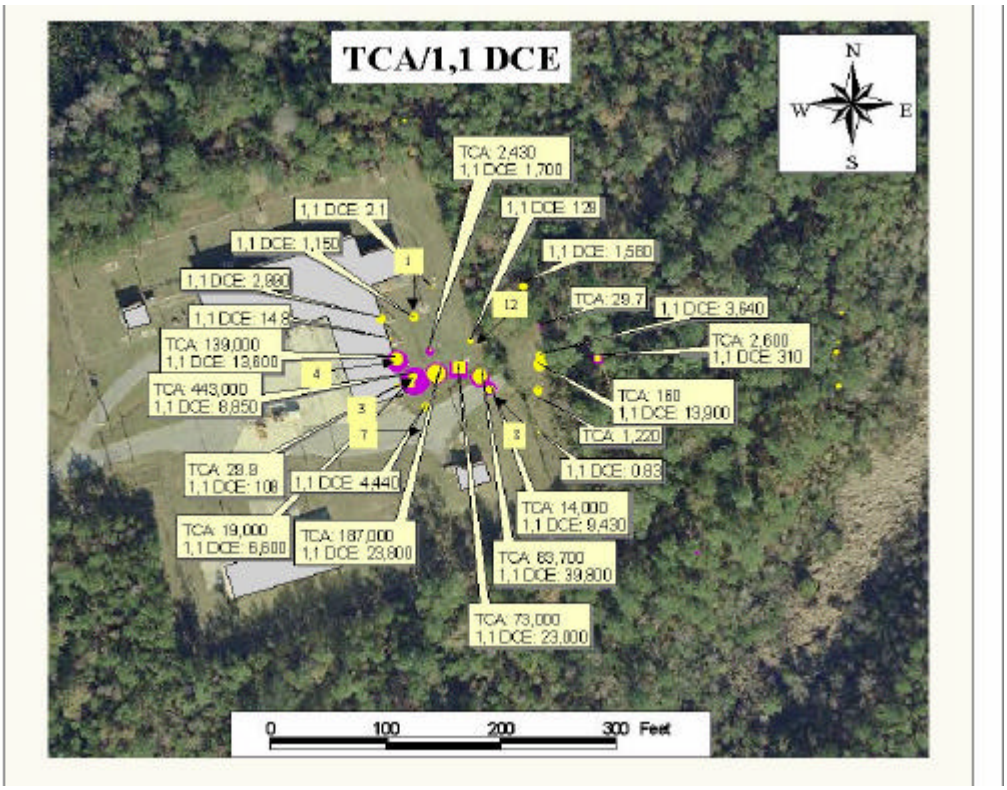

Figure 29. Location of water samples that were analyzed for TCA and 1,1 DCE and the concentrations of contaminants found. The yellow squares with a number are the MIP locations and the magenta and yellow circles are the locations where water samples were taken. Note that the water samples were taken within 2 feet of the MIP locations. Diagram provided by Naval Facilities Engineering Command Southern Division.

The water samples taken from the area adjacent to 12-MIP-03, which was selected based upon AVO analysis, had the highest concentration of TCA (Figure 28). MIP 12-MIP-04 located adjacent to shot point 290 (Figure 23) was located in the same AVO anomaly as 12-MIP-03 and has the second highest concentration of TCA and the second highest concentration of TCE (Figures 28 and 29).

MIP locations 12-MIP-07 and 12-MIP-08 (Figures 28 and 29, labeled 7 and 8 in the yellow squares) were drilled though the asphalt anomalies. At 12-MIP-07 no water samples were taken because the MIP probe data indicated that there were no chemical contaminates present at that location, which was suspected by project team. At location 12-MIP-08 there was a water sample taken adjacent to the location and the results were 14,000 ppb TCA, 9,430 ppb 1,1,DCE, 2,040 ppb PCE, 7,450 ppb TCE, and 1,670 ppb 1, 2 DCE. The total amount of chlorinated solvents and their daughter products is 34,590 ppb, which is most likely not enough to cause an AVO anomaly. Approximately 30 feet northwest of 12-MIP-08 another water sample was taken along seismic line CNWS-3. The concentrations were 83,700 ppb TCA, 39,800 ppb 1,1 DCE, 8,980 ppb PCE, 3,880 ppb TCE, and 2,250 ppb 1,2 DCE for a total of 138,610 ppb of chlorinated solvent and their daughter products. It appears that at that location there is not enough solvent to cause an

AVO anomaly. If the asphalt road were not there, perhaps there would be a slight anomaly that could be detected. That is, the effect of the asphalt road could be masking a genuine AVO effect.

At MIP locations 12-MIP-01 and 12-MIP-12 low concentrations of contaminants were found in accordance to what was predicted by the AVO analysis (Figures 28 and 29).

5.4 Geology (DUS)

In M-Area the "green clay" interval, located within the Warley Hill Formation, is the zone where DNAPL pooling occurs (Table 14). The term "green clay" is misleading. In the A/M area the Warley Hill Formation is composed mostly of fine to coarse grain poorly sorted sand with discontinuous clay beds. It does not appear to be the typical "green" silty sandy clay found in the southern half of the Savannah River Site (Aadland et al., 1995). As DNAPL migrates downward it tends to accumulate on clay layers and flow under the influence of gravity. This flow continues until a breach in the confining unit is encountered. The downward path continues through the breach into lower aquifers.

Figure 30 is a variable density plot of seismic profile DUS-1. The vertical blue dashed line is the location well DUS-010, which is the vapor extraction well for the DUS project. The only mappable reflection is located between shotpoints 190 and 280 at approximately 120 ms. This reflection is interpreted to be the location of the greatest amount of solvent directly above the "green clay" interval.

Table 14. Formation names, geologic age of sediments at the DUS site.

PERIOD/ EPOCH		NORTH AMERICAL STAGE	GROUP	FORMATION
TERTIARY		AGE UNKNOWN		UPLAND
	E O C E N E	JACKSONIAN	BARNWELL	TOBACCO ROAD DRY BRANCH
		CAIBONMIAN	ORANGEBURG	SANTEE/TINKER WARLEY HILL "**Green Clay**" CONGAREE

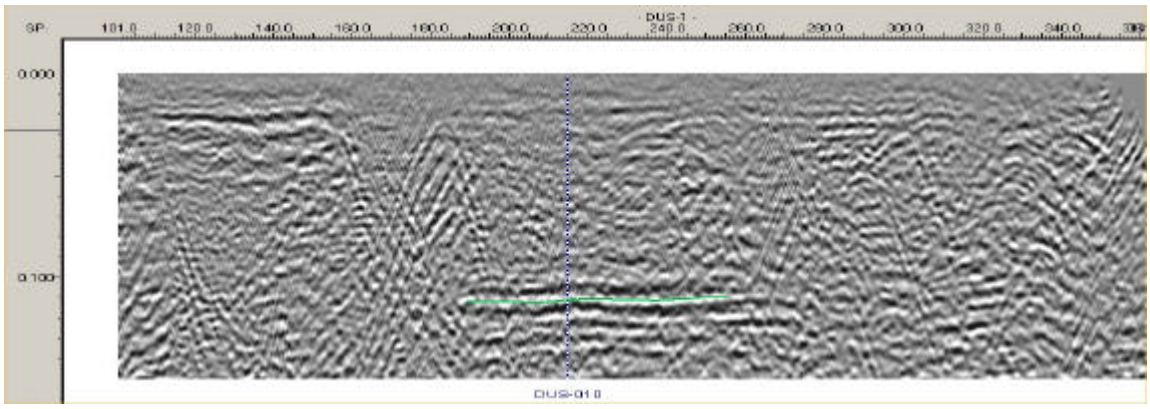

Figure 30. Variable density plot of seismic profile DUS-1. The green line is interpreted as the top of the "green clay" interval.

5.5 AVO Interpretation (DUS)

5.5.1 Seismic Profile DUS-1

At the DUS site the modeling data (Figure 17) suggest that, if TCE is present in the upper sand directly above the "green clay" interval, offset range stacks could be used for AVO analysis. That is, the reflection coefficient at large angles of incidence (long offsets) is sufficiently different than that at small angles of incidence (short offsets) so that stacking ranges of offsets reveal a change in reflection coefficient if the contaminant is present. The range of angles used in the offset range stack is determined from the AVO modeling.

At the base of the contaminant plume the sand overlying the "green clay" interval is saturated with DNAPL. According to the AVO model at an incident angle of approximately 25^0 the reflection coefficient at this interface should begin to increase and sharply increase as the angle of incidence increases. At the top of the plume the model indicates that the reflection coefficient should begin slightly negative and become more negative with increasing incident angle. Therefore, seismic profile DUS-1 was processed into a near offsets stack ($0\text{-}25^0$) and a far offsets stack ($25^0\text{-}50^0$) (Figure 31). In the near offsets stack there are not any mappable reflectors. This, according to the models, is an expected response (small reflection coefficient). On the far offsets stack there is an AVO anomaly in the location where it is believed to be the highest concentrations of DNAPL. Figure 32 shows the location of the AVO anomaly on seismic profile DUS-1 and the anomaly relationship to the steam injection wells and the extraction well.

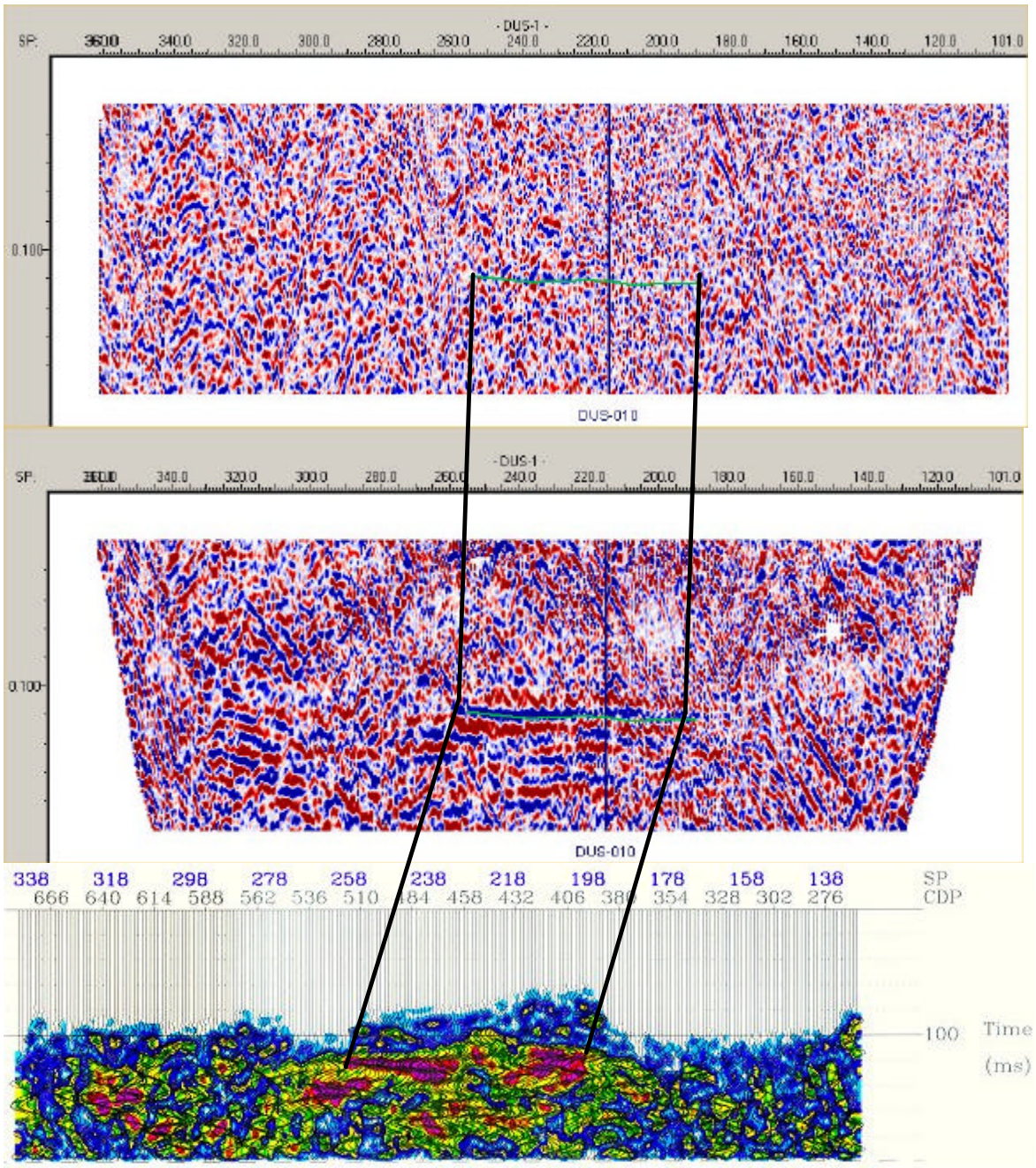

Figure 31. Seismic profile DUS-1 range limited offset stacks. The upper figure is the near offset stack (0 - 25^0), and the middle figure is the far offset stack (25^0 - 50^0). The lower stack is also a far offset stack but is plotted on a smaller scale in order to show the AVO anomaly. The dark blue amplitude within the outline represents negative amplitudes.

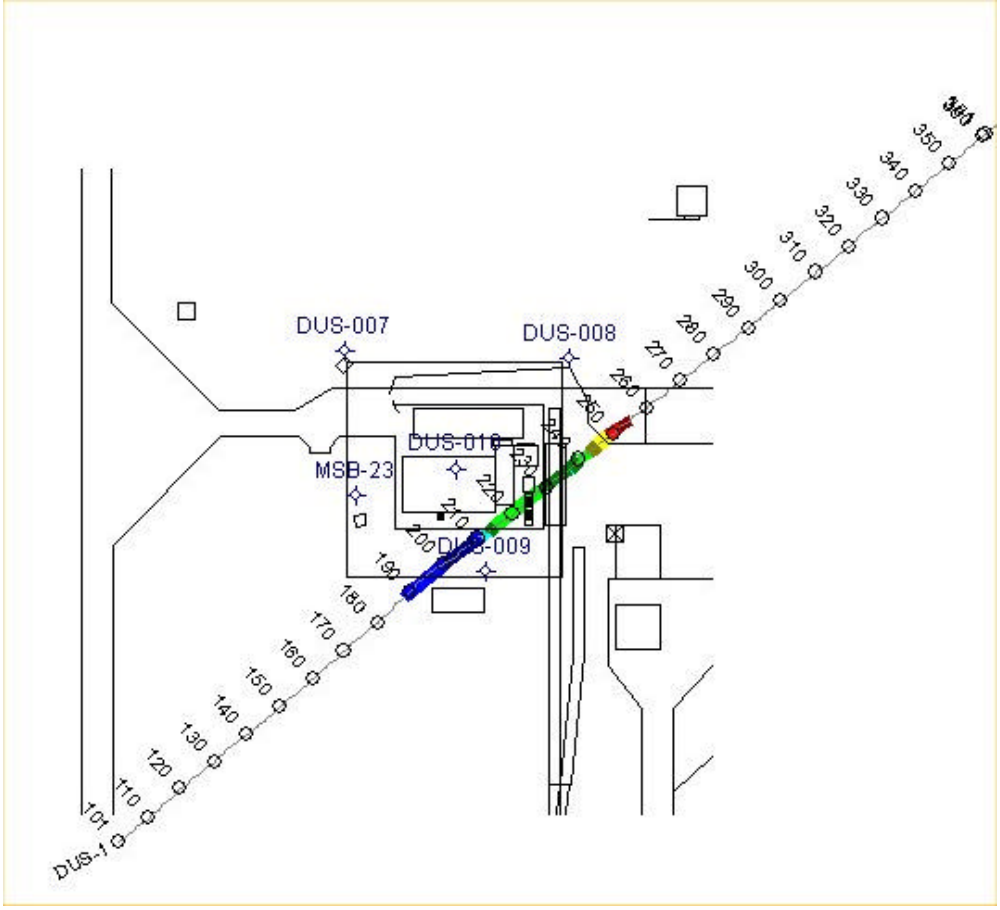

Figure 32. Location of seismic profile DUS-1 and the location of the AVO anomaly. Well DUS-010 is the extraction well and DUS-7, 8, and 9 are steam injection wells.

5.6 Validation (DUS)

At the Charleston Naval Weapons station the project team was allowed to drill as many boreholes as were necessary to validate the results. At the DUS site the initial scope of work proposed two deployments. One deployment before steam injection and another deployment after steam injection had been completed and the vapor extraction units had been turned off. As of the writing of this report the equipment has not been removed from the site; therefore, the project team is unable to complete the second deployment to determine if the AVO anomaly identified on the data was as a result of high concentrations of DNAPL. According to an article in the United States Environmental Protection Agency publication "Ground Water Currents" DOE reports that approximately 70,000 pounds of PCE and TCE have been removed during the 12 months of DUS operation (Ewart, 2001). It is possible that given the amount of DNAPL reportedly removed from the subsurface in such a small area that the AVO anomaly identified on the first deployment may have either disappeared or has been diminished.

6.0 Conclusion

Based upon the models and results of the different AVO analysis techniques applied to the data set, it appears that the project team was able to locate the area of the highest concentration of DNAPL. Unlike previous studies conducted using AVO analysis for direct detection of DNAPL, the project team was able to drill the anomaly to verify the results as well as drill in areas where the project team predicted there would not be high concentration of DNAPL. In the areas where the project team predicted no high concentration of DNAPL, no high concentrations were found. This does not mean that there were no concentrations of DNAPL above drinking water standards. It must be remembered that this technique is designed to locate areas of highest concentrations where DNAPL is either partially filling the pore spaces or completely replacing the interstitial fluids. Previous modeling studies as well as this study suggests that only 20% of the pore space need to be filled with DNAPL to cause an AVO anomaly. There were areas where the water samples had extremely elevated levels of solvents in excess of 130,000 ppb that appeared not to cause an AVO anomaly. In that instance, however, the effects of an asphalt road may have masked the anomaly.

At the DUS site at M-Area, Savannah River Site, there was an AVO anomaly identified on seismic profile DUS-1 that was consistent with the model study. As of the writing of this report the DUS technique has removed approximately 70,000 pounds of DNAPL from the site.

7.0 References

Aadland, R.K., Gellici, J.A., and Thayer, P.A., 1995, Hydrogeologic framework of west-central South Carolina: Water Resources Division Report 5, State of South Carolina Department of Natural Resources.

Castagna, J.P. and Backus, M. M., eds. 1993, Offset-dependent reflectivity - Theory and practice: SEG Investigations in Geophysics No. 8, Society of Exploration Geophysicists, Tulsa, OK, 345 p.

Castagna, J.P, Swan H.W., and Foster, D.J, 1998, Framework for AVO gradient and intercept interpretation: Geophysics, v. 65, no. 3, p. 571-581.

Ewart, M., 2001, DUS expedites ground-water cleanup at Savannah River Site: EPA Ground Water Currents, EPA 542-N-01-008, December, 2001, issue no. 42

Gardner, G.H.F., Gardner, L.W., and Gregory, A.R., 1974, Formation velocity and density-the diagnostic basics for stratigraphic traps: Geophysics, v. 39, p. 770-780.

Gassmann, F., 1951, Über die elastizität poröser medien: Vier. Der Natur. Gesellschaft in Zürich, p 96, 1-23

Graul, M., 2001, AVO seismic Lithology: SEG Continuing Education, San Antonio, TX.

Liu, X, 1999, Ground roll suppression using the Karhunen-Loeve transform (Short Note): Geophysics, v. 64, n. 2, p. 564-566.

Liu, X, and Goulty, N.R., 1999, Comparison of 2D filters for suppressing noise in common shot gathers: First Break, v. 17, n. 4, p. 105-110.

Shuey, R.T., 1985, A simplification of the Zoeppritz equations: Geophysics, v. 50, no.4, p. 609-614.

Tetra Tech Nus, Inc., 2000, Draft report SWMU12-Former south side PCP treatment area, Naval Weapons Station, Charleston, South Carolina.

Tsvankin, L, and Thomsen, L., 1994, Nonhyperbolic reflection moveout in anisotropic media: Geophysics, v.59, no.8, p1290-1304.

Verm, R. and Hilterman, F., 1995, Lithology color-coded seismic sections: The calibration of AVO crossplotting to rock properties: The Leading Edge, v. 14, n. 8, p. 847-853.

Zoeppritz, K., 1919, Uber reflexion und durchgang seismischer wellen durch Unstetigkerlsflaschen: Berlin, Uber Erdbebenwellen VII B, Nachrichten der Koniglichen Gesellschaft der Wissenschaften zu Gottingen, math-phys. K1., p. 57-84.

Acknowledgments

We thank Naval Facilities Engineering Command, South Division, for providing access to the CNWS SWMU-12 site and the drilling to validate the results of the study. Additional thanks goes to Hampson-Russell Software Services for support of the *AVO* software package and Seismic Micro-Technology, Inc. for donation of the *Kingdom Suite* software. The University of South Carolina-ESRI acknowledges support of this project by Landmark Graphics Corporation via the Landmark University Grant Program.

Appendix 1

MIP logs consist of six columns (left to right): temperature curve, ECD curve, FID curve, PID curve, penetration rate, and soil conductivity curve.

Charleston Naval Weapons Complex
MIP 01, July 31, 2001

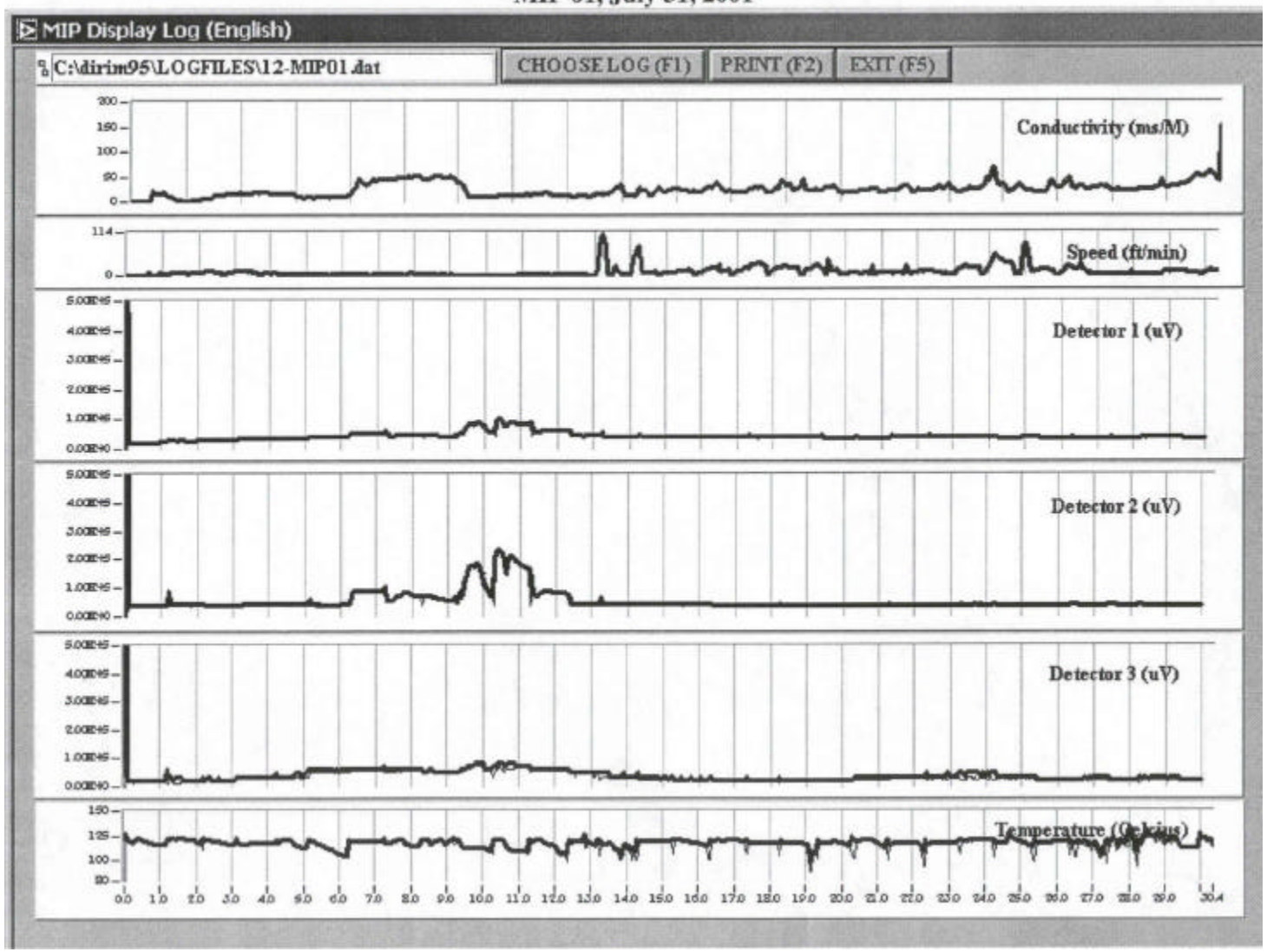

Charleston Naval Weapons Complex
MIP 03, July 31, 2001

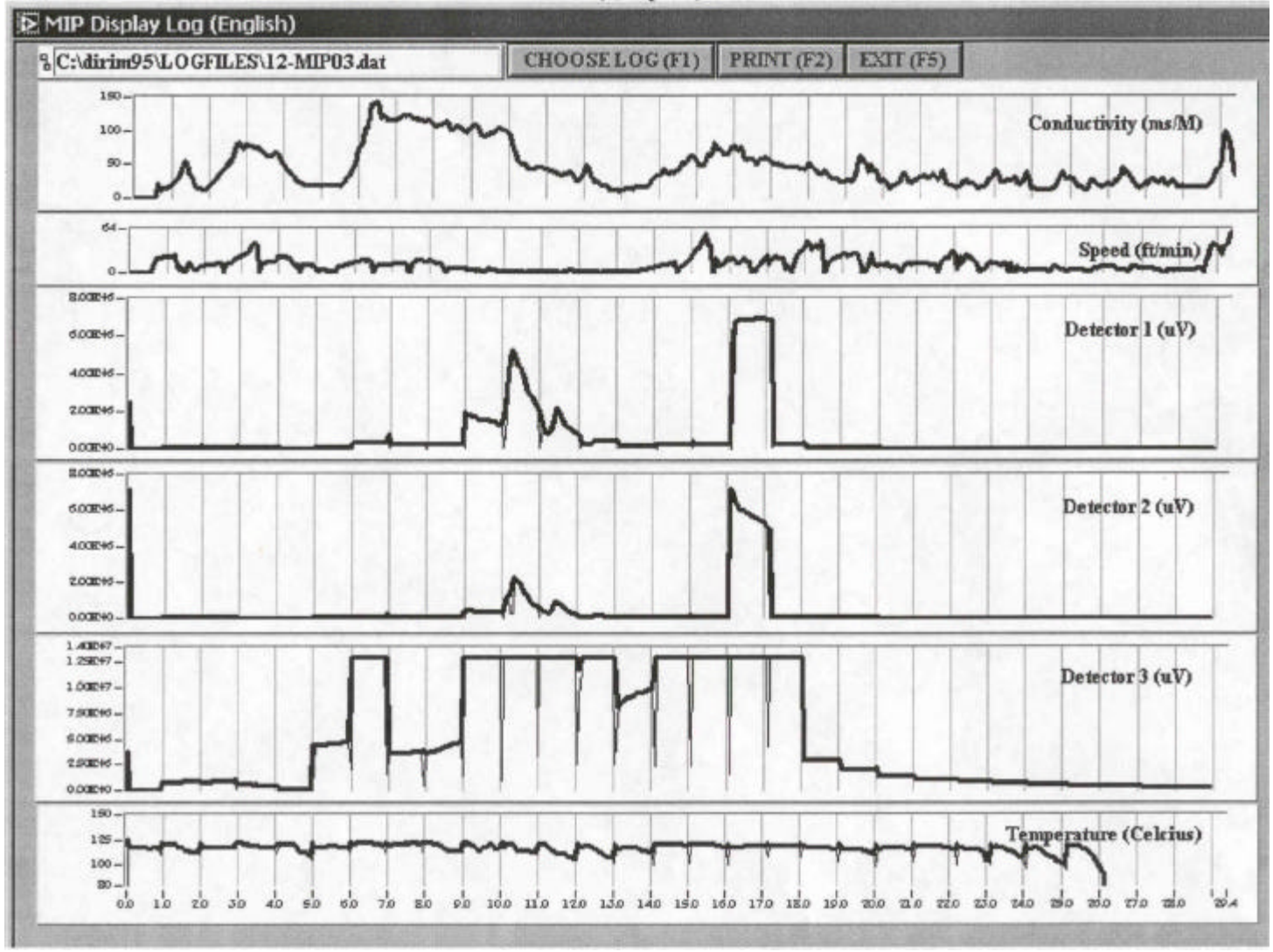

Charleston Naval Weapons Complex
MIP 04, August 1, 2001

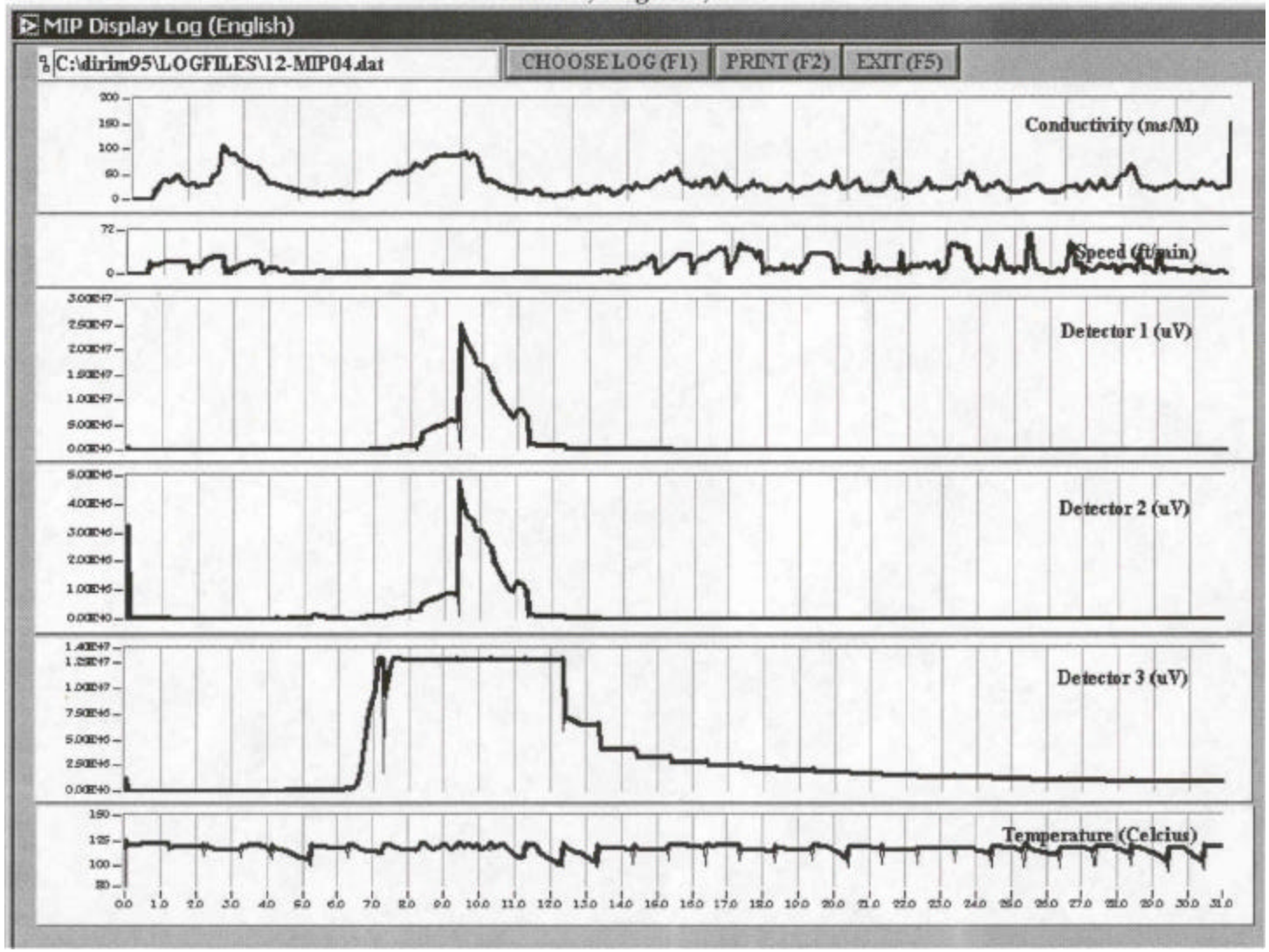

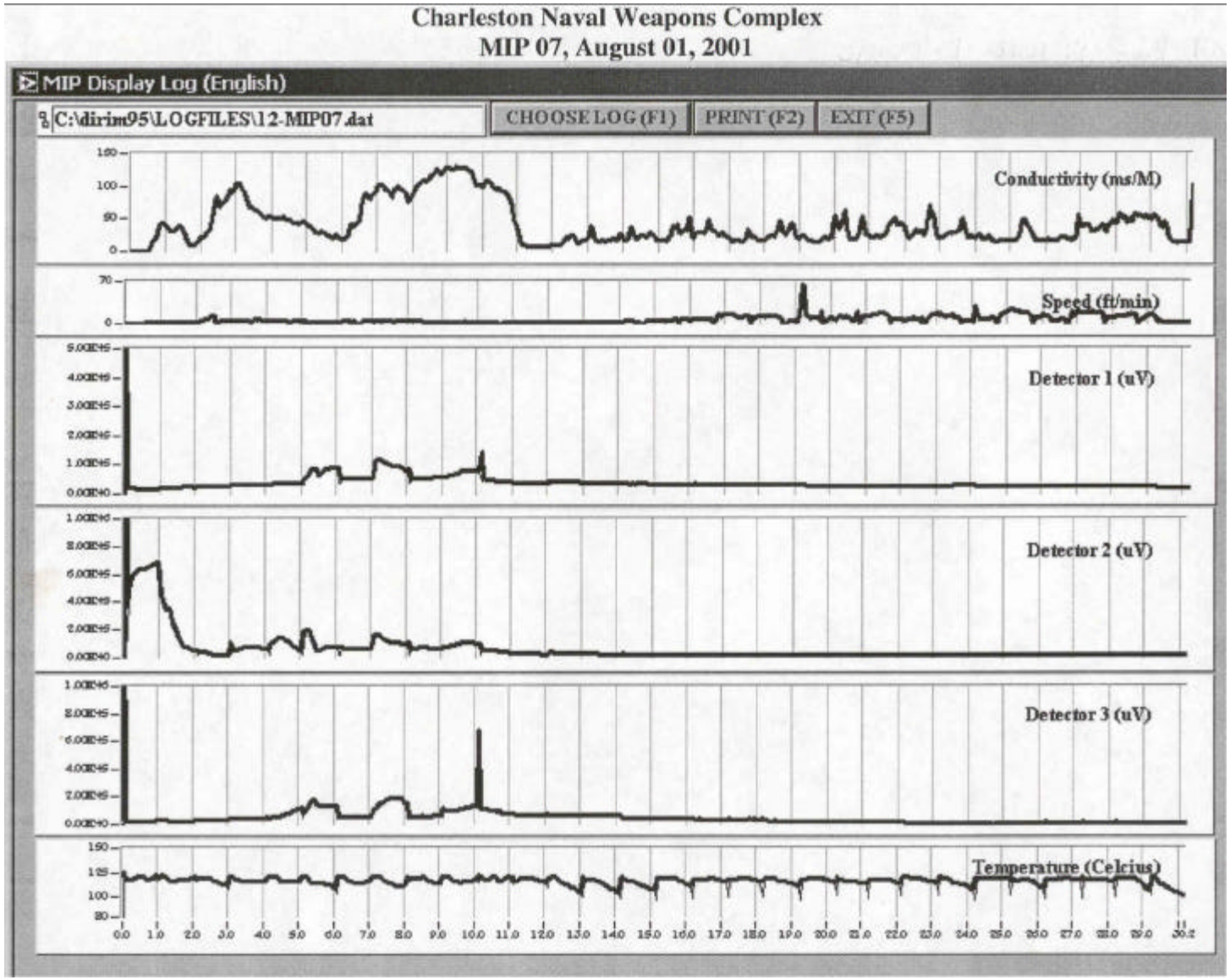
Charleston Naval Weapons Complex
MIP 07, August 01, 2001
MIP Display Log (English)
C:\dirim95\LOGFILES\12-MIP07.dat
CHOOSE LOG (F1)
PRINT (F2)
EXIT (F5)
Conductivity (ms/M)
Speed (ft/min)
Detector 1 (uV)
Detector 2 (uV)
Detector 3 (uV)
Temperature (Celcius)

Charleston Naval Weapons Complex
MIP 08, August 01, 2001

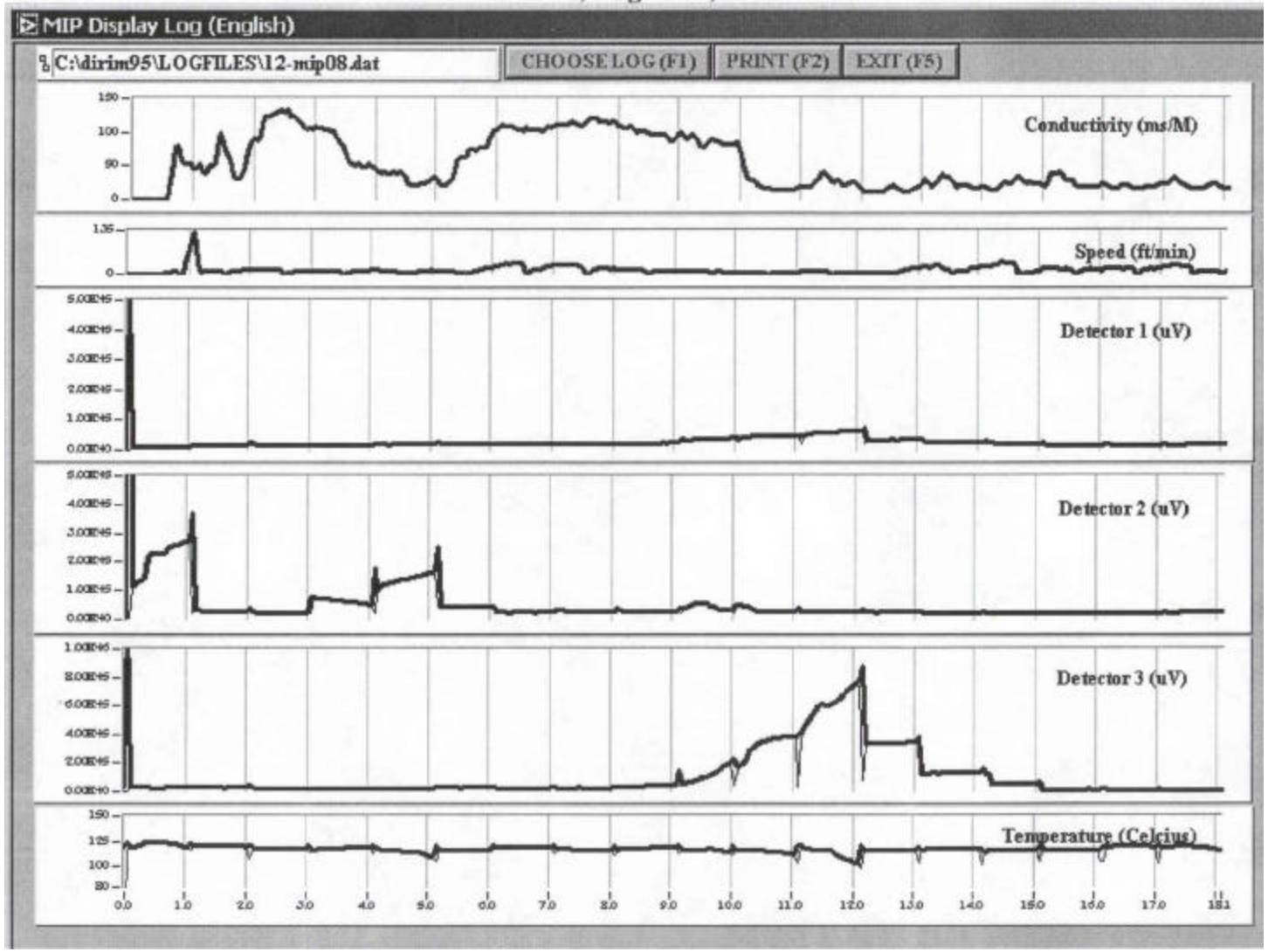

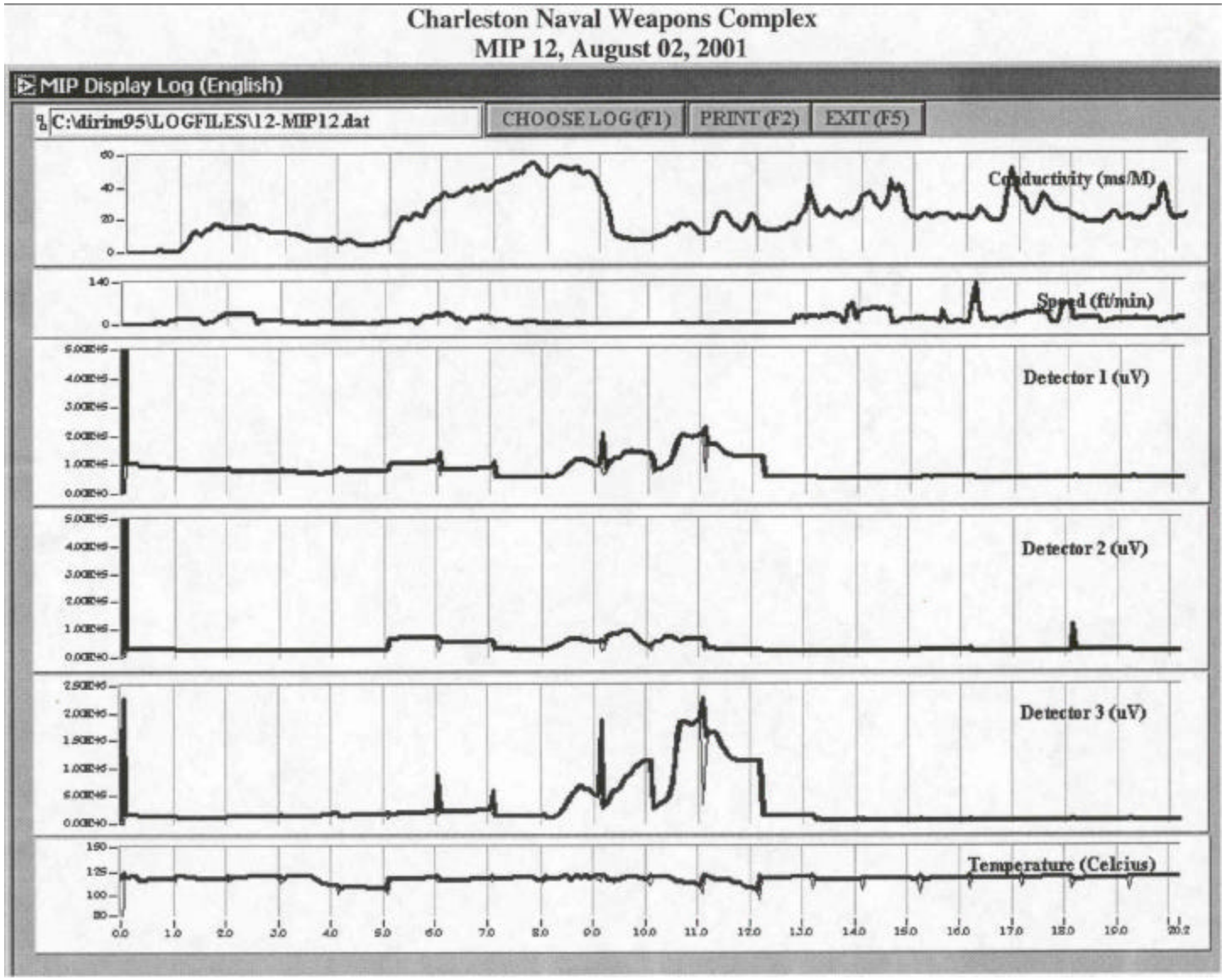
Charleston Naval Weapons Complex
MIP 12, August 02, 2001
MIP Display Log (English)
C:\dirim95\LOGFILES\12-MIP12.dat
CHOOSE LOG (F1)
PRINT (F2)
EXIT (F5)
Conductivity (ms/M)
Speed (ft/min)
Detector 1 (uV)
Detector 2 (uV)
Detector 3 (uV)
Temperature (Celcius)

This page is intentionality blank

Non-Invasive Determination
Of the
Location and Distribution of Free-Phase
Dense Nonaqueous Phase Liquids (DNAPL)
Or Light Nonaqueous Phase Liquids (LNAPL)
at
DOE Pantex, Playa 3
by
Seismic Reflection Techniques

Final Report

Tasks 7, 8, 9, 10, and 11

Reporting Starting Date: September, 1998
Reporting Ending Date: December, 2002

By

Michael G. Waddell
&
William J. Domoracki

Earth Sciences and Resources Institute
University of South Carolina
Columbia, South Carolina

January 2003

DOE Award Number DE-AR26-98FT40369

Disclaimer

Abstract

This document constitutes a final report for Task 7 (site evaluation), Task 8 (seismic reflection design, and acquisition), Task 9 (seismic reflection processing), Task 10 (seismic reflection interpretation), and Task 11 (final report) on DOE contact number DE-AR26-98FT40369.

The third deployment site for utilizing seismic methods for detecting DNAPL/LNAPL is the Department of Energy (DOE) Pantex Plant near Amarillo, TX. Previous investigations were conducted at DOE Hanford Site, DOE Savannah River Site, and the Charleston Naval Weapons Station. Pantex Plant was selected following a request by site personnel. The request focused on the possibility of using noninvasive techniques to map the geology and to attempt to use seismic Amplitude Versus Offset (AVO) analysis to image any DNAPL or LNAPL that might be present under Playa 3.

In the initial phase of the investigation, based on the review of existing data and the shallow target depth, the project team collected two Vertical Seismic Profiles (VSP) and walkaway noise tests. The VSP data were used to generate a series of AVO response models of two intervals of interest, the contact the contact between the overlying sand and caliche and the sand above the fine grained zone (FGZ).

The modeling results indicate that if DNAPL or LNAPL has replaced the existing pore fluid, which is either air or water, there should be an AVO effect at the contact between the upper sand and caliche. If LNAPL (toluene) has saturated the pore space of the lower sand, directly above the FGZ, there should be no discernable AVO effect. However, if the lower sand is saturated with 100% TCE there should be a detectable AVO effect. After it was established that an AVO anomaly might be present, the project team proceeded with Task 8. Task 8 involved acquiring four surface seismic lines for a total of 8200 feet. Task 9 was the processing of the seismic data. Task 10 consisted of interpreting data to map the subsurface geology beneath Playa 3, AVO analysis of profiles PTX-1 and PTX-2, and the integration of existing well data with the seismic data.

The interpretation of the seismic data suggests that neither the caliche nor the FGZ is continuous beneath the playa. Another feature mapped from the seismic data is an intraplaya depression. It appears that the formation of the depression affected the continuity of the caliche and especially the FGZ beneath the playa. However, based only on the seismic data, the geometry of the intraplaya depression is not the same as the present day surface expression of the playa. The data indicates that the intraplaya depression is smaller than the present day playa and this affects the configuration of the intraplaya boundaries as seen on the seismic.

Amplitude Versus Offset (AVO) analysis of seismic profiles PTX-1 and PTX-2 did not detect any amplitude anomalies that could be associated with either free-phase (separate phase) toluene or trichloroethylene.

Table of Contents

List of Figures

List of Tables

1.0 Introduction

This final report is for Task 7 (site evaluation), Task 8 (seismic reflection design and acquisition), Task 9 (seismic reflection processing), Task 10 (seismic reflection interpretation), and Task 11 (final report) under DOE contact DE-AR26-98FT40369. Previously we have reported on work at DOE Hanford and Savannah River Site and the DOD Charleston Naval Weapons Station. The additional site is Playa 3 at DOE Pantex Plant near Amarillo, TX (Figure 1). At Playa 3 there are possible concentrations of DNAPL and LNAPL located under the playa. It was decided to attempt to use noninvasive p-wave reflection seismic and AVO analysis to locate any areas that may have free-phase (separate phase) DNAPL or LNAPL.

In the initial phase of the investigation, based upon the review of existing data, the project team collected vertical seismic profiles (VSP) in wells PTX01-1009 and PTX01-1008 and walkaway noise tests (Figure 1). The VSP data were used to generate a series of AVO response models of two intervals of interest, the contact the contact between the overlying sand and caliche and the sand above the fine grained zone (FGZ). The noise tests were recorded to understand surface seismic recording conditions.

The AVO modeling results indicate that if DNAPL or LNAPL has replaced the existing pore fluid, which is either air or water, there should be an AVO effect at the contact between the upper sand and caliche. If LNAPL (toluene) has saturated the pores of the lower sand directly above the FGZ there should be no discernable AVO effect. However, if the lower sand is saturated with 100% TCE there should a detectable AVO effect.

Once it was established that an AVO anomaly might be present, the project team proceeded with Task 8. Task 8 involved the acquisition of four seismic lines for a total of 8200 feet. Task 9 was the processing of the seismic data. Task 10 consisted of interpreting data to map the subsurface geology beneath Playa 3, AVO analysis of profiles PTX-1 and PTX-2, and the integration of existing well data with the seismic data.

2.0 Executive Summary

This final report document is for DOE contact number DE-AR26-98FT40369 consisting of Task 7 (site evaluation), Task 8 (seismic reflection design and acquisition), Task 9 (seismic reflection processing), Task 10 (seismic reflection interpretation), and Task 11 (final report). This third project deployment for utilizing this methodology was conducted at the DOE Pantex Plant near Amarillo, TX. The project site is Playa 3, which is located adjacent to the burning grounds where there was thought to be possible chlorinated solvent contamination. If DNAPL or LNAPL is present under the playa, it was believed to occur either on top of a caliche layer located approximately 90 feet (27 meters) below land surface or on top of the fine grained zone (FGZ) approximately 287 feet (87 meters) below land surface. Seismic AVO modeling focused on the contact between the overlying sand and caliche and the sand above the fine grained zone (FGZ).

The modeling results indicated that if free-phase DNAPL or LNAPL has replaced the existing pore fluid, which is either air or water, there should be an AVO effect at the contact between the upper sand and the caliche. If free-phase LNAPL (toluene) has saturated the pores of the lower sand directly above the FGZ there should be no discernable AVO effect. However, if the lower sand is saturated with 100% TCE there should a detectable AVO effect.

Once it was established that an AVO anomaly might be present, the project team proceeded with Task 8. Task 8 involved acquiring four seismic lines for a total of 8200 feet. Task 9 was the processing of the seismic data. Task 10 consisted of interpreting the data to map the subsurface geology beneath Playa 3, AVO analysis of profiles PTX-1 and PTX-2, and the integration of existing well data with the seismic data.

The interpretation of the seismic data suggests that neither the caliche nor the FGZ is continuous beneath the playa. Another feature mapped from the seismic data is an intraplaya depression. It appears that the formation of the depression affected the continuity of the caliche and especially the FGZ. However, based on only the seismic, data the geometry of the intraplaya depression is not the same as the present day surface expression of the playa. The intraplaya depression appears to be smaller than the present day playa depression.

Amplitude Versus Offset (AVO) analysis of seismic profiles PTX-1 and PTX-2 did not detect any amplitude anomalies that could be associated with either free-phase (separate phase) toluene or trichloroethylene. There is a possibility that either or both toluene or trichloroethylene could be present and above MCL but is below the concentration level that can be detect by seismic techniques.

3.0 Project Objectives

The specific objectives of the research at DOE Pantex site are:

- Determine if the caliche and the FGZ are present and continuous under Playa 3 using subsurface imaging (seismic methods).

- Test the methodology of direct detection of DNAPL by use of seismic reflection amplitude versus offset (AVO) data and comparison with theoretical model responses.

4.0 Results

Playa 3 (Figure 1) offers a unique opportunity for the project team to document a third area having different geologic attributes than those previously worked. Areas previously worked include the DOE facility at Hanford, Washington and the Charleston Naval Weapons Station, Charleston, South Carolina.

At Playa 3 the shallow geology (< 300 feet, 91 meters) is not well known directly under the playa; therefore, the first objective was to determine if the caliche ("caprock") and the fine grained zone (FGZ) are continuous under the playa by the use of seismic reflection profiling. The second objective was to determine if there is high concentration of DNAPL (TCE) or LNAPL (toluene) either near the caliche or FGZ interval beneath the surface of Playa 3 by the use of seismic AVO analysis.

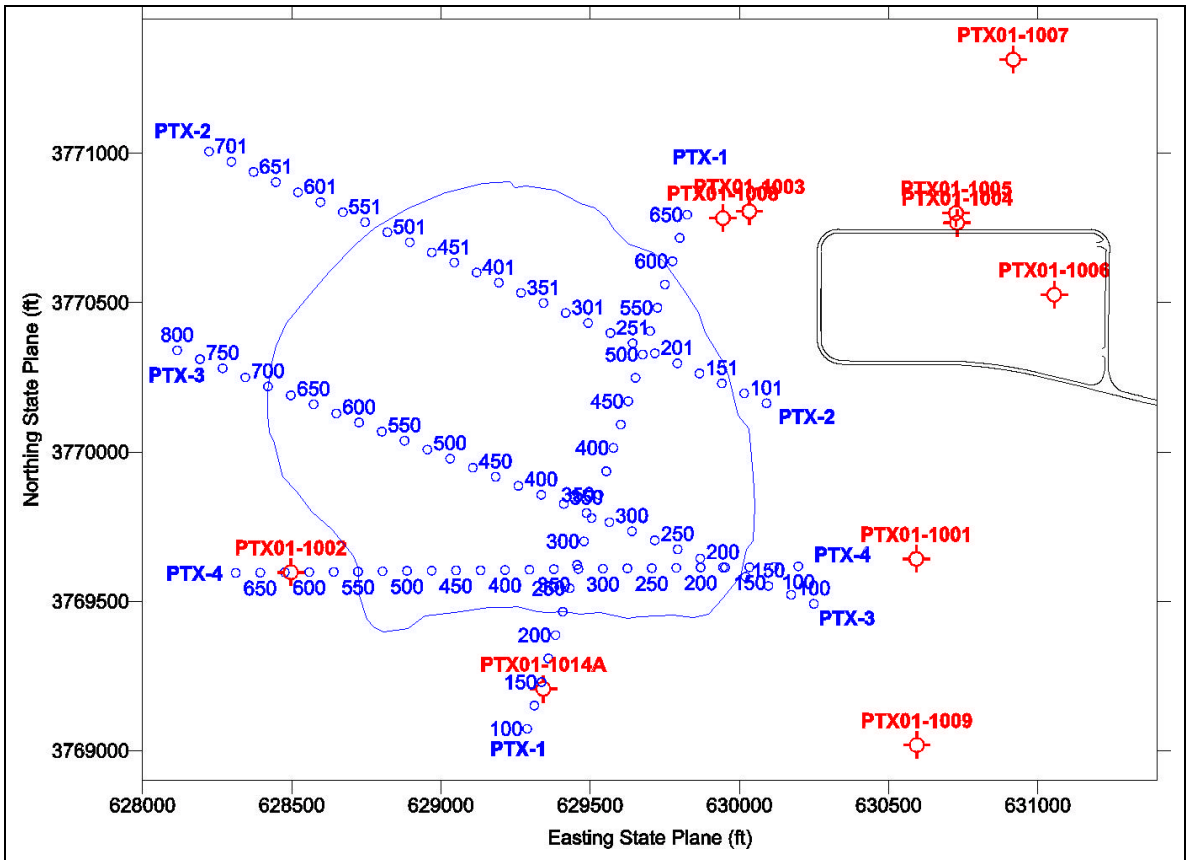

Figure 1. Location map of the seismic reflection profiles collected in this study. Irregular circular feature is outline of Playa 3.

4.1 Seismic Reflection Data

4.1.1 Vertical Seismic Profiles (VSP)

4.1.2 Vertical Seismic Profile Acquisition

Vertical seismic profiles were collected in wells PTX01-1008, and PTX01-1009 at Playa 3 (Figure 1). These data include both compressional wave (p) and shear wave (s) recordings. The VSPs were collected to provide information on the subsurface p and s wave velocities of the geologic strata at and above the location of possible DNAPL/LNAPL contamination (Figures 3-6).

The VSP data were used to construct seismic models to investigate the probable amplitude versus offset (AVO) response that could be recorded by the surface seismic survey if free-phase LNAPL or DNAPL has replaced existing pore fluids. In addition, the subsurface velocity information is needed to perform high-fidelity ties between the surface seismic profiles and the borehole lithology information. The velocity versus depth information obtained from the VSPs is used to convert the seismic times to depth.

Seismic recordings were made at 1 meter increments from the bottom of the borehole to approximately 1 meter below land surface using a three geophone (1 vertical, 2 horizontal) Geostuff™ sonde and a 10 lb. sledgehammer source. For p-wave acquisition a vertical steel cylinder was placed on the ground and struck four to six times. The data from each hit was vertically summed with the preceding hits in the seismograph and written to disk as a single record for each level. For s-wave acquisition strike plates were mounted on the ends of an 8 ft horizontal plank and a truck was driven on the plank to couple the plank to the ground. Each end of the plank was struck six to eight times, first from one side of the vehicle and then the other. The summed records for each source orientation were written to disk separately for each level. The recording parameters for each VSP are summarized in the Table 1.

Table 1. Summary of VSP recording parameters.

	PTX01-1008	**PTX01-1009**
No. of VSP runs	1 P, 1 S	1 P, 1 S
Recorded depth P wave (m from TOC)	3-85	3-87
Recorded depth S wave (m from TOC)	3-85	30-87
Source offset P wave (m)	3.0	3.0
Source offset S wave (m)	3.05	3.0
No. of source hits P-wave	6	6
No. of source hits S-wave	6	6
Depth increment (m)	1	1
Sample rate P-wave (ms)	0.125	0.125
Sample rate S-wave (ms)	0.250	0.250
Record length P-wave (ms)	500	700
Record length S-wave (ms)	500	700
Seismograph	Seistronix RAS-24	Seistronix RAS-24

4.1.3 Vertical Seismic Profile Data Processing

A generalized data processing flow diagram for the VSP data is included below (Figure 2). The PC based VISTA seismic processing software (Seismic Image Software, Ltd.) was used to process the data. In the field some rudimentary data processing was also performed for QA/QC purposes using VISTA. The field QA/QC ensured that usable data were recorded. First arrival times were picked on the p-wave records and the better of the two channels selected on the s-wave records. These times were corrected for source offset from the borehole to true vertical travel time (TVT), or zero-offset time, using a straight raypath assumption. The velocity profile, average velocity and interval velocity, for each borehole was computed (Tables 2-5, Figures 3-6). The average velocity (total depth divided by total time) from the surface to the recorded depth was used to convert the recorded time to depth. The interval velocity, or velocity of the material between recorded levels, is an approximate indicator of lithologic changes in the borehole.

For correlation of the VSP data to the surface seismic data, displays of the upward migrating wavefield data were shifted to two-way reflection time (twice TVT) and narrow (3-10 trace) front corridor stacks were produced. Because the time-depth relationship for the front corridor stack is known, the depth to the reflectors in the subsurface can be determined.

The data tables and interval velocity curves from the best VSP profiles, p-wave and s-wave, recorded in boreholes PTX01-1008, and PTX01-1009 are shown on the following pages. The times and velocities very near the surface are unreliable because the seismic ray path is not favorably oriented with respect to the geophone. Thus, no velocity information is reported for the upper few meters of the borehole. In addition, poor picks are edited. These occur where the time picked for a shallow level is later than for a deeper one (negative velocity). Often this is a result of poor well construction, tool slippage, or poor geophone coupling to the casing.

Generalized Vertical Seismic Profile Data Processing Flow

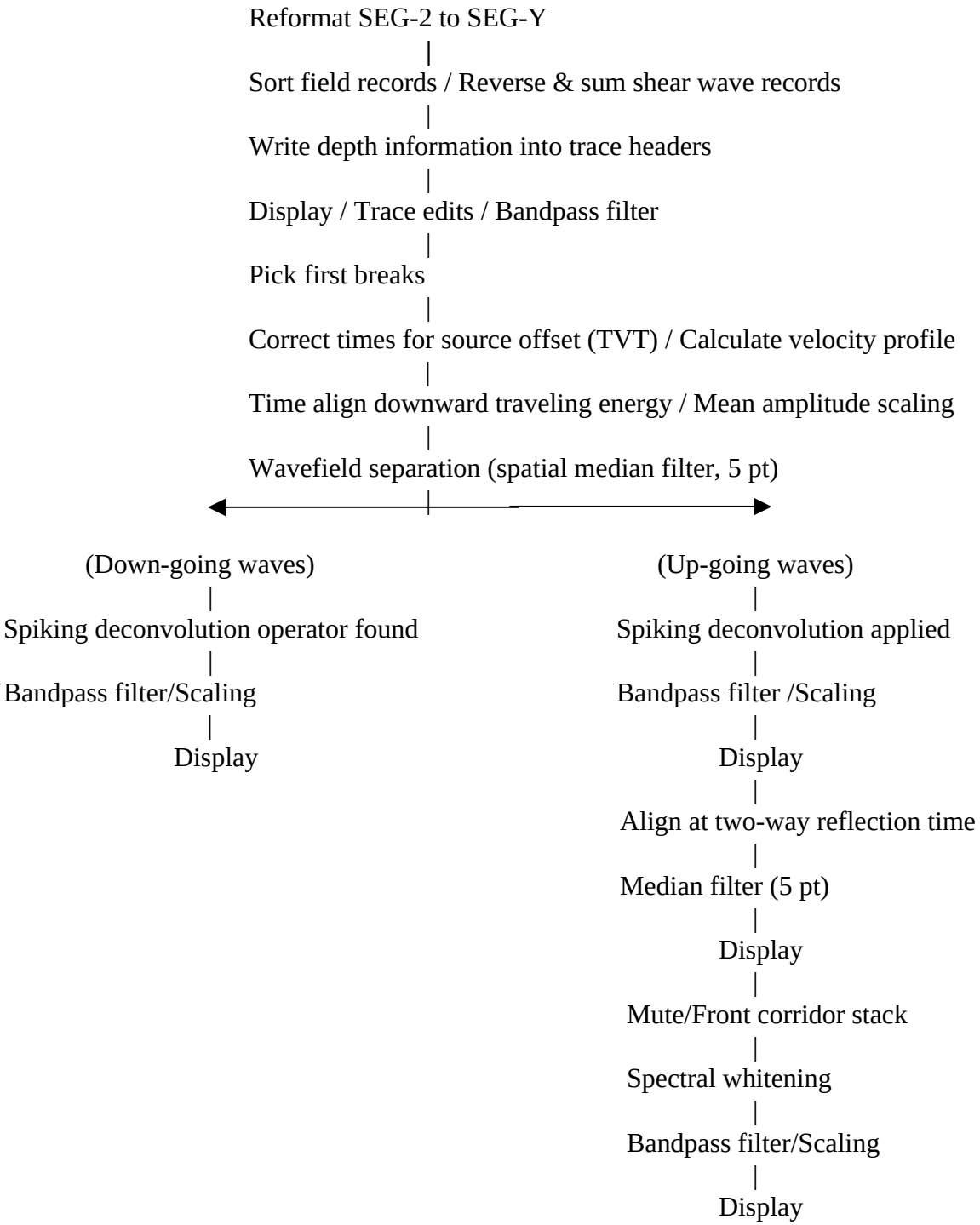

Figure 2. VSP data processing flow.

Table 2. P-wave velocity table from well PTX01-1008

Well PTX01-1008

P-Wave Vertical Seismic Profile
GL = 1087.14 m TOC = 1.0 m

(Offset = 3 m)

Seq. No.	Depth (TOC) (m)	Pick Time (ms)	Depth (GL) (ft)	True Vertical Time (ms)	Average Velocity (ft/s)	Interval Velocity (ft/s)	Two-way Time (ms)
48	3	18.7500	7.14	11.01	648	648	22.01
47	4	18.6250	10.42	13.54	769	1296	27.08
46	5	18.3750	13.70	14.92	918	2370	29.84
45	6	19.1250	16.98	16.55	1026	2021	33.09
44	7	19.2500	20.26	17.31	1170	4267	34.63
43	8	19.3750	23.54	17.88	1317	5852	35.75
42	9	19.8750	26.82	18.66	1437	4190	37.32
41	10	19.7500	30.10	18.77	1604	28863	37.54
40	11	20.0000	33.38	19.18	1740	7972	38.37
39	12	20.6250	36.66	19.92	1841	4457	39.84
38	13	21.7500	39.94	21.12	1891	2737	42.24
37	14	22.3750	43.23	21.82	1981	4699	43.63
36	15	23.1250	46.51	22.62	2056	4064	45.25
35	16	23.6250	49.79	23.18	2148	5937	46.35
34	17	24.5000	53.07	24.09	2203	3595	48.18
33	18	25.1250	56.35	24.75	2277	4963	49.50
32	19	25.8750	59.63	25.53	2336	4210	51.06
31	20	26.6250	62.91	26.31	2392	4231	52.61
30	21	27.2500	66.19	26.95	2456	5058	53.91
29	22	27.7500	69.47	27.48	2528	6285	54.95
28	23	28.3750	72.75	28.12	2587	5101	56.24
27	24	29.1250	76.03	28.88	2632	4288	57.77
26	25	29.7500	79.31	29.52	2686	5130	59.05
25	26	30.8750	82.60	30.66	2694	2892	61.32
24	27	31.2500	85.88	31.05	2766	8441	62.09
23	28	32.0000	89.16	31.81	2803	4317	63.61
22	29	32.3750	92.44	32.19	2871	8494	64.39
21	30	32.7500	95.72	32.58	2938	8517	65.16
20	31	33.6250	99.00	33.46	2959	3721	66.92
19	32	34.6250	102.28	34.47	2968	3262	68.93
18	33	35.6250	105.56	35.47	2976	3263	70.94
17	34	44.0000	108.84	43.82	2484	393	87.64
16	35	44.1250	112.12	43.96	2551	24343	87.91
15	36	44.3750	115.40	44.21	2610	12691	88.43
14	37	45.2500	118.68	45.10	2632	3725	90.19
13	38	45.5000	121.97	45.35	2689	12748	90.71
12	39	46.5000	125.25	46.36	2702	3266	92.71
11	40	47.7500	128.53	47.61	2700	2617	95.22
10	41	48.7500	131.81	48.61	2711	3268	97.23
9	42	50.0000	135.09	49.87	2709	2618	99.74
8	43	50.8750	138.37	50.75	2727	3733	101.49

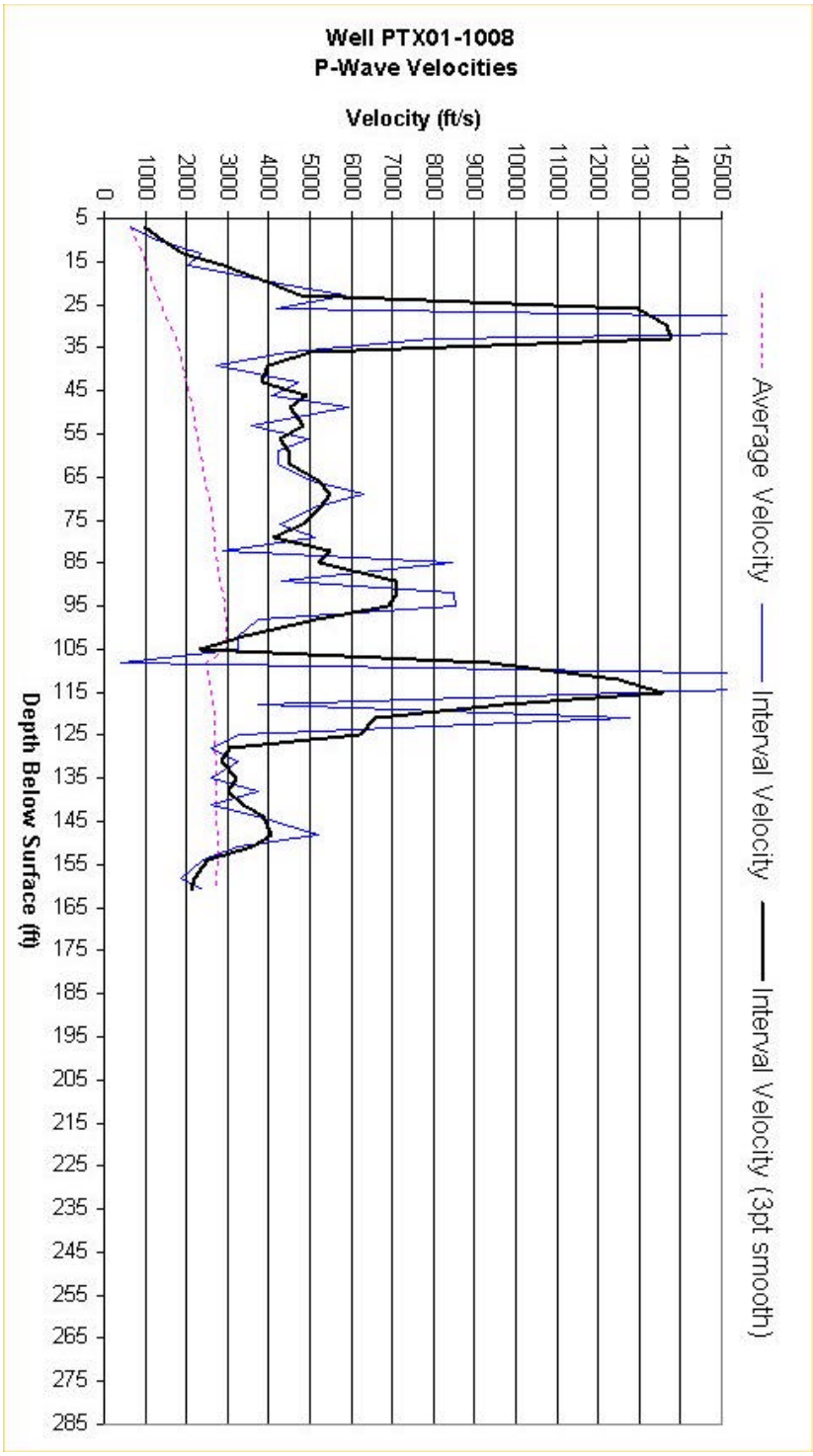

Figure 3. Graph of p-wave interval velocity, smoothed interval velocity, and average velocity versus depth in well PTX01-1008.

Table 3. S-wave velocity table from well PTX01-1008

Well PTX01-1008

GL = 1087.14 m TOC = 1.0 m

(Offset = 3.05 m)

Seq. No.	Depth (TOC) (m)	Pick Time (ms)	Depth (GL) (ft)	True Vertical Time (ms)	Average Velocity (ft/s)	Interval Velocity (ft/s)	Two-way Time (ms)
83	3	53.7500	7.14	31.21	229	229	62.42
82	4	49.9375	10.42	36.01	289	683	72.03
81	5	.	13.70	.	.	.	.
80	6	45.9375	16.98	39.58	429	1842	79.15
79	7	.	20.26				
78	8	44.6250	23.54	41.07	573	4395	82.14
77	9	46.6875	26.82	43.74	613	1227	87.48
76	10	48.3125	30.10	45.85	657	1560	91.69
75	11	.	33.38	.	.	.	.
74	12	50.5000	36.66	48.72	753	2284	97.44
73	13	54.6250	39.94	52.99	754	768	105.98
72	14	60.0000	43.23	58.45	739	600	116.91
71	15	.	46.51	.	.	.	.
70	16	.	49.79	.	.	.	.
69	17	.	53.07	.	.	.	.
68	18	.	56.35	.	.	.	.
67	19	.	59.63	.	.	.	.
66	20	.	62.91	.	.	.	.
65	21	.	66.19	.	.	.	.
64	22	.	69.47	.	.	.	.
63	23	.	72.75	.	.	.	.
62	24	65.4375	76.03	64.88	1172	5107	129.76
61	25	66.5000	79.31	65.98	1202	2985	131.95
60	26	69.8750	82.60	69.37	1191	968	138.74
59	27	76.5000	85.88	75.99	1130	496	151.97
58	28	81.6875	89.16	81.18	1098	632	162.36
57	29	85.2500	92.44	84.75	1091	917	169.51
56	30	86.6875	95.72	86.22	1110	2243	172.44
55	31	88.5625	99.00	88.11	1124	1731	176.23
54	32	90.3750	102.28	89.95	1137	1791	179.89
53	33	92.5625	105.56	92.15	1146	1489	184.30
52	34	.	108.84	.	.	.	.
51	35	94.3125	112.12	93.94	1194	3666	187.88
50	36	.	115.40	.	.	.	.
49	37	99.3750	118.68	99.02	1199	1291	198.05
48	38	.	121.97	.	.	.	.
47	39	100.6250	125.25	100.31	1249	5119	200.61
46	40	.	128.53	.	.	.	.
45	41	102.5000	131.81	102.21	1290	3453	204.41
44	42	107.1250	135.09	106.83	1264	709	213.66
43	43	108.1875	138.37	107.91	1282	3057	215.81

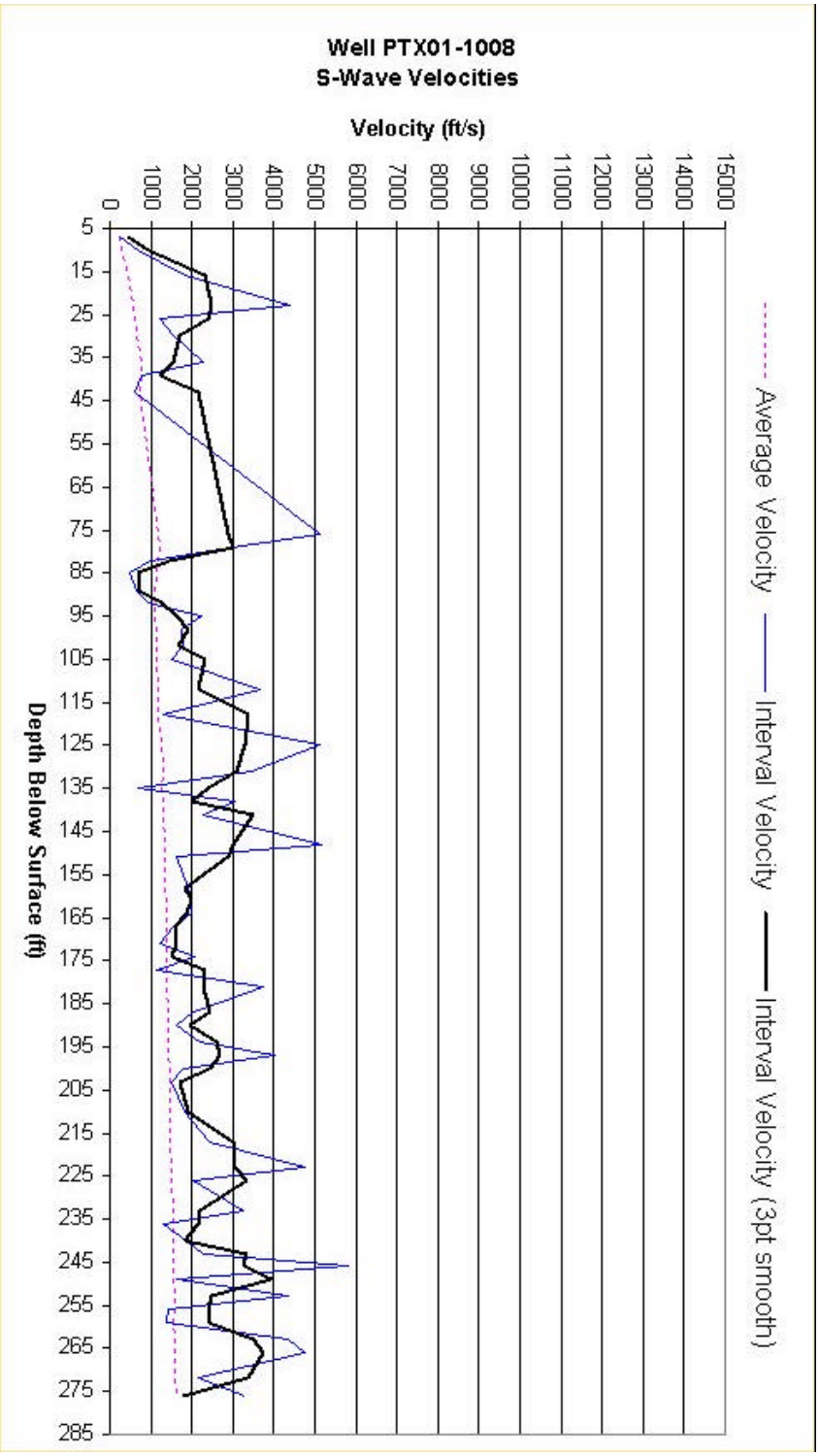

Figure 4. Graph of s-wave interval velocity, smoothed interval velocity, and average velocity versus depth in well PTX01-1008.

Table 4. P-wave velocity table from well PTX01-1009

Well PTX01-1009

GL = 1087.07 m TOC = 1.0 m

(Offset = 3 m)

Seq. No.	Depth (TOC) (m)	Pick Time (ms)	Depth (GL) (ft)	True Vertical Time (ms)	Average Velocity (ft/s)	Interval Velocity (ft/s)	Two-way Time (ms)
85	3	18.0000	6.56	9.98	657	657	19.97
84	4	17.8750	9.84	12.64	779	1236	25.28
83	5	17.5000	13.12	14.00	937	2412	28.00
82	6	16.5000	16.40	14.15	1159	22073	28.30
81	7	16.2500	19.69	14.53	1354	8504	29.07
80	8	16.6250	22.97	15.28	1503	4396	30.56
79	9	17.0000	26.25	15.92	1649	5152	31.84
78	10	17.6250	29.53	16.72	1766	4086	33.44
77	11	18.5000	32.81	17.72	1852	3283	35.44
76	12	19.5000	36.09	18.81	1918	3001	37.63
75	13	20.5000	39.37	19.89	1980	3052	39.78
74	14	21.3750	42.65	20.83	2048	3491	41.66
73	15	22.2500	45.93	21.76	2111	3534	43.51
72	16	23.2500	49.21	22.80	2159	3147	45.60
71	17	24.3750	52.49	23.96	2191	2831	47.92
70	18	25.2500	55.77	24.87	2243	3612	49.73
69	19	26.1250	59.06	25.77	2292	3630	51.54
68	20	27.1250	62.34	26.79	2327	3205	53.59
67	21	28.0000	65.62	27.69	2370	3657	55.38
66	22	28.8750	68.90	28.58	2410	3667	57.17
65	23	30.0000	72.18	29.72	2428	2878	59.45
64	24	30.8750	75.46	30.62	2465	3683	61.23
63	25	32.0000	78.74	31.75	2480	2885	63.51
62	26	33.1250	82.02	32.89	2494	2888	65.78
61	27	34.0000	85.30	33.78	2526	3699	67.55
60	28	35.1250	88.58	34.91	2537	2892	69.82
59	29	35.8750	91.86	35.67	2575	4313	71.34
58	30	37.1250	95.14	36.93	2576	2610	73.86
57	31	38.3750	98.43	38.18	2578	2611	76.37
56	32	38.8750	101.71	38.69	2628	6437	77.39
55	33	39.7500	104.99	39.58	2653	3719	79.15
54	34	40.3750	108.27	40.21	2693	5185	80.42
53	35	41.5000	111.55	41.34	2698	2903	82.68
52	36	42.1250	114.83	41.97	2736	5194	83.94
51	37	43.0000	118.11	42.85	2756	3727	85.70
50	38	43.8750	121.39	43.73	2776	3728	87.46
49	39	44.7500	124.67	44.61	2795	3729	89.22
48	40	45.6250	127.95	45.49	2813	3731	90.98
47	41	46.2500	131.23	46.12	2845	5209	92.24
46	42	47.5000	134.51	47.37	2839	2619	94.75

45	43	48.8750	137.80	48.75	2827	2382	97.50
44	44	50.0000	141.08	49.88	2828	2909	99.76
43	45	50.7500	144.36	50.63	2851	4353	101.26
42	46	52.0000	147.64	51.88	2845	2620	103.77
41	47	53.0000	150.92	52.89	2854	3272	105.78
40	48	54.2500	154.20	54.14	2848	2620	108.28
39	49	55.3750	157.48	55.27	2849	2910	110.53
38	50	56.1250	160.76	56.02	2870	4357	112.04
37	51	57.0000	164.04	56.90	2883	3739	113.80
36	52	57.8750	167.32	57.78	2896	3739	115.55
35	53	58.6250	170.60	58.53	2915	4360	117.06
34	54	59.6250	173.88	59.53	2921	3274	119.06
33	55	60.8750	177.17	60.78	2915	2621	121.56
32	56	61.8750	180.45	61.78	2921	3275	123.57
31	57	63.1250	183.73	63.03	2915	2622	126.07
30	58	64.7500	187.01	64.66	2892	2018	129.32
29	59	65.7500	190.29	65.66	2898	3275	131.32
28	60	66.8750	193.57	66.79	2898	2912	133.58
27	61	67.6250	196.85	67.54	2915	4363	135.08
26	62	68.5000	200.13	68.42	2925	3742	136.83
25	63	69.2500	203.41	69.17	2941	4364	138.34
24	64	70.2500	206.69	70.17	2946	3276	140.34
23	65	71.0000	209.97	70.92	2961	4365	141.84
22	66	71.8750	213.25	71.80	2970	3743	143.60
21	67	72.7500	216.54	72.67	2980	3744	145.35
20	68	73.7500	219.82	73.68	2984	3277	147.35
19	69	74.3750	223.10	74.30	3003	5236	148.61
18	70	75.0000	226.38	74.93	3021	5237	149.86
17	71	76.1250	229.66	76.06	3020	2914	152.11
16	72	76.7500	232.94	76.68	3038	5238	153.36
15	73	77.8750	236.22	77.81	3036	2914	155.61
14	74	79.0000	239.50	78.93	3034	2914	157.87
13	75	80.0000	242.78	79.93	3037	3278	159.87
12	76	80.6250	246.06	80.56	3054	5239	161.12
11	77	81.2500	249.34	81.19	3071	5239	162.37
10	78	82.0000	252.62	81.94	3083	4368	163.88
9	79	83.1250	255.91	83.06	3081	2914	166.13
8	80	84.0000	259.19	83.94	3088	3746	167.88
7	81	84.8750	262.47	84.82	3095	3746	169.63
6	82	85.7500	265.75	85.69	3101	3746	171.38
5	83	86.7500	269.03	86.69	3103	3278	173.38
4	84	87.6250	272.31	87.57	3110	3746	175.14
3	85	88.7500	275.59	88.69	3107	2915	177.39
2	86	89.3750	278.87	89.32	3122	5242	178.64
1	87	90.3750	282.15	90.32	3124	3279	180.64

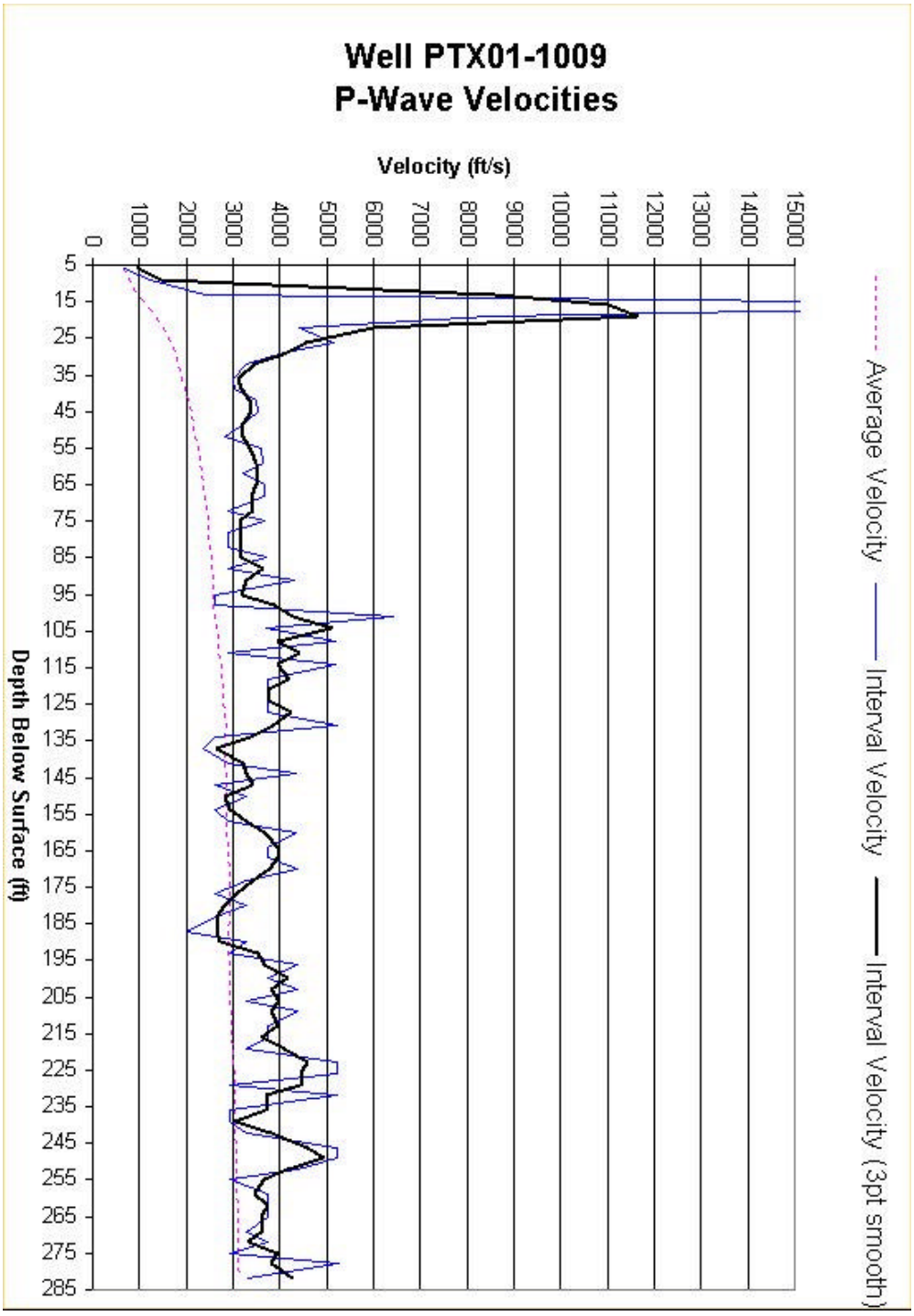

Figure 5. Graph of p-wave interval velocity, smoothed interval velocity, and average velocity versus depth in well PTX01-1009.

Table 5. S-wave velocity table from well PTX01-1009

Well PTX01-1009

GL = 1087.07 m TOC = 1.0 m

(Offset = 3 m)

Seq. No.	Depth (TOC) (m)	Pick Time (ms)	Depth (GL) (ft)	True Vertical Time (ms)	Average Velocity (ft/s)	Interval Velocity (ft/s)	Two-way Time (ms)
84	4	34.5625	9.84	24.44	403	403	48.88
83	5	36.7500	13.12	29.40	446	661	58.80
82	6	36.9375	16.40	31.67	518	1443	63.35
81	7	36.7500	19.69	32.87	599	2742	65.74
80	8	38.8750	22.97	35.73	643	1147	71.46
79	9	41.1250	26.25	38.51	682	1182	77.01
78	10	43.0000	29.53	40.79	724	1435	81.59
77	11	46.3125	32.81	44.36	740	920	88.72
76	12	48.0000	36.09	46.31	779	1683	92.62
75	13	51.3750	39.37	49.84	790	929	99.68
74	14	55.0625	42.65	53.65	795	861	107.30
73	15	56.6250	45.93	55.37	830	1912	110.74
72	16	58.6250	49.21	57.49	856	1549	114.97
71	17	62.4375	52.49	61.37	855	845	122.74
70	18	64.2500	55.77	63.27	881	1723	126.54
69	19	65.7500	59.06	64.86	911	2072	129.71
68	20	68.3125	62.34	67.48	924	1252	134.95
67	21	69.2500	65.62	68.48	958	3257	136.97
66	22	72.0000	68.90	71.28	967	1175	142.55
65	23	73.5000	72.18	72.83	991	2117	145.65
64	24	75.1250	75.46	74.49	1013	1967	148.99
63	25	77.1875	78.74	76.59	1028	1564	153.18
62	26	80.1875	82.02	79.62	1030	1085	159.23
61	27	81.4375	85.30	80.90	1054	2554	161.80
60	28	82.8125	88.58	82.31	1076	2335	164.61
59	29	83.1875	91.86	82.71	1111	8039	165.43
58	30	85.6875	95.14	85.23	1116	1303	170.47
57	31	85.9375	98.43	85.51	1151	11787	171.02
56	32	86.1250	101.71	85.72	1186	15366	171.45
55	33	86.5625	104.99	86.18	1218	7131	172.37
54	34	87.4375	108.27	87.08	1243	3671	174.16
53	35	89.0000	111.55	88.66	1258	2080	177.31
52	36	91.6875	114.83	91.35	1257	1216	182.71
51	37	93.0625	118.11	92.74	1274	2363	185.48
50	38	95.2500	121.39	94.94	1279	1493	189.88
49	39	96.1250	124.67	95.83	1301	3693	191.65
48	40	.	127.95	.	.	.	.
47	41	98.6250	131.23	98.35	1334	2602	196.70
46	42	101.6875	134.51	101.42	1326	1070	202.83
45	43	.	137.80	.	.	.	.
44	44	104.6250	141.08	104.37	1352	2221	208.74

43	45	105.6875	144.36	105.44	1369	3062	210.89
42	46	108.6875	147.64	108.45	1361	1092	216.89
41	47	110.7500	150.92	110.52	1366	1586	221.03
40	48	111.1875	154.20	110.96	1390	7348	221.92
39	49	112.4375	157.48	112.22	1403	2610	224.44
38	50	114.0000	160.76	113.79	1413	2092	227.57
37	51	.	164.04	.	.	.	.
36	52	115.8750	167.32	115.68	1446	3475	231.35
35	53	118.8125	170.60	118.62	1438	1116	237.23
34	54	.	173.88	.	.	.	.
33	55	121.6250	177.17	121.44	1459	2325	242.88
32	56	124.8750	180.45	124.69	1447	1009	249.38
31	57	125.8750	183.73	125.69	1462	3264	251.39
30	58	126.7500	187.01	126.57	1477	3728	253.15
29	59	129.1875	190.29	129.02	1475	1344	258.03
28	60	.	193.57	.	.	.	.
27	61	131.8125	196.85	131.65	1495	2492	263.30
26	62	133.5000	200.13	133.34	1501	1940	266.68
25	63	.	203.41	.	.	.	.
24	64	.	206.69	.	.	.	.
23	65	135.3125	209.97	135.16	1553	5392	270.33
22	66	136.0000	213.25	135.86	1570	4746	271.71
21	67	138.1250	216.54	137.98	1569	1542	275.97
20	68	.	219.82	.	.	.	.
19	69	141.4375	223.10	141.30	1579	1978	282.60
18	70	142.9375	226.38	142.80	1585	2184	285.61
17	71	143.5625	229.66	143.43	1601	5222	286.86
16	72	146.0000	232.94	145.87	1597	1345	291.74
15	73	146.9375	236.22	146.81	1609	3489	293.62
14	74	147.4375	239.50	147.31	1626	6522	294.63
13	75	150.0000	242.78	149.88	1620	1280	299.75
12	76	.	246.06	.	.	.	.
11	77	154.0000	249.34	153.88	1620	1639	307.76
10	78	156.8125	252.62	156.69	1612	1166	313.39
9	79	.	255.91	.	.	.	.
8	80	158.7500	259.19	158.64	1634	3379	317.27
7	81	160.0625	262.47	159.95	1641	2496	319.90
6	82	.	265.75	.	.	.	.
5	83	.	269.03	.	.	.	.
4	84	.	272.31	.	.	.	.
3	85	.	275.59	.	.	.	.
2	86	166.4375	278.87	166.33	1677	2570	332.67
1	87	167.1250	282.15	167.02	1689	4758	334.05

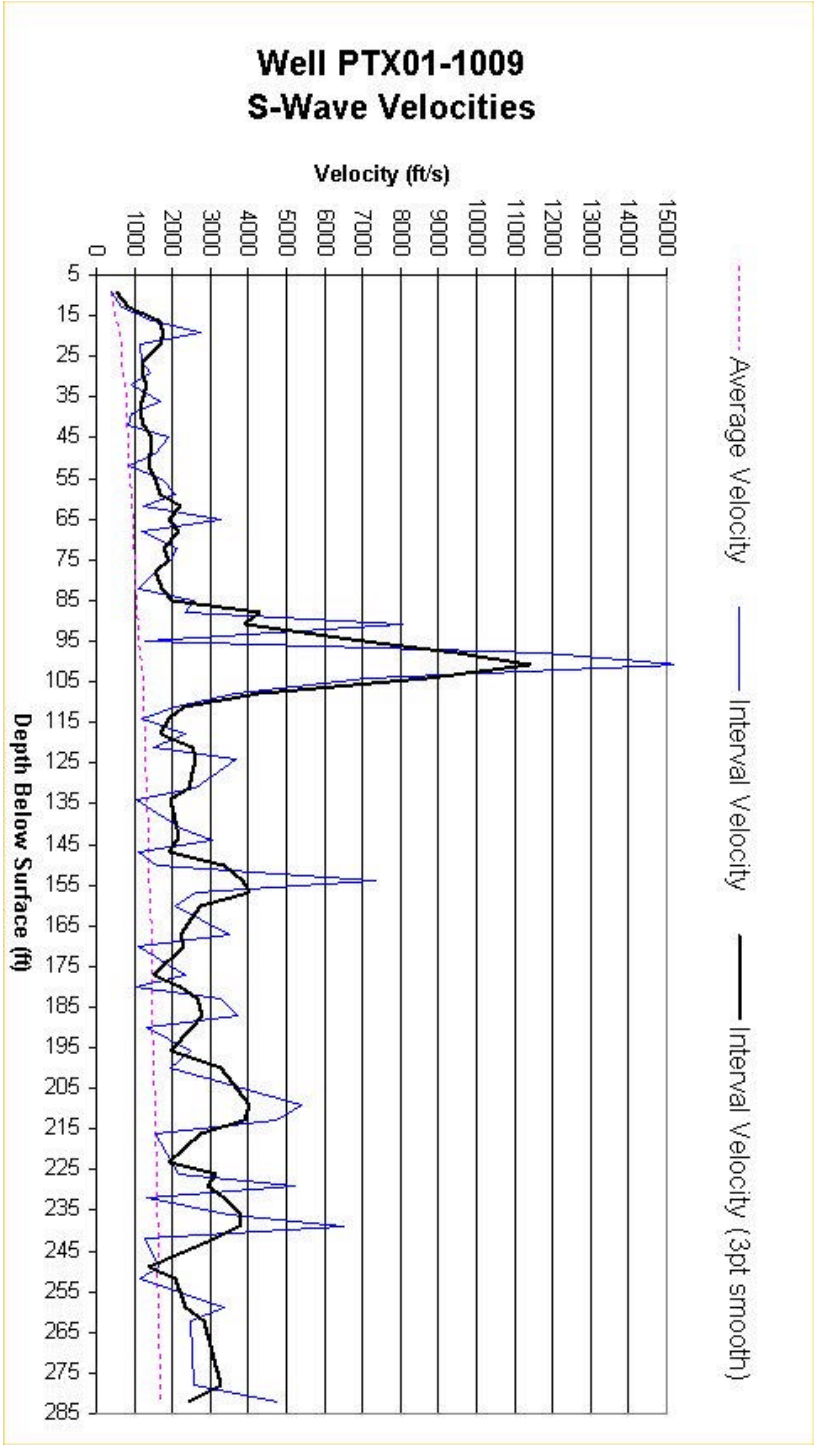

Figure 6. Graph of s-wave interval velocity, smoothed interval velocity, and average velocity versus depth in well PTX01-1009.

4.2 Amplitude Variation with Offset (AVO) Modeling

To use seismic amplitudes to detect DNAPL or LNAPL seismic modeling is performed. AVO modeling defines the background seismic amplitude response along an interface and the expected change, if any, in the reflection amplitude if the fluid type or lithology changes along the interface.

The modeling conducted in this study is a two layer one-dimensional model comparing reflection coefficient versus incident angle. The p-wave reflection coefficients were calculated using the full Zoeppritz (1919) equations as presented by Graul (2001). Zoeppritz developed a set of equations that describes the partitioning of energy in a wavefield relative to its angle of incidence at a boundary across which the bulk properties of rock change. The reflection coefficient describes the polarity (negative or positive) and amplitude of a reflected seismic wave. The inputs into the Zoeppritz equations are p-wave and s-wave velocities and bulk densities of both the substrate and superstrate.

The initial velocities were calculated from the VSPs and the densities were derived from calculations using the Gardner and others (1974) empirical relationship between p-wave velocity and density. The porosity values of the geologic units were calculated by using the difference between velocities calculated using the mineral constituents for the units reported in the core descriptions by Stoller Corp. (2001) and the VSP values. These porosities are: upper sand 31%, caliche 24%, lower sand 33%, and FGZ 27%. The physical properties of the mineral constituents, TCE, and toluene are from published values in the literature (Weast and Astle, 1980; Clark, 1966). To investigate the effect of pore fluid substitution, the Gassmann (1951; e.g. White, 1983) and Biot (1956) equations were used to calculate new velocity and density values, which were input into the Zoeppritz equations. The reflection coefficients were calculated for a range of incident angles (offsets) and plotted as a function of incident angle.

Based upon existing geologic and concentration data (Stoller Corp., 2001), any DNAPL (TCE) and/or LNAPL (toluene) contamination is accumulating either in the sand unit directly above the caliche (caprock) or in the sand unit directly overlying the fine grained zone (FGZ). The models were generated using the physical parameters listed in Table 6. For discussion and modeling proposes the sand unit above the caliche is referred to as the upper sand and the sand directly above the FGZ is referred to as the lower sand.

Figure 7 is a graph comparing reflection coefficients versus incident angles for a reflected p-wave between the sand directly overlying the caliche or “caprock”. The red solid line is a graph of reflection coefficients with various incidence angles along the contact of sand and caliche with air filling the pore spaces, i.e. the expected background response along this acoustic interface. The short dashed orange line is the response along the interface if the sand is 100% saturated with toluene and the caliche is 100% saturated with air. The long dashed green line is the expected response if both the sand and caliche are 100% saturated with toluene. Based upon p-wave and s-wave velocities from well

PTX01-1008 the expected background amplitude response is positive out to 15 degrees of incidence. Beyond 15 degrees of incidence the amplitude becomes more positive out to approximately 35 degrees. This is the critical angle, i.e., the angle where the incident wave grazes the interface between the two media rather than refracts into the lower medium. The short dashed orange line is the expected response if both the upper sand and caliche are 100% saturated with toluene. The long dashed green line is the expected amplitude response if the sand is saturated with 100% toluene and the caliche is 100% saturated with water. This last scenario was modeled because there is the possibility of perched water under the playa.

There were a number of different scenarios modeled to determine the reflection amplitude variability, if any, as a function of the amount of toluene. One scenario is when only 50% of the pores are filled with free-phase toluene and the other when 50% are filled with air. This model was identical to the response when the sand and caliche are both 100% saturated with toluene. The AVO modeling for the contact between the sand and caliche suggests that if toluene is present either in the sand, or in both the sand and caliche, the response will have higher positive amplitudes than background. Both scenarios with toluene pore filled sand suggest the reflection amplitudes go to critical angle of 10 to 15 degrees prior to the background response.

In Figure 7A the same contact as shown in Figure 7, the upper sand and caliche, is modeled. The only difference is that the p-wave and s-wave velocity and density values are derived from the VSP data from well PTX01-1009. There appears to be little or no AVO response between the background (Figure 7A solid red line) and when the upper sand pores are 100% saturated with toluene. However, if there is a mixture of air and free-phase toluene in the pores of upper sand there is a substantial AVO response. The blue, long and short dashed line is the expected response if only 10% of the upper sand pores are filled with air and 90% with free-phase toluene. The short dashed green line is the expected response if the upper sand pores are filled with 50% air and 50% free-phase toluene. This partial mixture of air and free-phase toluene is the mostly likely scenario in the subsurface under Playa 3.

Figures 8 and 8A are graphs of reflection coefficients versus incidence angle for the contact between the upper sand and the caliche, but with free-phase TCE replacing the existing pore fluid (air). The difference between the two figures is that the Figure 8 graph is based on velocities and densities from well PTX01-1008 and Figure 8A is based on velocities from well PTX01-1009. In Figure 8 the red solid line is considered the background response along the interface, which is the same as in Figure 7. Of significance is the change in the background response using different velocity and density values. The long dashed blue line is the expected response if the upper sand pores are 100% saturated with free phase TCE and the caliche is saturated with air. The short dashed green line is the expected response if both the upper sand and caliche are 100% saturated with free-phase TCE. There appears to be a difference in the background curve (solid red) and the curve representing a situation when only the upper sand is 100% saturated with free-phase TCE (long dashed blue line). If both the upper sand and caliche

are 100% saturated with free-phase TCE (short dashed green), there is only a slight difference. This is shown when the curve representing both upper sand and caliche are saturated with TCE. The reflection coefficients (amplitudes) are only slightly less than background and the background curve reach the critical angle approximately 5 to 6 degrees before the curve representing both the upper sand and caliche with 100% free phase TCE. If the upper sand is saturated with 100% TCE, the model curve response shows the reflection coefficients are much lower than background response. When the upper sand is 100% saturated with TCE the model indicates that the TCE saturated sand reaches critical angle approximately 10 to 12 degrees after the background curve response reaches critical angle. There also appears to be a slight difference in the AVO gradient between the background curve and 100% TCE saturated upper sand curve (long dash blue curve). The 100% saturated upper sand curve appears to flatten out to 35 degrees of incident angle with increasing slope. The background curve slope starts to increase in slope approximately at 20 degrees of incident angle. The curve responses in Figure 8 suggest that if TCE is present as a separate phase, the only AVO response that could be detected is where the TCE is present only in the upper sand. If TCE is present in both the upper sand and the caliche it most likely could not be detected on the seismic data (short dashed green).

Figure 8A are the expected curve responses for the same upper sand and caliche interface as Figure 8 except that velocities and densities were used from well PTX01-1009. There is considerable difference between the figures. The long dashed blue line is the expected response if the upper sand pores are 100% saturated with TCE and the caliche pores are 100% saturated with air. In this scenario the response is flat, even to an incident angle of 10 degrees. At 10 degrees the reflection coefficient increases to approximately 23 degrees. The critical angle is also approximately 23 degrees. The short dashed green line is the expected response if the both the upper sand and caliche pores are 100% saturated with TCE. If free-phase TCE saturates either the pores of the upper sand or both the pores in the upper sand and caliche, the model suggests that the critical angle is reached between 25 and 30 degrees, i.e. before the background response (Figure 8A). If TCE is present, both scenarios suggest that the AVO analysis might detect the free-phase. Overall, the project team opinion is that the velocity data from well PTX01-1009 is of higher quality than the data from well PTX01-1008.

Figure 9 represents AVO models for the contact between the lower sand and the FGZ. Velocity and density values were used from well PTX01-1009. In the bottom half of well PTX01-1008 the VSP sonde was not working properly, therefore there is no shear wave information for that interval. The solid red line is the background response. The orange line is the response if the lower sand is 100% saturated with toluene and the FGZ is 100% saturated with air. The short dashed blue line is the lower sand with 90% free-phase toluene and 10% water. The green line is the response if the lower sand is saturated with 50% free-phase toluene and 50% water and the FGZ is 100% saturated with air. In all the scenarios modeled it appears that, if there is free-phase toluene at the contact between the lower sand and the FGZ, there would not be a detectable AVO response.

Figure 10 shows AVO models for the contact between the lower sand and the FGZ with free-phase TCE replacing the existing pore fluid. The red graph is the expected background response with air filling the pores of both the lower sand and the FGZ. The long dashed orange graph is the expected response if the upper sand is 100% saturated with TCE and the FGZ pores are saturated with air. In this scenario there is a large AVO effect. If TCE is present, the reflection coefficients are much more negative than background and become more negative with increasing offset. This is also the case where the lower sand is 100% saturated with TCE and the FGZ is air filled. In this situation the slope of the graph is negative.

If both the lower sand and FGZ pores are 100% saturated with TCE, the reflection coefficients are more negative than the background response. Also, the background reaches critical angle approximately 10 degrees before the response where there is 100% TCE in the pores of both the lower sand and FGZ.

Table 6. P-wave, s-wave velocity and density values used for AVO modeling.

Lithology/ Unit	V_p ft/sec (m/sec)	V_s ft/sec (m/sec)	Density g/cc
Upper Sand Well PTX01-1008	5101 (1555)	1175 (358)	1.94
Upper Sand 100% Toluene	4039 (1231)	1096 (334)	2.10
Upper Sand 100% TCE Well PTX01-1008	6426 (1959)	1072 (327)	2.33
Upper Sand 100% TCE Well PTX01-1009	3185 (971)	1094 (333)	2.30
Caliche Well PTX01-1008	8494 (2590)	2335 (712)	2.21
Caliche Well PTX-01-1009	6437 (1962)	2335 (712)	2.06
Caliche 100% water Well PTX01-1008	10,039 (3061)	2254 (687)	2.20
Caliche100%Toluene Well PTX01-1008	8216 (2505)	2182 (665)	2.35
Caliche 100% TCE Well PTX01-1008	9396 (2865)	2191 (670)	2.51
Caliche 100% TCE Well PTX01-1009	7586 (2313)	2160 (658)	2.40
Lower Sand Well PTX01-1009	3746 (1142)	1166 (356)	1.80
Lower Sand 100% Toluene Well PTX01-1009	3532 (1077)	1107 (338)	2.17
Lower Sand 10% water, 90% Toluene Well PTX01-1009	3551 (1083)	1113 (339)	2.15
Lower Sand 50% water, 50%Toluene Well PTX01-1009	3635 (1108)	1135 (346)	2.06
Lower Sand 100% TCE Well PTX01-1009	5826 (1776)	1066 (325)	2.34
FGZ Well PTX01-1009	5242 (1598)	2570 (784)	1.96
FGZ 100% Toluene Well PTX01-1009	4961 (1512)	2444 (745)	2.16
FGZ 100% TCE Well PTX01-1009	6492 (1979)	2351 (717)	2.34

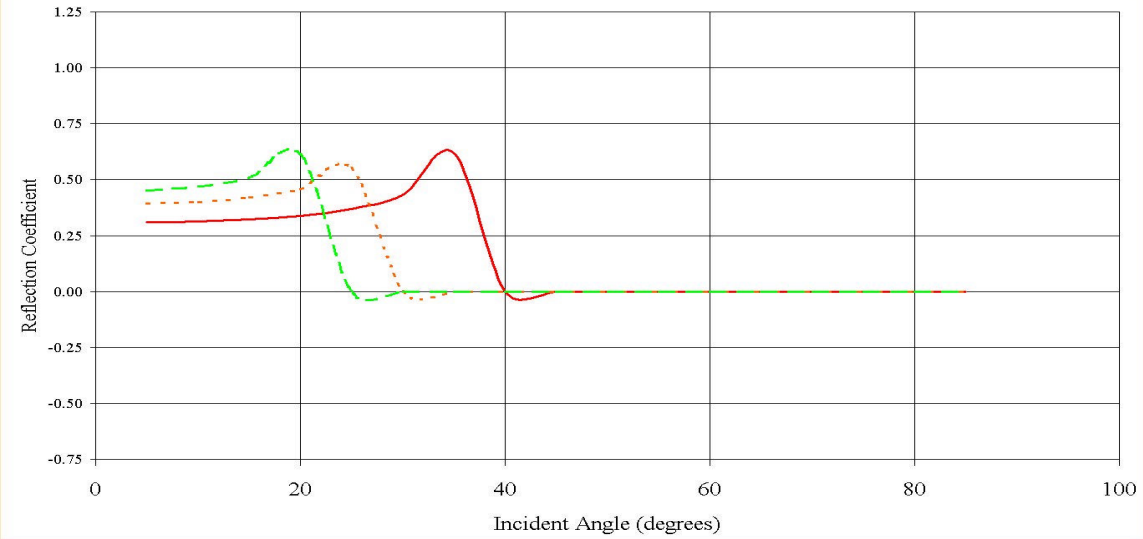

Figure 7. Graph of reflection coefficient versus incident angle for toluene at the caliche interval using input values derived from well PTX01-1008. The solid red line is the background response at the contact between the upper sand and the caliche (100% air). The orange short dashed line is the reflection coefficient versus incident angle of offset if the upper sand pores are 100% saturated with toluene. The long green dashed line is the response if the upper sand pores are 100% saturated with toluene and the caliche pores are saturated with 100% water.

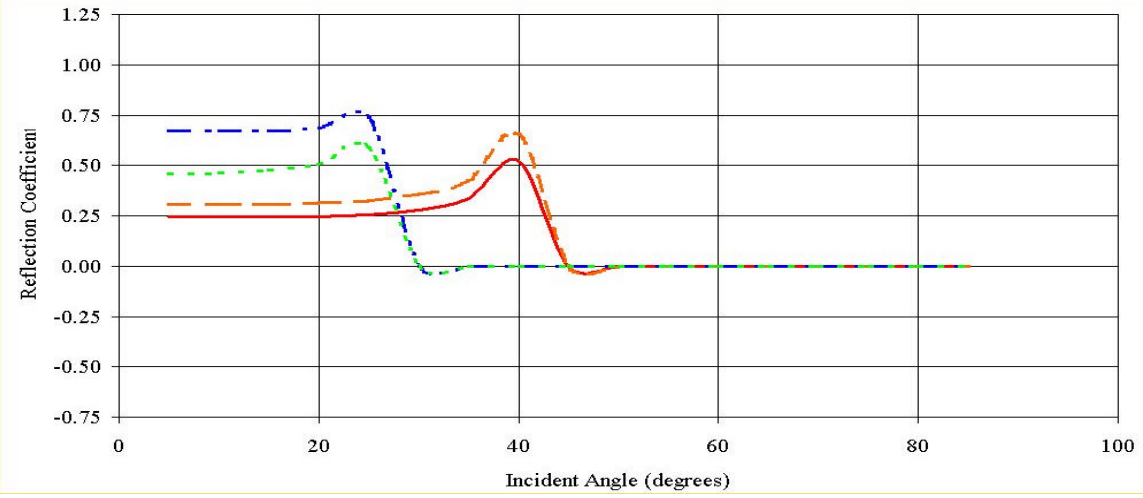

Figure 7A. Graph of reflection coefficient versus incident angle for toluene at the caliche interval using input values derived from well PTX01-1009. The solid red line is the background response at the contact between the upper sand and the caliche (100% air). The long dashed orange line is the expected response if the upper sand is 100% saturated with toluene. The two long, two short dashed blue lines represent the expected response if the upper sand pores are filled with 90% toluene, 10% air and the caliche pores are 100% saturated with air. The short dashed green line is the expected response if the upper sand pores are filled with 50% toluene, 50% air and the caliche pores are 100% saturated with air.

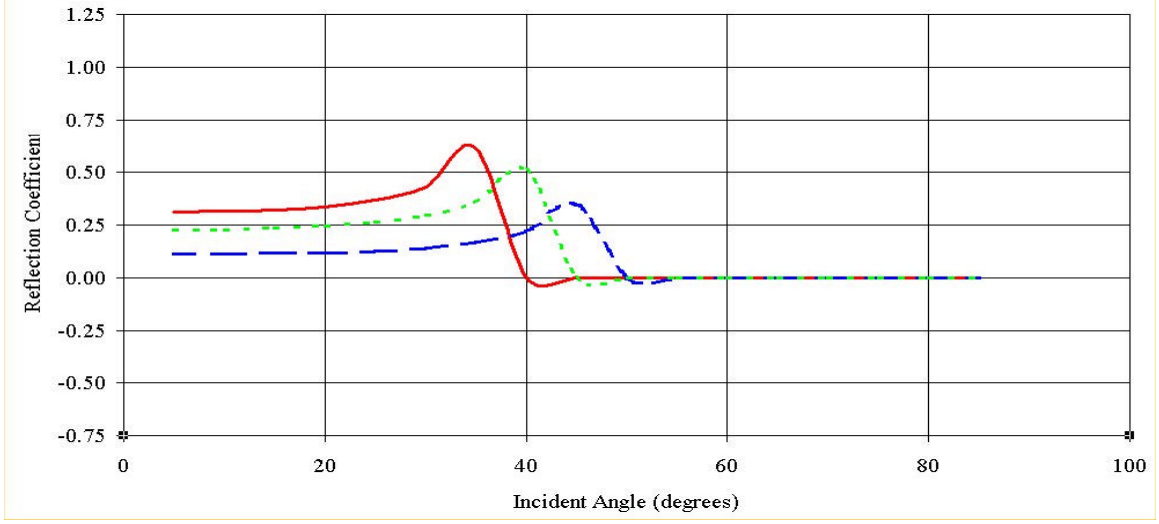

Figure 8. Graph of reflection coefficient versus incident angle of incidence for TCE at the caliche interval using input values derived from well PTX01-1008. The solid red line is the response of upper sand overlying the caliche. The blue long dashed line is the reflection coefficient versus the offset response when the upper sand pores are 100% saturated with TCE. The short dashed green line is the response if both the upper sand and caliche pores are 100% saturated with TCE.

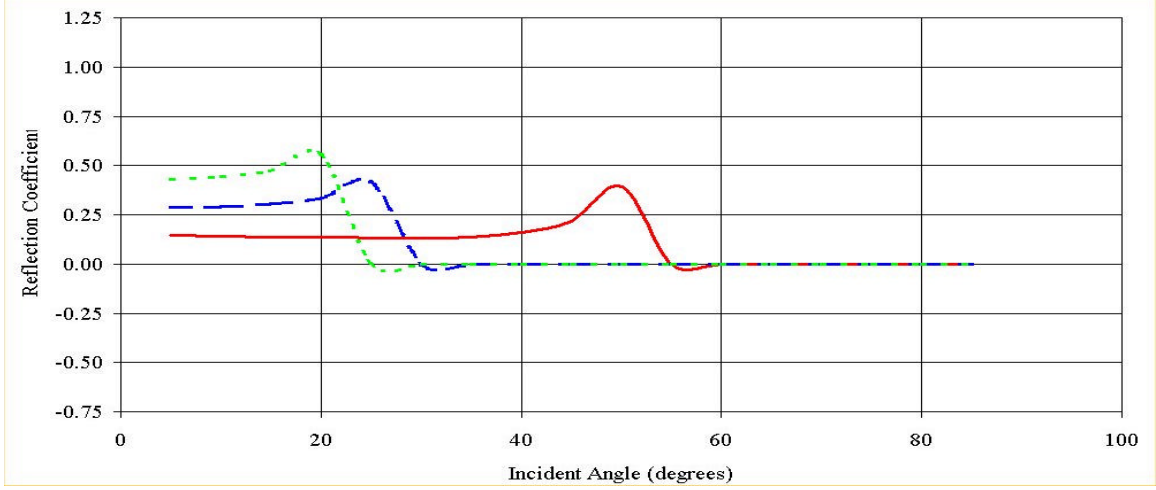

Figure 8A. Graph of reflection coefficient versus incident angle for TCE at the caliche interval using input values derived from well PTX01-1009. The solid red line is the response of upper sand overlying the caliche. The blue long dashed line is the reflection coefficient versus offset response when the upper sand pores are 100% saturated with TCE. The short dashed green line is the response if both the upper sand and caliche pores are 100% saturated with TCE.

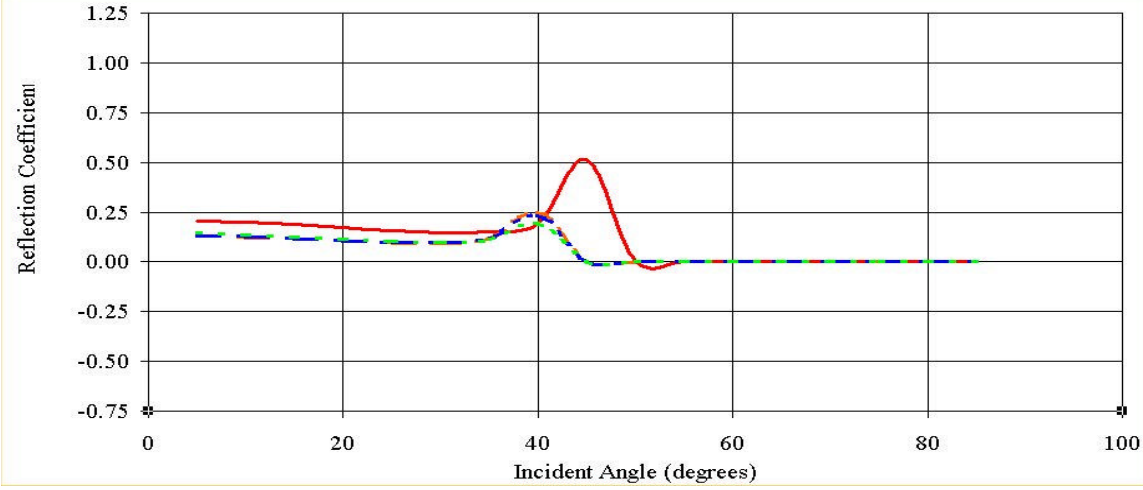

Figure 9. Graph of reflection coefficient versus incident angle for toluene at FGZ interval using input values derived from well PTX01-1009. The red solid line is the lower sand overlying the fine grain zone (FGZ) with air filling the pore spaces. The long dashed orange line is the response when the lower sand is 100% saturated with toluene and the FGZ pores are air filled. The blue and green dashed lines are the responses when there is 90% toluene and 10% water in the lower sand (blue line) and 50% toluene and 50% water in the lower sand (green) with 100 % air filling the pores in the FGZ.

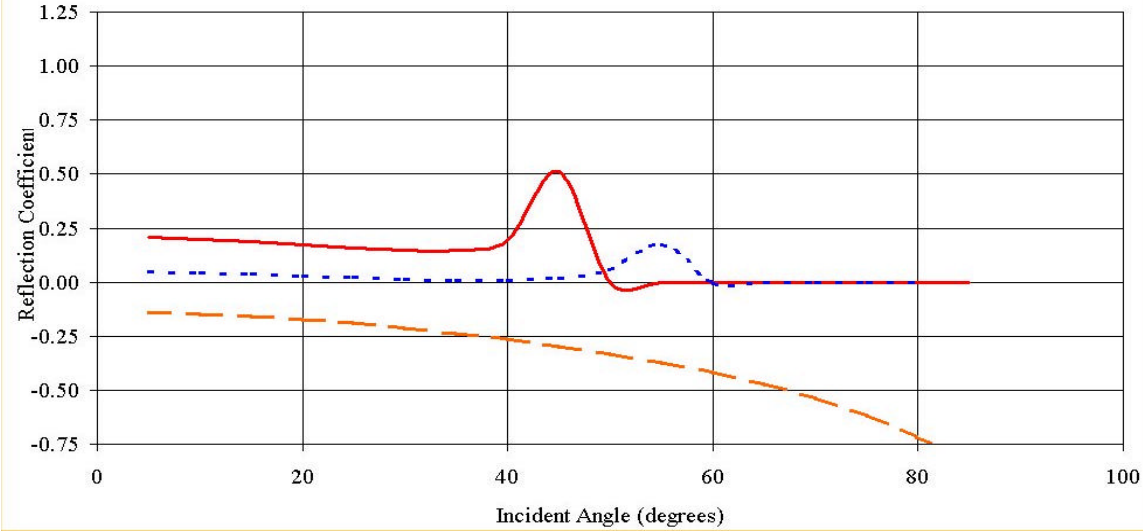

Figure 10. Graph of reflection coefficient versus incident angle for TCE at the FGZ interval using input values derived from well PTX01-1009. The solid red line is the background response where the pore spaces of both the lower sand and the FGZ are air filled. The long dashed orange line is the response if the lower sand is saturated with 100% TCE and the FGZ pores are air filled. The short dashed blue line is the expected response if both the lower sand and FGZ are 100% saturated with TCE.

4.3 Seismic Reflection Profiles

4.3.1 Seismic Reflection Acquisition

Four seismic reflection profiles were collected at Playa 3 (Figure 1). These profiles are designated lines PTX-1, PTX-2, PTX-3, and PTX-4. A single vibrator seismic source and a 120 channel Geometrics seismograph were used to record the data. The seismic acquisition parameters were chosen to optimally image both the caprock interval occurring at approximately 100 ft and the fine-grained zone occurring at approximately 300 ft depth. Other considerations were to have adequate temporal and spatial sampling necessary for high-resolution recording and to attenuate acoustic noise. In addition, the range of source-to-receiver offsets was chosen to enable AVO analysis of the target horizons. The parameters used to record the seismic profiles are compiled in Table 7.

Previous seismic reflection work at Playa 3 conducted by the Texas Bureau Economic Geology (BEG) (Paine, 1995) indicated that the seismic recording conditions were difficult. Records published from the BEG survey show surface wave energy to be quite strong and high frequencies to be greatly attenuated. The surface wave energy dominates near offsets to 300 ft. The BEG survey was designed to image the top of bedrock, whereas in this study the targets are much shallower. The requirements to image shallower targets results in recording data entirely within the seismic noise cone.

Prior to surface seismic data acquisition, walkaway noise tests were recorded in the playa and in the interplaya area (Figure 11). These noise tests confirmed the previous findings of the BEG survey. Surface waves (ground roll) are a severe problem and are present throughout the recording band. Wind noise is severe. High frequency reflections are greatly attenuated. Also, the hammer source used for the noise tests had insufficient energy to propagate seismic energy to the FGZ.

Based on the results of the noise tests, a vibrator was chosen for a seismic source. The ability to control the frequency band allows for higher resolution recording and the high energy output of the source enables propagation of energy to the deeper target. The requirement to do high-resolution recording, however, prohibited the use of source and receiver arrays used normally to attenuate ground roll. Consequently, data processing techniques were relied upon to attenuate ground roll.

The receiver group spacing and shot interval were set at one meter and three 40 Hz geophones wired in series were grouped and buried at each recording station. This arrangement resulted in nominal 60 CMP fold data. Shorter group and shot intervals were impractical given that the footprint of the vibrator pad was approximately one meter. To reduce the effect of wind noise each geophone group was buried. To further reduce the effects of wind noise (often in excess of 25 mph) much of the seismic recording was done during nighttime when the wind would be significantly reduced.

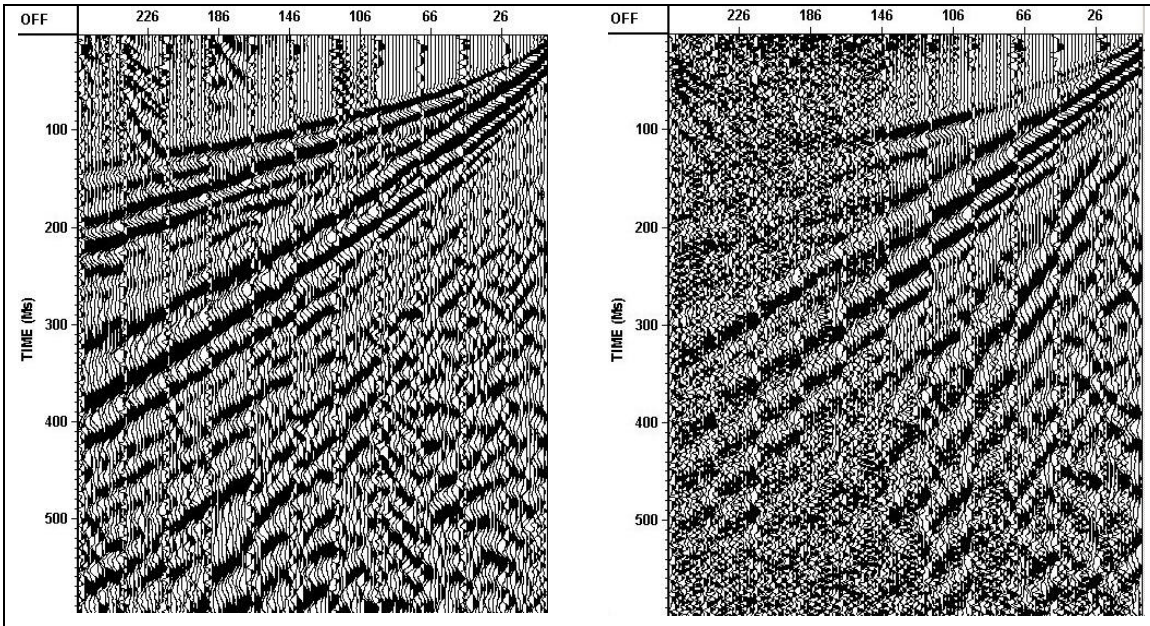

Figure 11. Walkaway noise tests. Noise test outside the playa (left), noise test inside the playa (right). Horizontal scale is offset in feet. Note the extremely strong surface wave energy. High frequency noise in playa walkaway caused by high winds. Geophone spacing 2 ft, 10 lb. hammer source. Display scaling 200 ms AGC, bandpass filter 5-10-150-200 Hz.

The spread was designed to enable AVO analysis of the target horizons and was guided by the AVO model study. For lines PTX-1 and PTX-2 an asymmetric split spread of 30 and 90 channels was used. For part of line PTX-3 and all of line PTX-4 a 50-70 channel asymmetric split spread was used. The change in the survey design was necessary when in-the-field data processing revealed that noise on the far offset channels swamped any usable signal.

After extensive field testing the vibrator sweep was set at 30-250 Hz for six seconds and six sweeps were summed per vibrator point (VP). The test program indicated that higher frequencies were not returned from the target horizons. The low frequencies were needed to image deeper layers and to stabilize residual statics computations and deconvolution operators. The vibroseis data were recorded uncorrelated. This allowed the flexibility to correlate the data with a synthetic sweep and for more data processing options in the laboratory.

Table 7. Seismic reflection profile recording parameters.

Type of survey	P-wave seismic reflection
Date recorded	February 19-27, 2002
Station interval	1 meter
Source	Industrial Vehicles International (IVI) MiniVib high-frequency vibrator 12000 lb. peak force.
Source interval	1 meter on half stations
Type of sweep	Linear
Sweep frequencies	30 to 250 Hz
Sweep length	6 seconds
Source Offset (Pad)	1.5 m nominal
Record Length	7 seconds
Listen time	1 second (7 s RL – 6 s sweep)
Recording instrument	Geometrics StrataView RX 24 bit A/D resolution
Number of channels	120
Instrument Gain	24 dB fixed
Sample interval	0.5 millisecond
Data format	SEG-Y
Data redundancy	60 Fold
Geophones	Geospace 40 Hz vertical 3 per station, bunch and buried.
Near offset	0.5 m (inline), 1.58 m (straight line)
Far offset	29.5 m, 89.5 m (lines 1,2,3) 49.5 m, 69.5 m (lines 3,4)
Cable Geometry (m)	29.5 m--0.5 m--VP--0.5 m--89.5 m (1,2,3) 49.5 m--0.5 m--VP--0.5 m--69.5 m (3,4)

4.3.2 *Seismic Reflection Data Processing*

During seismic acquisition, data were correlated and viewed daily for QA/QC purposes. Parts of seismic lines were also processed in the field to brute stack sections for quality control purposes. The platform used to process the data in the field was a laptop computer equipped with the Seismic Image Software, Ltd. VISTA seismic processing package and the Seismic Micro-Technology Kingdom seismic interpretation software

After completion of the field survey extensive detailed seismic data processing was performed at ESRI-USC's Environmental Geophysics Laboratory on the campus of the University of South Carolina. To process the data the Landmark Graphics Corp. ProMAX software operational on a Sun Microsystems Ultra-60 workstation was used. The generalized flow used to process the data is shown in Figure 13. Additional detail appears on the side panels of the seismic sections in Appendix 1.

Data processing in the laboratory began with the raw uncorrelated field data because of the greater stability of the ProMAX algorithms compared to the PC software. The in-field data processing revealed that the ground roll problem was so severe that no reflections were visible in the correlated field records (Figure 12). In addition, wind noise was often so severe that no seismic signal was discernible on the far offset channels. Various two-dimensional filtering techniques were tried and abandoned to reduce the effect of surface waves. High-pass filtering had little effect and it became quickly apparent that over much of the data set frequencies above 130 Hz were highly attenuated. Thus, the useful band of the data is approximately 30-130 Hz. Experiments with frequency-wavenumber (F-K) and slant stack (Tau-p) two-dimensional filtering techniques to attenuate surface wave energy were largely unsuccessful and resulted in the data having an unnatural "wormy" appearance. Simple intrashot and intershot trace mixing was also found to be ineffective. Only low-frequency array forming was found to be partly effective. This technique involves transforming the data into the frequency-space domain where frequency dependent mixes of traces are performed. After array forming, standard single channel spiking deconvolution and spectral whitening were preformed to balance the amplitude spectrum. Lastly, a narrow window F-K filter was applied to attenuate the residual airwave (Figure 12).

Casual examination of first arrivals on the shot records revealed that the near surface velocities within the playa and outside the playa vary considerably. Within in the playa, near surface velocities exhibit much more variation than outside the playa. In this area evidence exists of velocity inversions resulting in "blind" zones. On several shot records, particularly near the edge of the playa, a sharp increase in time of the refracted arrival indicates a rapid increase in the thickness of the near surface velocity layer. Whether this is evidence for faulting or a collapse feature is unknown. The stacked data are ambiguous in this regard. Because refracted arrivals could not be reliably picked or picked at all on many shots records, refraction statics were abandoned. Simple datum

statics were applied instead. All of the lines were processed to a flat datum of 3572 ft. using a correction velocity of 2800 ft/s.

Because of the relatively low signal-to-noise ratio of the seismic data, residual statics solutions would not converge. Various experiments with pilot trace construction, statics gate, data filtering, etc., did not measurably improve the residual static result. Rather than force a statics solution, the data were processed without residual statics corrections applied.

To enhance the continuity and interpretability of the stacked data, a post stack F-K filter was applied to attenuate very low velocity dipping noise trains in the stack. This was followed by application of spectral balancing, a mild 5 point trace mix, FX deconvolution, time-variant bandpass filter, and amplitude scaling. The passband of the final stack sections is 40-130 Hz in the upper 200 ms of data and 30-90 Hz from 350-1000 ms.

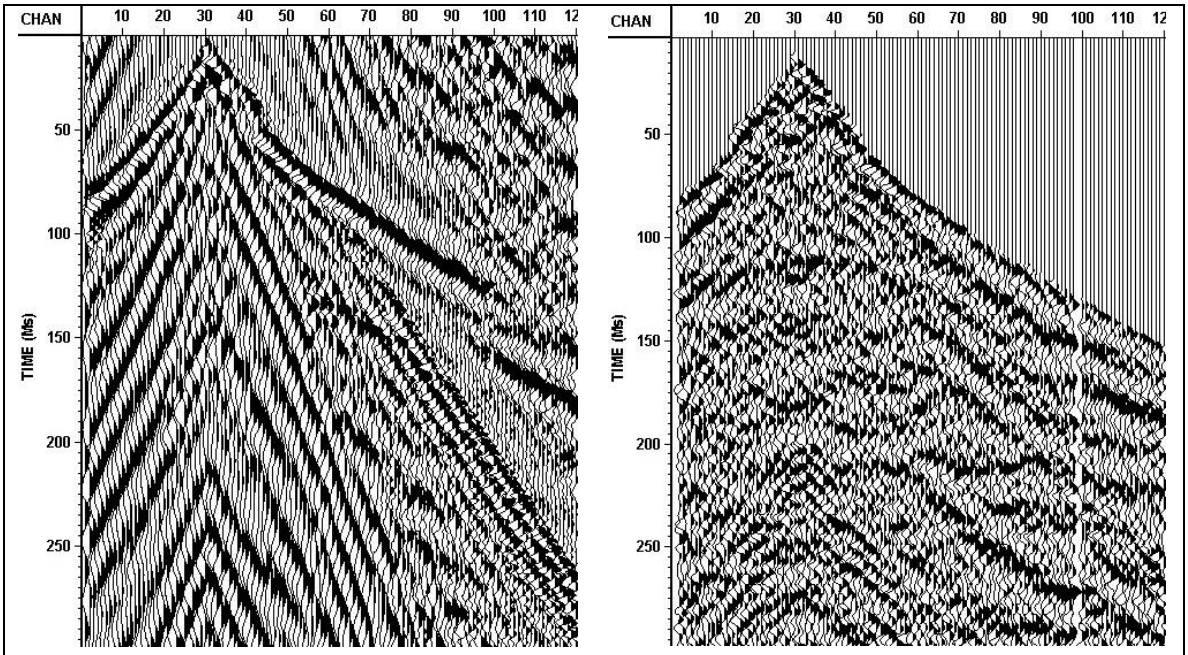

Figure 12. Raw correlated shot record (left) and preprocessed shot record (right). Note that reflected wave energy is entirely obscured in the raw data. In the preprocessed data reflections are apparent at 75 ms, 120 ms, and 225 ms. Also note that in the raw data at channel 45 the first arrival has a sharp offset indicating a rapid thickening of the low velocity layer.

SEISMIC DATA PROCESSING FLOW

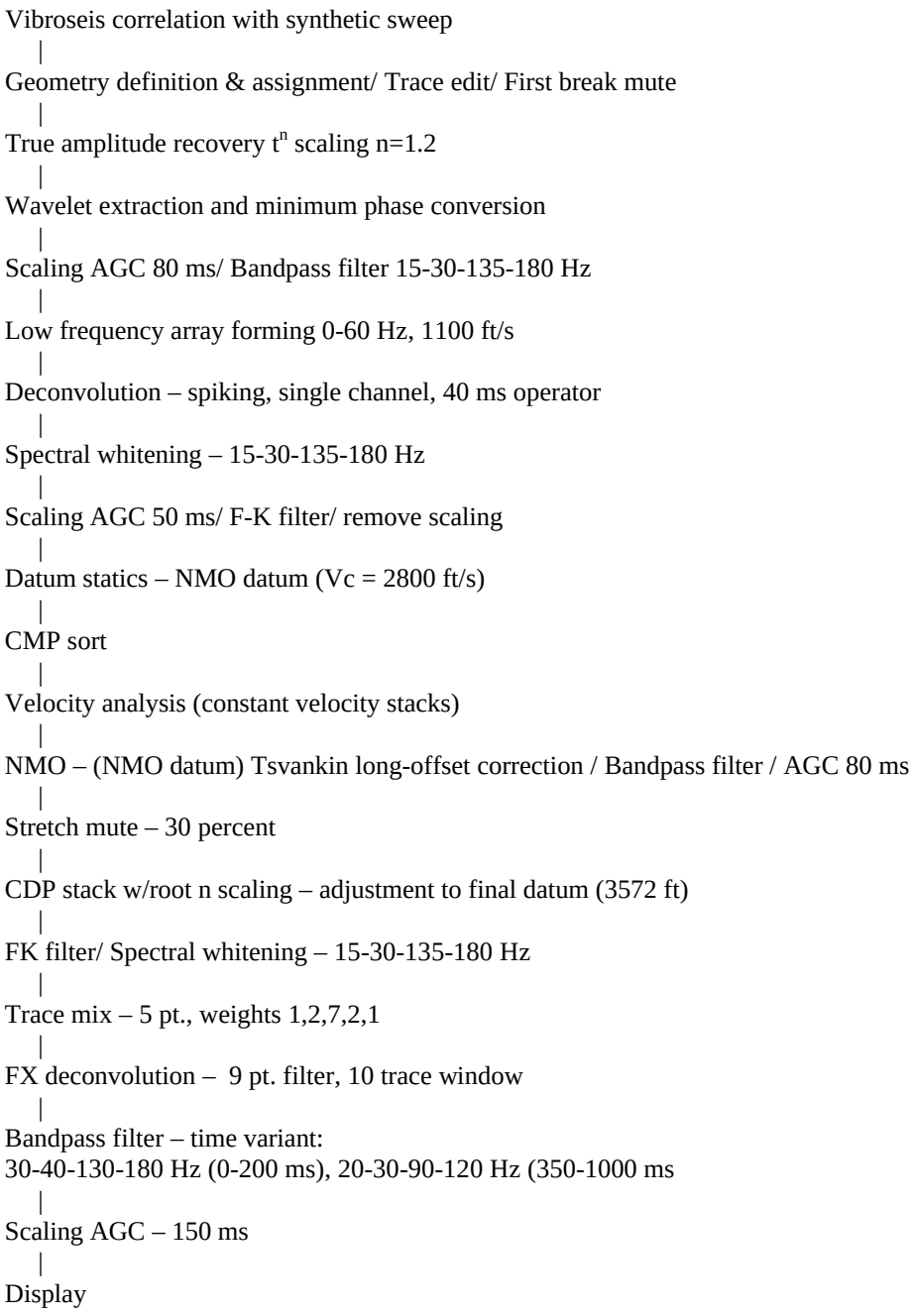

Figure 13. Seismic data processing flow. Diagram showing the data processing sequence followed to produce the seismic sections.

5.0 Results and Discussion

5.1 Seismic Stratigraphy Interpretation

Figure 1 shows the location of the four p-wave seismic reflection profiles across Playa 3. One of the objectives of the survey was to attempt to image the interval where the caliche is supposed to be present and determine if the caliche is continuous across the playa. Another objective was to determine the presence and continuity of the fine grained zone (FGZ) under the playa. Previous seismic studies across the playa focused on imaging the bedrock (Paine, 1995), which is much deeper than the objectives of this study. As previously stated, the shallow target depths in this study result in seismic recording entirely within the seismic noise cone. Overall, the data quality is fair. Outside of the playa the data tends to be better quality possibly due to the fine grained deposits, but within the playa the data quality degrades. Despite the quality of the data, the caliche interval, the FGZ, and, to a certain extent, the intraplaya zone were mapped.

5.1.1 *Seismic Profile PTX-1*

Seismic profile PTX-1 is a northwest/southeast trending profile located on the west side of the playa (Figure 1). There are three major contacts identified on the profile (Figure 14). On Figure 14 the blue line is interpreted as the caliche (caprock) interval, the green line is fine grained zone (FGZ), and the purple line is interpreted as intraplaya depression. The profile passes through well PTX01-1014A on the southeast end of the line and well PTX01-1008 is projected onto the profile. The vertical red lines to the left of the well are gamma logs that were converted from depth to time and plotted on the seismic line.

The caliche appears to be continuous across the entire seismic profile except at two locations. The first one is between shotpoints 250 and 260 at approximately 60 ms. This appears to be a statics problem, i.e. a distortion caused by near surface velocity changes. The other zone is between shotpoints 330 and 260 at about 60 ms. This feature is interpreted as a channel that has incised into and through the caliche interval. An observation on the caliche interval is that the character of the reflector varies across the profile. This would suggest that there are textural changes either in the upper sand and/or in the caliche along the edges of the playa and once inside the present playa depression there appears to be a textural change indicated by the a change in the acoustic impedance along the contact.

The FGZ (green line) interval appears to be present in areas outside of the playa and on the edge of playa. The area outlined by the purple line is being called an intraplaya depression. This is seen in Figure 14 where the FGZ reflector disappears inside the intraplaya depression. There are several explanations for this. The first explanation is that the FGZ is present, but because of the poor data quality it could not be traced. In the intraplaya depression, where the thickest playa deposits occur, the deposits

might be absorbing the seismic energy. Even though the survey used a vibrator with 12,000 pounds of down force, the nature of the sediments may have caused excessive scattering of the energy. A second explanation is that perhaps within the playa the FGZ is very thin and below the resolution of the data and therefore appears to be absent. A third possible theory is that the FGZ is actually absent within the playa.

The intraplaya depression (Figure 14 purple line) appears to be a collapse feature that subsequentially has been filled by later deposition of the Backwater Draw Formation (Paine, 1995). On the northwest end (right side) of the profile below the caliche and the FGZ intervals, the reflectors appear to be bending or dipping downward. This phenomenon also appears to be occurring below the purple line (Appendix 1, seismic profile PTX-1). On the southeast end (left side) of the profile it appears that the reflectors below the caliche interval dip downward below the FGZ and appear to terminate abruptly suggesting erosional processes rather than downwarping.

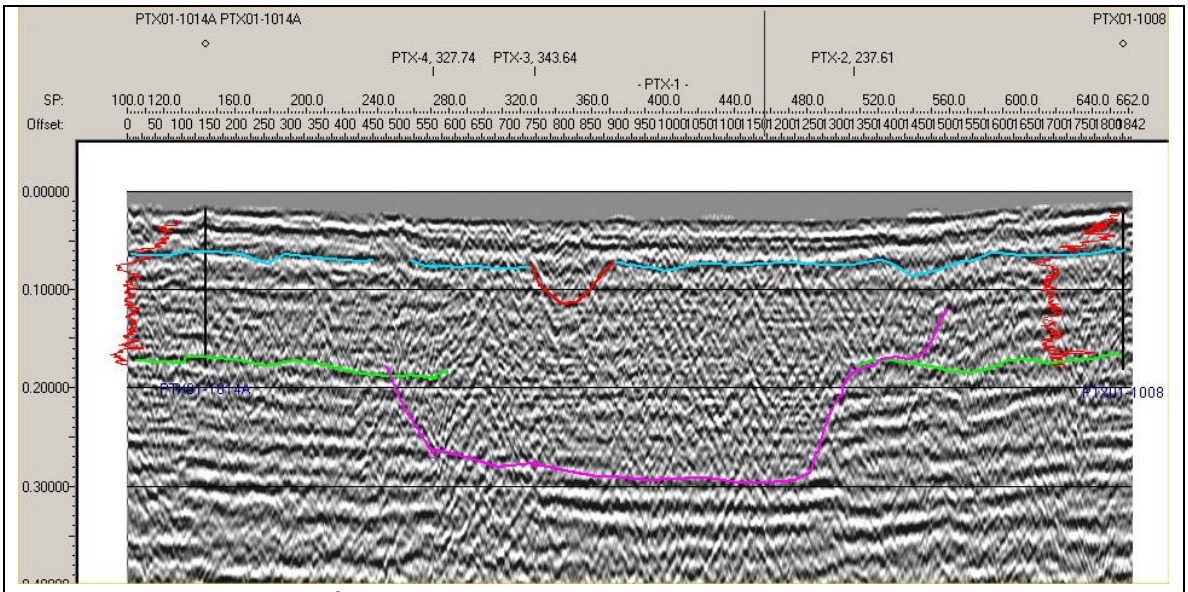

Figure 14. Seismic profile PTX-1 variable density plot. The blue line is interpreted as the caliche interval; the green line is the Fine Grain Zone (FGZ). The purple line defines the intraplaya depression and the red line incising into the caliche is interpreted as a channel. The vertical red lines to the left of the wells are gamma logs that have been converted from depth to time.

5.1.2 Seismic Profile PTX-2

Seismic profile PTX-2 is oriented in an east/southeast to west/northwest direction, (Figure 1). Profile PTX-1 ties with this profile at station 237. The mappable units are the same as on PTX-1. The uppermost mappable unit is the caliche interval (blue line), the FGZ (green line), intraplaya depression (purple line), and the channel (red line)(Figure 15). On profile PTX-2 the caliche appears to disappear inside the intraplaya depression.

On the east/southeast end (left) of the profile it appears that the caliche may be present into the playa as far as approximately shotpoint 240. On the west/northwest end (right) of the profile the caliche, as well as other reflectors below the caliche, appear to down warp and disappear along the edge of the intraplaya depression (Figure 15).

The FGZ, unlike on profile PTX-1, appears to be almost continuous across the playa except where the profile intersects PTX-1 along the edge of the playa. The absence of the FGZ reflection does not necessary mean the interval is missing. There are other plausible explanations. The first explanation is that the FGZ interval was eroded reducing the thickness below the resolution of the seismic data. A second explanation is that the quality of the data is such that it is present, but cannot be imaged. A third explanation is that there is perched water directly below the FGZ interval under the playa, which creates a high acoustic impedance (contrast) in areas where there are only air filled pores in the material above and below the FGZ. In Figure 15, between shotpoints 280 and 480 at approximately 200 ms, the reflector directly below FGZ marker is very bright. This suggests there may be a perched water table causing this bright reflector.

The intraplaya depression is outlined by the purple line. The characteristics are similar to profile PTX-1. The amplitudes appear to have a mottled texture and do not define reflectors that are prominent inside the depression. Toward the end of the profile (shotpoints 480-720) the reflectors from 60 ms down to the FGZ interval are dipping toward the center of the depression. At the beginning of the profile the reflectors appear to abruptly terminate suggesting erosional rather than gradual collapse.

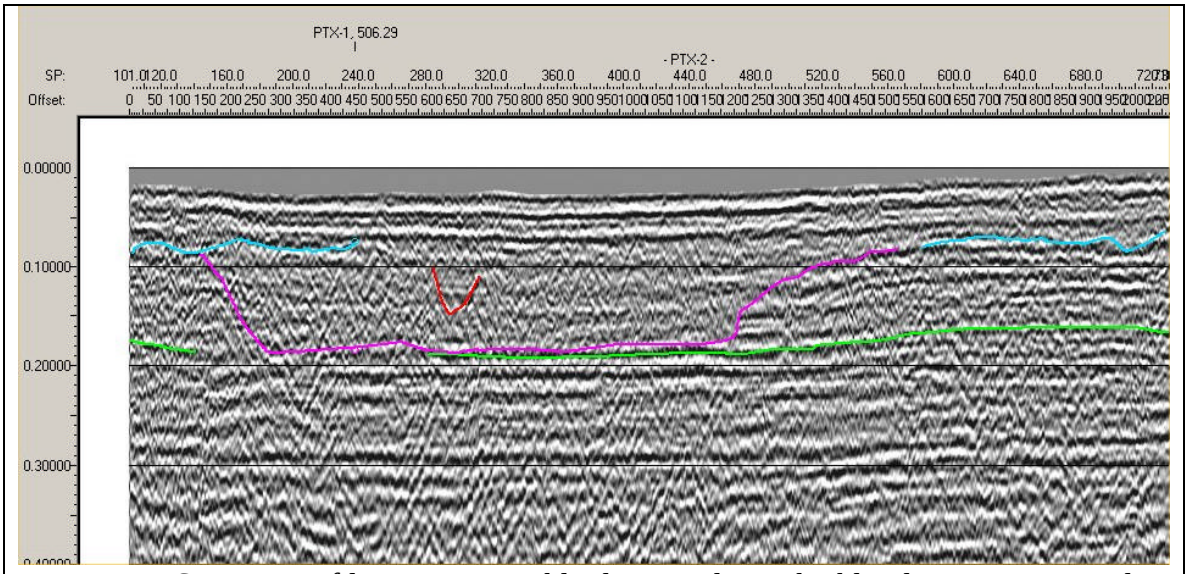

Figure 15. Seismic profile PTX-2 variable density plot. The blue line is interpreted as the caliche (caprock) interval, the green line is interpreted as the FGZ interval, the purple line defines the intraplaya depression, and the red line is a channel within the intraplaya area.

5.1.3 Seismic Profile PTX-3

Seismic profile PTX-3 is an east/southeast to west/northwest trending profile approximately parallel to PTX-2 (Figure 1). There are no wells located on this profile. Profile PTX-3 ties with PTX-1 at station 327 and PTX-4 at station 177 (Figure 16).

The uppermost mappable unit is the caliche interval (blue). Unlike the previous lines it appears at the beginning of the line at shotpoint 100 continuing to shotpoint 400. The caliche interval appears to be incised by two or three small channels (Figure 16). Two the channels are outlined in red and one possible channel, between shotpoints 200 and 240, is defined by a dip in the caliche horizon. For the most part, the caliche is interpreted as being fairly continuous along the profile.

The FGZ appears not to be continuous across the profile. It appears to dipping toward the center of intraplaya depression at the beginning of the profile from shotpoint 120 to 160 (Figure 16). The FGZ from shotpoint 360 to the end of line appears to be discontinuous, but this characteristic may be result of poor data quality and it may in fact be continuous. Another explanation is the thickness of the FGZ may be less than the resolution of the data.

The intraplaya depression (purple line) appears to thicken near the beginning of the line, but thins out to shotpoint 730 (Figure 16). Reflectors occurring between the caliche and FGZ on both sides of the intraplaya depression appear to be dipping downward and toward the center of depression. Another explanation for the asymmetrical shape is due to data quality in the west/northwest direction and the project team was not able to better define the lower contact.

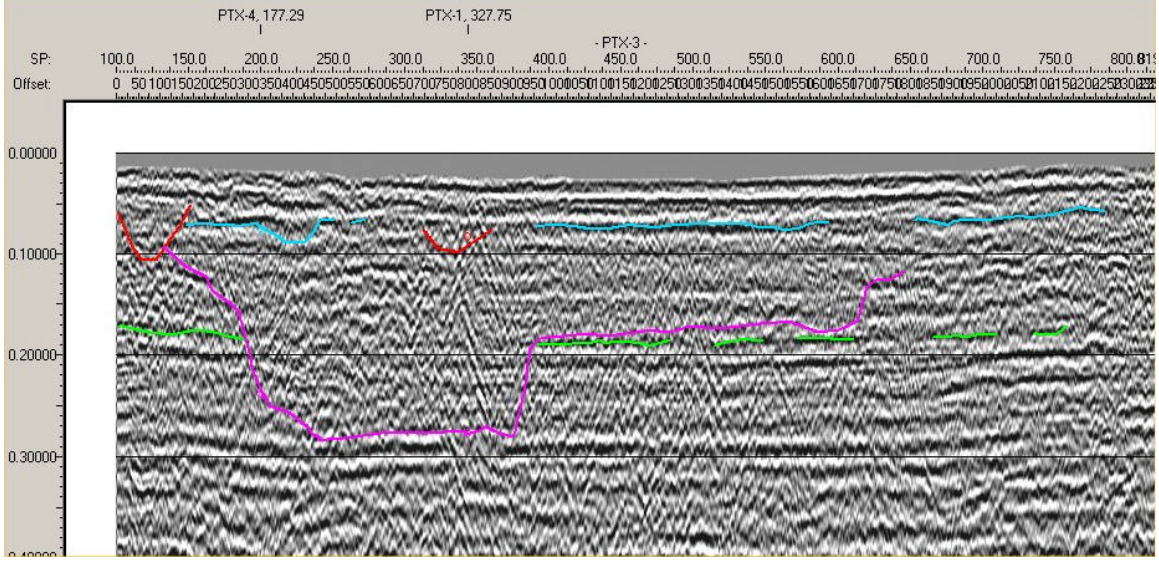

Figure 16. Variable density plot of seismic profile PTX-3. The blue marker is interpreted as the caliche interval, the green marker is the FGZ interval, the purple marker defines the intraplaya depression, and the red markers outline possible channels.

5.1.4 Seismic Profile PTX-4

Seismic profile PTX-4 is oriented east to west across Playa 3 (Figure 1). The blue line is interpreted as the caliche, the green line is the FGZ, the purple line is interpreted as the intraplaya depression, and the dark blue lines is a possible perched water table between the caliche and the FGZ (Figure 17). This profile ties with PTX-1 near shotpoint 327 and PTX-3 near station 176 and passes though well PTX01-1002 near station 618 (Figure 17).

The caliche (blue marker) is the first mappable unit even though there are some reflectors above that which correlate with the gamma log in well PTX01-1002. The caliche has been mapped across the profile, except for possibly an area between shotpoints 500 to 580 (Figure 17). This gap may be explained by data quality considering that the caliche is present in well PTX01-1002. The caliche may be thin and below the resolution of the data or absent from shotpoints 160 to 300, because the amplitude is lower than the areas between shotpoints 300 and 500 and between shotpoint 690 to the west end of the line.

The FGZ is present from shotpoint 410 to the west end of the line. The FGZ appears to be absent within the intraplaya depression. Alternatively, the data quality is such that the signal has been attenuated in the fine grain muddy sediment that is infilling the intraplaya depression and it cannot be identified on the seismic data.

Located on the west end of the profile, in the vicinity of well PTX01-1002 between 110 and 120 ms, there are some bright spots that may indicate perched water.

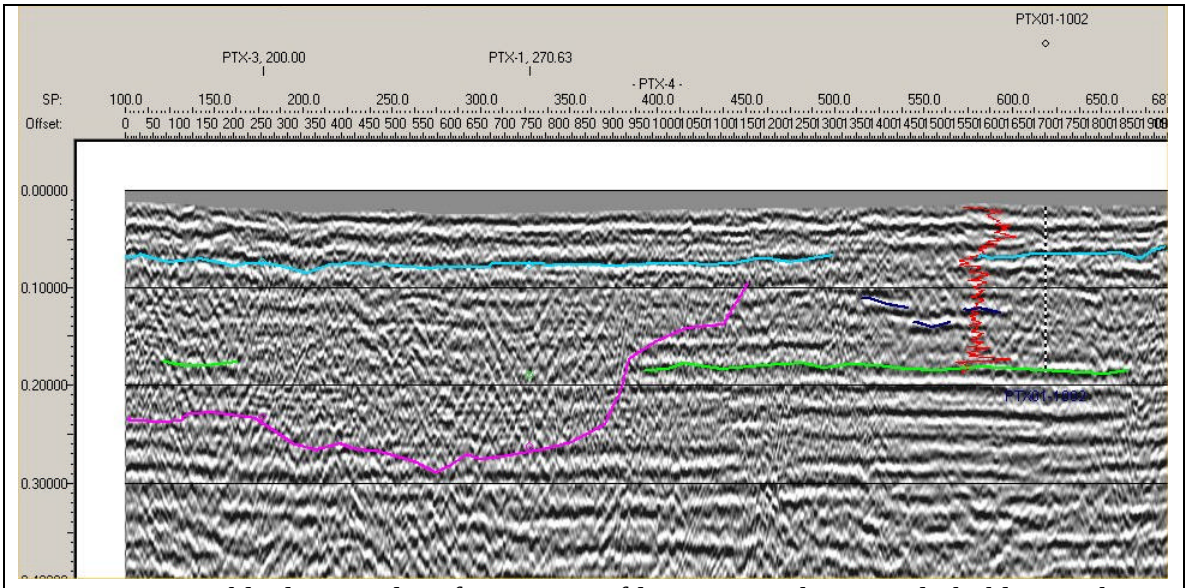

Figure 17. Variable density plot of seismic profile PTX-4. The upper light blue marker is interpreted as the caliche interval (caprock), the dark blue lines are interpreted as possible perched water, the green marker is the FGZ interval and the purple line is the base of the intraplaya depression. The vertical red line near well PTX01-1002 is a gamma ray log.

5.1.5 Stratigraphic Discussion

Figure 18 is a map of the areal extent of the caliche layer derived from the seismic data. The absence of the caliche on seismic profile PTX-2 could be the result of the erosion during the deposition of the channels in the Blackwater Draw Formation (example between shotpoints 601 and 651 PTX-3, and between shotpoints 501 and 601 PTX-4). Another possible explanation is that the caliche is so thin that it is below the resolution of the seismic data. However, well log descriptions suggest that the caliche, even if extremely thin, should still be a very good acoustic boundary.

Figure 19 is a map of the areal extent of the FGZ within the playa. The majority of the area where the FGZ appears to be absent is coincident with the deepest part of the intraplaya depression (Figure 19). A nongeologic explanation for the absence of the FGZ is the poor quality of the data and the poor resolution of the seismic data at that depth, especially where the intraplaya deposits are the thickest. The FGZ might have been eroded or incorporated with other sediments when the intraplaya depression was formed. It may not be coincidental that the FGZ is absent where the intraplaya deposits are the thickest.

If the two surfaces are plotted in their stratigraphic position (Figure 20), the areas where the caliche and FGZ are missing appear not to be related. The majority of the area where the FGZ appears to be absent occurs over the area of the maximum depth of the intraplaya depression. The area where the caliche could not be identified begins from the central part of the playa opening up to the northeast (Figure 18). It appears on seismic profiles PTX-2 and PTX-3 that the caliche might have been eroded away. On other areas of the profiles, there is no indication that the caliche is present. Where the FGZ is absent, some of the areas appear to be related either to the formation of the playa or the deposition of the intraplaya sediments or due to low resolution of seismic data. The areas on seismic profiles PTX-1 (shotpoints 251 to 501), PTX-3 (shotpoints 201 to 401), and PTX-4 (shotpoints 201 to 351) occur in the area where the intraplaya depression depth is the greatest (Figure 21). The other area where the FGZ is absent is perhaps due to poor resolution of the seismic data.

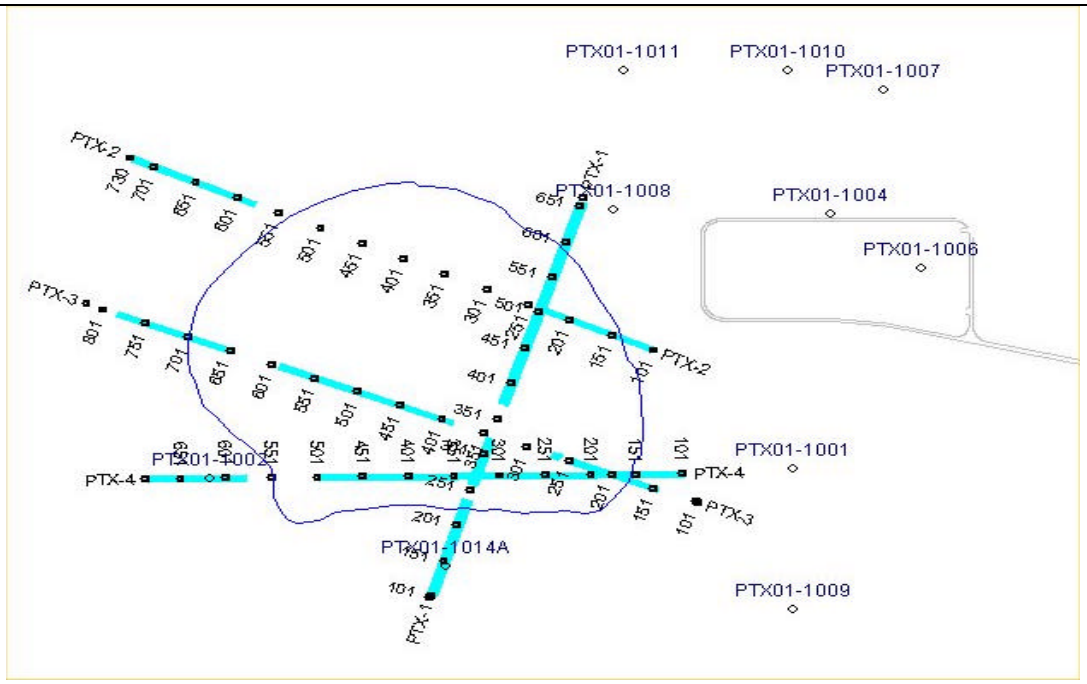

Figure 18. Map showing the presence (blue) and absence of the caliche.

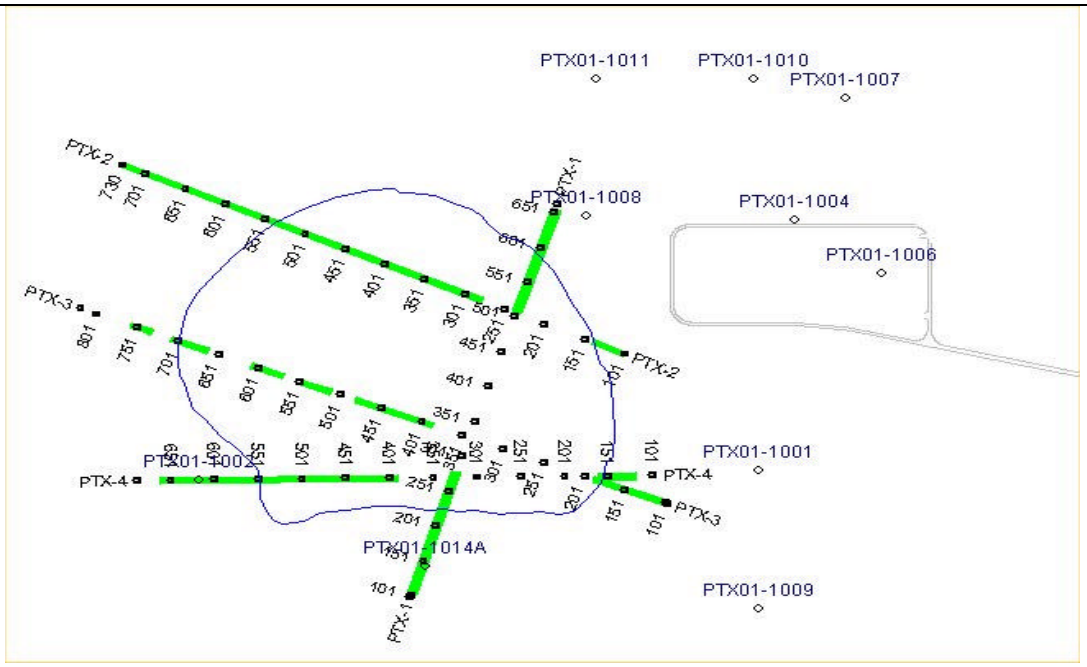

Figure 19. Map showing the presence (green) and absence of the FGZ.

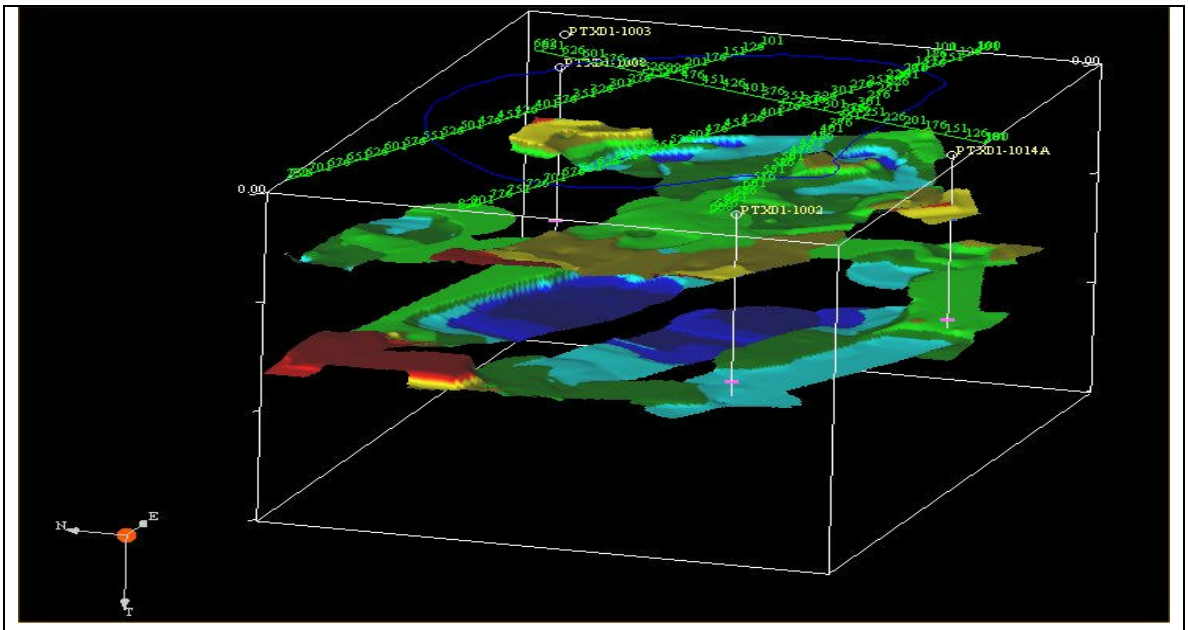

Figure 20. Three dimensional display of the caliche and FGZ surfaces. The surfaces are contoured in two-way travel time.

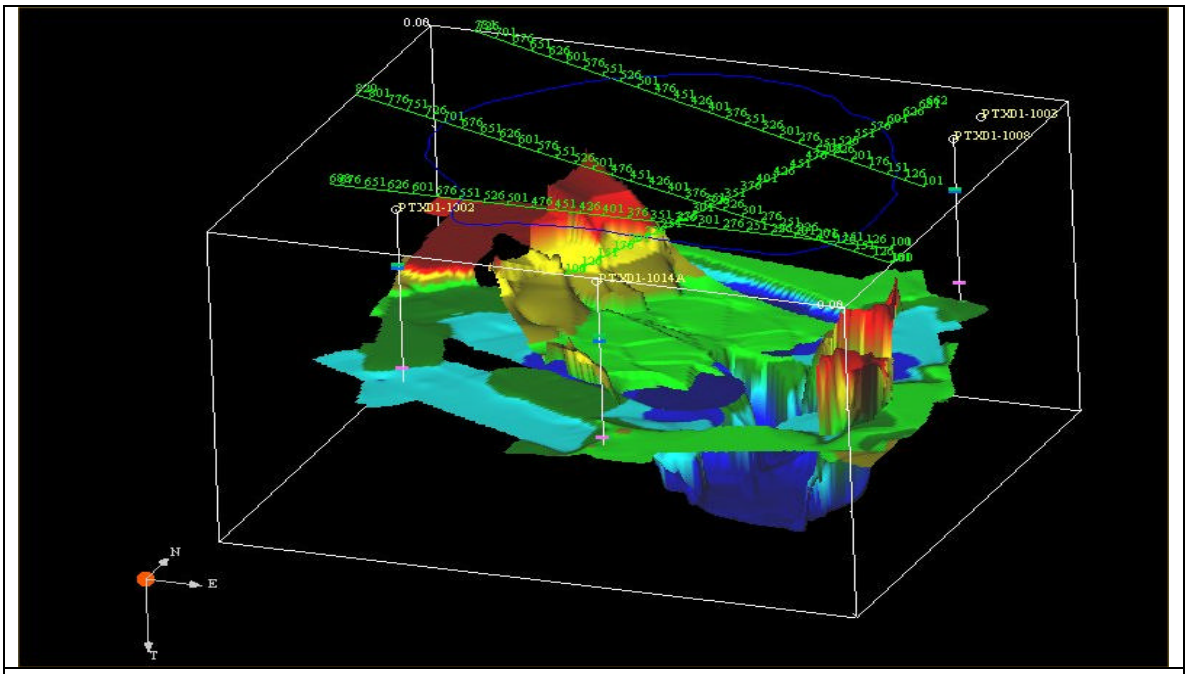

Figure 21. Three dimensional display of the FGZ surface and the intraplaya depression. The surfaces are contoured in two-way travel time.

5.2 Amplitude Versus Offset (AVO) Interpretation

At the Pantex Playa 3 the modeling data (Figures 7 and 7A, 8 and 8A, 9 and 10) suggest that, if TCE is present in the upper sand directly above the caliche and the lower sand directly above the FGZ, offset range stacks could be used for AVO analysis. That is, the reflection coefficient at large angles of incidence (long offsets) is sufficiently different than that at small angles of incidence (short offsets) so that stacking ranges of offsets will reveal the change in reflection coefficient if the contaminant is present. The range of angles used in the offset range stack is determined from the AVO modeling.

In Figure 7 using velocities from well PTX01-1008 the background reflection coefficient goes to a critical angle of 35^0 and if the upper sand is 100% saturated with free-phase toluene, the reflection coefficient goes critical at only 17^0 (Figures 7 and 7A). If velocities from well PTX01-1009 are used in the model, the response is about the same. If the pore spaces are saturated with 100% free phase TCE, a similar response is noted (Figures 8 and 8A). If the pore spaces are saturated with TCE in the lower sand above the FGZ, there is a detectable AVO response (Figure 10). However, if the pore spaces are 100% saturated with free phase toluene there is a slight AVO response, but it would not be detectable on the seismic data (Figure 9).

At Playa 3 a gradient stack was also performed on the seismic data for detection of TCE saturation in the lower sand, which directly overlies the FGZ. The reason it was performed only for this scenario is because it was the only model that has a detectable slope in the graph with increasing offsets. Castagna and others (1998) stated that AVO interpretation could be enhanced by crossplotting the AVO intercept (A) and gradient (B) provided that reasonable petrophysical parameters are used so that a well-defined background trend in the A-B plane is present. The B term (gradient) is the second term from the Shuey (1985) approximation of the Zoeppritz equations, which describes the amplitude characteristics from 15 degrees of offset to 30 degrees of offset (immediate angles of offset). In the shallow subsurface the background trend is generally positive. Any deviation from the background trend is a very good indicator of the presence of DNAPL or a change in the lithology with non-normal elastic properties. Stated differently, the AVO gradient is the change in slope of the reflection coefficient with increase in offset (Graul, 2001). In Figure 10 the slope of the line on each of the graphs (reflection coefficient versus offset) is the gradient.

Within Playa 3 there are two intervals where there may be the possibility of free-phase DNAPL (TCE) or LNAPL (toluene) accumulating. The upper interval is a caliche layer that, based on the seismic data, does not appear to be continuous through the playa area. However, where the caliche is present, there is the possibility of toluene or TCE accumulating in the sand directly above the caliche. The sand directly above the caliche is designated in this report as the upper sand. Two sets of p-wave and s-wave velocities were collected from wells PTX01-1008 and PTX01-1009. Based on which set of velocities were used, the AVO background response varied for both toluene and TCE. Due the variation in responses, a series of AVO analysis were designed for each possible response. The data quality for most of the seismic data collected in the playa is of fair

quality. The only profiles that AVO analyses were performed on are seismic profiles PTX-1 and PTX-2 (Figure 1).

Figure 22 consists of near and far range limited offset stacks for seismic profile PTX-1. The near offsets contained offsets from 0-17 degrees and the far offsets are from 17-34 degrees. In Figures 7 and 7A if toluene replaces the existing pore fluid, which is assumed to be air, there should be a detectable increase in the seismic amplitudes on offsets less than 17 degrees. At approximately 17 degrees the reflection coefficient response curve reaches the critical angle. On offsets greater than 17 degrees the amplitudes should decrease back to background level. On Figure 22 the red marker is the top of the caliche. The offset range limited stacks in Figure 22 are plotted in color, with each color representing reflection amplitudes. The lighter colors represent low amplitudes and the darker colors represent higher amplitudes (see Appendix 2 for plots with color scale). The amplitudes directly above the red marker are basically the same color scheme both for the near offset stack (upper figures) and the far offset stack (lower figures). On the far offset stack, between shotpoints 160 and 225, the amplitudes decrease slightly which is expected on the far offset according to the model. On the near offset stack there is significant increase in amplitudes (darker colors) on the near offset stack that would suggest the presence of free-phase toluene. The increase in amplitude is mostly due to a change in the texture of the upper sand or caliche, rather than free-phase toluene. Figure 14 shows the variable density plot of line PTX-1 where the caliche reflector is characterized by high amplitudes adjacent to the present playa depression and decrease in amplitude within the playa. Based on this information it appears that the amplitudes are affected by a change in the textual properties rather than a change in fluid content. One assumption that was made when constructing the AVO models was that the textural properties along the acoustic interface are constant. This appears to be not the case.

Figure 23 shows limited offset range stacks for seismic profile PTX-2. The ranges of offset are the same as on seismic profile PTX-1. The red marker is the top of the caliche. The interval directly above the red marker is the upper sand. There appears to be no significant amplitude in the interval across the entire profile. There is a low amplitude area between shotpoints 170 and 230. The decrease in amplitude is most likely attributed to a change in the texture of the sand. If there were free-phase toluene present, the amplitudes would be higher (darker colors), not lower (white color) than the surrounding amplitude. There appears to be no indication from AVO analysis that there is free-phase toluene along profile PTX-2. However, that does not mean toluene is not present. The toluene may be present in concentrations below the threshold limit that would cause an amplitude change.

Figure 24 consists of offset limited range stacks for seismic profile PTX-1. These stacks are designed to image amplitude changes if TCE replaces existing pore fluids (assumed to be air) in the upper sand directly over the caliche. Based on the model (Figure 8) with the upper sand saturated with 100% TCE, there is a slight increase in amplitude on the near offsets and on the far offsets the amplitude response increases

slightly. But the background amplitude response increases dramatically on the far offsets. Thus, the separation between the background amplitude response and the 100% TCE response increases with increase in offset. The model indicates that at about thirty degrees of incidence the background response reaches the critical angle and the curve representing the upper sand with 100% saturated TCE reaches critical angle at 40 degrees of incidence. On the far offset stack there should be lower amplitudes based on the model, but on the far offset stack the amplitudes appear to be higher than on the near offset stack. Based upon the models and range limited offsets stacks, there appears to be no change in amplitude response that can be correlated with free-phase TCE. The amplitude response is mostly attributed to changes in the composition of the caliche or the upper sand.

Using VSP velocities and derived density values from well PTX01-1009 (Figure 8A), the modeling results are very different than the values from well PTX01-1008 (Figure 8). Figure 25 shows range limited offsets for seismic profile PTX-1. According to the model if free-phase TCE is present, there should be detectable increases in amplitudes on the near offsets (0-15 degrees) and lower background amplitudes on the far offsets (15-30 degrees). On the near offset stack the amplitudes are for the most part consistent except between shotpoints 101 to 225 where the amplitudes decrease. On the far offset stack the amplitudes along the upper sand and caliche contact are constant across the entire profile.

Figure 26 shows range limited offsets stacks for seismic profile PTX-2 using velocities and derived density values from well PTX01-1008. The offset ranges are the same as on seismic profile PTX-1. On the near offset stacks (0-22.5 degrees) the amplitudes along the caliche-upper sand contact (red marker) are the same along the entire profile. On the far offset stacks (22.5-45 degrees) between shotpoints 175 and 236 there appears to be decrease in amplitudes (white color) which also occurs between shotpoints 575 and 625. The modeling data suggests that on the far offset stacks the difference between the background response and the free-phase TCE response should be large enough to be detected on the seismic data. If there were good control on the geology at the caliche interval within the playa, a plausible explanation would be that there is free-phase TCE. However, there is not good geologic control and the seismic data suggest that the caliche is discontinuous. The data also suggest that the textural properties of both the caliche and upper sand change across the seismic profile. Thus, the amplitude changes observed on the offset stacks are probably caused by textural changes such change in grain size or amount of cementation.

Figure 27 shows range limited offset stacks for seismic profile PTX-2 and the modeling results using the velocities and derived density values from well PTX01-1009. As stated in discussion of seismic profile PTX-1 (Figure 26), if there were free-phase TCE along the upper sand-caliche contact (red marker) there would be high amplitudes (dark blue) on the near offset stack (upper). The amplitudes are consistent across the entire profile. The amplitudes along the contact on the far offset stack (lower) are fairly

constant with the exception between shotpoints 170 and 325 where amplitudes actually decrease (white).

The modeling results for the contact between the lower sand and the FGZ (Figure 9) indicate that if the lower sand is 100% saturated with toluene, there is no discernable difference between the background amplitude responses with increasing offset. On the other hand, if the lower sand along the FGZ is 100% saturated with free-phase TCE, there is a noticeable AVO effect. Figure 28 shows offset range limited stacks for seismic profile PTX-1 designed to specifically to analyze for AVO anomalies along the lower sand-FGZ contact. If the model response for the pores saturated with 100% TCE is correct (Figure 10), on the near offset range limited stack the amplitudes should be lower than background and on far offset stack there should a dramatic decrease in amplitudes with increase in offset. At the contact between the lower sand and the FGZ there appears to be no detectable change across the profile (see appendix 2 for seismic profile with color scale bar). This would suggest that there is not any free-phase TCE present. The model curve for 100% TCE saturation has a well-defined gradient of the curve with increasing offset. Figure 29 is the gradient stack for seismic profile PTX-1. At the lower sand-FGZ contact there are no gradient anomalies. This would suggest that there is no free-phase TCE present. However, we should use caution because the data quality at that depth is poor, and the geology is not well understood for that interval in the playa. There is the possibility that TCE is present, but not at the concentrations that would cause an AVO anomaly.

On the offset range limited stacks for seismic profile PTX-02 (Figure 30) the amplitudes along the contact of the lower sand-FGZ appear lower on the near offset stack than on profile PTX-1 (lighter color)(see appendix 2 for seismic profile with color scale bar). On the far offset stack the amplitudes between shotpoints 112 and 175 and between shotpoints 400 and 512 appear to have lower amplitudes than the adjacent amplitudes and much lower than on profile PTX-1. This would suggest, according to the model (Figure 10), that there maybe free-phase TCE present. However, as stated in the previous section, the data quality at the lower sand-FGZ contact is fair and the geology is not well understood under the playa. The amplitude anomaly is most likely caused by either an increase in data quality from profile PTX-1 and/or a change in the geology. A gradient stack was performed on profile PTX-2 (Figure 31), but there does not appear to be any AVO anomalies along the contact across the entire profile.

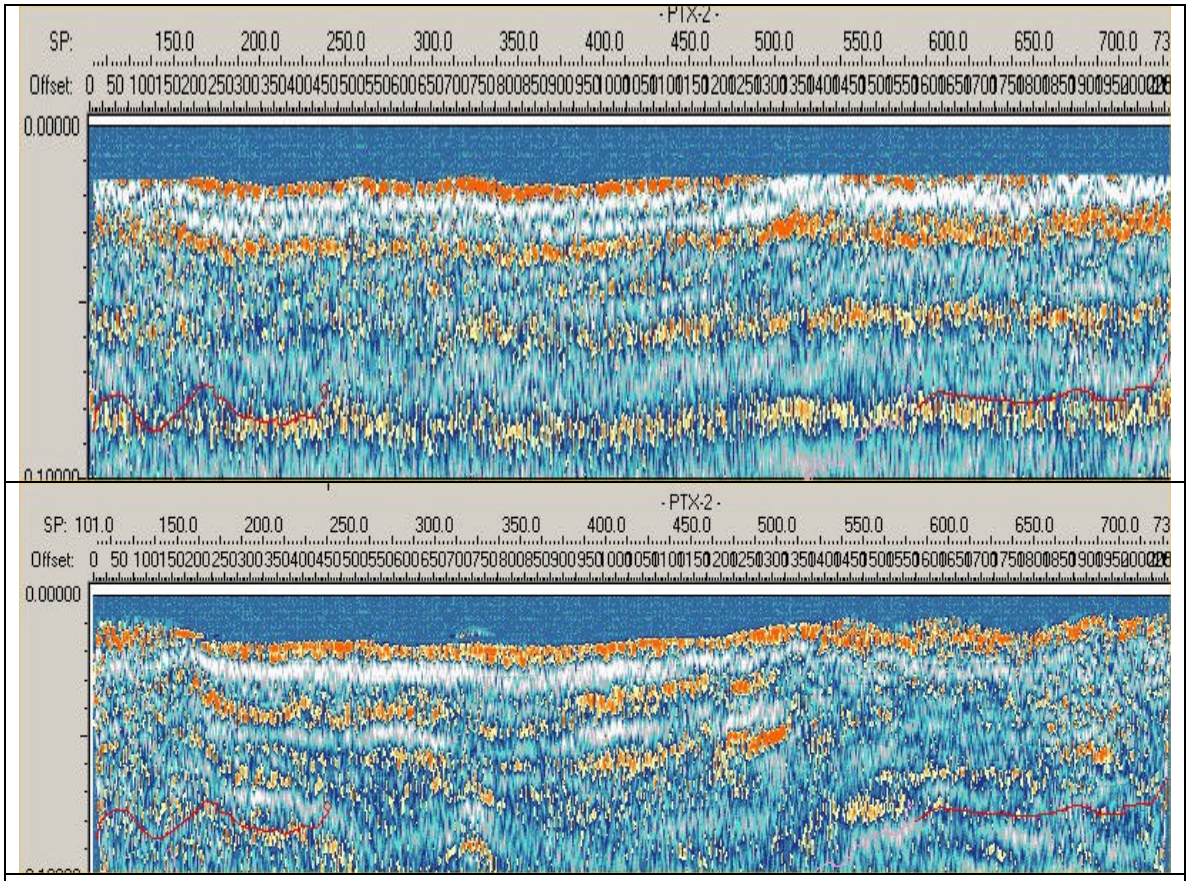

Figure 22. Seismic profile PTX-1 offset range limited stacks for the caliche interval containing toluene. The upper sand directly above the caliche is assumed in the model to be 100% saturated with toluene. The upper figure is a near offset stack using offsets from 0-17 degrees. The lower figure is the far offset using offsets from 17-34 degrees. If the models are correct, there should be an increase in amplitudes on the near offset stack, but not on the far offset stack. The darker colors are higher amplitudes and there appears to be no detectable increase in amplitudes in the zone above the red marker. See Appendix 2 for seismic profile with color amplitude bar.

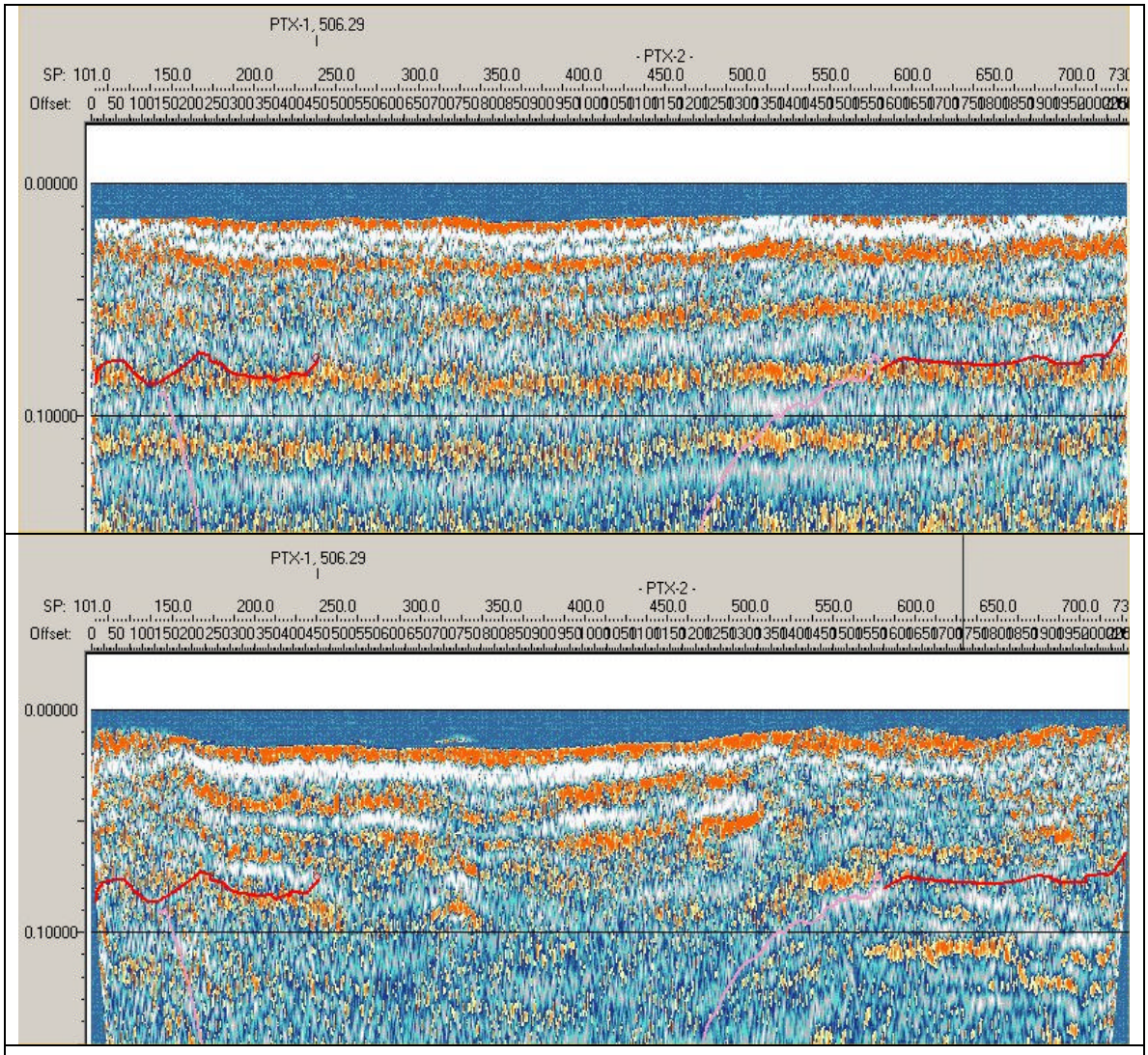

Figure 23. Seismic profile PTX-2 offset range limited stacks for the caliche interval containing toluene. The upper sand directly above the caliche is assumed in the model to be 100% saturated with toluene. Velocities and densities from wells PTX01-1008 and 1009 were used to determine the stack ranges. The near offset range limited stack is from 0-17 degrees (upper) and far offset range limited stack is from 17-34 degrees (lower). The red marker is top of the caliche. If the models are correct, there should be an increase in amplitudes on the near offset stack but not on the far offset stack. The darker colors are higher amplitudes and there appears to be no detectable increase in amplitudes in zone above the red marker. See Appendix 2 for seismic profile with color amplitude bar.

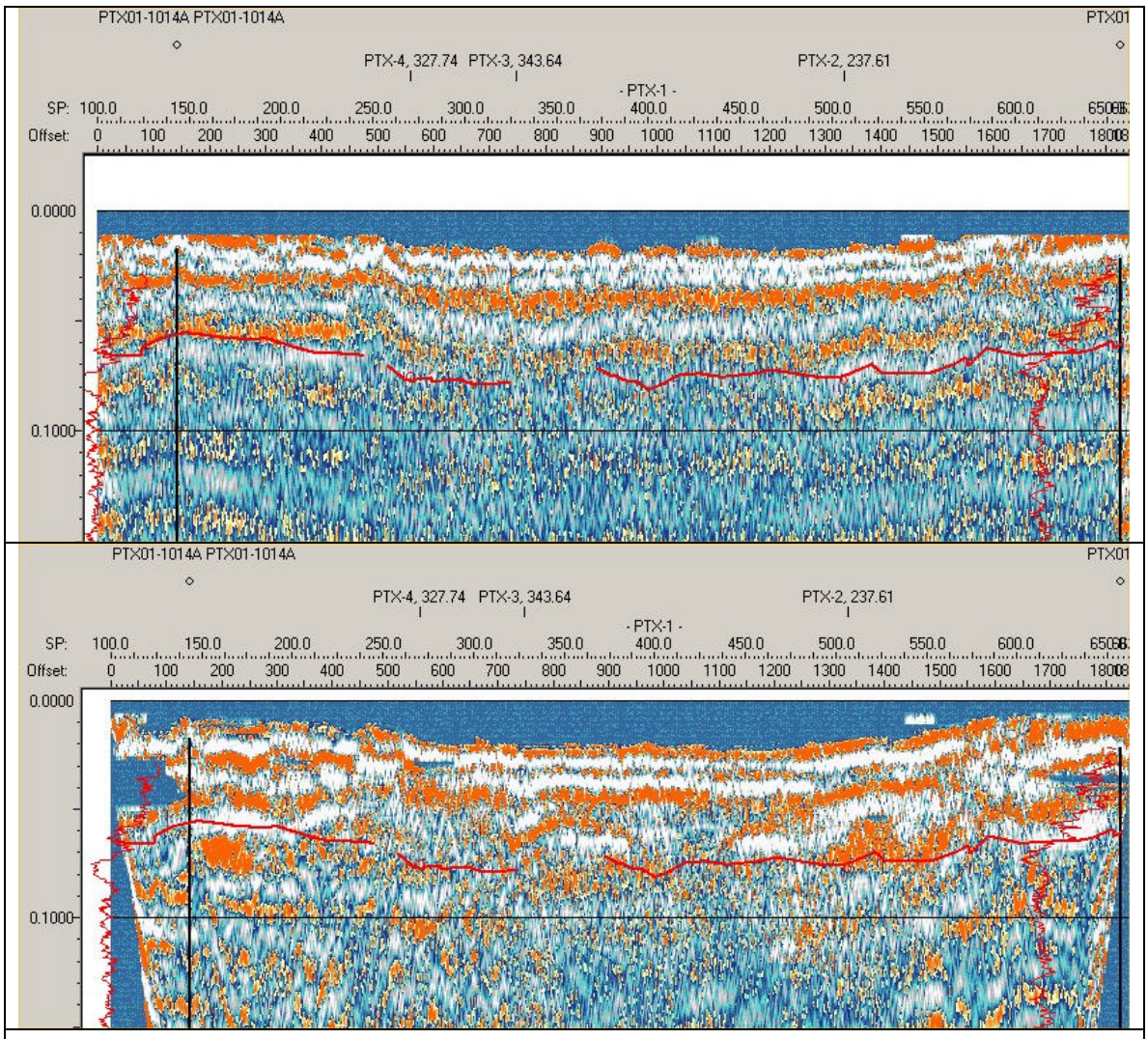

Figure 24. Seismic profile PTX-1 offset range limited stacks for the caliche interval containing TCE using velocities and densities from well PTX01-1008. The upper sand directly above the caliche is assumed in the model to be 100% saturated with TCE. The near offset range limited stack is from 0-22.5 degrees (upper) and far offset range the limited stack is from 22.5-45 degrees (lower). The red marker is the top of the caliche. If the models are correct, there should be a slight decrease in amplitudes on the far offset stack (lower) but not on the near (upper) offset stack. The darker colors are higher amplitudes and there appears to be no detectable increase in amplitudes in zones above the red marker. See Appendix 2 for seismic profile with color amplitude bar.

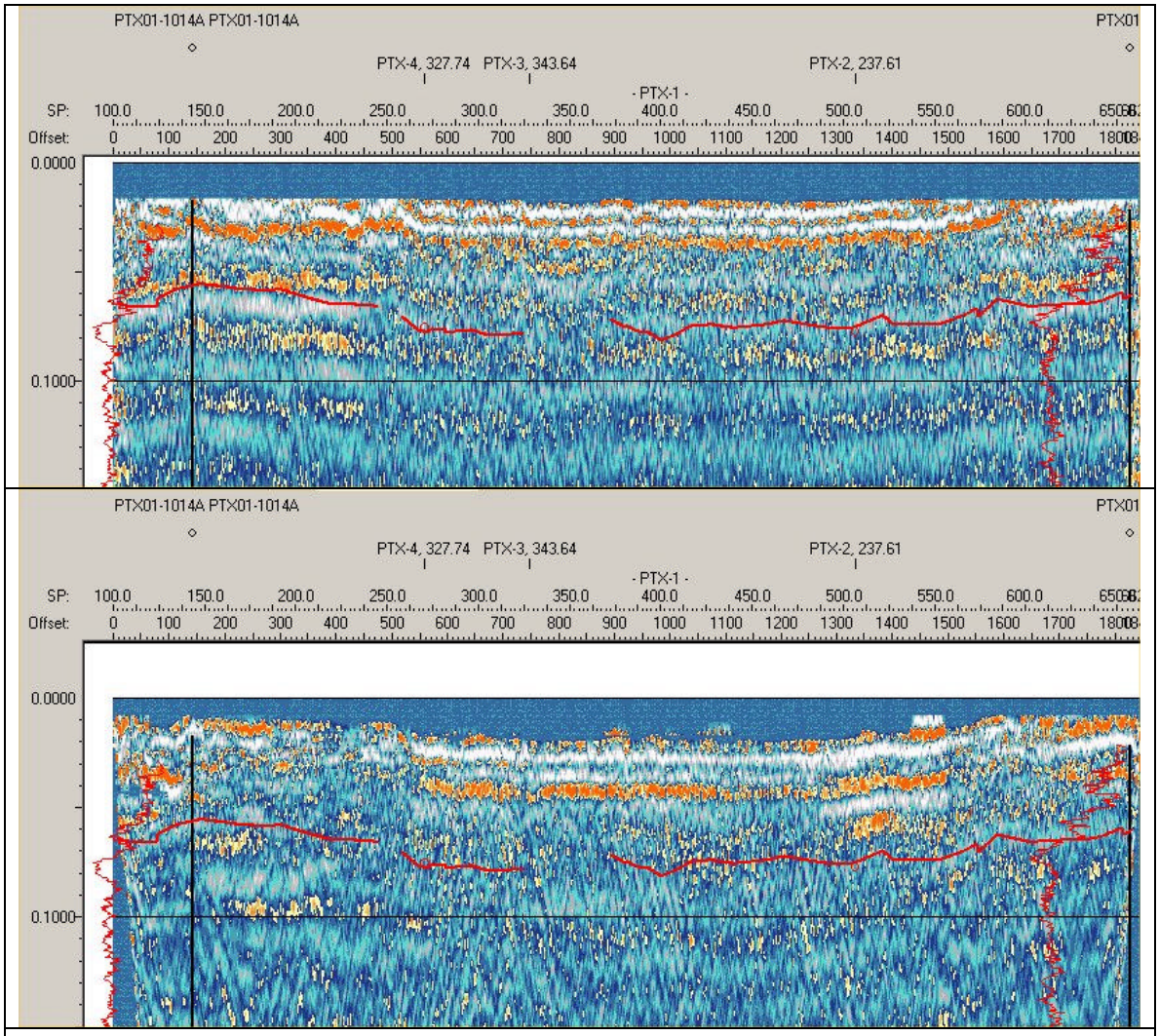

Figure 25. Seismic profile PTX-1 offset range limited stacks for the caliche interval containing TCE using velocities and densities from well PTX01-1009. The upper sand directly above the caliche is assumed in the model to be 100% saturated with TCE. The near offset range limited stack is from 0-15 degrees (upper) and far offset range limited stack is from 15-30 degrees (lower). The red marker is the top of the caliche. If the models are correct, there should be a slight decrease in amplitudes on the far offset stack (lower) but not on the near (upper) offset stack. The darker colors are higher amplitudes and there appears to be no detectable increase in amplitudes in zone above the red marker. See Appendix 2 for seismic profile with color amplitude bar.

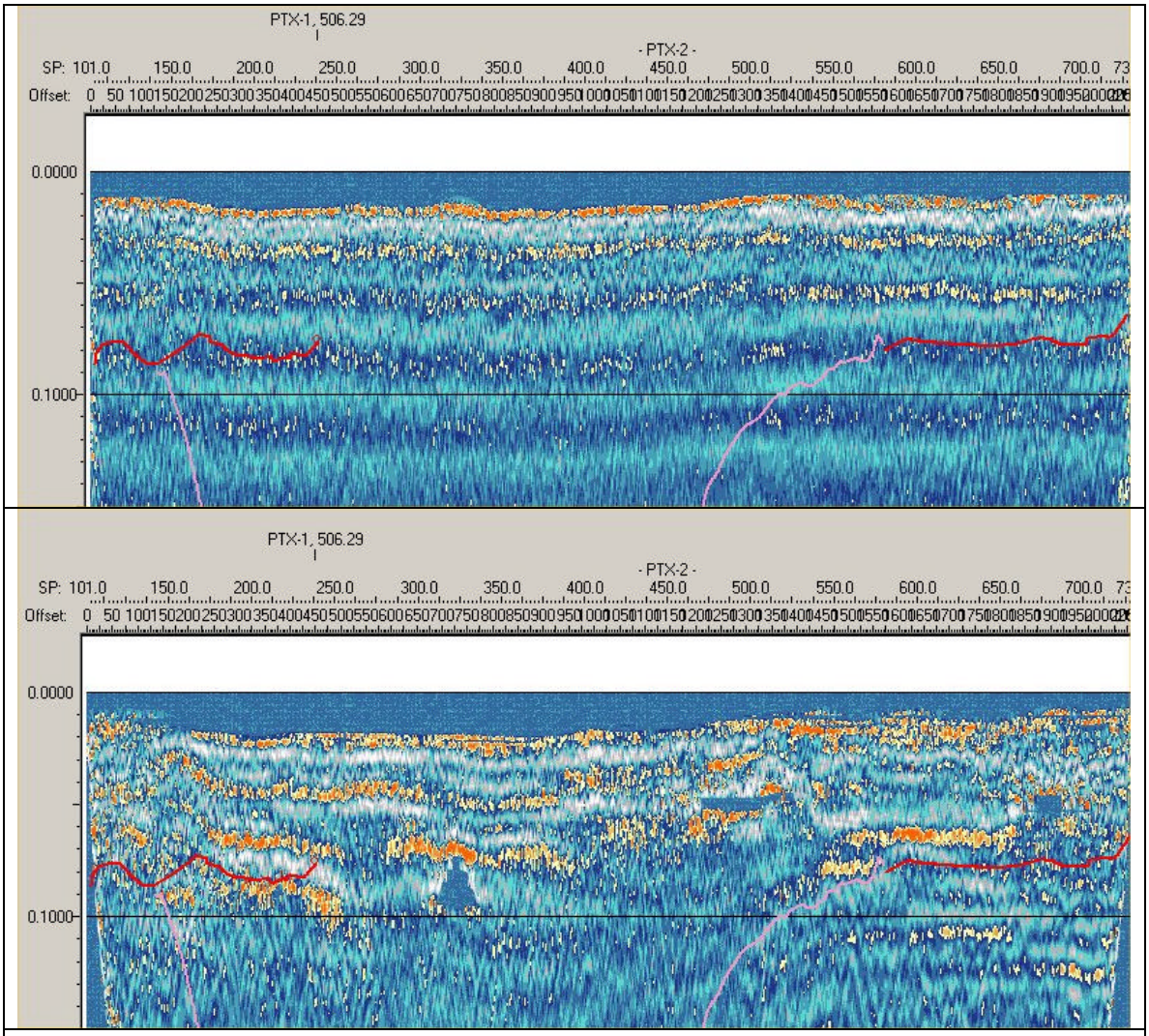

Figure 26. Seismic profile PTX-2 offset range limited stacks for the caliche interval containing TCE using velocities and densities from well PTX01-1008. The upper sand directly above the caliche is assumed in the model to be 100% saturated with TCE. The near offset range limited stack is from 0-22.5 degrees (upper) and far offset range limited stack is from 22.5-45 degrees (lower). The red marker is the top of the caliche. If the models are correct, there should be a slight decrease in amplitudes on the far offset stack (lower) but not on the near (upper) offset stack. The darker colors are higher amplitudes and there appears to be no detectable increase in amplitudes in zone above the red marker. See Appendix 2 for seismic profile with color amplitude bar.

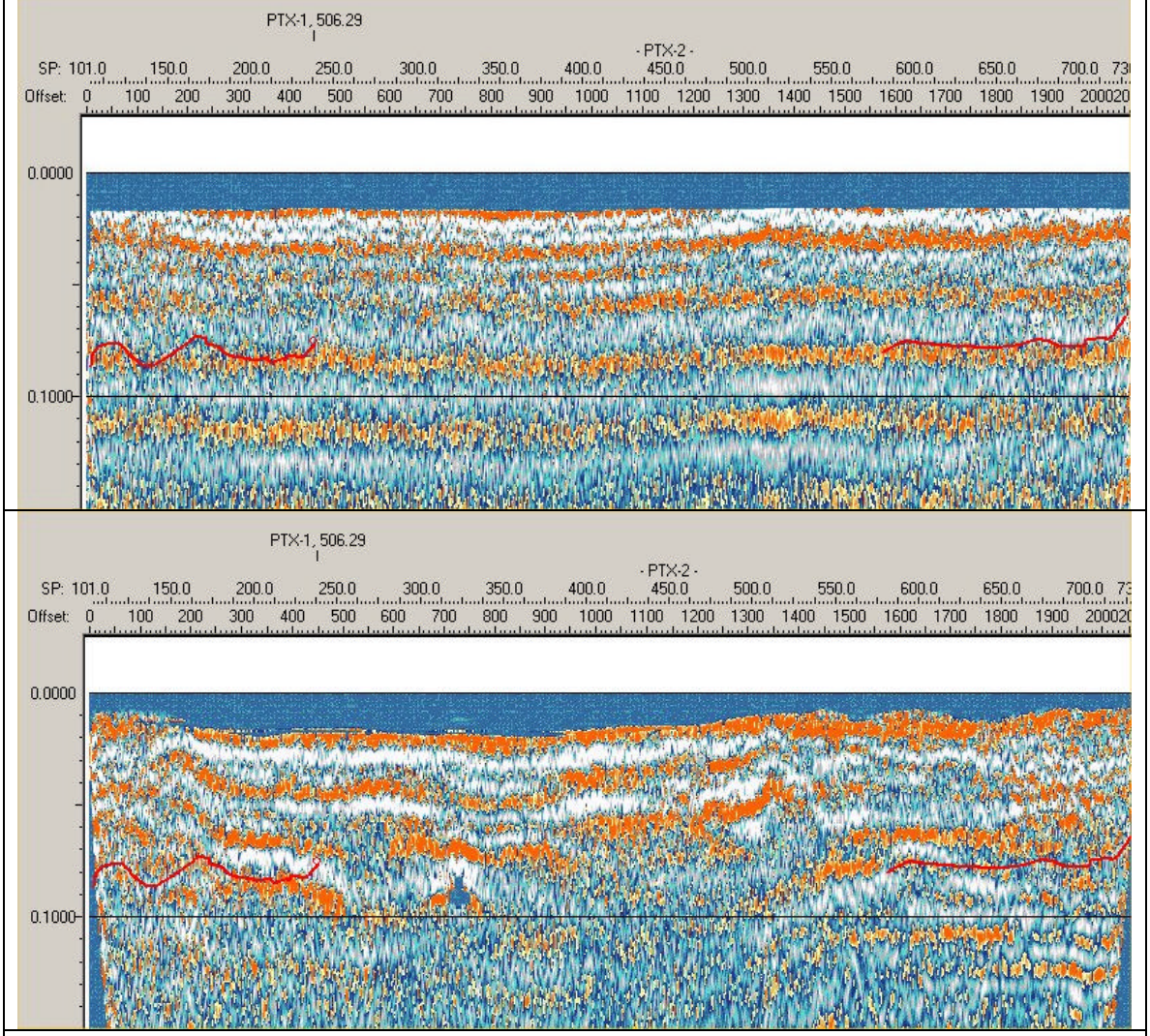

Figure 27. Seismic profile PTX-2 offset range limited stacks for the caliche interval containing TCE using velocities and densities from well PTX01-1009. The upper sand directly above the caliche is assumed in the model to be 100% saturated with TCE. The near offset range limited stack is from 0-15 degrees (upper) and far offset range limited stack is from 15-30 degrees (lower). The red marker is the top of the caliche. If the models are correct, there should be a slight decrease in amplitudes on the far offset stack (lower) but not on the near (upper) offset stack. The darker colors are higher amplitudes and there appears to be no detectable increase in amplitudes in zone above the red marker. See Appendix 2 for seismic profile with color amplitude bar.

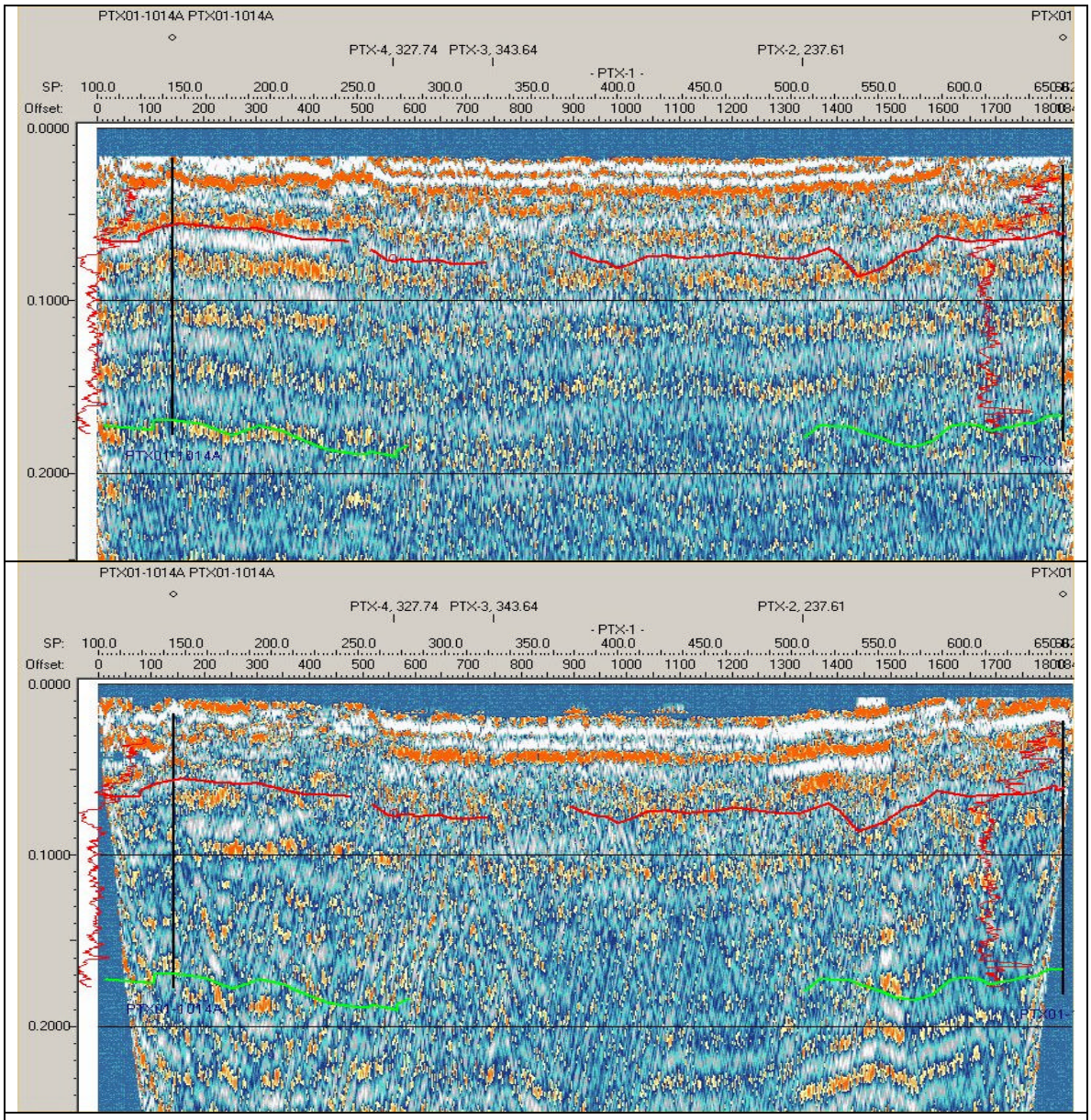

Figure 28. Seismic profile PTX-1 offset range limited stacks for the FGZ interval containing TCE using velocities and densities from well PTX01-1009. The lower sand directly above the FGZ is assumed in the model to be 100% saturated with TCE. The near offset range limited stack is from 0-20 degrees (upper) and far offset range limited stack is from 20-40 degrees (lower). The red marker is the top of the caliche and the green marker is the top of the FGZ. If the models are correct, there should be a decrease in amplitudes on the far offset stack (lower) but not on the near (upper) offset stack if the upper sand is 100% saturated with TCE. The amplitudes appear to be consistent across the contact. However, toward the end of the line (right side) the data quality deteriorates, but the amplitudes appear to be consistent with the amplitudes along the contact. See Appendix 2 for seismic profile with color amplitude bar.

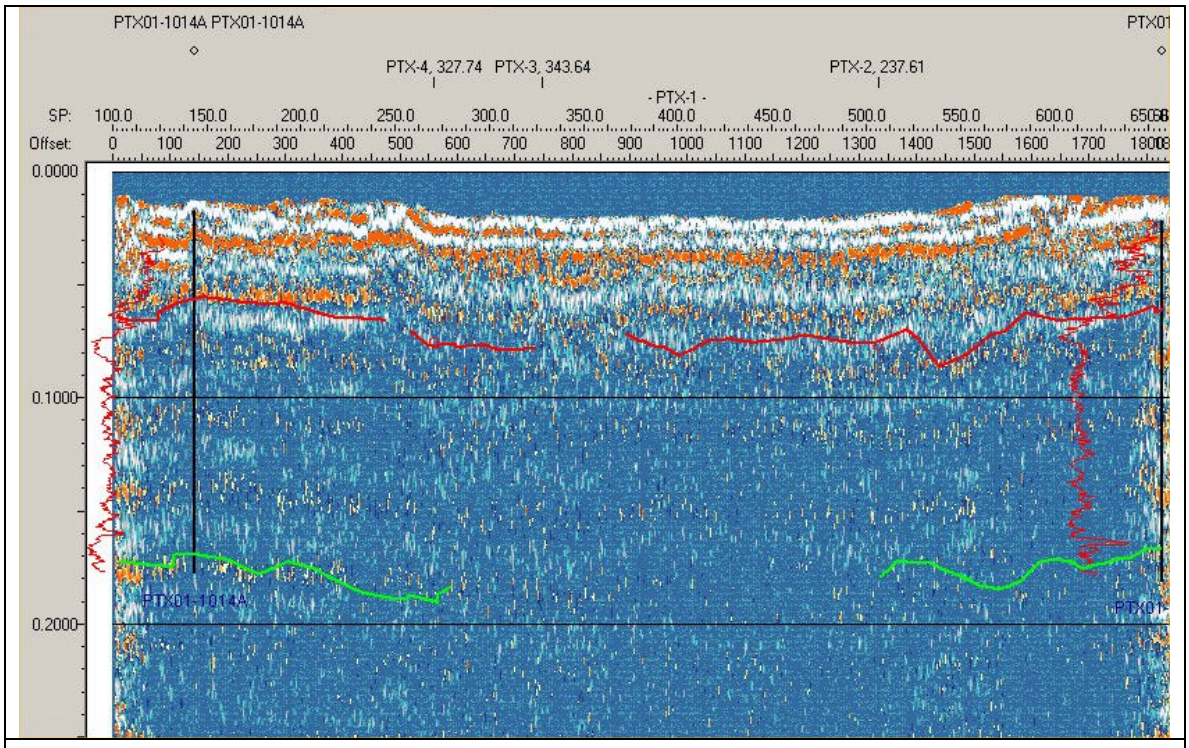

Figure 29. Seismic profile PTX-1 gradient stack for the FGZ interval containing TCE using velocities and densities from well PTX01-1009. The model suggests that if the lower sand, which directly overlies the FGZ, is 100% saturated with TCE the amplitudes should dramatically decrease with offset. Therefore, there should be a change in the gradient with offset. There are not any anomalies present of the stack suggesting there is no free-phase TCE.

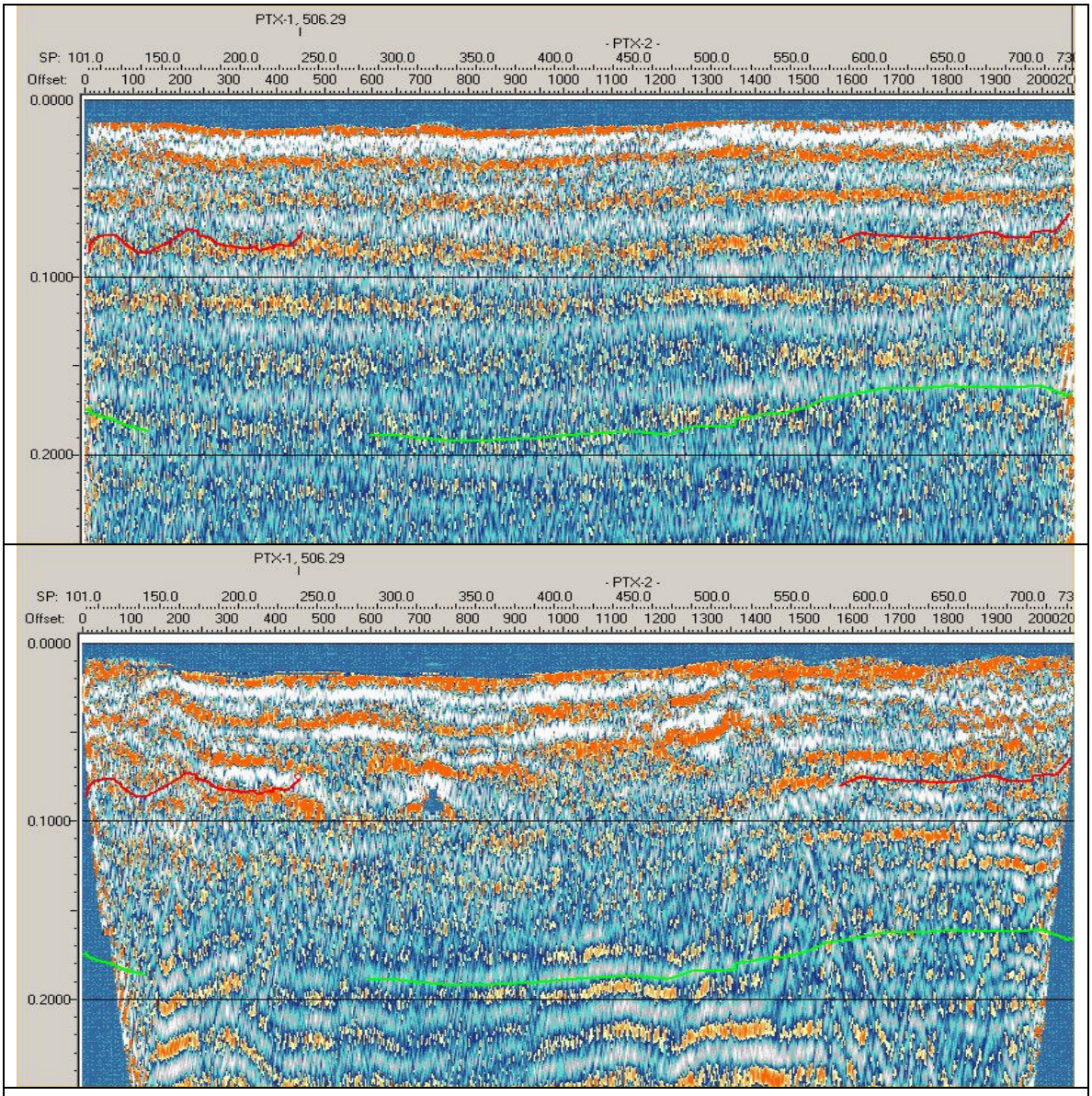

Figure 30. Seismic profile PTX-2 offset range limited stacks for the FGZ interval containing TCE using velocities and densities from well PTX01-1009. The lower sand directly above the FGZ is assumed in the model to be 100% saturated with TCE. The near offset range limited stack is from 0-20 degrees (upper) and far offset range limited stack is from 20-40 degrees (lower). The red marker is top of the caliche and the green marker is the top of the FGZ. If the models are correct, there should be a decrease in amplitudes on the far offset stack (lower) but not on the near (upper) offset stack if the upper sand is 100% saturated with TCE. There does not appear to be a change in colors suggesting the amplitudes are consistent across the contact. However, toward the end of the line (left side) the data quality deteriorates, but the amplitudes appear to be consistent with the amplitudes along the contact. See Appendix 2 for seismic profile with color amplitude bar.

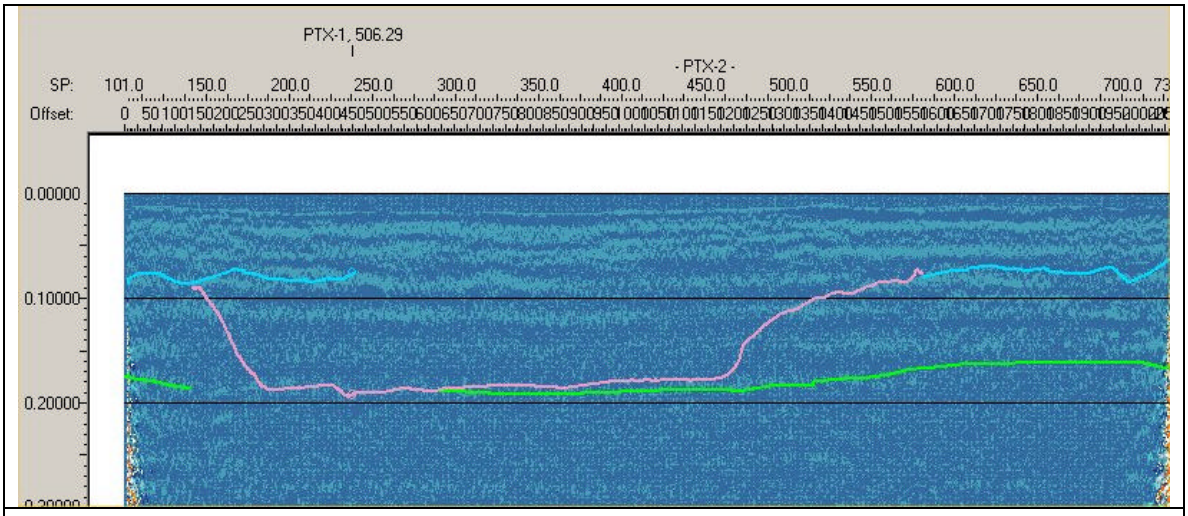

Figure 31. Seismic profile PTX-1 gradient stack for the FGZ interval containing TCE using velocities and densities from well PTX01-1009. The model suggests that if the lower sand, which directly overlies the FGZ, is 100% saturated with TCE, the amplitudes should dramatically decrease with offset. Therefore, there should be a change in the gradient with offset. There are not any anomalies present on the stack suggesting that there is no free-phase DNAPL.

6.0 Conclusions

Four p-wave seismic reflection profiles were acquired across Playa 3. The data were collected with two objectives: the first was to determine the continuity of the caliche and the fine grained zone (FGZ) beneath the playa and the second was to apply seismic Amplitude Versus Offset (AVO) analyses to the data set to determine if there was any free-phase toluene or TCE accumulating in either the caliche or FGZ. The following conclusions can be made from the seismic.

- Even though the quality of the seismic data was fair, the data did provide some insight to the subsurface geology beneath the playa.

- Interpretation of the seismic data indicates that the caliche is not continuous across the playa. The amplitude analysis of the seismic data suggests that where the caliche is present the composition (texture) appears to also vary across the playa.

- The seismic data also suggests that the fine grained zone is also not continuous beneath the playa. However, the areas where the caliche is missing and where the FGZ appear to be absent do not correspond to each other, possibly suggesting that the process that removed portions of the FGZ was most likely not the same process that affected the overlying caliche.

- There is an intraplaya depression into which reflectors appear downwarped. On profiles PTX-1, 2, and 3 the depression extends below the FGZ, however, on profile PTX-4 it appears that the FGZ is not downwarped and the depression lower boundary stops slightly above the FGZ. Another observation is the intraplaya depression does not have the same geometry as the present surface expression of the playa. The formation of the intraplaya depression maybe part of the process that assisted in the formation of the playa.

- AVO analysis of seismic profiles PTX-1 and PTX-2 did not detect any anomalies that could be the result of either free phase (separate phase) toluene or TCE replacing the existing pore fluid at either the upper sand-caliche or lower sand-FGZ contacts. This does not imply there are not concentrations of either toluene or TCE along either one the contacts. The concentration levels could be below the level at which would cause a seismic anomaly.

7.0 References

Boit, M.A., 1956, Theory of propagation of elastic waves in a fluid saturated porous solid. I. Low frequency range and II. Higher-frequency range: J. Acoustic Society of America, v.28, p. 168-191.

Castagna, J.P. and Backus, M. M., eds. 1993, Offset-dependent reflectivity - Theory and practice: SEG Investigations in Geophysics No. 8, Society of Exploration Geophysicists, Tulsa, OK, 345 p.

Castagna, J.P, Swan H.W., and Foster, D.J, 1998, Framework for AVO gradient and intercept interpretation: Geophysics, v. 65, no. 3, p. 571-581.

Clark, S.P., ed., 1966, Handbook of Physical Constants Revised Edition: Geological Society of America Memoir 97, Geological Society of America, New York, 587p.

Gardner, G.H.F., Gardner, L.W., and Gregory, A.R., 1974, Formation velocity and density-the diagnostic basics for stratigraphic traps: Geophysics, v. 39, p. 770-780.

Gassmann, F., 1951, Über die elastizität poröser medien: Vier. Der Natur. Gesellschaft in Zürich, p 96, 1-23

Graul, M., 2001, AVO seismic Lithology: SEG Continuing Education, Society of Exploration Geophysicists, San Antonio, TX.

Paine, J.P., 1995, Shallow-seismic evidence for playa basin development by dissolution-induce subsidence on the southern high Plains, Texas: Bureau of Economic Geology, The University of Texas, Austin, Texas, 47 p.

Shuey, R.T., 1985, A simplification of the Zoeppritz equations: Geophysics, v. 50, no.4, p. 609-614.

S.M. Stoller Corp., 2001, Final burning grounds RCRA facility investigation report (AL-PX-01): S.M. Stoller Corp., Boulder, Colorado, 125 p.

Weast, R.C. ed. and Astle, M.J., assoc. ed., 1980, CRC Handbook of Chemistry and Physics: CRC Press, Boca Raton, Florida.

White, J.E., 1983, Underground Sound-Application of Seismic Waves: Elsevier, New York, 253 p.

Zoeppritz, K., 1919, Uber reflexion und durchgang seismischer wellen durch Unstetigkerlsflaschen: Berlin, Uber Erdbebenwellen VII B, Nachrichten der Koniglichen Gesellschaft der Wissenschaften zu Gottingen, math-phys. K1., p. 57-84.

Appendix I

Seismic Profile PTX-1
Variable Density Plot
Without Interpretations

Earth Sciences and Resouces Inst.

Project: PANTEX Playa_3

Project Location:

Line PTX-1
Variable Density Plot

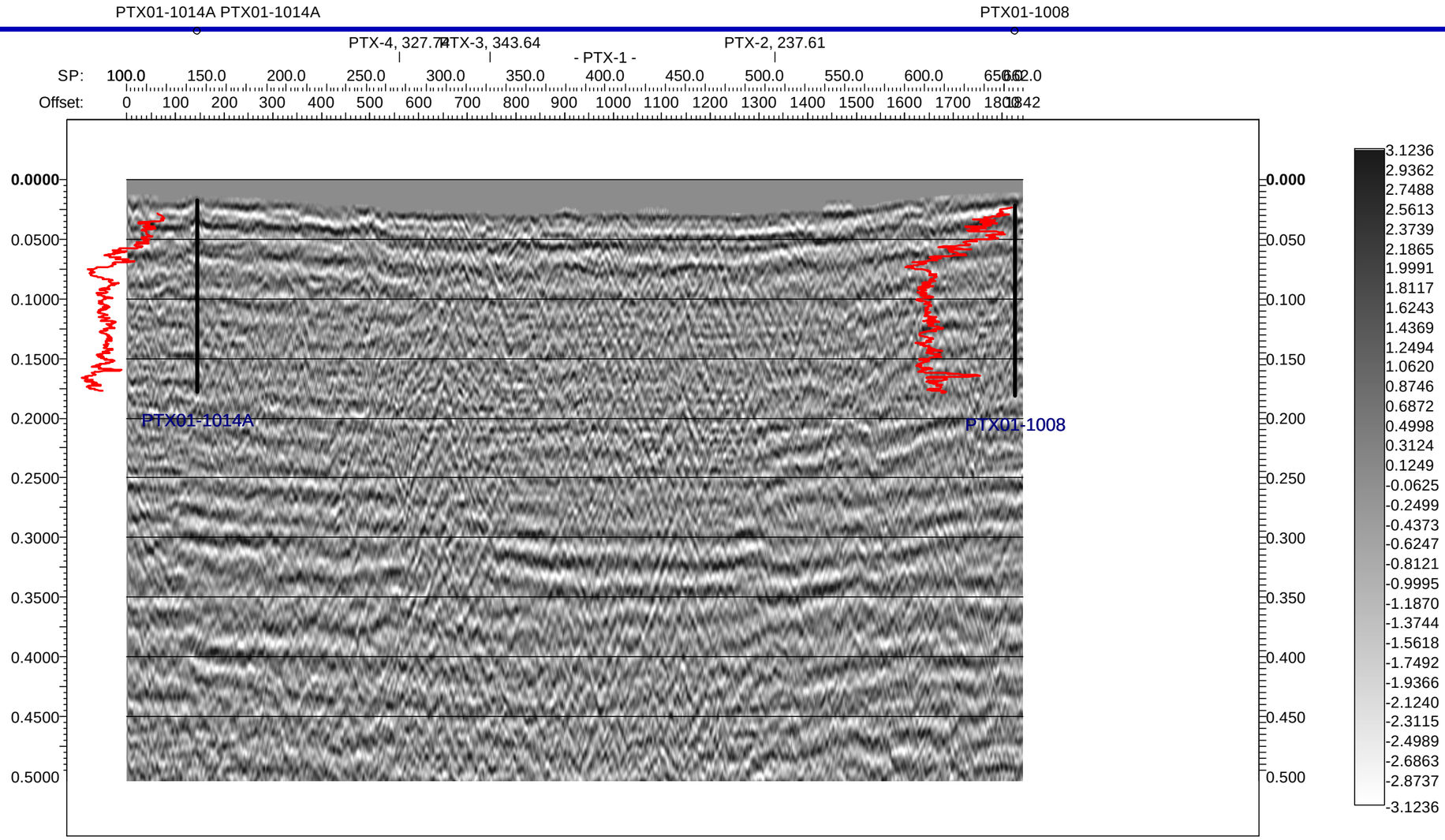

Seismic Profile PTX-1
Variable Density Plot
With Interpretations

Earth Sciences and Resouces Inst.

Project: PANTEX Playa_3

Project Location:

Line PTX-1
Variable Density Plot

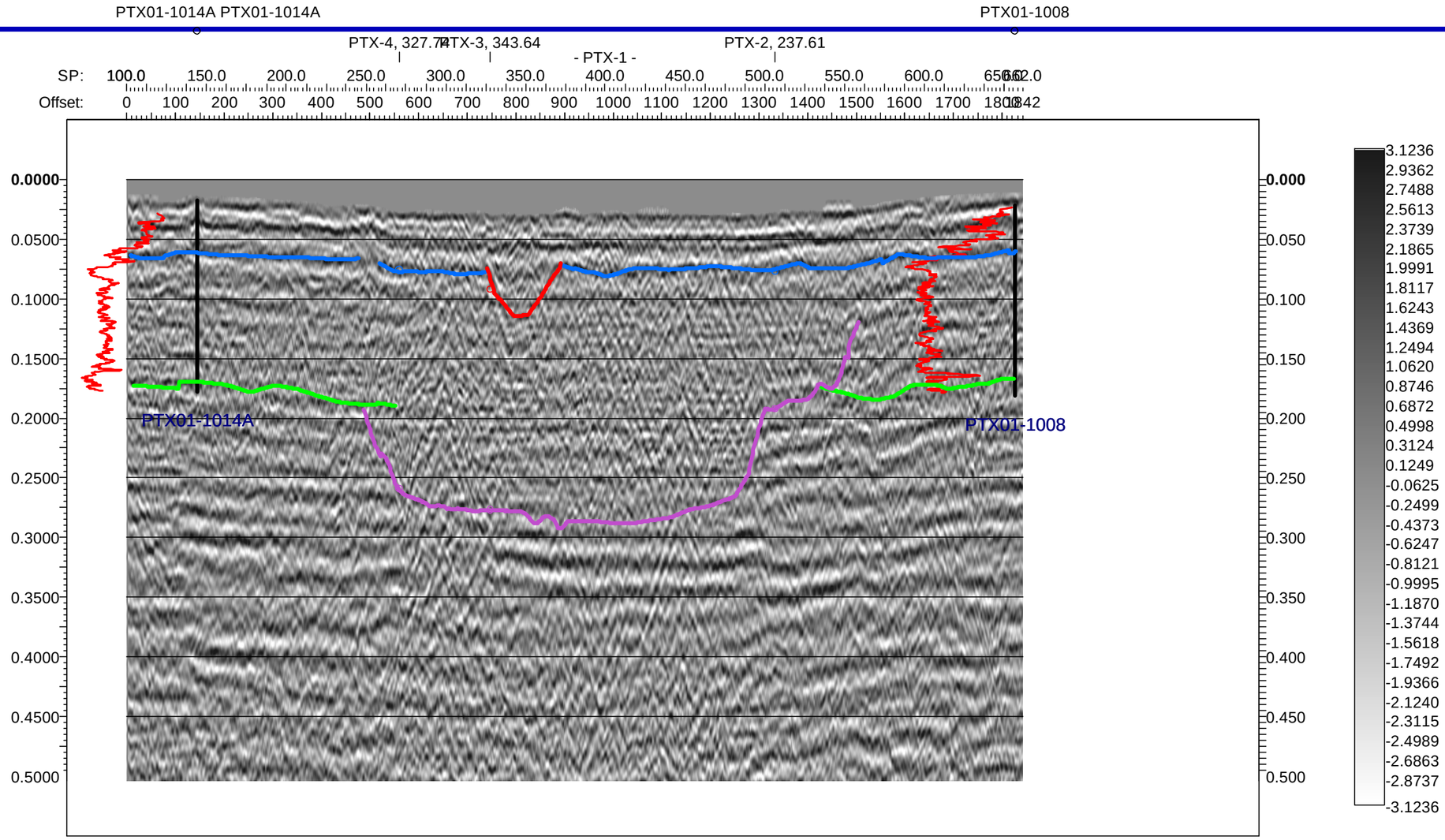

Seismic Profile PTX-2
Variable Density Plot
Without Interpretations

Earth Sciences and Resouces Inst.

Project: PANTEX Playa_3

Project Location:

Line PTX-2
Variable Density Plot
Without Interpretations

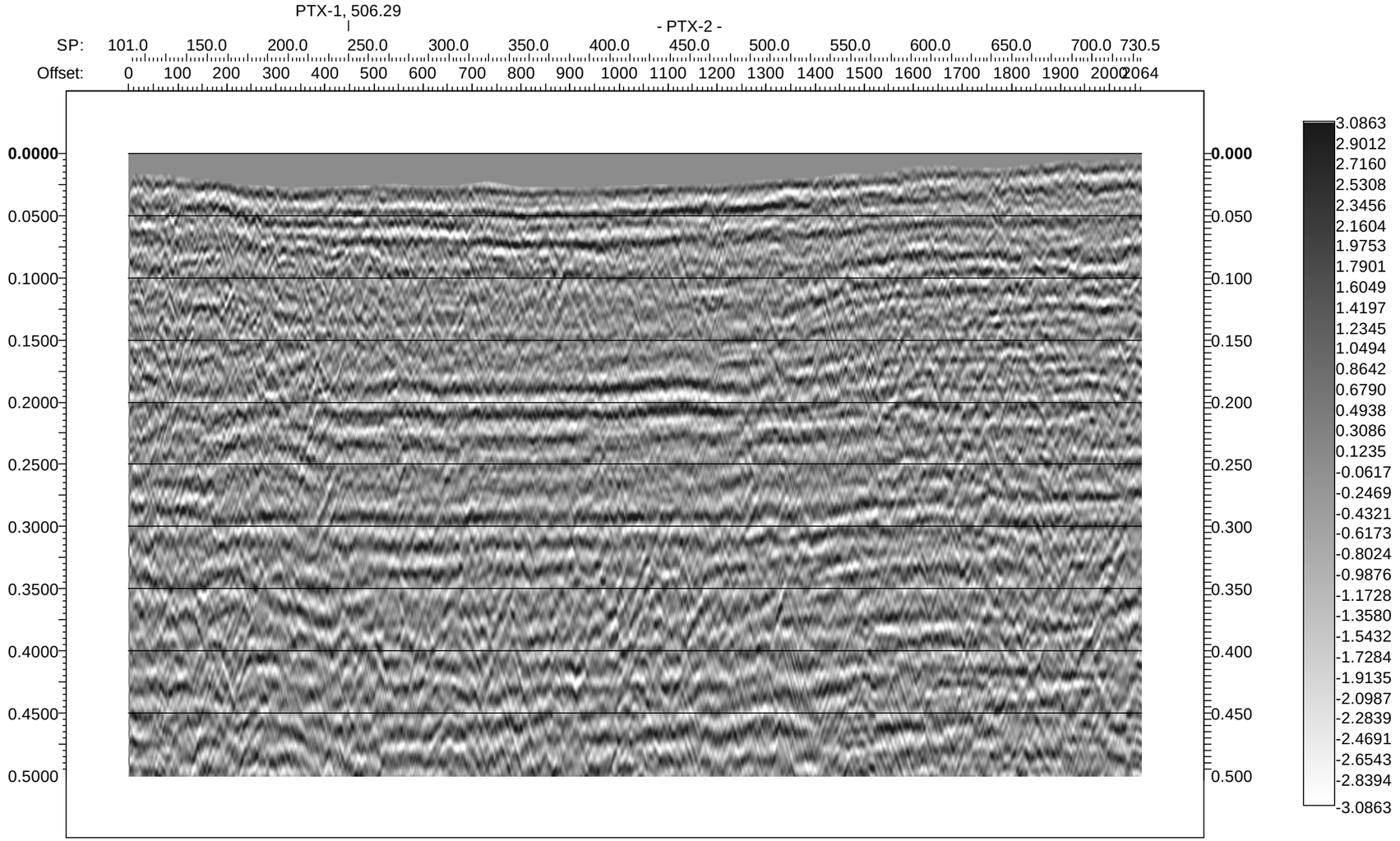

Seismic Profile PTX-2
Variable Density Plot
With Interpretations

Earth Sciences and Resouces Inst.

Project: PANTEX Playa_3

Project Location:

Line PTX-2
Variable Density Plot
With Interpretations

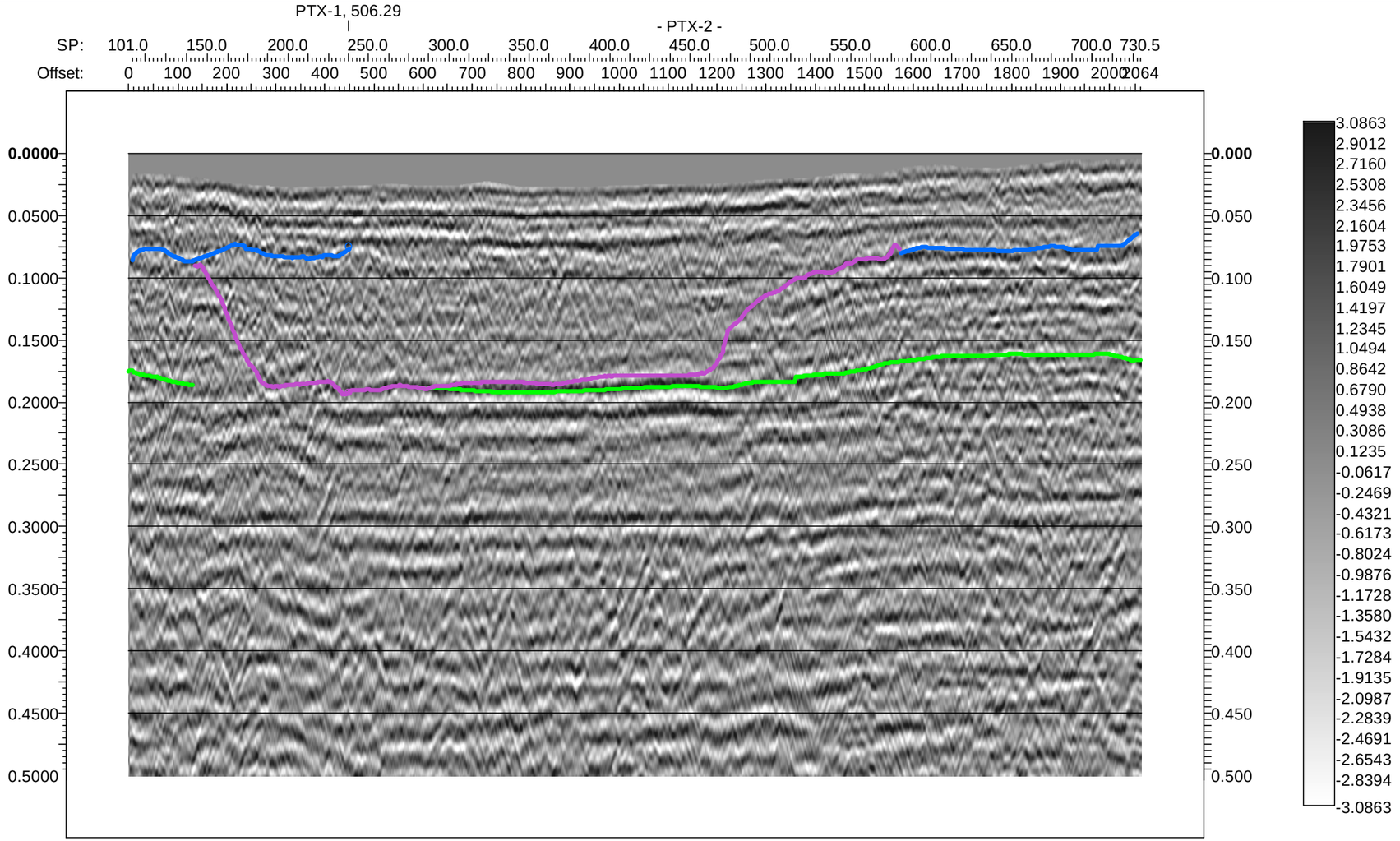

Seismic Profile PTX-3
Variable Density Plot
Without Interpretations

Earth Sciences and Resouces Inst.

Project: PANTEX Playa_3

Project Location:

Line PTX-3
Variable Density Plot

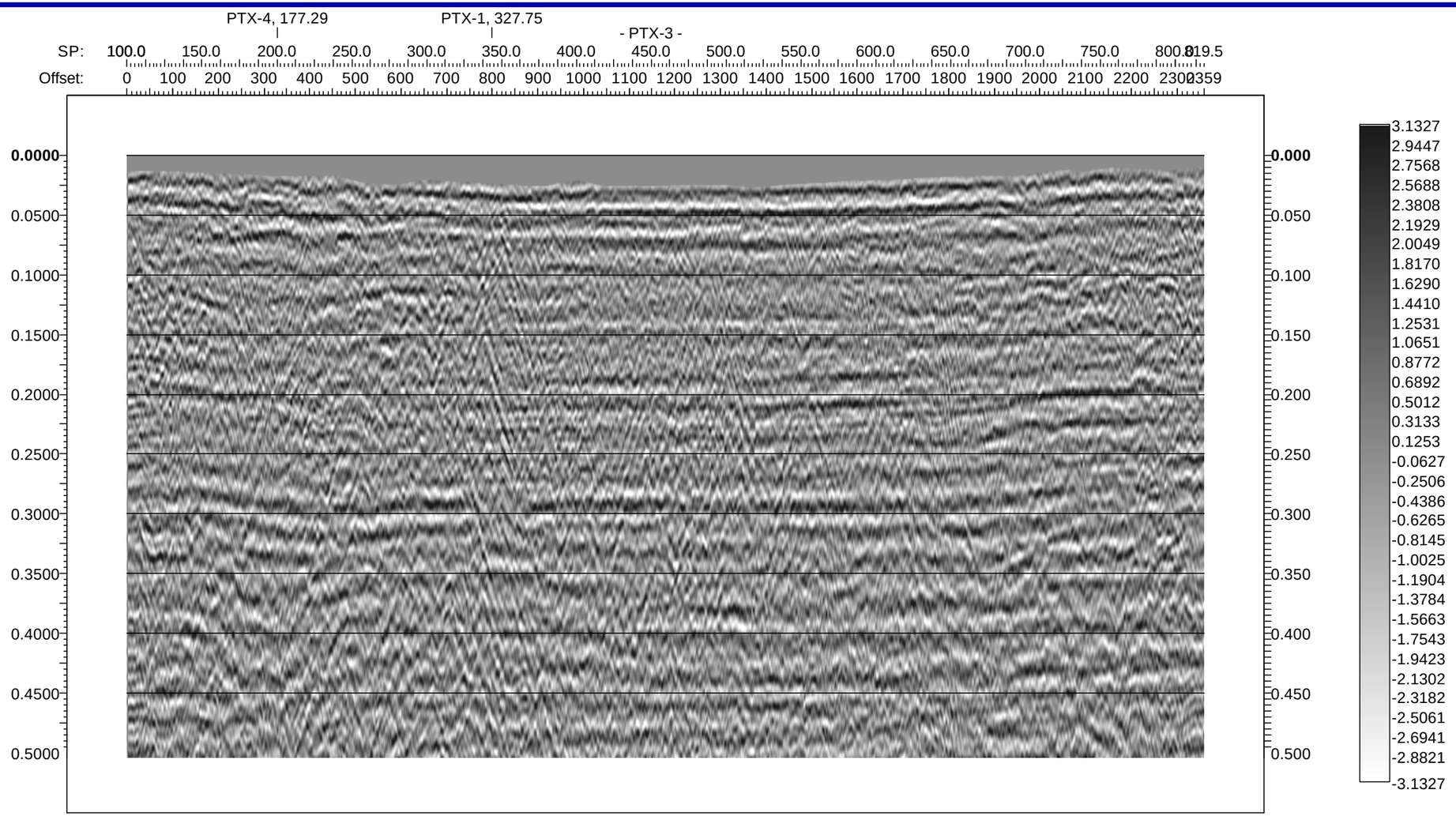

Seismic Profile PTX-3
Variable Density Plot
With Interpretations

Earth Sciences and Resouces Inst.

Project: PANTEX Playa_3

Project Location:

Line PTX-3
Variable Density Plot
With Interpretations

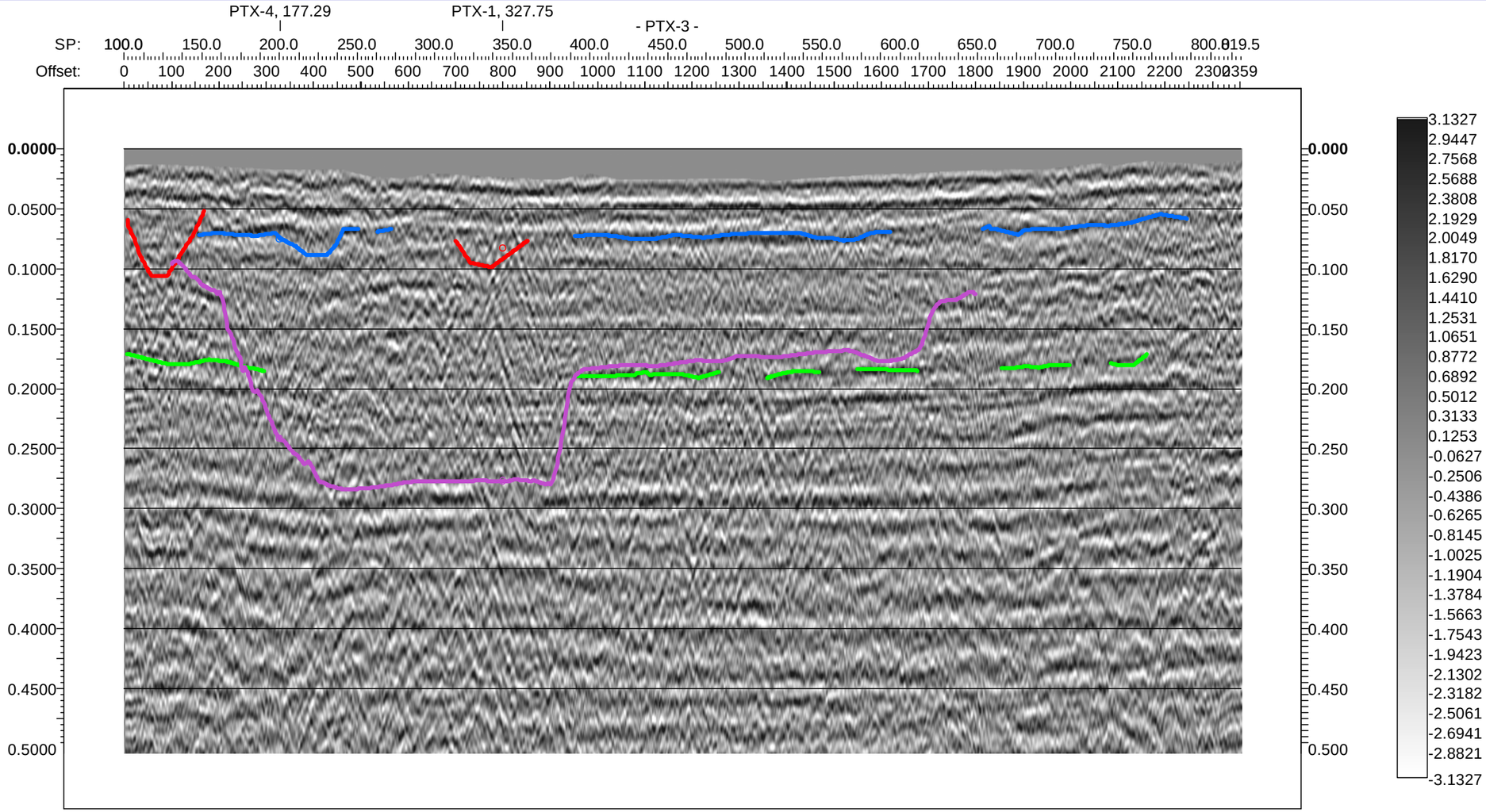

Seismic Profile PTX-4
Variable Density Plot
Without Interpretations

Earth Sciences and Resouces Inst.

Project: PANTEX Playa_3

Project Location:

Line PTX-4
Variable Density Plot
Without Interpretations

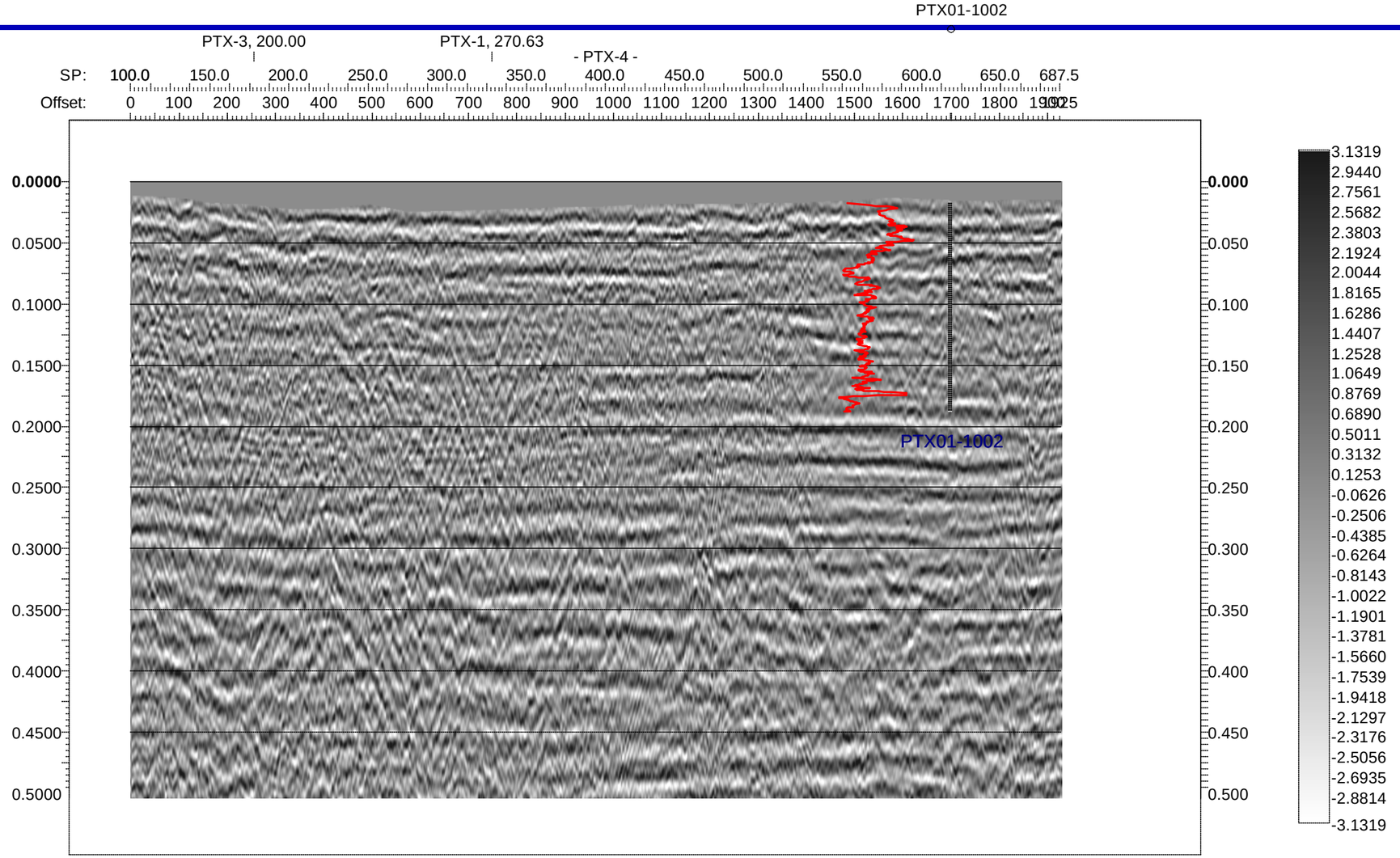

Seismic Profile PTX-4
Variable Density Plot
With Interpretations

Earth Sciences and Resouces Inst.

Project: PANTEX Playa_3

Project Location:

Line PTX-4
Variable Density Plot
With Interpretations

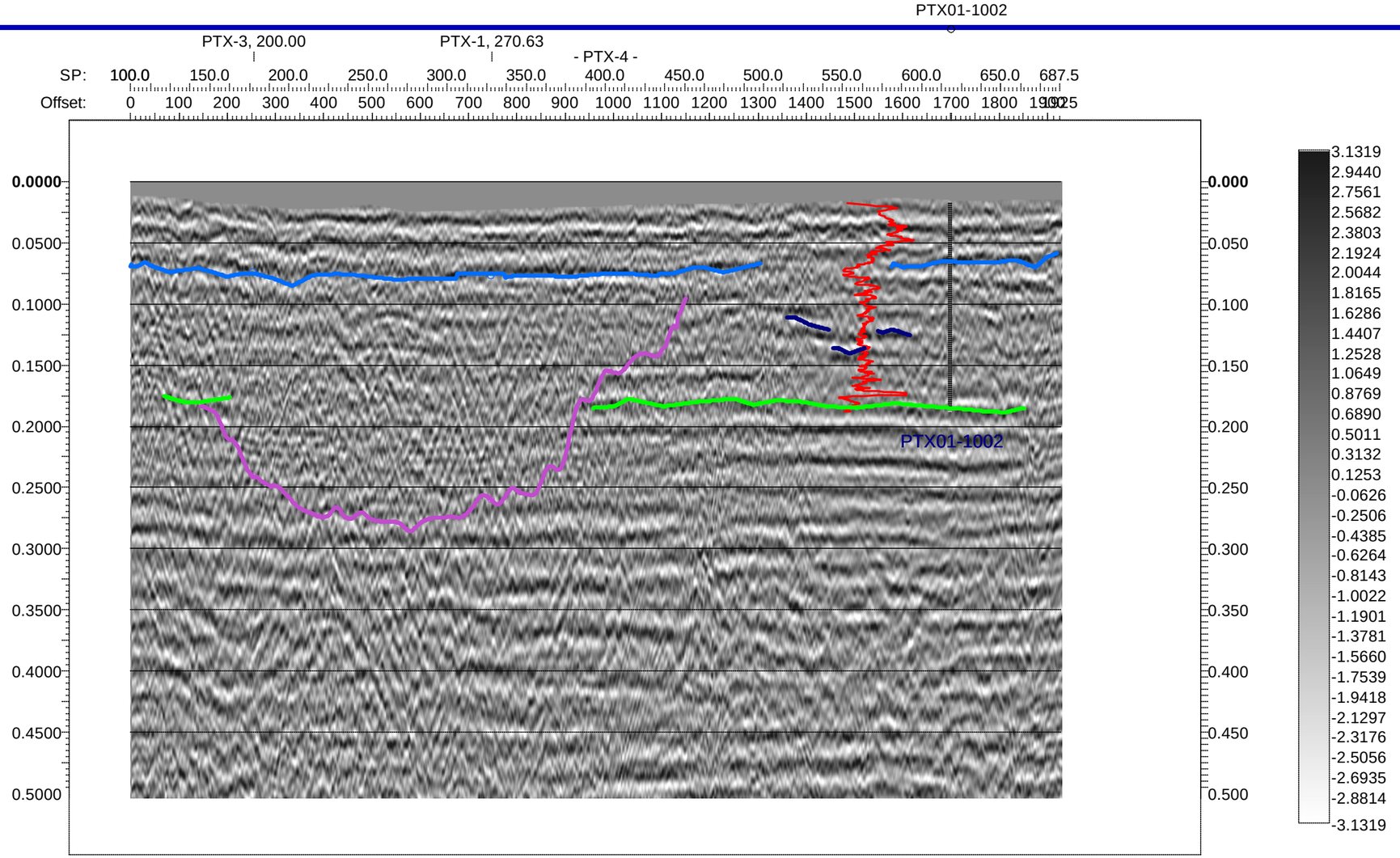

Appendix II

Seismic Profile PTX-1
Offset Range Limited Stack
Angles 0^0-17^0
Caliche Interval
Toluene
Model Velocities and Densities, Well PTX01-1008 and 1009

Earth Sciences and Resouces Inst.

Project: PANTEX Playa_3

Project Location:

Line PTX-1
Offset Range Limited Stack
Angles 0-17 Degrees
Caliche Interval
Toluene
Model Velocities and Densities
Well PTX-1008 and 1009

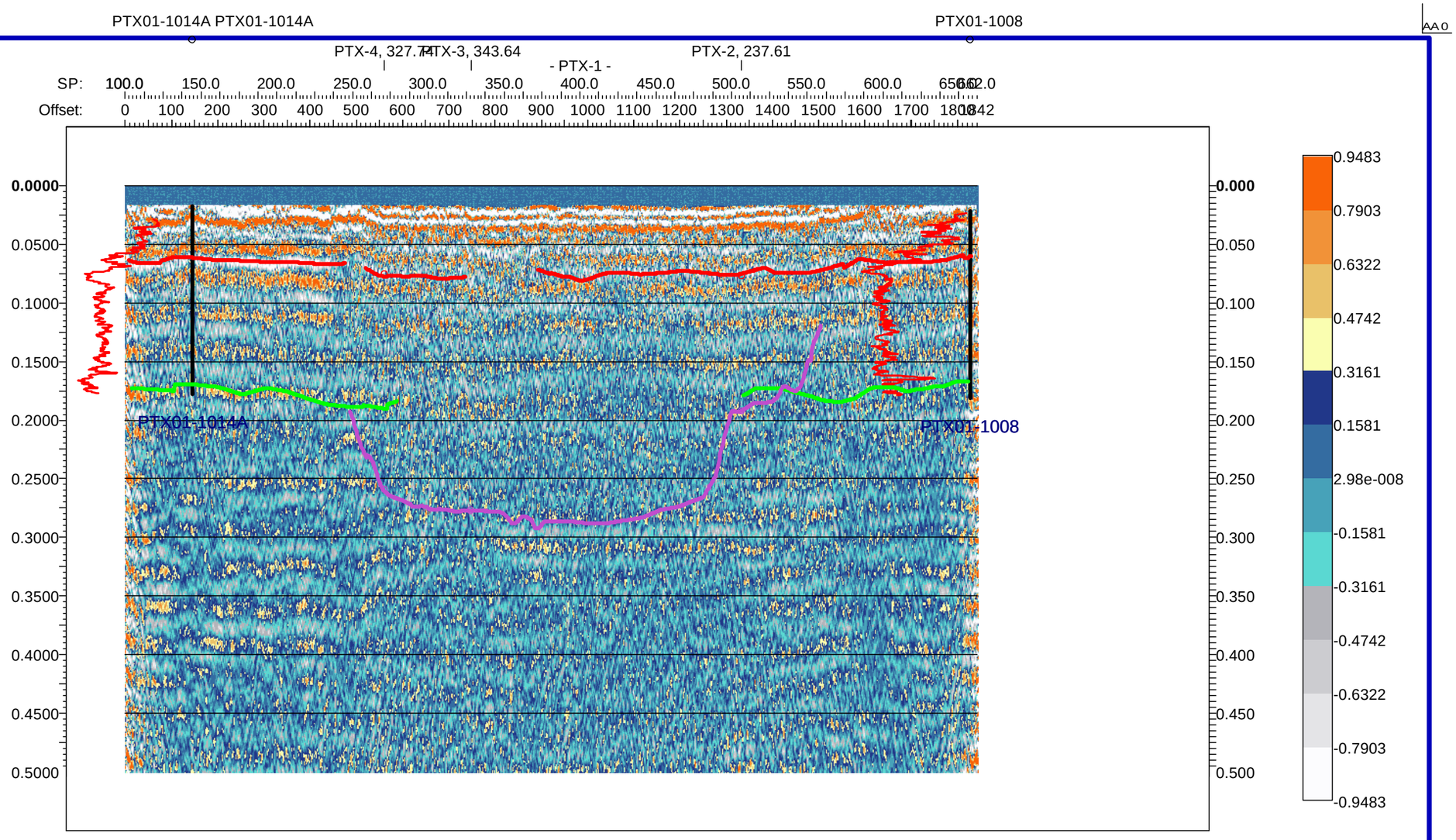

Seismic Profile PTX-1
Offset Range Limited Stack
Angles 17^0-34^0
Caliche Interval
Toluene
Model Velocities and Densities, Well PTX01-1008 and 1009

Earth Sciences and Resouces Inst.

Project: PANTEX Playa_3

Project Location:

Line PTX-1
Offset Range Limited Stack
Angles 17-34 Degrees
Caliche Interval
Toluene
Model Velocities and Densities
Well PTX01-1008 and 1009

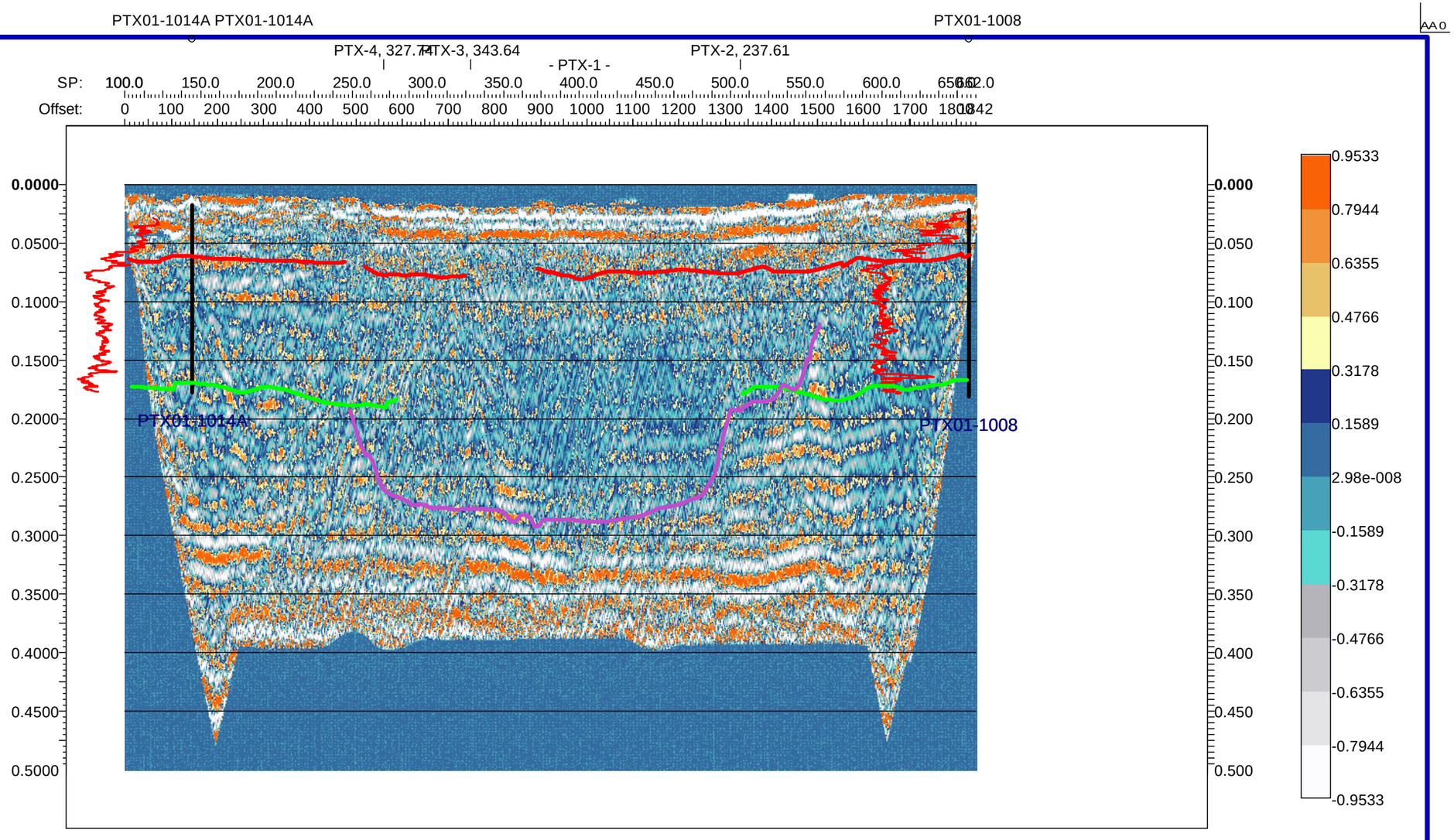

Seismic Profile PTX-2
Offset Range Limited Stack
Angles 0^0-17^0
Caliche Interval
Toluene
Model Velocities and Densities, Well PTX01-1008 and 1009

Earth Sciences and Resouces Inst.

Project: PANTEX Playa_3

Project Location:

Line PTX-2
Offset Range Limited Stack
Angles 0-17 Degrees
Caliche Interval
Toluene
Model Velocities and Densities
Well PTX01-1008 and 1009

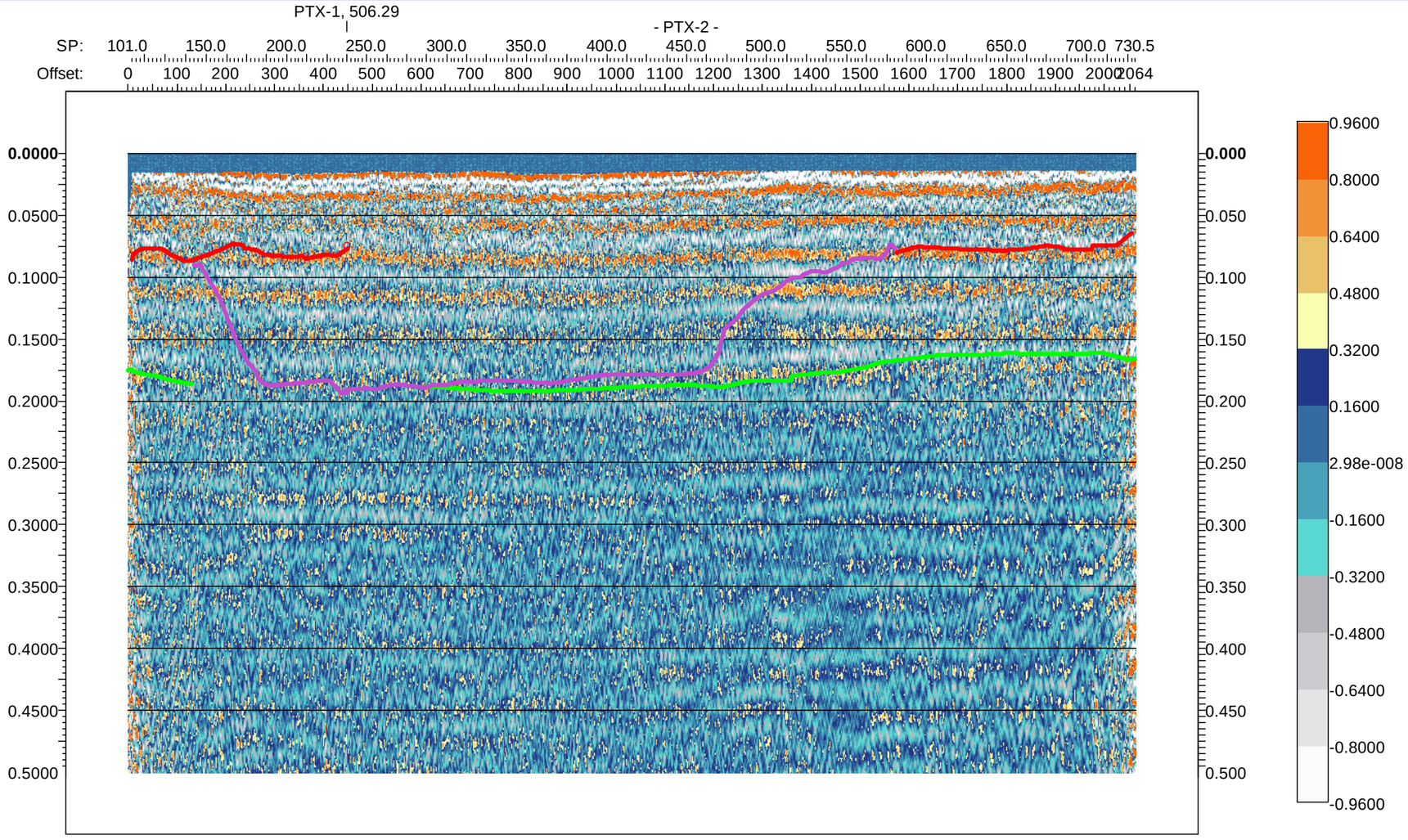

Seismic Profile PTX-2
Offset Range Limited Stack
Angles 17^0-34^0
Caliche Interval
Toluene
Model Velocities and Densities, Well PTX01-1008 and 1009

Earth Sciences and Resouces Inst.

Project: PANTEX Playa_3

Project Location:

Line PTX-2
Offset Range Limited Stack
Angles 17-34 Degrees
Caliche Interval
Toluene
Model Velocities and Densities
Well PTX01-1008 and 1009

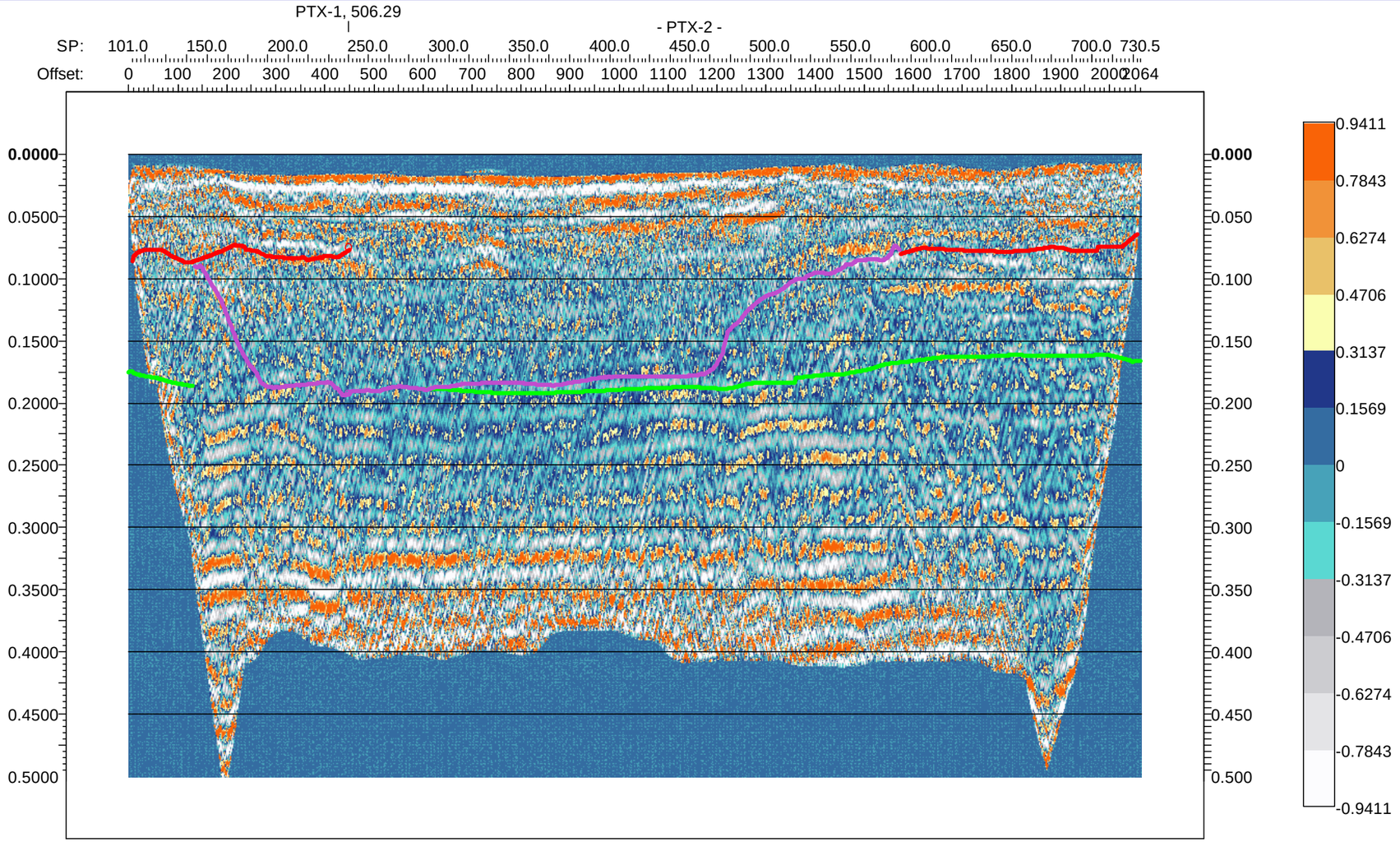

Seismic Profile PTX-1
Offset Range Limited Stack
Angles 0^0-22.5^0
Caliche Interval
TCE
Model Velocities and Densities, Well PTX01-1008

Earth Sciences and Resouces Inst.

Project: PANTEX Playa_3

Project Location:

Line PTX-1
Offset Range Limited Stack
Angles 0-22.55 Degrees
Caliche Interval
TCE
Model Velocities and Densities
Well PTX01-1008

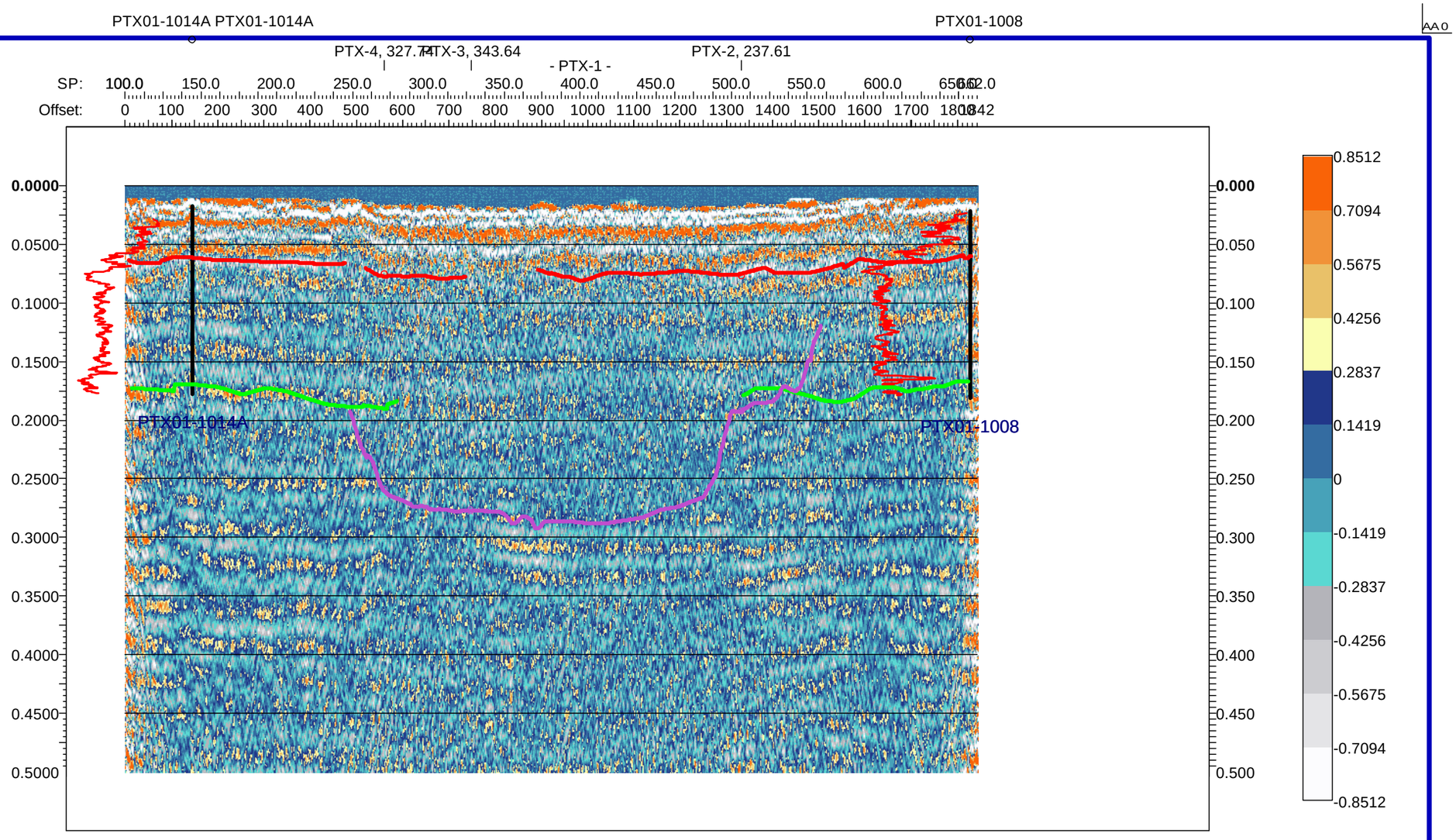

Seismic Profile PTX-1
Offset Range Limited Stack
Angles 22.5^0-45^0
Caliche Interval
TCE
Model Velocities and Densities, Well PTX01-1008

Earth Sciences and Resouces Inst.

Project: PANTEX Playa_3

Project Location:

Line PTX-1
Offset Range Limited Stack
Angles 22.5-45 Degrees
Caliche Interval
TCE
Model Velocities and Densities
Well PTX01-1008

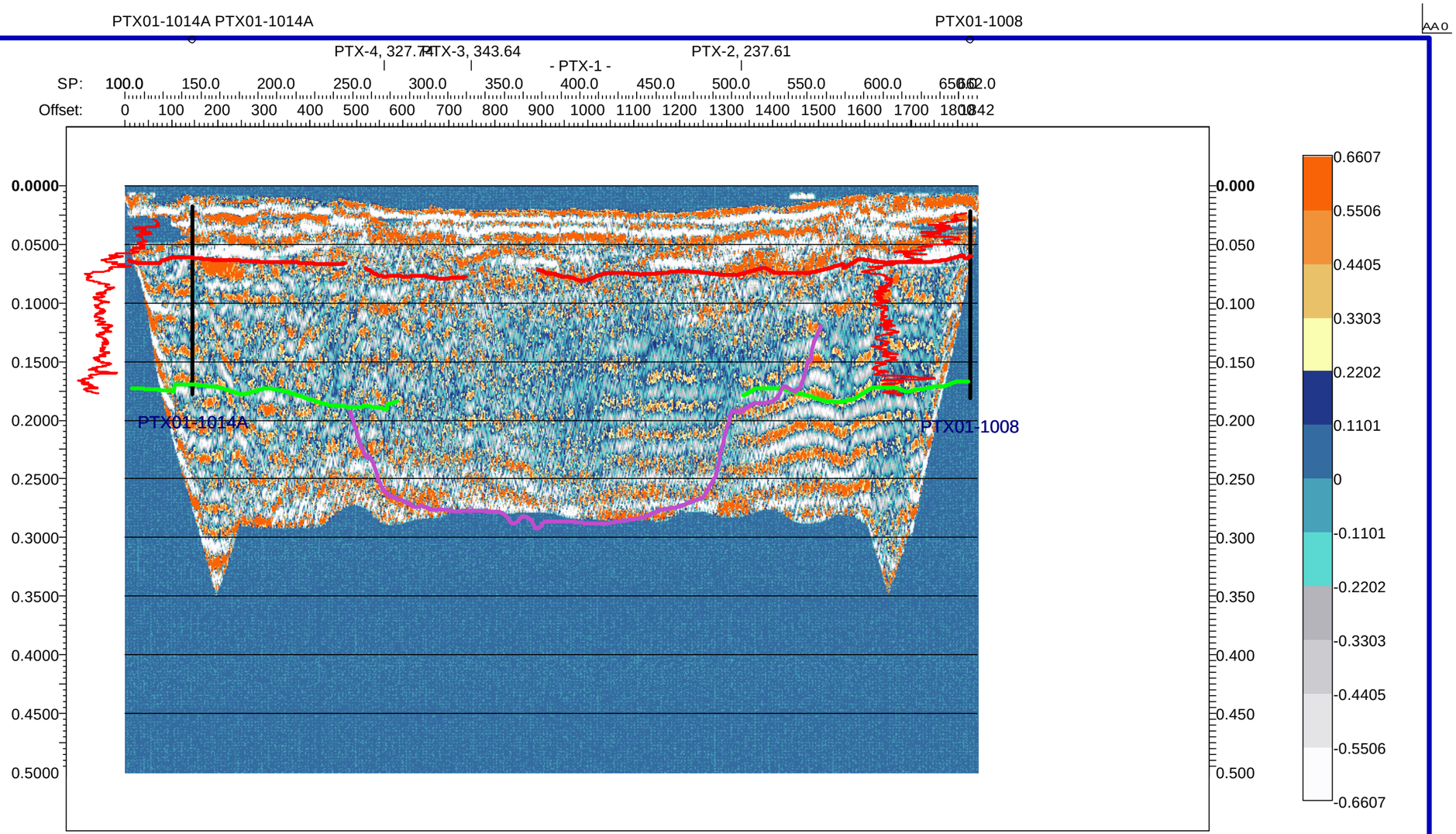

Seismic Profile PTX-1
Offset Range Limited Stack
Angles 0^0-15^0
Caliche Interval
TCE
Model Velocities and Densities, Well PTX01-1009

Earth Sciences and Resouces Inst.

Project: PANTEX Playa_3

Project Location:

Line PTX-1
Offset Range Limited Stack
Angles 0-15 Degrees
Caliche Interval
TCE
Model Velocities and Densities
Well PTX01-1009

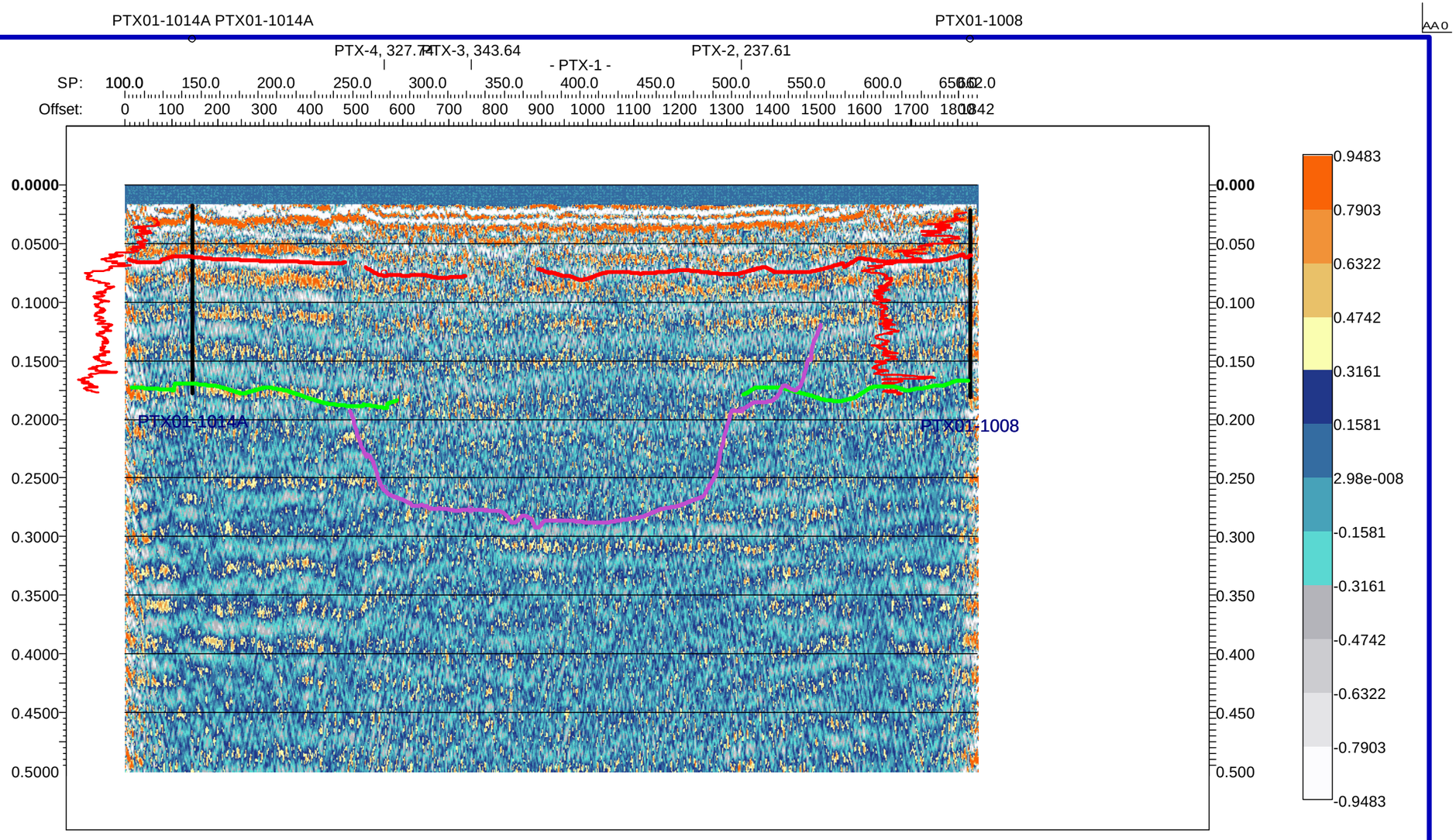

Seismic Profile PTX-1
Offset Range Limited Stack
Angles 15^0-30^0
Caliche Interval
TCE
Model Velocities and Densities, Well PTX01-1009

Earth Sciences and Resouces Inst.

Project: PANTEX Playa_3

Project Location:

Line PTX-1
Offset Range Limited Stack
Angles 15-30 Degrees
Caliche Interval
TEC
Model Velocities and Densities
Well PTX01-1009

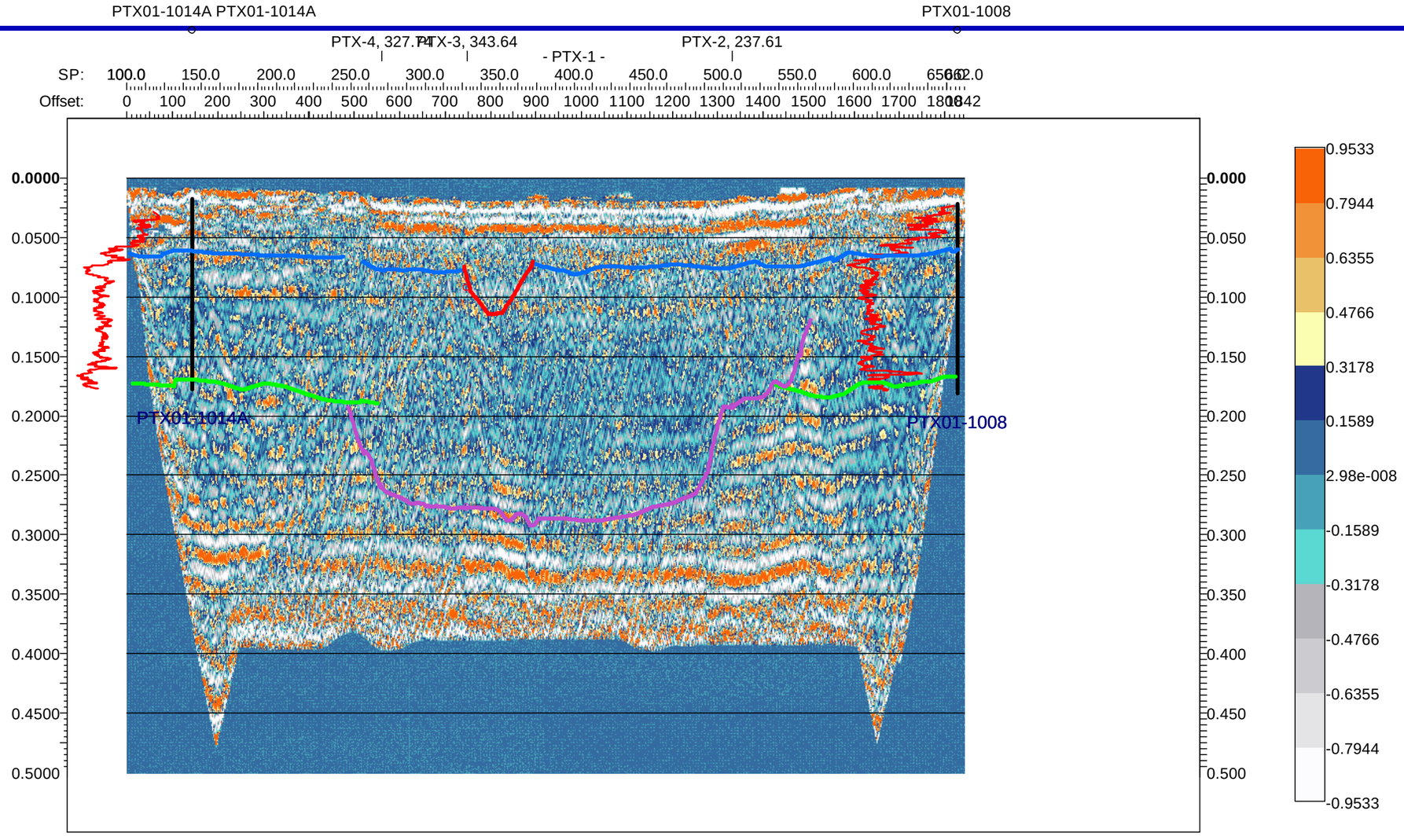

Seismic Profile PTX-2
Offset Range Limited Stack
Angles 0^0-22.5^0
Caliche Interval
TCE
Model Velocities and Densities, Well PTX01-1008

Earth Sciences and Resouces Inst.

Project: PANTEX Playa_3

Project Location:

Line PTX-2
Offset Range Limited Stack
Angles 0-22.5 Degrees
Caliche Interval
TCE
Model Velocities and Densities
Well PTX01-1008

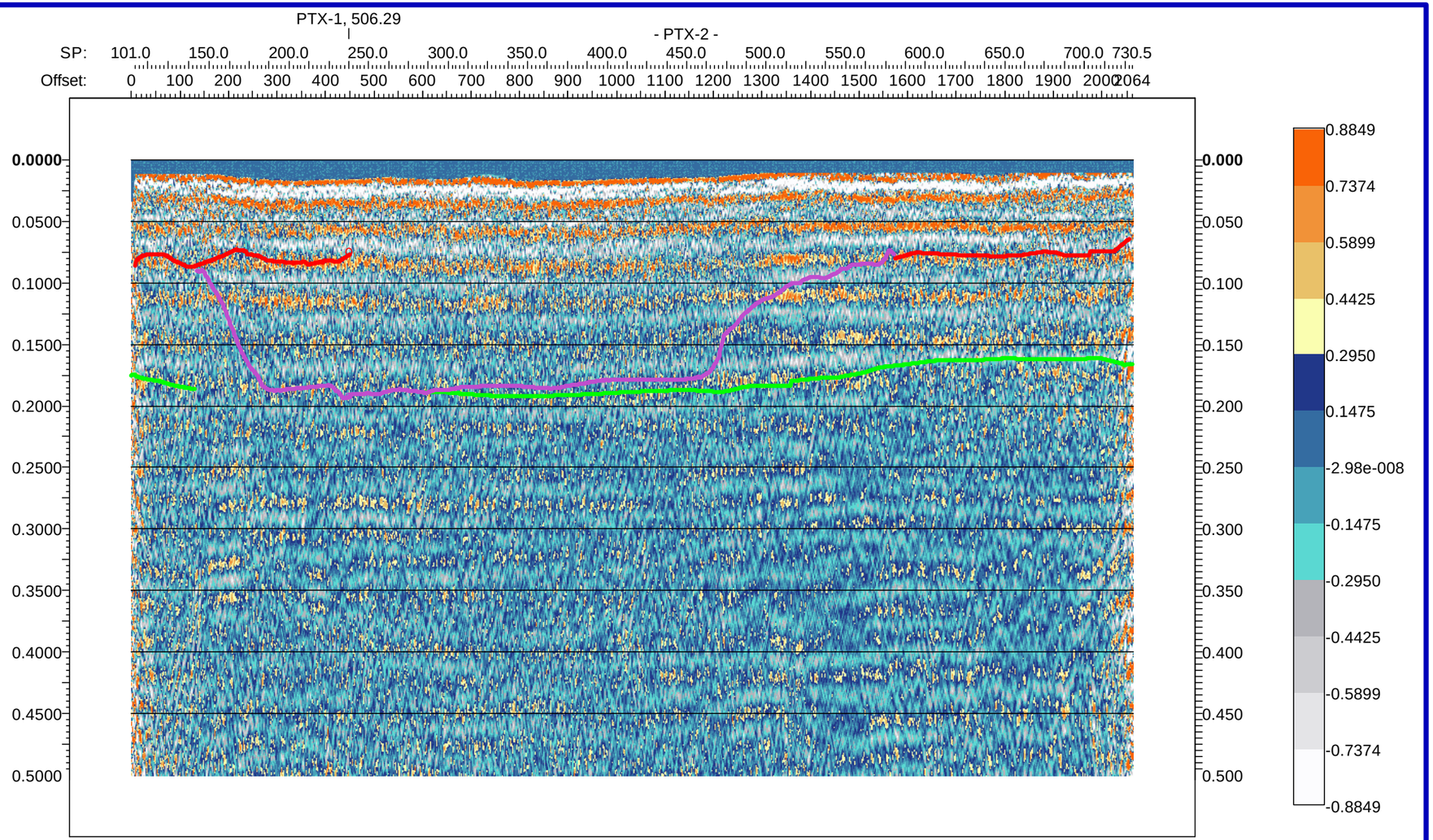

Seismic Profile PTX-2
Offset Range Limited Stack
Angles 22.5^0-45^0
Caliche Interval
TCE
Model Velocities and Densities, Well PTX01-1008

Earth Sciences and Resouces Inst.

Project: PANTEX Playa_3

Project Location:

Line PTX-2
Offset Range Limited Stack
Angles 22.5-45 Degrees
Caliche Interval
TCE
Model Velocities and Densities
Well PTX01-1008

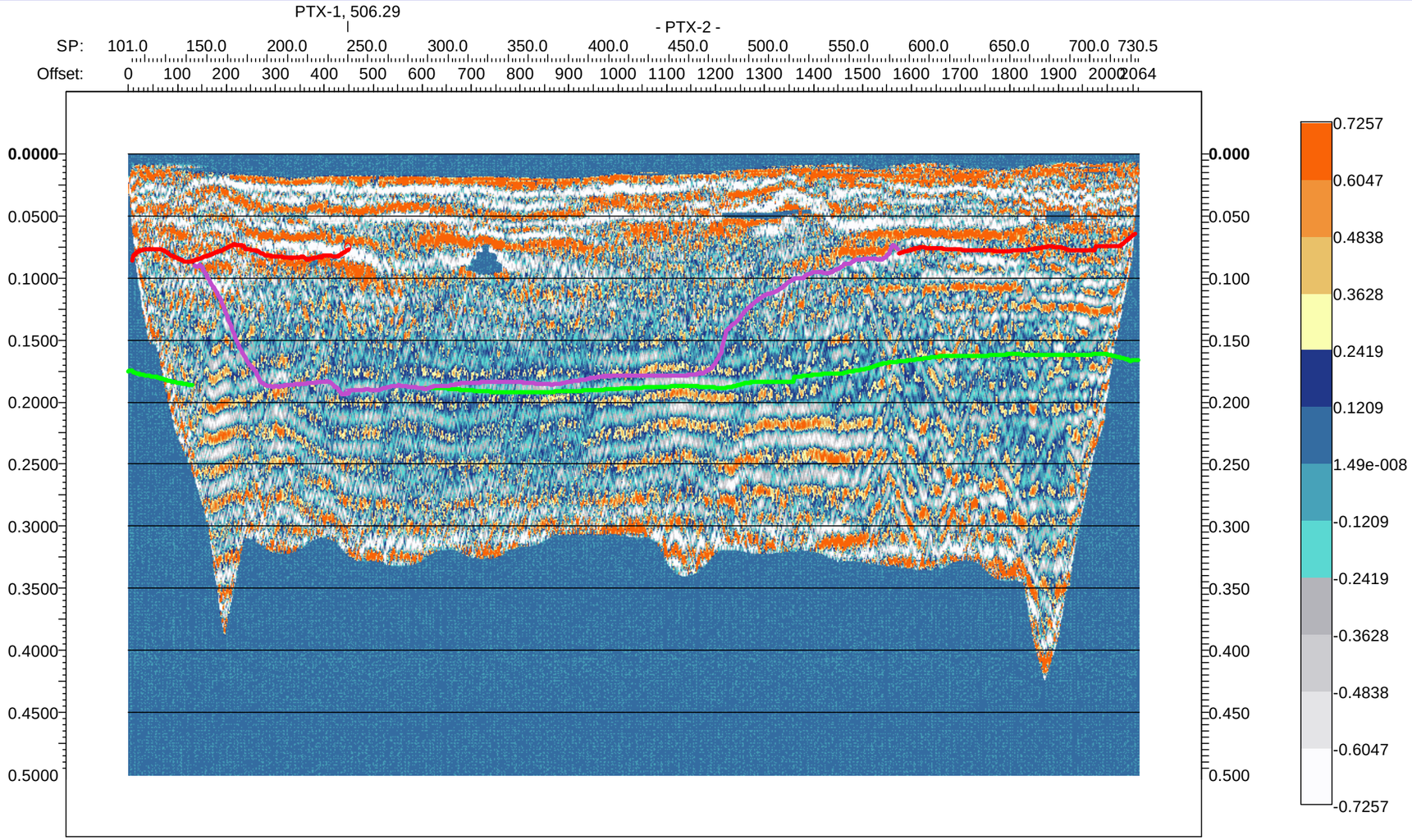

Seismic Profile PTX-2
Offset Range Limited Stack
Angles 0^0-15^0
Caliche Interval
TCE
Model Velocities and Densities, Well PTX01-1009

Earth Sciences and Resouces Inst.

Project: PANTEX Playa_3

Project Location:

Line PTX-2
Offset Range Limited Stack
Angles 0-15 Degrees
Caliche Interval
TCE
Model Velocities and Densities
Well PTX01-1009

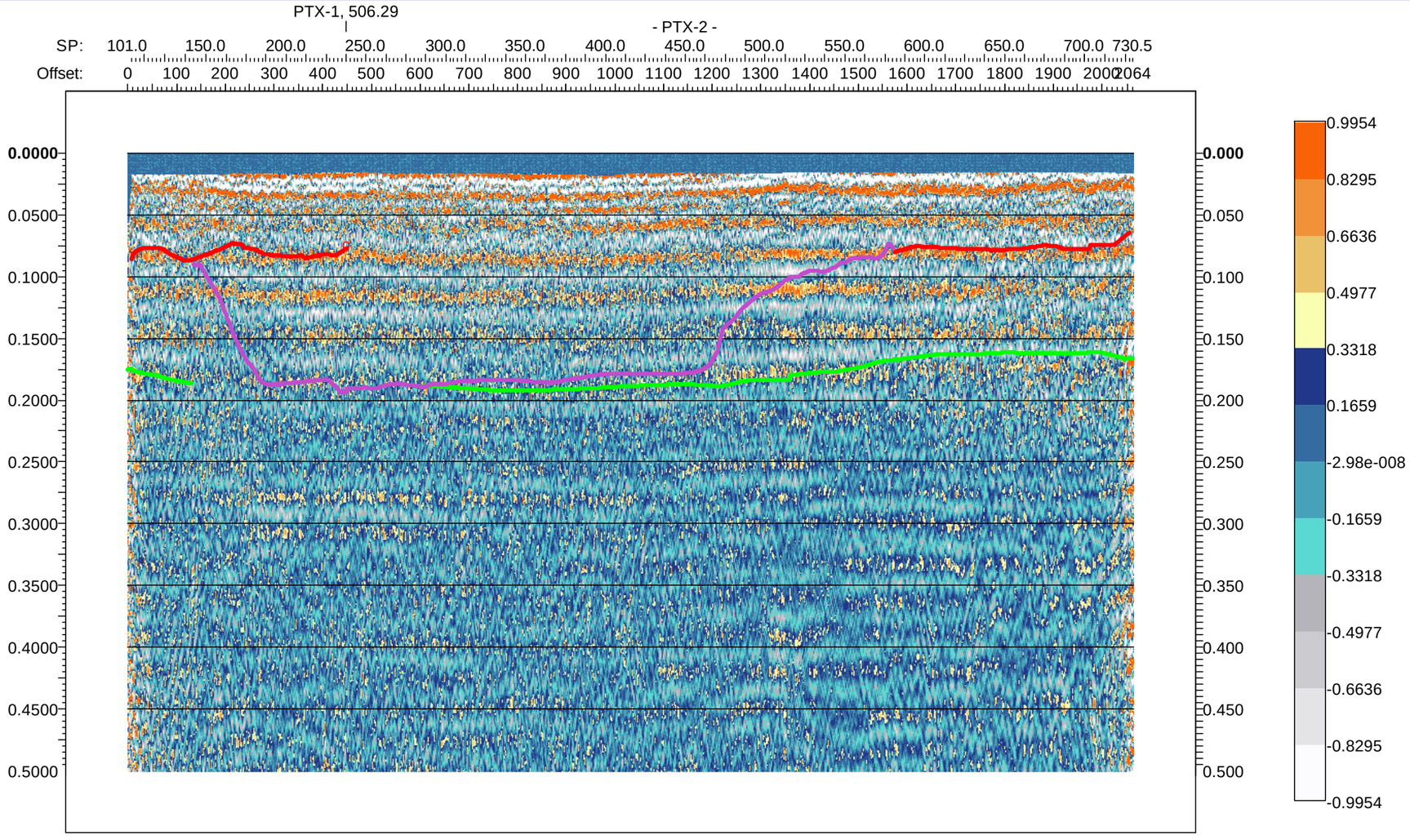

Seismic Profile PTX-2
Offset Range Limited Stack
Angles 15^0-30^0
Caliche Interval
TCE
Model Velocities and Densities, Well PTX01-1009

Earth Sciences and Resouces Inst.

Project: PANTEX Playa_3

Project Location:

Line PTX-2
Offset Range Limited Stack
Angles 15-30 Degrees
Caliche Interval
TCE
Model Velocities and Densities
Well PTX01-1009

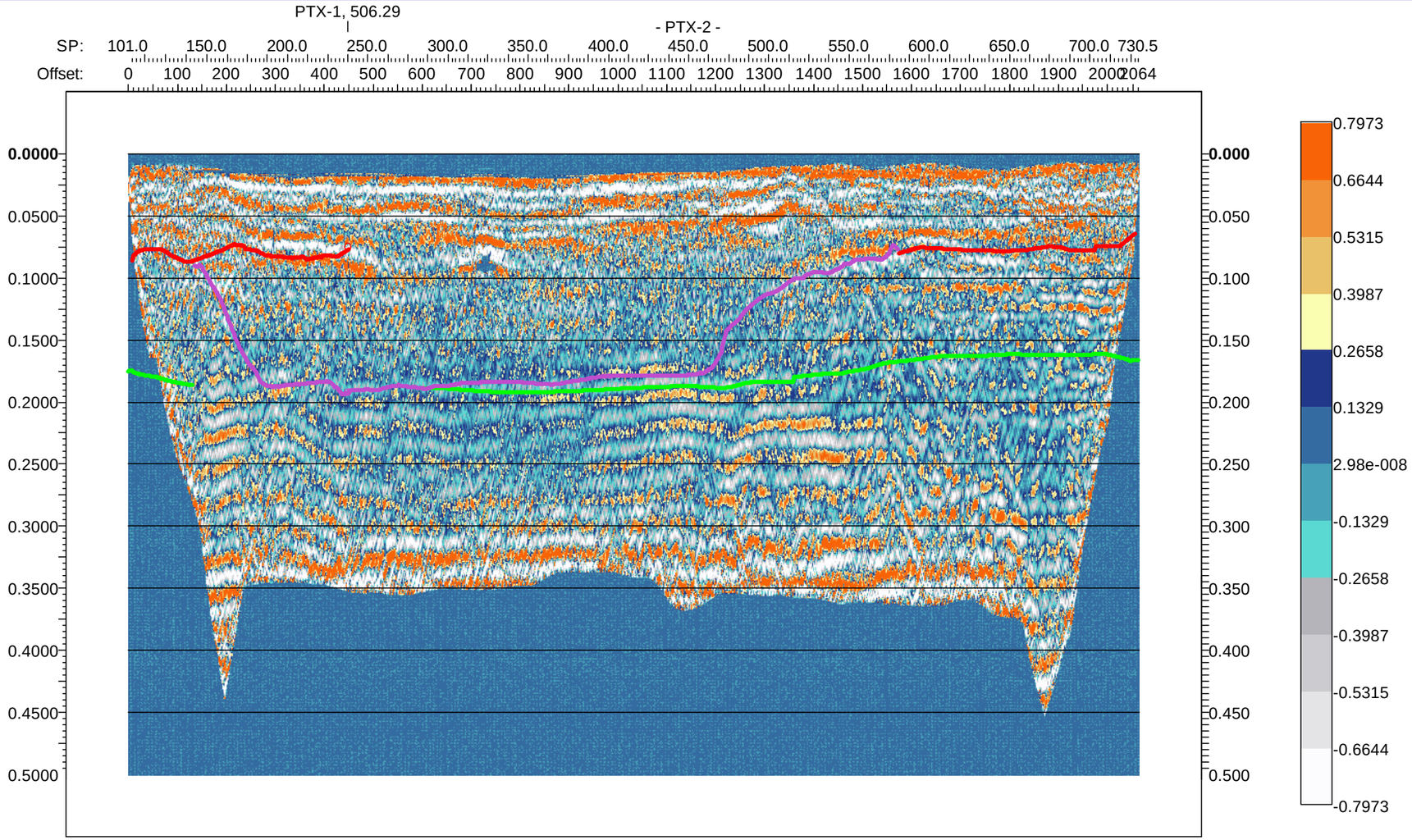

Seismic Profile PTX-1
Offset Range Limited Stack
Angles 0^0-20^0
FGZ Interval
TCE
Model Velocities and Densities, Well PTX01-1009

Earth Sciences and Resouces Inst.

Project: PANTEX Playa_3

Project Location:

Line PTX-1
Offset Range Limited Stack
Angles 0-20 Degrees
FGZ Interval
TCE
Model Velocities and Densities
Well PTX01-1009

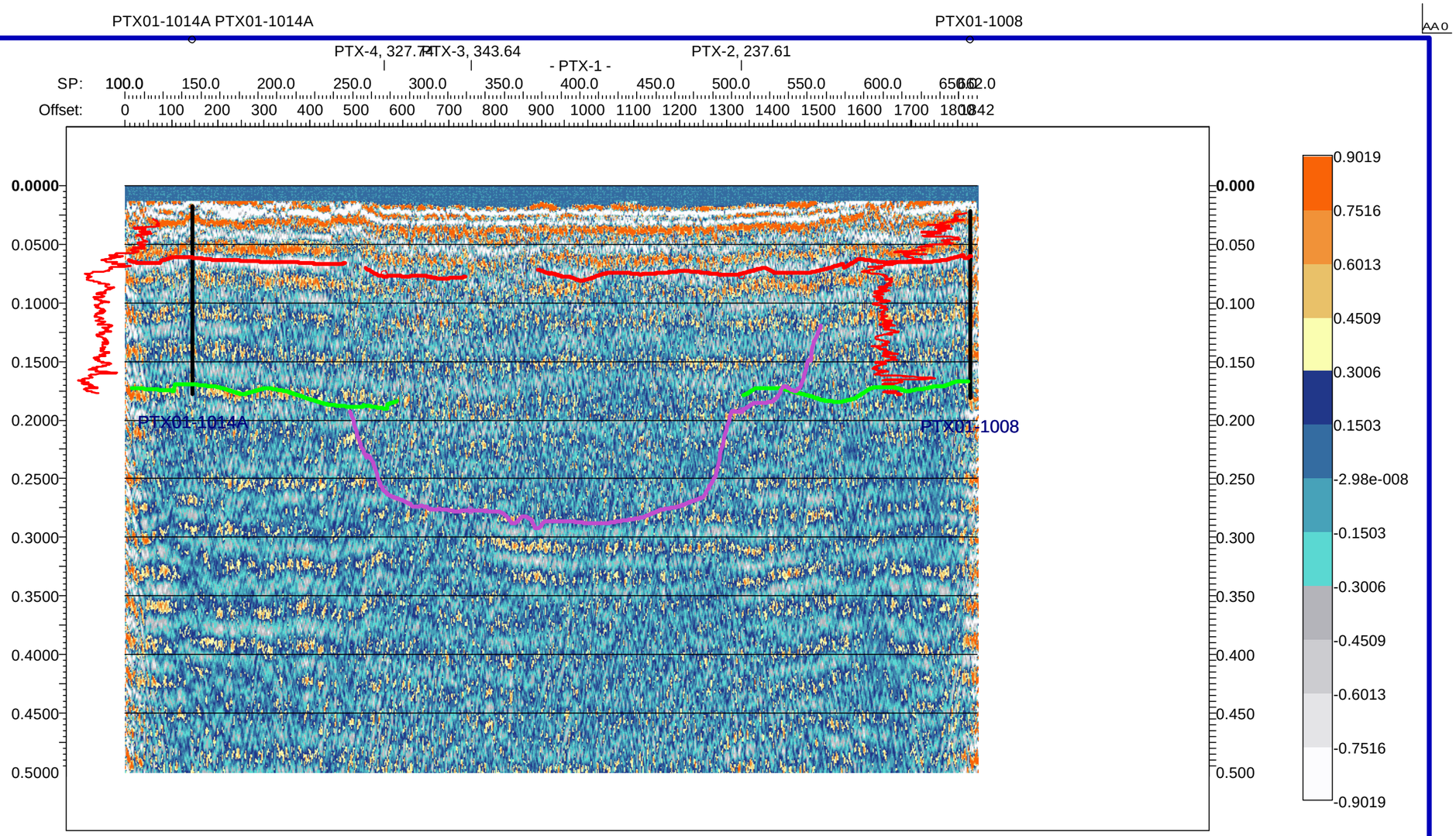

Seismic Profile PTX-1
Offset Range Limited Stack
Angles 20^0-40^0
FGZ Interval
TCE
Model Velocities and Densities, Well PTX01-1009

Earth Sciences and Resouces Inst.

Project: PANTEX Playa_3

Project Location:

Line PTX-1
Offset Range Limited Stack
Angles 20-40 Degrees
FGZ Interval
TCE
Model Velocities and Densities
Well PTX01-1009

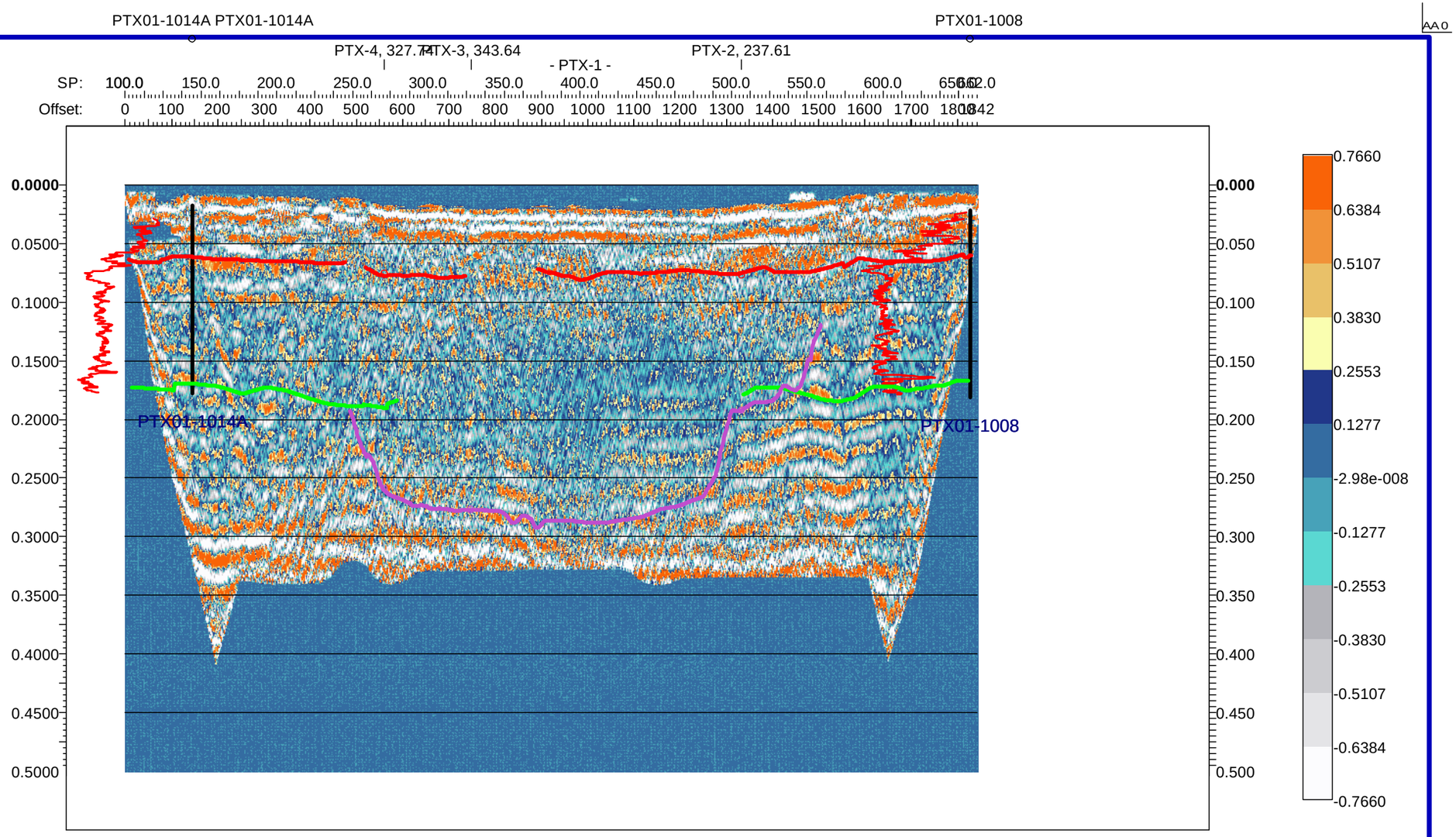

Seismic Profile PTX-1
Gradient Stack
FGZ Interval
TCE
Model Velocities and Densities, Well PTX01-1009

Earth Sciences and Resouces Inst.

Project: PANTEX Playa_3

Project Location:

Line PTX-1
Gradient Stack
FGZ Interval
TCE
Model Velocities and Densities
Well PTX01-1009

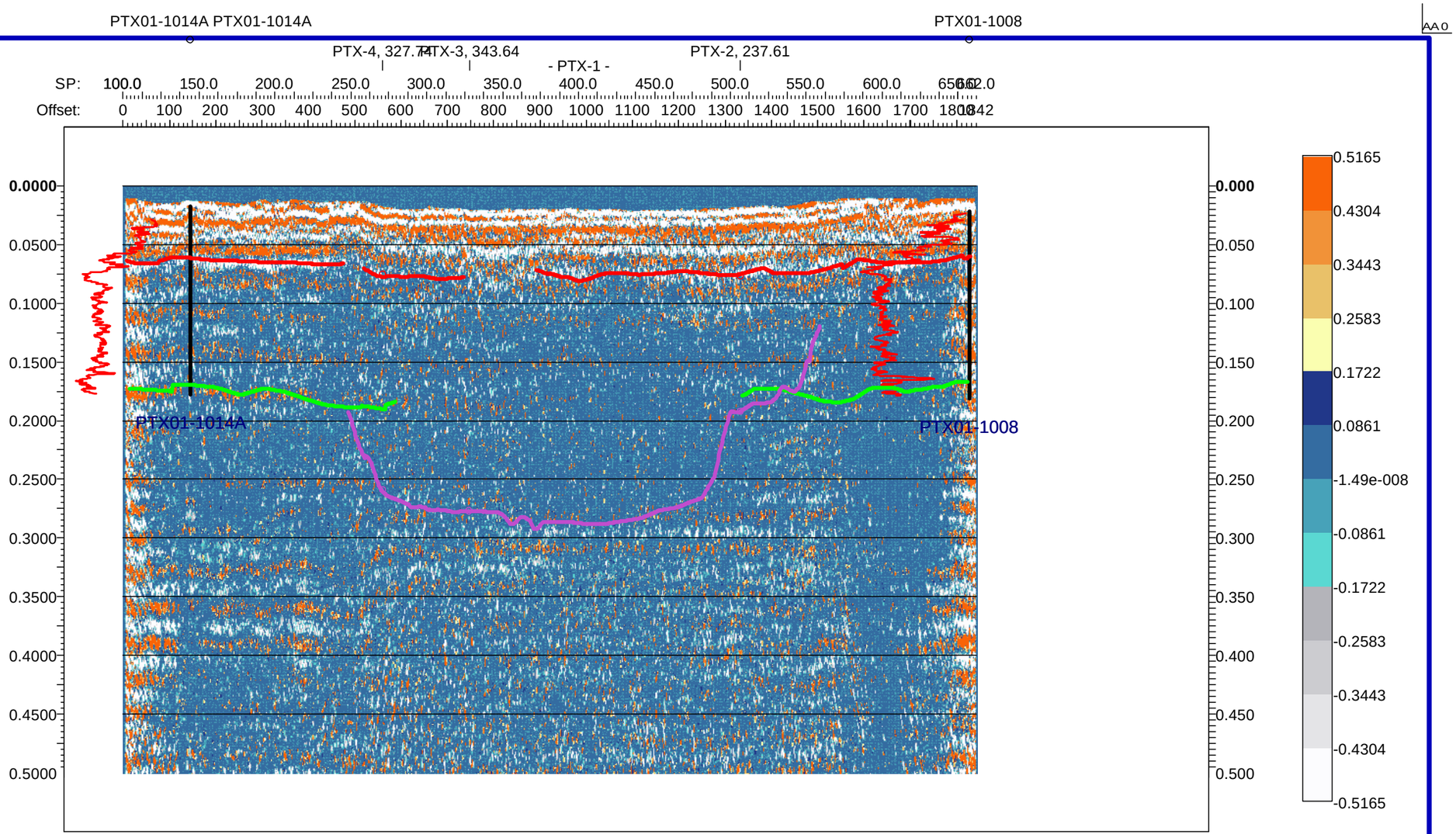

Seismic Profile PTX-2
Offset Range Limited Stack
Angles 0^0-20^0
FGZ Interval
TCE
Model Velocities and Densities, Well PTX01-1009

Earth Sciences and Resouces Inst.

Project: PANTEX Playa_3

Project Location:

Line PTX-2
Offset Range Limited Stack
Angles 0-20 Degrees
FGZ Interval
TCE
Model Velocities and Densities
Well PTX01-1009

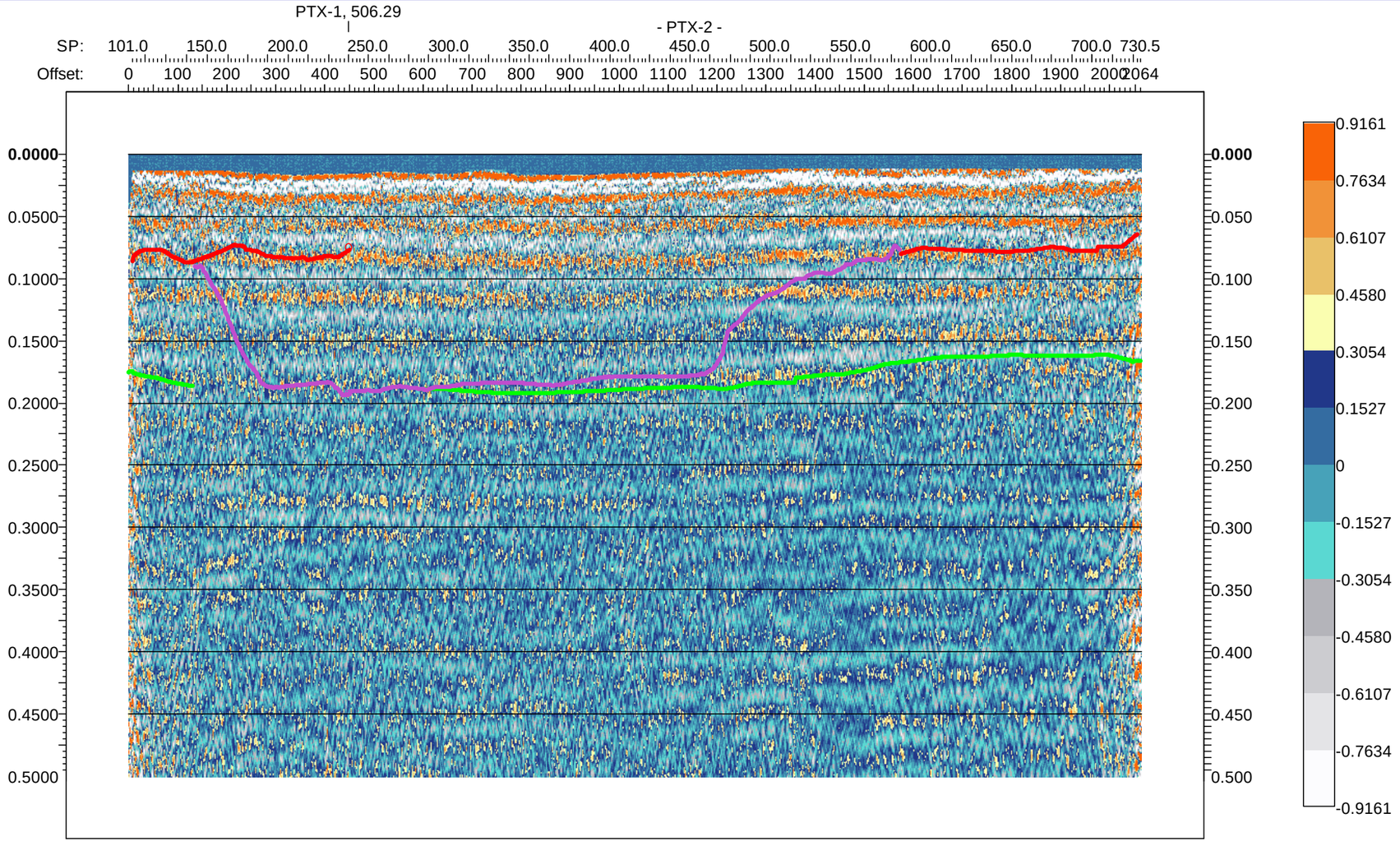

Seismic Profile PTX-2
Offset Range Limited Stack
Angles 20^0-40^0
FGZ Interval
TCE
Model Velocities and Densities, Well PTX01-1009

Earth Sciences and Resouces Inst.

Project: PANTEX Playa_3

Project Location:

Line PTX-2
Offset Range Limited Stack
Angles 20-40 Degrees
FGZ Interval
TCE
Model Velocities and Densities
Well PTX01-1009

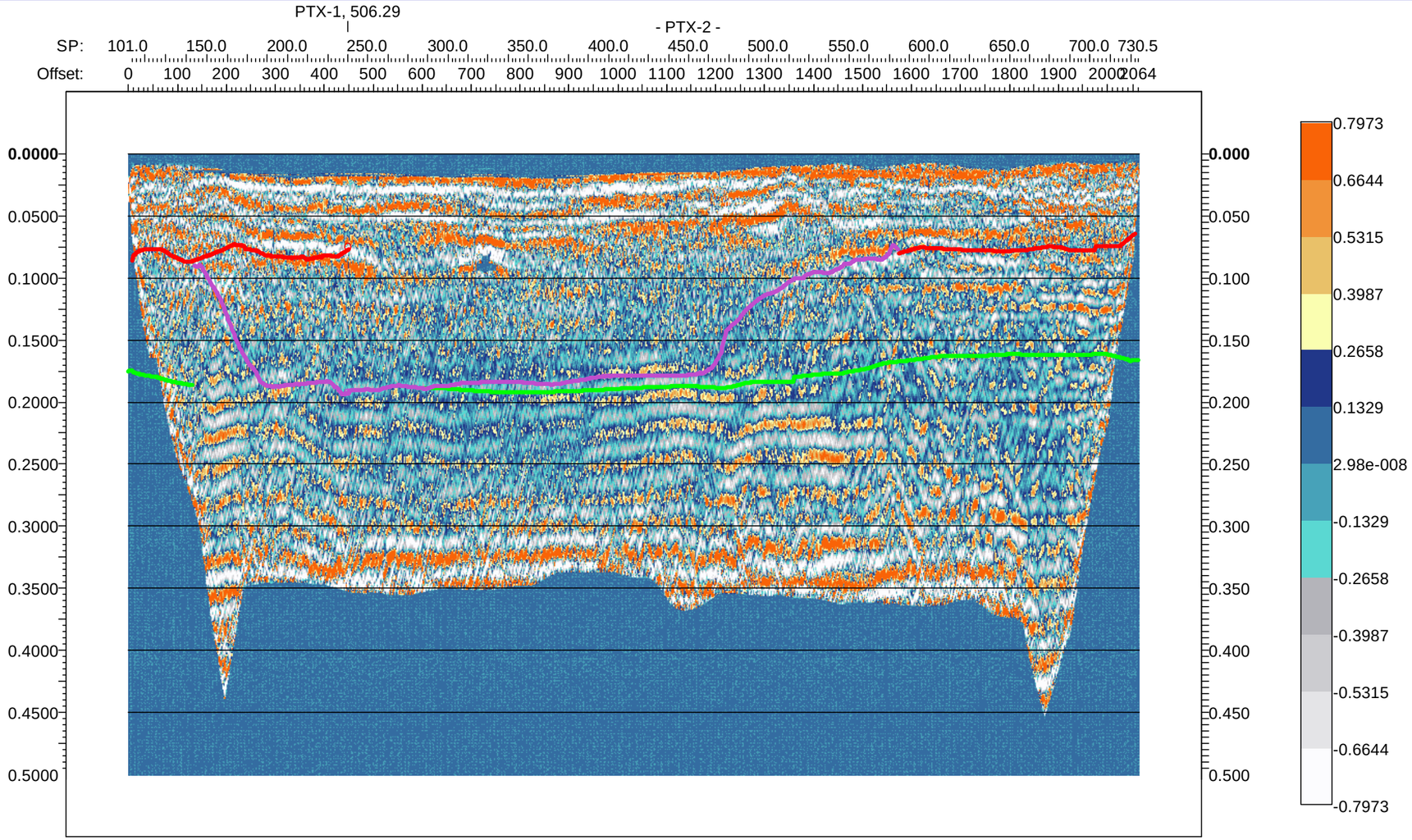

Seismic Profile PTX-2
Gradient Stack
FGZ Interval
TCE
Model Velocities and Densities, Well PTX01-1009

Earth Sciences and Resouces Inst.

Project: PANTEX Playa_3

Project Location:

Line PTX-2
Gradient Stack
FGZ Interval
TCE
Model Velocities and Densities
Well PTX01-1009